Modeling and Analysis for Optimization of Unsteady Aeroelastic Systems

Mehdi Ghommem

Dissertation submitted to Virginia Polytechnic Institute and State University
in partial fulfillment of the requirements for the degree of

Doctor of Philosophy
in
Engineering Mechanics

Muhammad R. Hajj, Chairman
Ishwar K. Puri, Co-Chairman
Philip S. Beran
Robert Canfield
Serkan Gugercin
Dean T. Mook

November 3, 2011
Blacksburg, Virginia

Keywords: Model reduction, micro air vehicles, optimization, sensitivity analysis

Modeling and Analysis for Optimization of Unsteady Aeroelastic Systems

Mehdi Ghommem

(ABSTRACT)

Simulating the complex physics and dynamics associated with unsteady aeroelastic systems is often attempted with high-fidelity numerical models. While these high-fidelity approaches are powerful in terms of capturing the main physical features, they may not discern the role of underlying phenomena that are interrelated in a complex manner. This often makes it difficult to characterize the relevant causal mechanisms of the observed features. Besides, the extensive computational resources and time associated with the use these tools could limit the capability of assessing different configurations for design purposes. These shortcomings present the need for the development of simplified and reduced-order models that embody relevant physical aspects and elucidate the underlying phenomena that help in characterizing these aspects. In this work, different fluid and aeroelastic systems are considered and reduced-order models governing their behavior are developed.

In the first part of the dissertation, a methodology, based on the method of multiple scales, is implemented to show its usefulness and effectiveness in the characterization of the physics underlying the system, the implementation of control strategies, and the identification of high-impact system parameters. In the second part, the unsteady aerodynamic aspects of flapping micro air vehicles (MAVs) are modeled. This modeling is required for evaluation of performance requirements associated with flapping flight. The extensive computational resources and time associated with the implementation of high-fidelity simulations limit the ability to perform optimization and sensitivity analyses in the early stages of MAV design. To overcome this and enable rapid and reasonably accurate exploration of a large design space, a medium-fidelity aerodynamic tool (the unsteady vortex lattice method) is implemented to simulate flapping wing flight. This model is then combined with uncertainty quantification and optimization tools to test and analyze the performance of flapping wing MAVs under varying conditions. This analysis can be used to provide guidance and baseline for assessment

of MAVs performance in the early stages of decision making on flapping kinematics, flight mechanics, and control strategies.

Dedicated to my beloved parents,
Mohamed & Ikram.

Acknowledgements

I would like to express my sincere gratitude and deep appreciation to my advisors, Prof. Muhammad Hajj and Prof. Ishwar Puri for giving me the opportunity to work on many interdisciplinary projects. Their great inspiration, generous assistance, beneficial advices and precious guidance have contributed enormously to shape and collate properly the different aspects of my research. It is a great honor for me to having worked closely with them.

I would also like to thank Dr. Philip Beran, Prof. Dean Mook, Prof. Serkan Gugercin, and Prof. Robert Canfield for serving on my committee and for their valuable questions and useful feedback about my research. Special thanks go to Dr. Philip Beran for his collaboration in my research and careful reading and review of the dissertation. A particular recognition goes to Prof. Dean Mook for having introduced me to the unsteady vortex lattice method and for contributing significantly to my work with helpful suggestions and meaningful discussions.

Professor Ali Nayfeh is an excellent teacher and his contributions to my research have been tremendous. He taught me three graduate courses on perturbation methods and nonlinear dynamics that were very useful in my research. I thank him as well for his interesting discussions, comments and precious directions when applying the method of multiple scales on aeroelastic systems.

I am also very grateful to my collaborators, namely Prof. Abdullah Nuhait of King Saud University, Dr. Imran Akhtar, and Dr. Bret Stanford, who were generous in sharing their knowledge and time. It has been a great pleasure to work closely with all of them. A particular mention goes to Prof. Layne Watson who introduced me to global and local optimizations which were among the fundamental pieces of my work.

I would like also to thank all of my fellows who participated in the MAV weekly meetings

(Dr. Philip Beran, Prof. Mayuresh Patil, Prof. Robert Canfield, Prof. Craig Woolsey, Dr. Richard Snyder, Prof. Balakumar Balachandran, Eric Stewart, Ben Leonard, and Tim Fitzgerald) for enhancing my work with many important suggestions and fruitful discussions. I am also grateful for the financial support from the Collaborative Center for Multidisciplinary Sciences (CCMS) under AFRL grant 8650-09-02-3938 and the Virginia Tech Institute for Critical Technology and Applied Science (ICTAS) Doctoral Scholars Program.

The help of all staff members of the Department of Engineering Science and Mechanics is acknowledged. In particular, I would like to deeply thank Lisa Smith, Sally Shrader, and Anne-Marie Bracken, for their pleasant personalities and precious help with the paperwork.

I shall also mention all of my colleagues in the Department of Engineering Science and Mechanics, namely former students (Drs. Andrea Mola, Giovanni Sansavini, Ganesh Balasubramanian, and Giancarlo Bordonaro) and current students (Abdessattar Abdelkefi, Yasser Aboelkassem, Sameh Ben Ayed, Mohamed Jrad, Nejib Masghouni, Youssef Bichiou, Bilel Aydi, Haithem Taha, Hassan Fayed, Arshad Mehmood, Brendan Kullback, and Grant Vogl) who have made my studies more enjoyable. I also extend my thanks to all my friends in Blacksburg, namely Dr. Saher Lahouar and his nice family, Faycel Beji, Shouib Al-Qudah, Dr. Mohamed Ben Ramadhan, Idir Mechai, Omar Al-Abbasi, Amr Hilal, and Ahmed Kamal Ali. Being surrounded with such nice people helped me a lot to overcome the difficulty of being away from home. I also thank to my close friends in Tunisia, Wajdi Tekaya, Amine Bouassida, Seif-Eddine Beldi, Marouan Dhiab, Dr. Hassen Ouakad, and others.

I am also grateful to Prof. Sami El-Borgi and Prof. Slim Choura from Tunisia Polytechnic School for having introduced me to the Department of Engineering Science and Mechanics.

My deep thanks go to my fiancé Asma whose encouragement, love, and presence were the permanent source of my strength to achieve my professional goals.

Special thanks, beyond what any words can express, go to my parents for their prayers and continuous support. They have always been present with their affection and encouragement. They have been very careful in providing me the best conditions for success. I hope that they are proud of me. My thanks also go to my brother Zied and my sister Meriem for their affection. I extend my thanks as well to all my family for their support, with a special thought to my aunt Saida.

Contents

Abstract **ii**

Acknowledgments **iv**

Contents **vii**

List of Figures **xi**

List of Tables **xviii**

1 Introduction **1**

1.1 Model Reduction Framework 2

1.2 A Multidisciplinary System: Micro Air Vehicle 5

1.2.1 Multi-physics aspects of propulsive systems 5

1.2.2 Multifidelity modeling of aerodynamic flow and forces 8

1.2.3 Modeling of structural response of flapping wings 12

1.3 Objectives and Approaches 14

1.4 Outline of the Thesis 14

2 Model Reduction **17**

2.1 Example 1: Low-dimensional Tool for Predicting Force Coefficients on a Circular Cylinder 17

2.1.1 Numerical simulations 18

2.1.2 Low-dimensional representation of flow quantities 18

2.1.3 The proper orthogonal decomposition 19
2.1.4 Reduced-order model of the velocity field 25
2.1.5 Reduced-order model for the pressure field 27
2.1.6 Pressure POD modes 27
2.1.7 Linear stochastic estimator (LSE) 28
2.1.8 Force weight coefficients 30
2.1.9 Modeling of unsteady flows 33
2.2 Example 2: Normal Form Representation of The Aeroelastic Response of The Goland Wing 37
2.2.1 Problem formulation 38
2.2.2 Analysis 44
2.2.3 Results and discussion 55
2.2.4 Summary 60
2.3 Example 3: Uncertainty Analysis Near Bifurcation of an Aeroelastic System 61
2.3.1 Representation of the aeroelastic system 63
2.3.2 Uncertainty quantification via intrusive polynomial chaos 66
2.3.3 Uncertainty quantification via normal form of Hopf bifurcation 73
2.4 Example 4: Control of Limit Cycle Oscillations of a Two-Dimensional Aeroelastic System 80
2.4.1 Static feedback control 82
2.4.2 Case study 83
2.4.3 Summary 87

3 Stochastic Modeling of Incident Gust Effects on Aerodynamic Lift 88
3.1 Stochastic Gust Representation 89
3.2 2-D Unsteady Vortex Lattice Method Implementation 90
3.2.1 Formulation 90
3.2.2 Wake development 92
3.2.3 Aerodynamic lift 94
3.3 Uncertainty Quantification 95

3.3.1 Background . . . 95
3.3.2 Polynomial chaos expansion . . . 96
3.3.3 Gust uncertainties . . . 97
3.3.4 Intrusive formulation . . . 100
3.4 Results and Discussion . . . 101
3.4.1 Global sensitivity analysis . . . 101
3.4.2 Validation . . . 102
3.5 Summary . . . 104

4 Optimization of Flapping Kinematics in Hovering Flights 108
4.1 Aerodynamic Modeling of Hovering Flights . . . 108
4.1.1 2-d unsteady vortex lattice method . . . 108
4.1.2 Flapping wing kinematics . . . 111
4.2 Kinematics Optimization . . . 113
4.2.1 Problem formulation . . . 113
4.2.2 Results and discussion . . . 116
4.3 Sensitivity Analysis of Optimized Kinematics . . . 122
4.4 Summary . . . 123

5 Robust-based Analysis of Flapping Kinematics for Micro Air Vehicles 131
5.1 3-D Unsteady Vortex Lattice Method . . . 132
5.2 Aerodynamic loads . . . 138
5.3 Wing Kinematics . . . 140
5.3.1 Implementation of wing motion . . . 142
5.3.2 Implementation of wing deformation (active shape morphing) . . . 142
5.4 Numerical Simulations and Validation . . . 143
5.4.1 Flow past a plunging rectangular wing . . . 143
5.4.2 Flow past a flapping/twisting rectangular wing . . . 145
5.4.3 Flow past a flapping cambered wing . . . 147
5.5 Global Optimization . . . 148
5.5.1 Problem formulation . . . 150

5.5.2 Morphing parametrization 151
5.5.3 Results: optimization with a trigonometric morphing parametrization 153
5.5.4 Results: optimization with a spline-based morphing parametrization . 155
5.6 Global vs. Local Optimization 159
5.7 Robustness of Optimal Points 162
5.8 How Wing Morphing Can Help in Thrust Generation? 164

6 Conclusions and Recommendations for Future Work 174
6.1 Summary and Conclusions 174
6.2 Recommendations for Future Work on Micro Air Vehicles 177

Bibliography 178

List of Figures

1.1 Model reduction framework of multidisciplinary systems. 3

2.1 Time histories of the lift and drag coefficients obtained from the CFD simulation at $Re = 180$ 19

2.2 A descriptive schematic showing the implementation of the low-dimensional method. 20

2.3 Normalized singular values and cumulative energy content of POD modes. . . 22

2.4 Contours of the streamwise velocity POD modes ($\phi_i^u, \quad i = 1, 2, ..., 6$) for the case of steady mean flow 23

2.5 Contours of the crossflow velocity POD modes ($\phi_i^v, \quad i = 1, 2, ..., 6$) for the case of steady mean flow 24

2.6 A two dimensional projection of the POD phase portrait on (q_1, q_2)-plane (solid) and snapshot portrait (stars). 10 POD modes are kept in the truncated expansion given by Equation (2.3). 26

2.7 Normalized singular values and cumulative energy content of pressure POD modes. 28

2.8 Pressure POD modes for steady mean flow condition. 29

2.9 Pressure coefficients for steady mean flow conditions: Snapshot projection vs. LSE. 31

2.10 Lift and drag coefficients: ROM vs. CFD. 33

2.11 A Streamwise velocity at the probe from CFD and POD (unsteady mean flow case). 10 POD modes are kept in the truncated expansion given by Equation (2.13). 36
2.12 Lift and drag coefficients for the unsteady inflow: reduced-order model (ROM) vs direct numerical simulation (CFD). 36
2.13 A Cantilever Wing Geometry. 39
2.14 Variations of the eigenvalues with the air speed in the complex plane. 56
2.15 Complex-valued aerodynamic response at the Hopf bifurcation. 58
2.16 LCO amplitudes of bending and torsion motions at the wing tip. 60
2.17 Schematic of LCO response of an aeroelastic system. Arrows denote path of system response that may occur due to uncertainty in structural or aerodynamic parameters: ($\rightarrow$) increasing, ($\leftarrow$) decreasing. 62
2.18 Sketch of a two-dimensional airfoil 64
2.19 Variations of (a) the real (dampings) and (b) imaginary (frequencies) parts of the ρ_j with the freestream velocity U (m/s). 66
2.20 Variation of the real part of ρ_j with the freestream velocity U (m/s). (a) $\sigma_1 = 0.05\overline{k}_{\alpha 0}$ ($U_{fl} = 8.84929$, $U_{fu} = 9.40177$), (b) $\sigma_1 = 0.1\overline{k}_{\alpha 0}$ ($U_{fl} = 8.57824$, $U_{fu} = 9.68138$), and (c) $\sigma_1 = 0.15\overline{k}_{\alpha 0}$ ($U_{fl} = 8.31217$, $U_{fu} = 9.96227$) 69
2.21 Variation of flutter onset speed U_f (m/s) with σ_1 70
2.22 Time histories of the pitch motion. The solid line represents the time history obtained by integrating numerically the deterministic model. The dashed line is from the stochastic model based on the 1^{st} order PCE. (a) $\xi_2 = 1$ and $\sigma_2 = 0.1\overline{k}_{\alpha 2}$ and (b) $\xi_2 = 5$ and $\sigma_2 = 0.1\overline{k}_{\alpha 2}$. 73
2.23 LCO amplitudes of plunge and pitch motions: -, analytical prediction, $*$, numerical integration. (a) plunge motion and (b) pitch motion. 78
2.24 LCO amplitudes of pitch motion. Arrows show path of system response that may occur due to the effect of combined uncertainties in linear and nonlinear parameters: ($\rightarrow$) increasing, ($\leftarrow$) decreasing. 78

2.25 Sensitivity of the flutter speed to variations in the structural stiffnesses. The solid line represents the flutter speed obtained from the perturbation analysis. The stars represent the exact flutter speed. (a) plunge structural stiffness and (b) pitch structural stiffness. 79
2.26 Variation of Λ_r with $k_{\alpha 1}$ and $k_{\alpha 2}$: effect of the pitch stiffness nonlinearity on the type of instability. 81
2.27 Hysteretic response of the aeroelastic system (subcritical instability). The steady-state amplitudes are plotted as a function of U. 84
2.28 Measured pitch and plunge responses: blue line, without linear control, red stars, with linear control. 85
2.29 LCO amplitudes of plunge and pitch motions (controlled configuration): -, analytical prediction, $*$, numerical integration 86
2.30 A schematic of the proposed controller. 87

3.1 Representation of a model of a fixed flat plate with panels, each one has a concentrated vortex located at $xv(i)$, and a control point located at $xc(i)$. . . 91
3.2 The PCE coefficients of the components of the random freestream flow speed. The zero-order coefficients are the estimated mean values of the stochastic gust. The first-order coefficient provide a measure of the sensitivity of the stochastic gust to each of the uncertain parameters. 99
3.3 Time histories of the zeroth-order polynomial chaos coefficient, c_{l_0}, and the first-order coefficients, c_{l_1} through c_{l_4}, for the lift coefficient due to atmospheric turbulence. 102
3.4 Lift coefficient at $t = 1s$ versus ξ_i. (I) depicts the original data, (II) and (III) show the same data simulated by the 1^{st}-order and 2^{nd}-order PCE, respectively. The results are plotted separately for ease of comparison. 105
3.5 Empirical density functions for C_L at t=0.5, 1.0, 1.5 and 2.0 s. The solid blue lines is the estimated density function from the original time histories. The dashed red and blue line represent the estimated density function from the 1^{st}-order and 2^{nd}-order PCE, respectively. 107

4.1 Representation of a model of a flat plate with panels, each one with a concentrated vortex located at $xv(i)$, and a control point located at $xc(i)$. Wake vortices are shown in red. 110
4.2 Variations of the lift coefficient for (a) plunging and (b) pitching airfoils in a uniform stream. Comparison of current results -solid line with numerical results of Liang et al. (107) (N-S solver) -blue circles and Nuhait and Zedan 1993 (108) (UVLM) -red rectangles. 111
4.3 Vortical patterns for (a) plunging and (b) pitching airfoils in a uniform stream: (left plot) wake pattern obtained by Liang et al. (107), (right plot) wake pattern obtained from current UVLM. 112
4.4 Vorticity contours over a flapping wing as computed with UVLM. 113
4.5 Boxes produced and points sampled by the code VTdirect (serial subroutine from VTDIRECT95) for a two-dimensional problem over a square design space. 116
4.6 Elliptical vs. rectangular wing. 118
4.7 The aerodynamic power (upper plots) and normalized lift (lower plots) values at the best point found versus the number of evaluations for GCMMA using different initial conditions. 125
4.8 Optimal motions predicted from the present analysis (upper plots) and by Berman and Wang (14) (lower plots) for the hawkmoth and bumblebee cases. Circles represent the wing's leading edge. The arrows are introduced to show the sequence of the flapping motion and differentiate between the two midstrokes. 126
4.9 Optimized hawkmoth hovering kinematics: Comparison with Berman and Wang (14) and Willmott and Ellington (9). 127
4.10 Sensitivity of the optimized configuration to disturbances in the kinematics parameters. The blue lines show the variations of the dimensionless lift L^* with each of the kinematics parameters and the black lines represent the variations of aerodynamic power P. The red dashed lines indicate the optimal solution for the parameter. 128
4.11 Flow field around the flapping wing for different values of the sharpness parameter κ. 129

4.12 x-translation velocity (upper frame), angular velocity (second frame), dimensionless lift (third frame), and aerodynamic power (lower frame) for different values of the sharpness parameter κ. 130

5.1 Wing discretization and an example of a typical vortex element. 133
5.2 Velocity field induced by a straight vortex segment. 134
5.3 Vortex lattice sheets that model the boundary layer at the lifting surface (wing) and its wake at the first three time steps. 137
5.4 Local lift and drag vectors (for each panel). 140
5.5 Wing mode shapes used in the active shape morphing. 144
5.6 Variations of the averaged-value of the thrust coefficient with the reduced frequency. Comparison with the results of Stanford and Beran (15) and Heathcote et al. (36). 145
5.7 UVLM simulation of the wake of a flapping wing. 146
5.8 Variations of the lift and thrust coefficients for a flapping/twisting wing. Comparison with numerical results of Neef and Hummel 2002 (8) (Euler solver) and Stanford and Beran 2010 (15) (UVLM). 147
5.9 Variations of the lift and thrust coefficients for one flapping cycle of a cambered wing. Comparison with numerical results of Vest and Katz (28) and experimental results of Fejtek and Nehera (124). 148
5.10 Spline-based description of the wing morphing. 152
5.11 Lift coefficient vs. thrust coefficient for the optimal flight kinematics (trigonometric-based morphing). 156
5.12 Flapping, morphing, and pressure distribution over the deformed wing for the optimal flight kinematics. 157
5.13 Variations in time (spline-based) of the optimal wing morphing using the first bending and twisting modes. Comparison with variations of Stanford and Beran (15). 159

5.14 Variations in time (spline-based) of the optimal wing morphing using the first and second bending and twisting modes. Comparison with variations of Stanford and Beran (15). 160
5.15 Lift coefficient vs. thrust coefficient for the optimal flight kinematics (spline-based morphing). 161
5.16 The objective function value at the best point found versus the number of evaluations for VTDIRECT, GCMMA, and FMINCON. 162
5.17 The objective function value at the best point found versus the number of evaluations for GCMMA. 163
5.18 Histograms: sensitivity of optimal design points to perturbations in the design variables. 170
5.19 Simulated wing shapes of the *Giant petrel* and *Dove prion* birds. Sweep and taper are introduced in the wing geometry of each bird to reproduce its real shape. 171
5.20 Variations of the estimated lift in terms of mass and thrust with the wing root angle of attack α for the *Giant petrel* and *Dove prion* bird (rigid wings). For each bird, rectangular and swept/tapered wings are considered to investigate how wing geometry affects flight performance. The latter shape is based on the actual wing shape as shown in Figure 5.19. Clearly, the bird benefits from the wing taper and sweep to improve the performance of flight (leading to higher thrust). The results also indicate that to get enough lift to match the actual mass of the bird, the wing root should be placed at specific angle of attack. However, the generated thrust is very small (or negative depending on the bird wing shape) indicating that the bird is utilizing some sort of active wing twisting/bending to produce enough thrust for forward motion. 172

5.21 Optimal flight paths of the swept/tapered wings: rigid (thin lines) and morphed shapes (colored surfaces). For the *Giant petrel*, the wing root angle of attack is set equal to 4.7°. Morphing the wing increases its thrust from 0.187 N to 0.38 N and its propulsive efficiency (Thrust power U/Aerodynamic power) from 0.0459 to 0.38. For the *Dove prion*, the wing root angle of attack is set equal to 2.35°. Morphing the wing increases its thrust from -0.00689 N to 0.059 N and its propulsive efficiency from (-)0.0442 to 0.147. 173

List of Tables

2.1 Lift and drag weight coefficients. 33
2.2 Geometric and physical properties of the Goland wing. 45
2.3 Flutter speed using different approaches 57
2.4 Normal Form: Direct vs. Discretized Solution 59
2.5 System variables 65

3.1 Mean values and assumed standard deviations of the von Karman spectrum parameters. 98
3.2 Comparison between the slope obtained from the regression analysis and the corresponding PCE coefficient at $t = 1.0s$. The 95% confidence intervals for the slopes are calculated for Monte Carlo simulations using the Bootstrap method. 103
3.3 The mean and standard deviation of the lift coefficient C_L obtained with intrusive PCE and MC combined with LHS. 104

4.1 Morphological and kinematic parameters used for the analysis (5; 14). 114
4.2 Control variables constraints. 117
4.3 Kinematics, dimensionless lift force $\overline{L}^*$, and aerodynamic power for optimized wing motions of the hawkmoth and bumblebee. 119

5.1 Fixed Kinematics Parameters 149
5.2 Baseline case results 150
5.3 Kinematic variables constraints 153
5.4 Optimal kinematics results (four design variables) from VTdirect, NACA 83XX154

5.5 Optimal kinematics results (eight design variables) from VTdirect 155
5.6 Kinematic variables constraints (spline-based morphing) 157
5.7 Optimal design results, NACA 83XX (spline-based morphing) 158
5.8 Optimal results 161
5.9 Percentage of feasible perturbed vectors for different numbers of samples (Case 3). 164
5.10 Bird characteristics and estimated aerodynamic forces. The wing camber ratio† is defined as the maximum deviation of the center of the wing from the line connecting leading and trailing edges relative to the chord length (132). Results are obtained from UVLM simulations of flapping rigid wing. The estimated mass‡ is computed based on $\overline{L}$/g where $\overline{L}$ is the average value of the lift and g is the acceleration due to gravity (g=9.81 m/s^2). The propulsive efficiency is defined as the ratio of the power used to move the wing in the forward direction over the aerodynamic power (15). The minus sign (-) indicates that the bird is unable to move forward. 166
5.11 Flight performance enhancement through morphing. Active shape morphing using first and second bending and twisting mode shapes is used to mimic local bird's wing deformations. These shapes are generated using the material and geometric properties of the birds wings (134; 140). Results are determined by combining UVLM with an optimization algorithm GCMMA(115; 116) (globally convergent method of moving asymptotes). The value of the wing root angle of attack α was chosen so that the average value of the lift $\overline{L}$ balances the weight of the bird for the base (no morphing) case. 168

Chapter 1

Introduction

The performance of multidisciplinary engineered systems (e.g., aerospace vehicles, ships, submarines, offshore structures, high-rise buildings, and wind turbines) could be significantly enhanced through understanding their governing dynamics and possibly exploiting specific phenomena. Equations governing the performance of these systems comprise nonlinear partial differential equations (PDEs). The sources of the nonlinearities in these equations may be material or constitutive, geometric, inertial, body forces, fluid-structure interactions, or friction. Recent advances in computing power in terms of speed and storage capacity (e.g. parallel computing) have enabled the use of direct numerical simulations whereby the aforementioned equations are discretized and integrated with robust numerical algorithms. For instance, higher-order finite-difference schemes on curvilinear and deforming meshes, finite volume, and finite element methods have been implemented and used to solve such equations. While these high-fidelity approaches are powerful in terms of capturing the main physical features, they fail to discern the role of the underlying phenomena that are usually interrelated in a complex manner. This often makes it difficult to characterize the relevant causal mechanisms. Besides, the extensive computational resources and time associated with the use of high fidelity models usually limit the capability to simulate a large number of configurations for design purposes. These shortcomings lead to the need for the development of simplified and reduced-order models that are capable of embodying relevant physical phenomena and of yielding relevant response characteristics. Such models would place lesser demands on the

computational resources and time and (i) enable the reproduction of results of high-fidelity simulations within certain accuracy, (ii) aid in the understanding of the underlying physics and dynamics that govern the system's response, (iii) quantify system response uncertainties to variations in its parameters, and (iv) perform a rapid and reasonably accurate exploration of a large design space.

1.1 Model Reduction Framework

The model reduction framework of multidisciplinary systems, such as the ones considered in this dissertation, is presented in Figure 1.1. The response and performance of these systems are usually predicted by mathematical models that are derived from fundamental laws such as conservation of mass, energy, and momentum. The need to capture properly the physics and dynamics of these systems may lead to models of high complexity. Solving such models usually requires the use of powerful hardware and software capabilities. One alternative to simulate the behavior of these systems is to conduct a full-scale experiment. The high computational cost and time associated with these approaches presents the main motivation for performing reduced-order modeling and analysis.

Depending on the nature of the system and its application, the complexity of governing equations can be significantly reduced by introducing simplifications justified by known physical characteristics. For instance, the prediction of the flutter speed and natural frequencies of a wing under an incoming freestream and the study of their variations as caused by uncertainties of different system parameters could be determined from linear analysis. In aircraft design, aerodynamic loads can be well approximated using simplified governing equations, such as the Euler equations. Furthermore, if the flow is assumed to be irrotational, the velocity field can be extracted from a potential function satisfying the Laplace equation. Such mathematical models and simplifications can be efficiently used to determine system's behavior or flow quantities. Yet, further simplifications might be needed to enable the implementation of a control strategy to reach a desired performance specification, determine optimized configurations or perform sensitivity analysis.

To this end, the PDEs governing the behavior of a given dynamical system are usu-

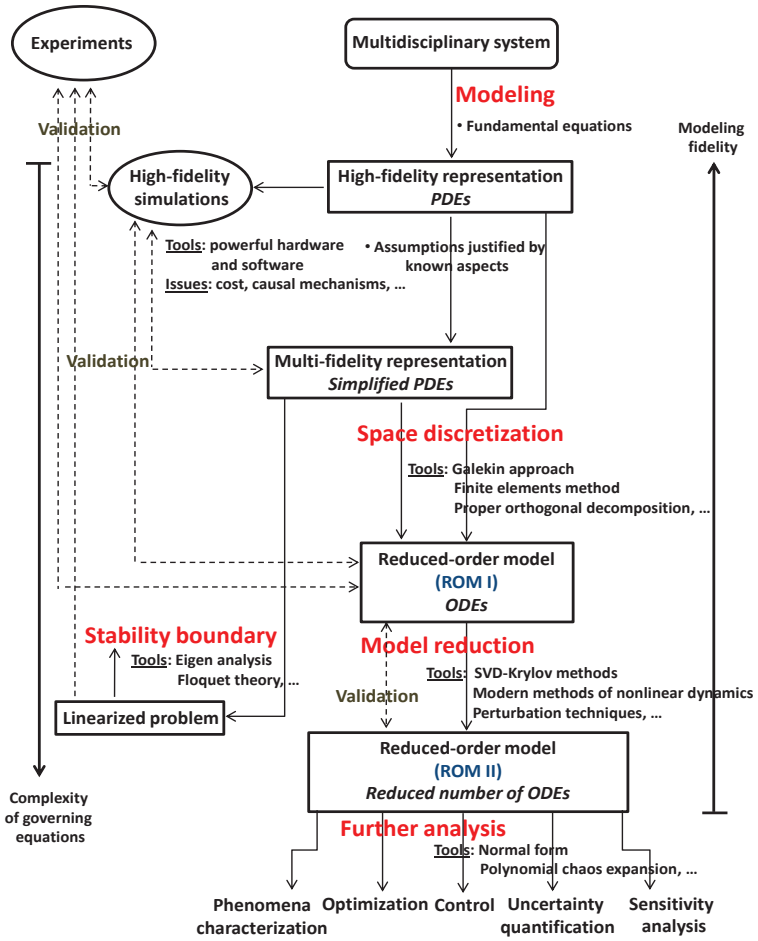

Figure 1.1: Model reduction framework of multidisciplinary systems.

ally discretized in the space variables to yield a system of ordinary differential equations (ODEs). The Galerkin projection constitutes a widely used solution methodology for modal discretization. For instance, for problems involving structures such as beams and plates etc, one could use the mode shapes to approximate the system response and discretize the PDEs. For systems involving fluid flows, a common approach to derive a reduced-order model is proper orthogonal decomposition (POD). The implementation of this approach is based on representing flow quantities, such as velocity and pressure fields, by a collection of flow values of the fluid system (commonly referred as snapshots). These snapshots are originally obtained through numerical simulations or experiments. Then, a low-dimensional set of ba-

sis functions (analogue to mode shapes for structures) is obtained by processing snapshot data. These functions present dominant structures of the flow and that are represented by a low-dimensional dynamical system that is typically obtained by Galerkin projection. As such, a reduced-order model for the velocity field can be obtained by projecting the Navier-Stokes equations onto the space formed by the velocity POD modes. This projection yields a set of ODEs that can be directly integrated to reconstruct the velocity field. The obtained model can be easily connected with a controller to achieve a specific behavior. Akhtar et al. (1) developed a reduced-order model of the velocity field for incompressible flow past a cylinder. This model was then used to control the flow field and suppress vortex shedding. Furthermore, they presented a pressure model based on the Galerkin projection of the Poisson equation onto the velocity and pressure POD modes. This model was used then to reproduce the fluid loads on the cylinder.

To allow for more simplified representations, one could follow two different approaches. These can be categorized into physics-based and phenomenological methods. The first model reduction category is based on governing equations of a given system. For instance, perturbation techniques, such as method of multiple scales and center manifold theorem, can be used to derive the normal form of nonlinear systems. This form constitutes an effective tool to capture the main physical behaviors of such systems near the Hopf bifurcation (flutter onset). In addition to yielding a systematic means to gain a better understanding of the physics, the normal form can also serve as the basis for additional analysis. In fact, it enables the immediate characterization of the type of dynamic instability and the identification of the effects of the system's parameters on its response. Besides, it allows for an implementation of linear and nonlinear control to delay an instability and/or avoid catastrophic responses associated with the subcritical instability. The second model reduction category is based on modeling a particular phenomenon from experimental or numerical data and describing it with analytical functions. Nayfeh et al. (2) and later Akhtar et al. (3) simulated flow past circular cylinder using a parallel incompressible computational fluid-dynamics (CFD) solver. Their numerical results showed that the long time history of the lift on the cylinder is periodic and independent of the initial conditions. Based on these observations, they used some system identification tools to come up with a representative model of the lift coefficient

based on Van der Pol oscillator.

While reduced-order models find their potential use in many analyses and applications, there is always a need to identify the boundaries where such models remain valid. As such, at each level of modeling fidelity, one should validate the reduced-order model against experiments and higher-fidelity simulations.

1.2 A Multidisciplinary System: Micro Air Vehicle

An example of a multidisciplinary system modeled in this dissertation pertains to the design and performance of micro air vehicles (MAVs). These vehicles are small flying aeroelastic systems that are expected to operate in urban environments and confined spaces (inside buildings, caves, tunnels). They are expected to be used for the inspection of harsh environments inaccessible to other types of vehicles, detection, and tracking of small and hidden mobile targets in a battlefield. To successfully achieve the aforementioned missions, these systems must be designed to satisfy some performance requirements, such as high maneuverability at low speeds, hovering capabilities, high lift to sustain flight, and structural strength to survive gust loads. These requirements can be achieved mainly through two propulsion mechanisms: rotating helicopter blades or flapping wings (4). Through observing the efficiency of insects and birds, it has been concluded that flapping wings offer greater efficiency, especially at small scales (5–8). Studying these flying animals as a step toward designing flapping-wing vehicles has been the topic of many investigations (9–12).

1.2.1 Multi-physics aspects of propulsive systems

Biological propulsion systems, such as birds and insects, flap their wings to exploit unsteady aerodynamic effects in their flight (5–7; 13). These natural flyers may operate at high angles of attack and frequencies of flapping motions. These flyers also rely on unsteady motions to generate aerodynamic loads to sustain flight. Next, a brief description of some unsteady aspects and mechanisms of flapping wing flights is presented. More details of these aspects are provided in Refs (5–7; 12).

Wing kinematics

Flying animals use varying kinematics depending on their morphology and type of flight. For instance, birds have internal skeletons connected to muscles which enable local actuation and then more flexibility. In comparison, insects lack this feature and, as such, all actuation is forced from the wing root (6). This feature has justified the parametrization of their wing kinematics by a sequence of three consecutive angles namely stroke angle ϕ, elevation or deviation angle θ, and pitching angle η (9; 14). The flapping motion can be divided into two half strokes: downstroke and upstroke. At the end of each half stroke, the rotational motion causes the wing to change its direction for the subsequent half stroke. Through a cycle, the motion of flapping wings can be described by a combination of translations and angular oscillations. Experimental studies have been conducted to identify the kinematics of insects and birds using high-speed cameras (9–11). These kinematics are usually fitted by trigonometric functions or periodic splines (14–16) to enable modeling and analyses of flapping wings using computational tools.

Aerodynamics

Katzmayr effect As defined by Jones et al. (17), the Katzmayr or Knoller-Betz effect is the ability of a sinusoidally plunging airfoil to produce thrust. This effect has been investigated experimentally and numerically by Jones et al. (17). They presented comparisons of wake structures (flow visualizations) and velocity profiles obtained from experiments and numerical computations. In particular, they showed the vortex street produced in the wake behind a plunging wing for different reduced frequencies. There was a set of counterrotating vortical structures which entrain the fluid in between to yield a jet flow. If the upper and lower rows of vortices rotate clockwise and counterclockwise, respectively, the velocity profile in the wake exhibits a momentum deficit, which indicates drag generation. This vortex street is called the von Karman vortex street. In the opposite case, the vortex structures lead to a jet profile or momentum gain. This vortex street is referred as reverse von Karman vortex street (17). Furthermore, Jones et al. (17) defined the wake wavelength as the distance between the vortices of upper and lower rows and determined that it is related to the magnitude of drag

(or thrust). As such, reducing this distance to zero, where the two rows of counterrotating vortices are on the same level, results in zero net drag or thrust production.

Leading-edge vortex One important unsteady aspect for flapping wings aerodynamics is the leading edge vortex (LEV) which is created when wings sweep through the surrounding fluid at high angles of attack. Under steady flow regimes, this leads to flow separation and stall. However, in unsteady flows, this vortex, which originates from the roll up of the shear layer in the leading-edge region, induces an area of lower pressure above the wing and leads to an increase in the lift force. This effect is more pronounced in low-Reynolds number flapping regimes and is usually exploited by insects to enhance their flight performance (5; 7; 12). Being a pure effect of the translational portion of the stroke, Dickinson et al. (18) estimated the contribution of LEV through measuring the forces generated solely from translating a wing. They came up with approximate relationships of the translation component of this force as functions of angle of attack. Using a Navier-Stokes solver that is based on finite volume, Liu (19) modeled flapping kinematics of insects. He used representative bodies of hawkmoth, honeybee and fruitfly to simulate hovering flights and showed through flow visualization the formation and development of LEV during the stroke cycle. Milano and Gharib (20) considered lift maximization of a flapping plate and showed that the optimal flapping leading to maximum lift is associated with the formation of a leading-edge vortex with maximum circulation. This presents a clear indication that flapping wings benefit from the leading-edge vortex to enhance lift generation. Using digital particle image velocimetry (PIV) measurements, Muijres et al. (21) showed that bats may benefit from attached LEVs to increase lift by 40% during slow forward flight. Their results indicate that this unsteady effect in flapping flight is not limited to insects but is also exploited by larger flying animals.

Tip vortex Under steady flow conditions, vortices created at the tip of fixed finite aspect ratio wings are observed to reduce the lift and induced drag (22). However, in unsteady flows, tip vortices may increase the lift generation, thereby improving flight performance of flapping wings. For instance, Shyy et al. (23) found that for a low-aspect ratio flapping wing following specific kinematics, tip vortices may affect significantly flow structures and yield an

increase in the lift. They associated this aerodynamic influence of tip vortices to the creation of a low-pressure region near the wing tip and the anchoring of the LEV to delay or prevent it from shedding.

Wake capture During a flapping motion, especially for hovering and low-speed forward flights, wings might encounter the wake created during previous cycles (18). This phenomenon is referred to as wake capture. Sane and Dickinson (24) investigated experimentally this unsteady effect. They compared the experimental force measurements data from a dynamically scaled robotic insect-like model with those obtained from quasi-steady models to isolate and quantify the aerodynamic influence of the wake. Their results demonstrated a great role of the wake capture in flapping flight. Birch and Dickinson (25) investigated further this unsteady mechanism. They measured the aerodynamic effect of the wake by subtracting forces and flow fields obtained from the first stroke, when the wake has just developed, from those generated during the fourth stroke, when the wing wake interactions are pronounced as shown in their flow visualizations. They showed that its effectiveness in terms lift generation depends on wing kinematics and vortical structures surrounding the flapping wing. Ansari et al. (6) pointed out that the wake shed behind a flapping wing contains energy provided to the surrounding fluid in the form of momentum and heat. So, the flapping wing might get back some of this energy and use it to improve its flight performance. As such, Grodnitsky and Morozov (26) suggested that birds and insects use some particular mechanisms to extract energy back from their near vortex wake. Unlike the other unsteady flow aspects that have been incorporated, to some degree, in low-fidelity models by introducing empirical corrections, there has been no attempt to construct a quasi-steady estimate of the wake capture.

1.2.2 Multifidelity modeling of aerodynamic flow and forces

As discussed in the previous section, the physics and dynamics associated with flapping wing MAV flight are quite complicated. Simulating these complicated physics is often attempted with high-fidelity numerical models, but the extensive computational resources and time associated with the use of these models limit the capability to run many simulations as required

for a large design space. On the other hand, the use of computational tools lacking much physics might lead to erroneous prediction of the aerodynamic response and drive the design process improperly. Thus, there is a need to develop and use mathematical models with different fidelity levels and implement simulation and analysis tools that are capable of predicting their aerodynamic response, optimize their performance, and limit their sensitivities to parameter variations and environment noise.

The best approach to examine the aerodynamic response of flapping wings would be to simulate the complete viscous flow. This would require solving the full Navier-Stokes equations for three-dimensional and unsteady flowfields. Such task is quite challenging and computationally expensive. Introducing flexibility to the body (e.g. wing morphing) would complicate the problem further. Different computational tools to tackle this aerodynamic problem have been reported in the literature (13; 24; 27–29). These tools present different levels of modeling fidelity, ranging from low-fidelity models, such as quasi-steady methods, to high-fidelity models, such as Navier-Stokes solvers (e.g., direct numerical simulations (DNS), large eddy simulation (LES), detached eddy simulation (DES), ...). The Reynolds number (the ratio of inertial to viscous effects) and reduced frequency (a measure of the degree of unsteadiness of the flapping motion) constitute two relevant quantities to identify the boundaries of the validity domain of different aerodynamic tools. Quasi-steady approaches are fairly appropriate to model and analyze slowly flapping wings (low reduced frequencies) over a wide range of Reynolds number, but they may loose their predictive capability for high-frequency flapping flight where the unsteadiness effects become significant. Inviscid flow methods, such as potential flow models, panel methods, and Euler solvers present great capability to simulate flapping wing flights (8; 28; 29). However, they remain applicable only to relatively high Reynolds number flows. Navier-Stokes solvers would be the most appropriate to simulate flows past moving bodies under any flight and flow condition.

Quasi-steady approaches

The quasi-steady approach is based on deriving a model whereby unsteady wake effects are ignored; that is, flapping frequencies are assumed to be slow enough that shed wake effects are negligible. This assumption leads to a significant simplification to the aerodynamic modeling.

In this approach, the aerodynamic loads are usually explicit functions of the kinematics variables. One example is given by Sane and Dickinson (24) where an aerodynamic model was developed using blade element theory. The wing is divided along the spanwise direction into chordwise strips. The aerodynamic forces are computed on each strip and then integrated along the span. To enable a more accurate prediction and capture unsteady flow aspects to some extent, they introduced some form of empirical corrections based on experimental measurements. However, since the formulation of this model is based on interpolating a set of experimental data rather than fundamental equations that reflect the actual physics of the problem, their prediction may be very specific to a particular configuration and may not be applicable once kinematics or flow conditions are changed. Berman and Wang (14) used a quasi-steady representation to model hovering insect flights. This model was initially formulated to study the motion of a free-falling plate and combined with a blade element theory. They combined the aerodynamic model with a hybrid optimization algorithm using a genetic algorithm and a gradient-based optimizer to identify the optimal wing kinematics that minimize power consumption under a lift constraint equal to the weight of the insect. Of interest is that their optimization study yielded kinematics that are qualitatively and quantitatively similar to the experimentally observed kinematics for different insects.

Inviscid flow methods

The complexity of the fluid equations can be significantly reduced by assuming the flow to be inviscid. This leads to the Euler equations. Neef and Hummel (8) used an Euler solver to simulate and analyze the flow around a two-dimensional airfoil under a combined plunging and pitching motions. They used a moving structured mesh to handle different geometries (airfoil profiles) and employed the finite volume approach for spatial discretization and a five-stage Runge-Kutta scheme for the integration of the discretized system. They verified their CFD code by comparing their results with those obtained from analytical approaches. Also, they simulated the three-dimensional flow around a flapping and twisting wing of finite span. Their aim was to mimic a large bird in cruising flight and test its efficiency in terms of propulsive energy obtained to propel the wing in the forward direction.

If the flow is assumed to be irrotational, the velocity field can be extracted from a potential

function Ψ satisfying the Laplace equation. A well-established method, which is based on solving this equation, is called unsteady vortex-lattice method (sometimes referred in the literature as the panel method). Unlike other approaches like finite difference and finite volume, this method requires a mesh only on the wing surface, thereby leading to a significant reduction in the computational cost. The main advantage of this method is that only the continuity equation (decoupled from the momentum equation) is used to solve for the velocity field and the pressure distribution and corresponding fluid loads are calculated separately by using the unsteady Bernoulli equation. Details of the derivation and implementation of this method for different aeroelastic configurations are provided by Katz and Plotkin (30). The UVLM has been extensively used to simulate flapping flights and conduct further analyses (15; 28; 29). Stanford and Beran (15) used this method to optimize a flapping wing in forward flight with active shape morphing. Their goal was to maximize propulsive efficiency under lift and thrust constraints. Palacios et al. (31) considered both strip theory and vortex lattice method for aerodynamic modeling of a flapping wing. They showed that the use of UVLM is adequate for large-amplitude wing deformations and can be efficiently coupled to a structural dynamics model. Although the classical formulation of the panel method does not allow for modeling viscous effects, flow separation, and some flow conditions with substantial wing-wake interactions, there have been some efforts to incorporate viscous corrections and prediction in numerical models based on UVLM. Fritz and Long (29) introduced viscous dissipation in a potential flow model by letting the circulation of wake rings to decrease with time according to a decay model. Furthermore, Zdunich (32) developed a 2-D vortex panel model capable of modeling separated flows. To allow for capturing this flow feature, the effective angle of attack at the leading-edge α_{LE} is calculated and compared to a stall trigger angle α_{Stall}, which may be set from experiments or according to results from higher-fidelity models, at each instant. If $\alpha_{LE} > \alpha_{Stall}$, a stall model is turned on. This model introduces a correction to the leading-edge vortex strength. His results compared very well with Navier-Stokes solutions obtained from Fluent simulations.

Navier-Stokes simulations

The complex aspects of flapping wing flight are at times determined from numerical simulations of the Navier-Stokes equations (13; 19; 33; 34). These high-fidelity models require mesh generation of the entire fluid domain and robust numerical schemes to handle the linear and nonlinear terms of the governing equations. From a design perspective, it is very hard to deal with such models due the computational costs. For instance, searching in the design space to identify optimal configurations may require many performance function evaluations, which makes the use of direct numerical simulations (DNS) impractical. These tools have, however, been used to check results obtained from lower-fidelity models. Willis et al. (35) showed that the use of models with different levels of geometric and physical modeling fidelity can be well exploited to ease the design process. Vanella et al. (33) performed a computational study to understand the influence of flexibility on the aerodynamic performance of a hovering wing. They used DNS to solve for the flowfield and coupled with a structural model, based on a nonlinear oscillator, using the predictor-corrector scheme. The aerodynamic loads predicted by their DNS compared well with those obtained from experiments. Yuan et al. (13) performed numerical simulations for two-dimensional pitching-plunging airfoils and three-dimensional flapping wings at hover conditions using DNS. They used this tool to investigate physical aspects of unsteady flows around flapping wings. Their results showed a good agreement with those obtained from experiments conducted in a water tunnel.

1.2.3 Modeling of structural response of flapping wings

During flapping motions, insect or bird wings may undergo large spanwise and chordwise deformations. Many numerical and experimental studies have been conducted to investigate the impact of such deformations on the flapping wing performance. As such, Heathcote et al. (36) performed water-tunnel experiments on a rectangular wings in pure heave. Different materials have been used for wing construction to enable the study of the effect of spanwise flexibility on the thrust, lift, and propulsive efficiency. Based on their experimental results, they reported that natural flyers may benefit from their wing flexibility to improve significantly their flight performance.

To date, most of the aerodynamic models used to simulate flapping wings assume rigid structures, where the flapping kinematics is prescribed, or actively deformable structures where the deformations are approximated using shape functions (15). In reality, insects and birds rely on the flexibility of their wings to manoeuver and control their flights (7; 37). For instance, Weis-Fogh (38) found that the elastic material properties of insect wings play an important role in reducing the power required to sustain the flight through storing and releasing energy mechanisms. Such observations point to the need to account for the flexibility in simulating flapping wing motions. Zhu (39) considered the use of a potential flow model coupled with structural dynamics to study the flapping motion of a foil with chordwise and spanwise flexibility. The structural model was based on nonlinear plate theory. One important issue related to such problems is that the fluid affects the structural response and vice versa. Thus, the fluid governing equations and structural responses need to be solved simultaneously. To allow for a simultaneous integration of both aerodynamic and structural models, Zhu (39) developed an iteration algorithm. Stanford and Beran (40) developed a computational framework for the aeroelastic analysis of flexible wings. A nonlinear shell finite element model is coupled to UVLM to capture the aeroelastic interactions between the wing and the surrounding fluid. The structural model has capability to capture strong geometric nonlinearities and flexible multibody dynamics. Validation of the aeroelastic framework has been done through comparisons with experimental results of Heathcote et al. (36). The solver is then combined with a gradient-based optimizer to perform the optimization of three design problems: increasing maximizing propulsive forces generated by a plunging wing, minimizing the limit cycle amplitude of a fixed wing in a steady freestream, and optimizing the gust alleviation of a fixed wing under an incoming vertical gust. In other work, the same authors (41) employed the same approach to analyze the aeroelastic response of flexible flapping wings. They studied the effects of the flexibility on the aerodynamic loads. Vanella et al. (33) performed a computational study to investigate the effect of flexibility on the aerodynamic performance of a wing in low-Reynolds number hovering flight. Their 2-D wing model consists of two rigid links that are joined at the center with a linear torsional spring. The kinematics of the top link is prescribed and the other link is free to move according to a nonlinear oscillator which constitutes a low-fidelity representation of structural dynamics.

They used a CFD code to solve for the flowfield and coupled to the structural model using the predictor-corrector scheme. Their study provides a good insight on how flexibility affects the aerodynamic performance in low Reynolds number flapping flights.

The dissertation will solely focus on the aerodynamic modeling, analysis, and optimization of flapping wings. The structural modeling is out of the scope of the present work.

1.3 Objectives and Approaches

The objective of this dissertation is to show how reduced-order models can be used to model, analyze, and assess the performance of unsteady aeroelastic systems. Particularly, different levels of developing reduced-order models, as shown in Figure 1.1, are used to achieve this objective. The approach is to develop methodologies and techniques to simulate the behavior and analyze the performance of such systems with a reduced computational cost. In particular, the modeling, analysis, and optimization of the kinematics of flapping wings in the context of using them in micro air vehicles are stressed.

To achieve the objective,

1. Generic examples of fluid and aeroelastic systems are considered to show how reduced-order models can be used to efficiently characterize physical aspects of dynamical systems. Furthermore, the present analysis shows how such models can be used to implement control strategies and perform uncertainty quantification and sensitivity analyses.

2. Two and three-dimensional versions of the unsteady vortex lattice method to simulate the aerodynamic response of flapping wings are implemented. The UVLM requires much less computational resources than methods based solving the Navier-Stokes or Euler equations, but applies only to incompressible, inviscid flows where the separation lines are known a priori. This tool is capable of simulating flows past moving thin wings and capturing the unsteady effects of the wake, but not viscous effects, flow separation at the leading-edge, and extreme situations with strong wing-wake interactions.

3. The aerodynamic model based on UVLM is combined with uncertainty quantification and optimization tools to test and analyze the performance of flapping wing MAVs

under varying conditions.

1.4 Outline of the Thesis

The thesis is organized as follows:

In chapter 2, generic examples of fluid and aeroelastic systems are considered to emphasize how reduced-order models can be used to perform sensitivity analysis of the response of these systems and characterize their physical aspects. In one problem, model reduction techniques are used to develop a low-dimensional tool for predicting force coefficients acting on a circular cylinder. In a second problem, two aeroelastic systems, namely, the Goland wing and the two-dimensional pitching-plunging airfoil, are considered and their normal forms are drived. This form is then used to identify the type of Hopf bifurcation and determine the impact of variations in structural and aerodynamic nonlinearities on their dynamic behavior. Furthermore, the analysis shows that this form can be used to implement control strategies to delay the flutter onset and avoid subcritical bifurcations.

In the following chapters, the focus is on the study of micro air vehicles. In chapter 3, a two-dimensional version of the unsteady vortex lattice method is implemented to simulate unsteady flow past a thin rigid plate. Then, the intrusive polynomial chaos expansion is used to determine uncertainty in gust loads on the plate due to imprecision in an incoming gust characteristics. This study yielded the sensitivity of the lift coefficient to variations in the intensities and integral length scales of the gust fluctuations.

In chapter 4, a two-dimensional version of the unsteady vortex lattice method is used again to simulate hover flight of a flapping wing. Then, an efficient search of optimal configurations for flapping wing kinematics that minimize the aerodynamic power under lift constraint is performed.

In chapter 5, a three-dimensional version of the unsteady vortex lattice method is implemented to simulate the aerodynamic response of a flapping wing with active shape morphing. Then, global and local optimization algorithms are used to identify the optimal wing morphing that maximizes the propulsive efficiency under lift and thrust constraints. The results show that morphing the wing improves significantly the flight performance. Also, the analysis

investigates the accuracy and computational costs associated with the use of different optimization tools. Furthermore, a sensitivity analysis of the optimal design points is performed to investigate the effects of perturbing various parameters on the propulsive efficiency and solution feasibility. Finally, an innovative analysis is carried out to explain how birds morph (deform) their wings and employ specific wing shapes to control their flight performance, as well as to make it more efficient. It is found that, based on the material and geometric properties of its wing and the flapping frequency, each bird employs some sort of active wing twisting/bending through its internal skeleton to produce enough thrust for its forward motion.

Chapter 2

Model Reduction

In this chapter, it is shown through generic examples of fluid and aeroelastic sytems the usefulness of reduced-order models for performing sensitivity analysis of the response of multidisciplinary systems. In one problem, model reduction techniques are used to develop low-dimensional tool for predicting force coefficients acting on a circular cylinder under varying inflow conditions. In a second problem, two aeroelastic systems, which are the Goland wing and the two-dimensional pitching-plunging airfoil, are considered to show how the normal form can be used to identify the type of Hopf bifurcation and to determine the impact of variations in structural and aerodynamic nonlinearities on their dynamic behavior. Furthermore, it is shown how this form can be used to implement control strategies to delay the flutter onset and avoid subcritical bifurcations (leading to catastrophic behavior).

2.1 Example 1: Low-dimensional Tool for Predicting Force Coefficients on a Circular Cylinder

In this section [1], a low-dimensional method to predict force coefficients acting on a circular cylinder is developed. The approach is based on combining proper orthogonal decomposition (POD) and linear stochastic estimator (LSE) techniques. Proper orthogonal decomposition is used to derive a reduced-order model of the velocity field. In particular, the use of POD is

[1] Development and implementation of the CFD code used in this effort are not part of my contribution.

extended to cover unsteady flows. Then, to overcome the difficulty of developing a reduced-order model (ROM) based on projecting the pressure Poisson's equation on the space formed by POD modes (as has been performed by Akhtar et al. (42)), the pressure field is related to the velocity field through a mapping function obtained by the application on linear stochastic estimator.

2.1.1 Numerical simulations

A parallel CFD code (43) is used to simulate the steady and unsteady flow fields past a circular cylinder at Re=180. The objective of these simulations is to obtain the flow field data which is used to compute the POD-basis functions. Details of the implementation, validation, and verification of the CFD code can be found in Ref. (43).

Figure 2.1 shows the time histories of the lift and drag coefficients for $Re = 180$ under steady conditions. The lift time history shows a periodic oscillations with the nondimensional frequency (Strouhal number) $f_s = fD/U \approx 0.186$ where D is the cylinder diameter, U is the freestream velocity, and f is the shedding frequency. The drag time history shows that the drag fluctuates periodically with a non-zero mean value at twice the shedding frequency.

2.1.2 Low-dimensional representation of flow quantities

A schematic of different components of the proposed method to derive a reduced-order model for the force coefficients is shown in Figure 2.2. The approach combines POD-based models to predict the flow field and LSE for approximating the pressure on the cylinder. The POD approach has been implemented successfully in the low-dimensional modeling of flows past airfoils and cylinders (44–48). In this method, instantaneous solutions or snapshots of the velocity and pressure fields are first generated from flow simulations. Then, the method of snapshots is applied to compute the velocity and pressure POD modes. By projecting the Navier-Stokes equations onto the space formed by the POD modes, a reduced-order model for the velocity field is derived. The result is a set of ODEs in the form of $\dot{q} = F(q, \gamma, \dot{\gamma})$ that governs the variations of the temporal coefficients of the velocity field. These equations represent the level of reduced-order modeling ROM I in the schematic shown in Figure 1.1. The development of the reduced order model for the velocity field is expanded to cover

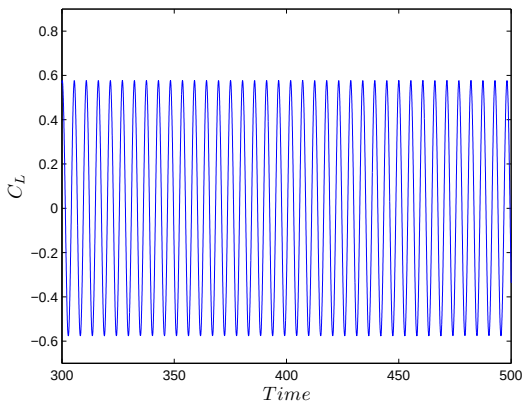

(a) Time history of the lift coefficient

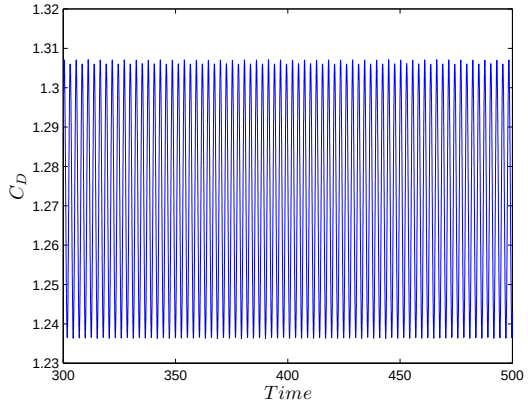

(b) Time history of the drag coefficient

Figure 2.1: Time histories of the lift and drag coefficients obtained from the CFD simulation at $Re = 180$

unsteady mean flow cases. To develop a reduced-order model for the pressure field, one approach is to project Poisson equation onto the space formed by the pressure POD modes (45). The result is a set of algebraic equations which relate the temporal velocity and pressure coefficients. As noted by Akhtar et al. (45), this model works well only for low Reynolds numbers and cannot be extended to unsteady mean flow cases. In the present approach, the temporal coefficients of the pressure fluctuations are generated using a mapping function $M(q)$ that is based on LSE technique. These coefficients are used with pressure POD modes to compute the pressure distribution, which is integrated to determine the fluid loads. Again the idea here is to relate pressure and velocity coefficients through the LSE instead of using the Poisson equation and then build a ROM that can directly yield the pressure coefficients. The final outcome is a representation of the lift and drag coefficients in terms of the velocity and pressure temporal coefficients.

2.1.3 The proper orthogonal decomposition

A classical way to compute the POD modes is to perform a singular value decomposition (SVD) of a snapshot matrix (43), however, this approach may have a limited application,

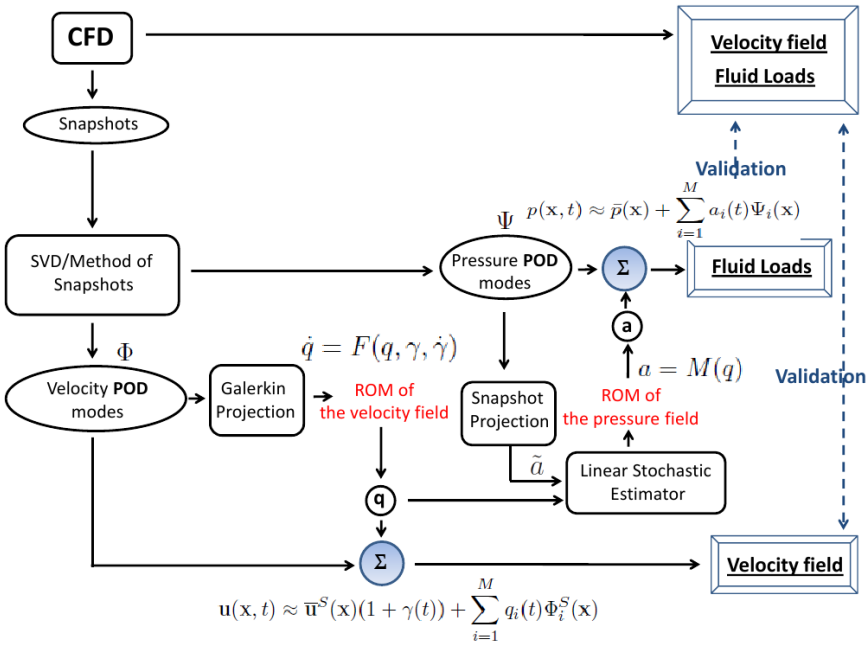

Figure 2.2: A descriptive schematic showing the implementation of the low-dimensional method.

especially when dealing with a large mesh size as in CFD cases which require fine mesh and high computational cost. Alternatively, one could use the method of snapshots (49) which allows for a significant reduction of the large data sets. In this method, sets of instantaneous solutions (or snapshots) of the flow parameters (velocity and pressure fields) obtained from the CFD simulations are first generated and stored in $N \times n$ matrices, denoted by S where N and n denote, respectively, the number of grid points and snapshots. Then, an eigen analysis of the matrix $S^T S$ is performed; that is, (49)

$$S^T S \in \mathbf{R}^{n \times n} : S^T S V_i = \sigma_i^2 V_i \quad and \quad U_i = \frac{1}{\sigma_i} S V_i$$

The selection of POD modes is optimal in the sense that the error between each snapshot and its projection on the space spanned by those modes is minimized (50). The square of the singular values represent a measure of the energy content of each POD mode and, as such, provide guidance for the number of modes that should be considered in order to capture the main physics of the system.

The POD basis vectors Φ_i and their corresponding singular values σ_i are obtained by applying the method of snapshots as described above to data from flow simulations over a circular cylinder.

In Figure 2.3(a), the singular values of the first 20 modes obtained from a steady mean flow conditions are plotted. All singular values are normalized with the corresponding value of the first mode (i.e. σ_i/σ_1). It is observed that the two modes of each pair have values of the same order. These values decrease from one pair to the next in approximately a geometric progression.

To gain insight into the contribution of each mode to the total energy of the system, the cumulative energy is defined as $E = \sum_{i=1}^{M} \sigma_i$ and the cumulative contribution of the first j modes as $c_j = (\sum_{i=1}^{j} \sigma_i)/E$. It is remarked that most of the energy is contained in the first few modes (see Figure 2.3(b)). More specifically, the first ten modes contain more than 99.9% of the total flow energy.

The streamwise and crossflow velocity modes in the steady flow are plotted in Figures 2.4 and 2.5, respectively. These modes constitute the dominant spatial structures of the flowfield.

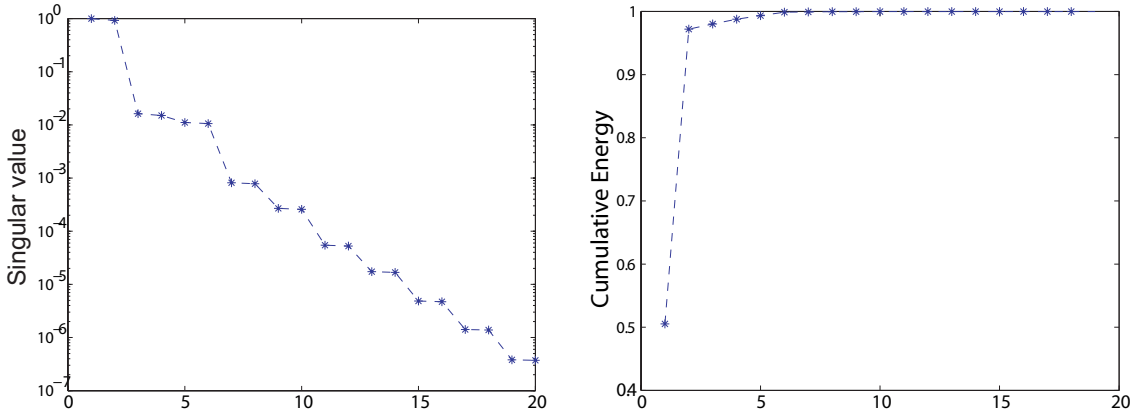

(a) Normalized singular values of POD modes

(b) Normalized cumulative energy of POD modes

Figure 2.3: Normalized singular values and cumulative energy content of POD modes.

Similarly to the singular values, the POD modes show a pattern of pair similarities. Looking at the first six POD modes of the streamwise and crossflow velocity components in Figures 2.4 and 2.5, respectively, it is observed that the POD modes $\phi_i^u (i = 1, 2, 5, 6)$ of the streamwise component are antisymmetric with respect to the x-axis; that is,

$$\phi_i^u(x, -y) = -\phi_i^u(x, y), \tag{2.1a}$$

while the $\phi_i^u (i = 3, 4)$ are symmetric; that is,

$$\phi_i^u(x, -y) = \phi_i^u(x, y). \tag{2.1b}$$

On the other hand, the POD modes ϕ_i^v of the crossflow component are symmetric for $i = 1, 2, 5, 6$ with respect to the x-axis; that is,

$$\phi_i^v(x, -y) = \phi_i^v(x, y), \tag{2.2a}$$

and antisymmetric for $i = 3, 4$; that is,

$$\phi_i^v(x, -y) = -\phi_i^v(x, y). \tag{2.2b}$$

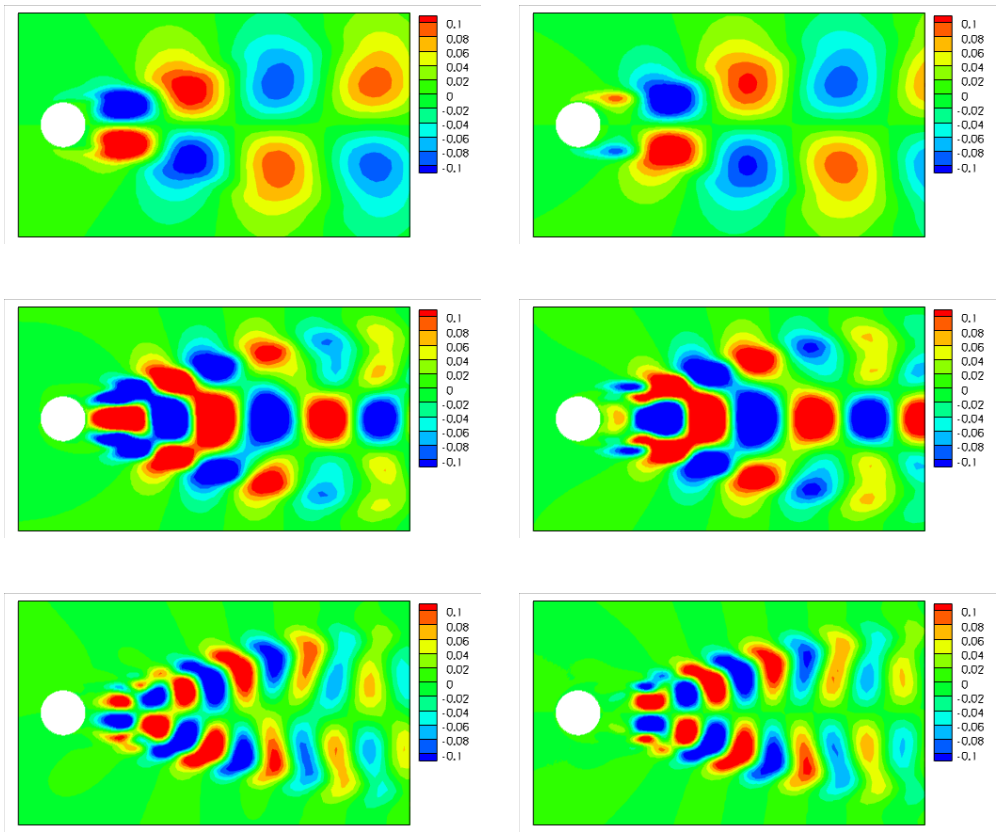

Figure 2.4: Contours of the streamwise velocity POD modes ($\phi_i^u, \quad i = 1, 2, ..., 6$) for the case of steady mean flow

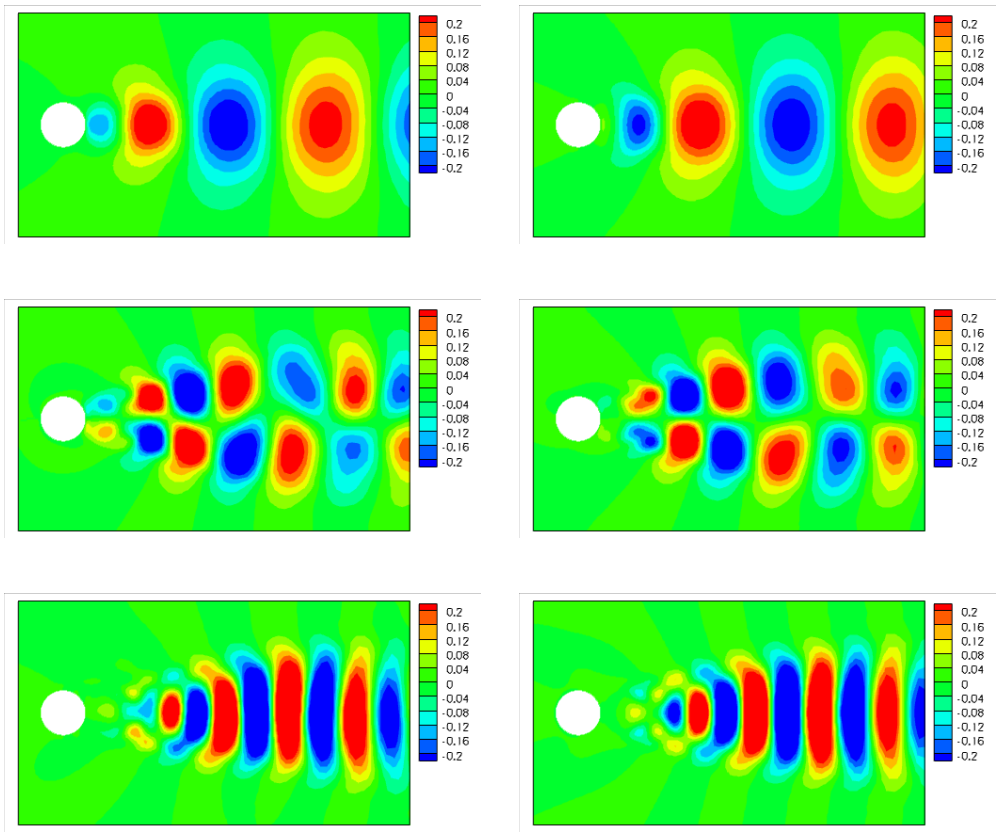

Figure 2.5: Contours of the crossflow velocity POD modes ($\phi_i^v, \quad i = 1, 2, ..., 6$) for the case of steady mean flow

2.1.4 Reduced-order model of the velocity field

To obtain the reduced-order model, the fluctuations are expanded in a Galerkin representation in terms of the POD modes (Φ_i); i.e.

$$\mathbf{u}(\mathbf{x},t) \approx \overline{\mathbf{u}}(\mathbf{x}) + \sum_{i=1}^{M} q_i(t)\Phi_i(\mathbf{x}) \tag{2.3}$$

where $\mathbf{u}(\mathbf{x},t) = (u,v)^T$, $\overline{\mathbf{u}}(\mathbf{x})$ is the mean flow, $\Phi_i(\mathbf{x}) = (\phi_i^u(\mathbf{x}), \phi_i^v(\mathbf{x}))^T$, and M is the number of POD modes used in the projection. Then, the Navier-Stokes equations are projected onto the space formed by the POD modes as

$$< \Phi_k, \frac{\partial \mathbf{u}}{\partial t} + (\mathbf{u}.\nabla)\mathbf{u} + \nabla p - \frac{1}{Re_D}\nabla^2\mathbf{u} >= 0, \tag{2.4}$$

where $< F, G >= \int_\Omega F.G d\Omega$ represents the inner product between F and G and $k = 1, 2, ..., M$. Substituting Equation (2.3) into Equation (2.4) and based on the orthogonality of the POD basis functions, one obtains a set of M ordinary differential equations (43)

$$\dot{q}_k(t) = \mathcal{A}_k + \sum_{i=1}^{M} \mathcal{B}_{ki} q_i(t) + \sum_{i=1}^{M}\sum_{j=1}^{M} \mathcal{C}_{kij} q_i(t) q_j(t), \tag{2.5}$$

where

$$\begin{aligned}
\mathcal{A}_k &= \frac{1}{\mathrm{Re}} < \Phi_k, \nabla^2\overline{\mathbf{u}} > - < \Phi_k, \overline{\mathbf{u}}.\nabla\overline{\mathbf{u}} >, \\
\mathcal{B}_{ki} &= - < \Phi_k, \overline{\mathbf{u}}.\nabla\Phi_i > - < \Phi_k, \Phi_i.\nabla\overline{\mathbf{u}} > + \frac{1}{\mathrm{Re}} < \Phi_k, \nabla^2\Phi_i > \\
\mathcal{C}_{kij} &= - < \Phi_k, \Phi_i \nabla\Phi_j > .
\end{aligned}$$

In Equation (2.5), $\mathcal{A}$ is an $M \times 1$ vector resulting from the average flow field, $\mathcal{B}$ is the linear part of the dynamical system, which originates from the interaction of the average field with the eigenfunctions and the linear dissipative operator, and $\mathcal{C}$ is a tensor representing the quadratic nonlinearity of the Navier-Stokes equations (43; 51). It should be noted here that using Green's theorem and the divergence-free property and for the case of $p = 0$ on the outerflow boundary Ω_{so}, the pressure term is not part of Equation (2.5) (52). The POD eigenfunctions are identically zero on the inflow boundary because the average flow is subtracted from the total flow. However, in case of Neumann boundary conditions on Ω_{so}, the contribution of the pressure term is not exactly zero for the cylinder wake. At $10D$

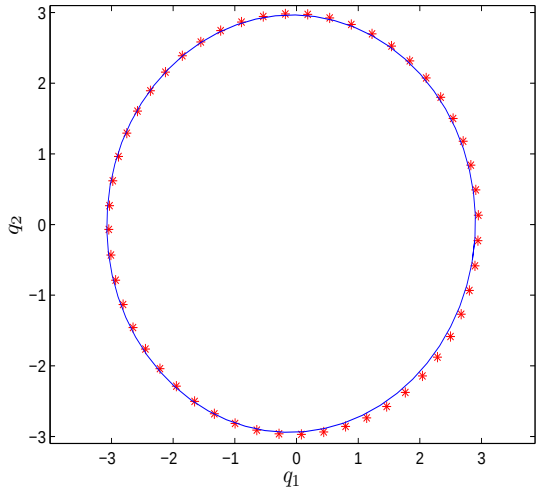

Figure 2.6: A two dimensional projection of the POD phase portrait on (q_1, q_2)-plane (solid) and snapshot portrait (stars). 10 POD modes are kept in the truncated expansion given by Equation (2.3).

downstream from the cylinder, i.e. the outflow boundary, the pressure effects of the wake are minimal. As such, their representative terms can be assumed to vanish in the reduced-order model (51).

To assess the validity of the reduced-order model, each snapshot is projected onto the POD modes and compute the following inner product

$$\tilde{q}_i(t_j) =< \Phi_i(\mathbf{x}), (\mathbf{u}(\mathbf{x}, t_j) - \overline{\mathbf{u}}(\mathbf{x})) >, \tag{2.6}$$

The first 10 POD modes are used to develop a reduced-order model for the case of steady mean flow. The Galerkin projection is performed andv$\mathcal{A}_k$, $\mathcal{B}_{ki}$, and $\mathcal{C}_{kij}$ are computed, where $k,\ m,\ n\ =\ 1, 2, ..., 10$ in Equation (2.5). Thus, the CFD problem with 193×257 degrees of freedom is reduced to a dynamical system with ten dimensions. Then, Equation (2.5) is integrated and a two-dimensional projection of the phase portrait on the plane (q_1, q_2) is performed and compared with the projection obtained on the $(\tilde{q}_1, \tilde{q}_2)$ plane in Figure 2.6. Clearly, the two projections of the ROM and the computed modes from the numerical simulations are in perfect agreement.

2.1.5 Reduced-order model for the pressure field

In incompressible flows, the Poisson equation relates the velocity and the pressure fields. In the fractional-step method used in the current numerical methodology, most of the computation time at every time iteration is consumed in solving the pressure-Poisson equation. POD-based models do not lend themselves easily for a direct computation of the loads. Thus, a modest approach is to apply the POD technique on the pressure field and later integrate the pressure field onto surface to compute the loads. Hence, similar to the velocity field, the pressure field is decomposed into mean and fluctuating components. Expanding the latter in terms of the pressure POD modes Ψ_i, one can write

$$p(\mathbf{x},t) \approx \bar{p}(\mathbf{x}) + \sum_{i=1}^{M} a_i(t)\Psi_i(\mathbf{x}), \tag{2.7}$$

where $\bar{p}(\mathbf{x})$ is the average pressure. Using Equation (2.7) in the pressure-Poisson equation leads to an algebraic reduced-order model for the pressure (42). The model works well for low Reynolds number steady cases. However, explicit nonlinear dependence on the velocity field may result in errors at the higher Reynolds numbers where more modes may be needed in the model. Furthermore, the extension of the use of the reduced-order model developed under a particular flow condition (e.g. steady mean flow) to other flow and geometric conditions has failed. To overcome these issues, stochastic estimation techniques are used to estimate the pressure field as discussed below.

2.1.6 Pressure POD modes

The pressure POD mode are computed from the pressure snapshot data obtained in a similar manner as in the case of the velocity field. However, the interest is only in the distribution of the POD pressure modes on the surface of the cylinder rather than the whole domain. Using the method of snapshots, the singular values of the pressure are computed. Unlike the velocity POD modes, the lower singular values of the pressure do not occur in pairs while the higher ones do occur in pairs, as shown in Figure 2.7(a). From Figure 2.7(b), it is clearly observed that the first pressure POD mode is the most dominant and contains more than 85% of the cumulative energy contribution.

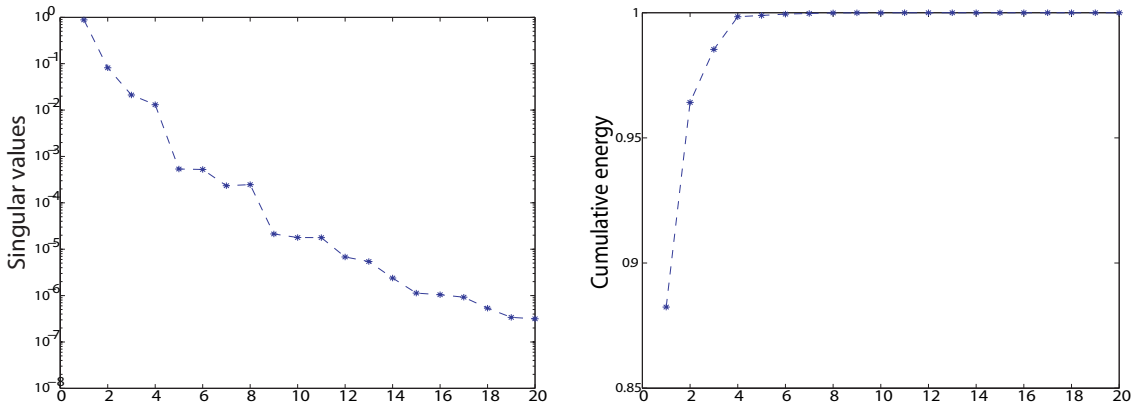

(a) Normalized singular values of POD modes

(b) Normalized cumulative energy of POD modes

Figure 2.7: Normalized singular values and cumulative energy content of pressure POD modes.

Figure 2.8 shows the distribution of the pressure POD modes on the cylinder surface. In figure 2.8(a), the average pressure over the cylinder surface is plotted. It is noted that $\theta = 0^\circ$ corresponds to the base point and $\theta = 180^\circ$ corresponds to the stagnation point on the cylinder. Figures 2.8(b)-2.8(f) show the first five pressure POD modes on the cylinder surface. From Figure 2.8(b), it is observed that the absolute maxima of the first POD mode occur at $\theta \approx 90^\circ$ and $\theta \approx 270^\circ$. For the higher modes, the absolute maxima occur close to the base point. Based on the singular values, the contributions of the higher modes are much less than that of the first mode. As such, Akhtar et al. (53) used this result and showed that placing fluidic suction actuators at the location of maximum pressure of the first POD mode could produce significant reduction in the lift and drag coefficients.

2.1.7 Linear stochastic estimator (LSE)

For each mode n, the estimated pressure POD temporal coefficients are described as a series expansion of velocity POD temporal coefficients which can be determined from a reduced-

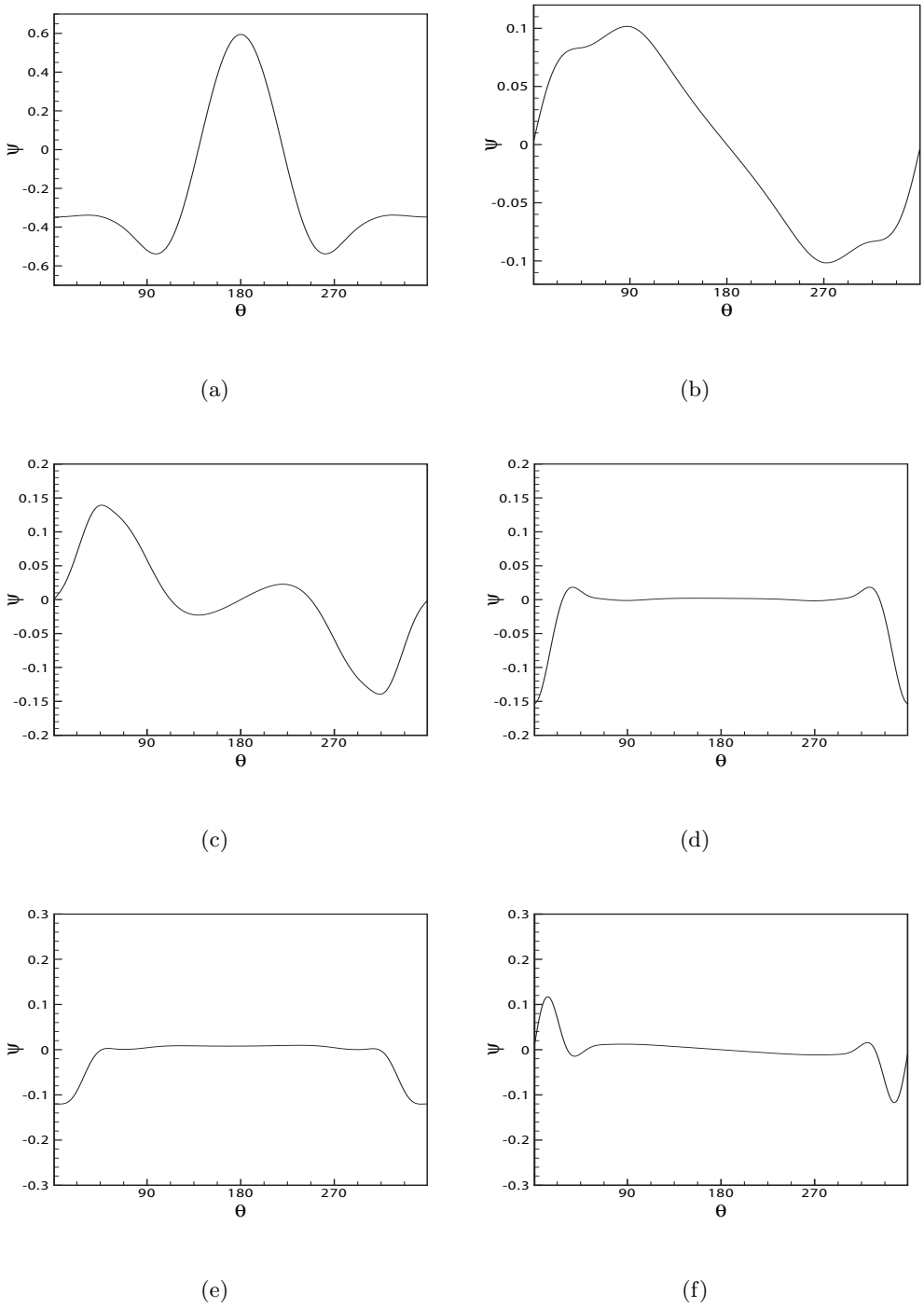

Figure 2.8: Pressure POD modes for steady mean flow condition.

order model or a snapshot projection as shown above; that is,

$$a_n(t) = L_{ni}q_i(t) + Q_{nij}q_i(t)q_j(t) + C_{nijk}q_i(t)q_j(t)q_k(t) + \cdots \tag{2.8}$$

This equation can be truncated to include just the linear term and neglecting higher-order terms. This technique is called Linear Stochastic Estimator (LSE). Including quadratic term leads to Quadratic Stochastic Estimator (QSE), and so on (54; 55). Denoting by $\tilde{a}_i$ the temporal coefficients obtained by projecting each pressure snapshots onto the POD mode Ψ_i; that is,

$$\tilde{a}_i(t) =< \Psi_i(\mathbf{x}), (p(\mathbf{x},t) - \bar{p}(\mathbf{x})) >, \tag{2.9}$$

The mapping matrix L is computed by minimizing the mean square error defined as (54; 55)

$$E_{a_n} = \left\langle \left(a_n(t) - \tilde{a}_n(t)\right)^2 \right\rangle_T, \quad \text{where} \quad \left\langle (.),(.) \right\rangle_T = \int_0^T (.)(.)dt$$

The solution of this minimization problem is obtained by solving the following linear system:

$$\begin{pmatrix} \left\langle q_1, q_1 \right\rangle_T & \left\langle q_1, q_2 \right\rangle_T & \cdots & \left\langle q_1, q_M \right\rangle_T \\ \vdots & \vdots & & \vdots \\ \left\langle q_M, q_1 \right\rangle_T & \left\langle q_M, q_2 \right\rangle_T & \cdots & \left\langle q_M, q_M \right\rangle_T \end{pmatrix} \begin{pmatrix} \left\langle \tilde{a}_n, q_1 \right\rangle_T \\ \vdots \\ \left\langle \tilde{a}_n, q_M \right\rangle_T \end{pmatrix} = \begin{pmatrix} L_{n1} \\ \vdots \\ L_{nM} \end{pmatrix}$$

The first eight POD modes (which contain more than 99 % of the total energy) are considered. Figure 2.9 shows a comparison of the estimated pressure POD temporal coefficients obtained from LSE against those obtained by projecting snapshots data for the pressure as given by Equation (2.9). A good match between the two sets of data shows that LSE is an efficient tool to estimate the pressure POD temporal coefficients.

2.1.8 Force weight coefficients

The forces (lift and drag) applied on the cylinder can be written as the addition of the contributions of the pressure and shear stresses acting on the surface of the cylinder; that is, (42)

$$\begin{aligned} C_L(t) &= -\int_0^{2\pi} \left(p(\mathbf{x},t)\sin(\theta) - \frac{1}{\mathrm{Re}}\left(\frac{\partial v(\mathbf{x},t)}{\partial x} - \frac{\partial u(\mathbf{x},t)}{\partial y}\right)\cos(\theta) \right) d\theta \\ C_D(t) &= -\int_0^{2\pi} \left(p(\mathbf{x},t)\cos(\theta) + \frac{1}{\mathrm{Re}}\left(\frac{\partial v(\mathbf{x},t)}{\partial x} - \frac{\partial u(\mathbf{x},t)}{\partial y}\right)\sin(\theta) \right) d\theta \end{aligned} \tag{2.10}$$

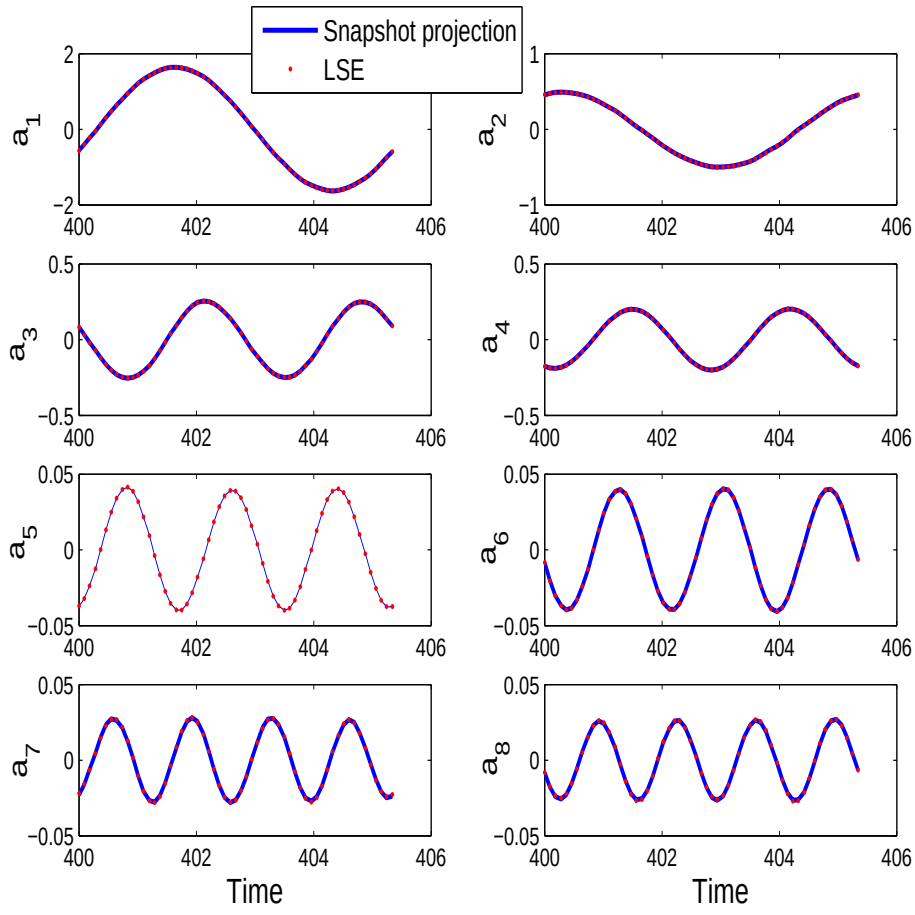

Figure 2.9: Pressure coefficients for steady mean flow conditions: Snapshot projection vs. LSE.

Substituting Equations (2.3) and (2.7) into Equations (2.10), and integrating over the cylinder surface, one obtains

$$\begin{aligned} C_L(t) &= \sum_{i=0}^{M} L_{p_i} a_i(t) + \sum_{i=0}^{M} L_{v_i} q_i(t) \\ C_D(t) &= \sum_{i=0}^{M} D_{p_i} a_i(t) + \sum_{i=0}^{M} D_{v_i} q_i(t) \end{aligned} \tag{2.11}$$

where

$$\begin{aligned} &L_{p_0} = -\int_0^{2\pi} \Big(\bar{p}(\mathbf{x})\sin(\theta)\Big)\, d\theta, \;\; D_{p_0} = -\int_0^{2\pi} \Big(\bar{p}(\mathbf{x})\cos(\theta)\Big)\, d\theta \\ &L_{p_i} = -\int_0^{2\pi} \Big(\Psi_i(\mathbf{x})\sin(\theta)\Big)\, d\theta, \;\; D_{p_i} = -\int_0^{2\pi} \Big(\Psi_i(\mathbf{x})\cos(\theta)\Big)\, d\theta. \;\; i = 1, 2, \cdots, M \\ &L_{v_0} = \int_0^{2\pi} \Big(\frac{1}{\mathrm{Re}_D}(\frac{\partial \bar{v}(\mathbf{x})}{\partial x} - \frac{\partial \bar{u}(\mathbf{x})}{\partial y})\cos(\theta)\Big)\, d\theta, \\ &D_{v_0} = -\int_0^{2\pi} \Big(\frac{1}{\mathrm{Re}_D}(\frac{\partial \bar{v}(\mathbf{x})}{\partial x} - \frac{\partial \bar{u}(\mathbf{x})}{\partial y})\sin(\theta)\Big)\, d\theta \\ &L_{v_i} = \int_0^{2\pi} \Big(\frac{1}{\mathrm{Re}_D}(\frac{\partial \phi^v(\mathbf{x})}{\partial x} - \frac{\partial \phi^u(\mathbf{x})}{\partial y})\sin(\theta)\Big)\, d\theta, \\ &D_{v_i} = -\int_0^{2\pi} \Big(\frac{1}{\mathrm{Re}_D}(\frac{\partial \phi^v(\mathbf{x})}{\partial x} - \frac{\partial \phi^u(\mathbf{x})}{\partial y})\cos(\theta)\Big)\, d\theta. \;\; i = 1, 2, \cdots, M \end{aligned} \tag{2.12}$$

Equation (2.11) provides a representation of the lift and drag forces in terms the velocity and pressure temporal coefficients. The q's are obtained through a reduced-order model as given by Equations (2.5), and a's are obtained using the LSE technique. Table 1 provides values for the lift and drag weight coefficients (L_{p_i} and D_{p_i}) for the first six modes. It is noted that L_{p_0} and D_{p_0} are the mean values of the lift and drag coefficients, respectively.

It is interesting to note that $L_{p_0} = 0$ which suggests that there is zero mean lift on the cylinder. Similarly, $D_{p_0} = 1.0146$ pertains to the mean pressure drag of the circular cylinder. Clearly, the parameters used in reduced-order have physical attributes and signify flow physics.

From the values given in Table 1 and the amplitudes of the a's as shown in Figure 2.9, one could identify the relative contribution of the pressure POD modes to the force weight

Table 2.1: Lift and drag weight coefficients.

L_{p_0}	L_{p_1}	L_{p_2}	L_{p_3}	L_{p_4}	L_{p_5}	L_{p_6}
0	-0.314	-0.210	-0.0007	0.0002	-0.0451	0.0517
D_{p_0}	D_{p_1}	D_{p_2}	D_{p_3}	D_{p_4}	D_{p_5}	D_{p_6}
1.0146	-0.0001	0.0002	0.0750	0.1315	-0.0006	0.0003

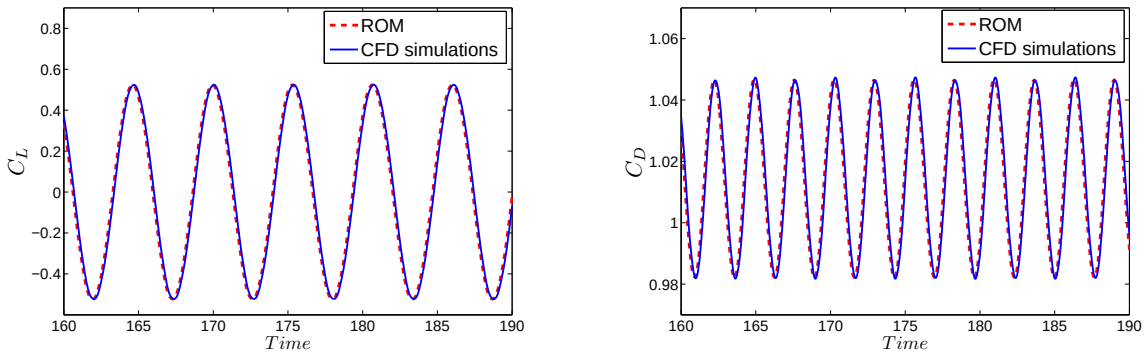

(a) Lift

(b) Drag

Figure 2.10: Lift and drag coefficients: ROM vs. CFD.

coefficients. Clearly, the first few pressure POD modes contribute the most to the lift and drag coefficients.

In Figure 2.10, the lift and drag weight coefficients obtained from CFD and reconstructed from the low-dimensional method by combining POD and LSE are plotted. It is noted that 10 POD modes are used in Equation (2.11) to compute the lift and drag coefficients. A good agreement between these data is clearly observed. This demonstrates the capability of the developed tool to accurately predict the loads.

2.1.9 Modeling of unsteady flows

Flow quantities such as aerodynamic or hydrodynamic loads, heat transfer and noise radiation can be significantly affected by mean flow unsteadiness which is inevitably a part of many

natural flows and is encountered in many technological applications. Here, the approach is expanded to develop reduced-order models that cover unsteady flow cases.

In the unsteady case, a sinusoidal component with a specific amplitude $A/U_\infty = 0.0532$ (approximately 5% disturbance in the freestream direction) and nondimensional frequency $f_m = 0.2052$ that is considered close to the shedding frequency of the steady flow $f_s = 0.1862$ is added to the mean flow ; that is,

$$\mathbf{U}_\infty(t) = U_\infty + \gamma(t) = U_\infty(1 + \frac{A}{U_\infty}\sin(2\pi f_m t))$$

To enable modeling of the unsteady mean flow in terms of the steady flow POD modes, the velocity field is expanded as

$$\mathbf{u}(\mathbf{x},t) \approx \overline{\mathbf{u}}^S(\mathbf{x})(1+\gamma(t)) + \sum_{i=1}^{M} q_i(t)\Phi_i^S(\mathbf{x}) \tag{2.13}$$

where Φ_i^S are the POD modes of the steady mean flow $\overline{\mathbf{u}}^S$.

The use of the Φ_i^S is emphasized since it constitutes a key contribution of this effort, at least for the velocity field. Computing new POD modes for the modified flow field, i.e. unsteady inflow, and developing a ROM based on modified POD modes is not the objective of this work. In fact, it is one of the drawbacks of the POD-based reduced-order models which has been addressed by developing the reduced-order model for unsteady inflow using the POD basis of the steady flow field. This approach will add robustness to the POD-based reduced-order models and increase the spectrum of its application. As a first step in modeling the inflow unsteadiness, the frequency of disturbance (f_m) is kept close to the shedding frequency (f_s). Adding unsteadiness to the mean flow that has multiple frequencies will render the flow field complex and is beyond the scope of current paper and can be addressed in future using a similar approach.

Substituting Equation (2.13) into the Navier-Stokes equations, expanding each term, and projecting these equations on the Φ_i^S, one obtains

$$\begin{aligned}\dot{q}_k(t) &= \mathcal{A}_k + \sum_{i=1}^{M}\mathcal{B}_{ki}q_i(t) + \sum_{i=1}^{M}\sum_{j=1}^{M}\mathcal{C}_{kij}q_i(t)q_j(t) \\ &+ \mathcal{H}_k\dot{\gamma}(t) + \sum_{i=1}^{M}\mathcal{I}_{ki}q_i(t)\gamma(t) + \mathcal{K}_k\gamma(t) + \mathcal{L}_k\gamma^2(t)\end{aligned} \tag{2.14}$$

where

$$\begin{aligned}
\mathcal{H}_k &= - < \Phi_k^S, \overline{\mathbf{u}}^S >, \\
\mathcal{I}_{ki} &= - < \Phi_k^S, \overline{\mathbf{u}}^S . \nabla \Phi_i^S > - < \Phi_k^S, \Phi_i^S . \nabla \overline{\mathbf{u}}^S > \\
\mathcal{K}_k &= \frac{1}{Re_D} < \Phi_k^S, \nabla^2 \overline{\mathbf{u}}^S > -2 < \Phi_k^S, \overline{\mathbf{u}}^S . \nabla \overline{\mathbf{u}}^S >, \\
\mathcal{L}_k &= - < \Phi_k^S, \overline{\mathbf{u}}^S . \nabla \overline{\mathbf{u}}^S > .
\end{aligned}$$

It is important to note that Equation (2.13) contains two time-dependent states; q_i and γ. Therefore, two time derivatives in the modified reduced order model are obtained. The convection and diffusion terms of Navier-Stokes equations give rise to linear and quadratic terms in q_i, γ, and their combinations in the model. In the modified reduced order model given by Equation (2.14), the first part is the same as the usual reduced-order model for steady flow and the second part is an explicit function of time that models the unsteadiness in the mean flow. Ten POD modes are used (i.e. $M = 10$) and integrate Equation (2.14) simultaneously and compute the $q_k(t)$. Then, the velocity field is recreated using Equation (2.13). In Figure 2.11, the streamwise velocity at the probe in the vortex shedding region of the cylinder as obtained from CFD and reconstructed from the POD-based reduced order model given by Equation (2.14) is plotted. The fairly good match between the two sets of data shows that the reduced order model captures the main features of the velocity field.

It should be noted that an attempt was made to follow a similar approach to use the steady POD modes to compute the mapping function which relate the pressure and velocity fields. However, it is found that the use of the steady pressure POD modes is not appropriate to capture the unsteadiness effects. Alternatively, the unsteady pressure POD modes and Equations (2.11) and (2.12) are used to reconstruct the lift and drag coefficients for the unsteady mean flow case. In Figure 2.12 the lift and drag coefficients for the unsteady case obtained from CFD simulations and reconstructed from the low-dimensional tool using the unsteady POD modes are plotted. A good match between the two sets of data is observed and shows the capability of the developed tool to reconstruct the force coefficients even for the unsteady mean flow case. It should be noted that the use of the CFD simulations in the construction of the low-dimensional tool constitutes a major limitation.

In this section, a low-dimensional method to predict the effects of unsteadiness in the

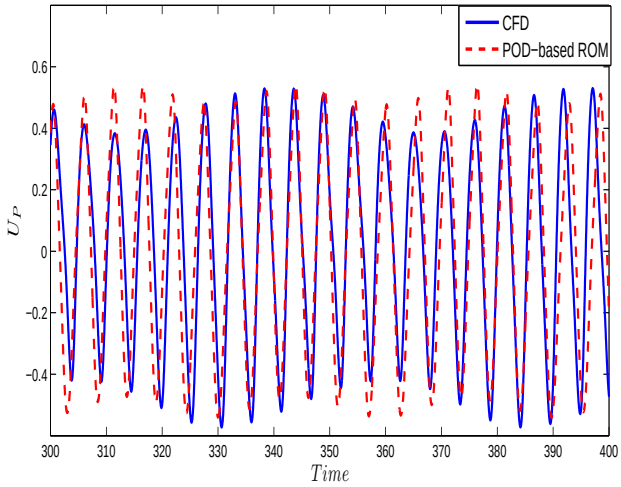

Figure 2.11: A Streamwise velocity at the probe from CFD and POD (unsteady mean flow case). 10 POD modes are kept in the truncated expansion given by Equation (2.13).

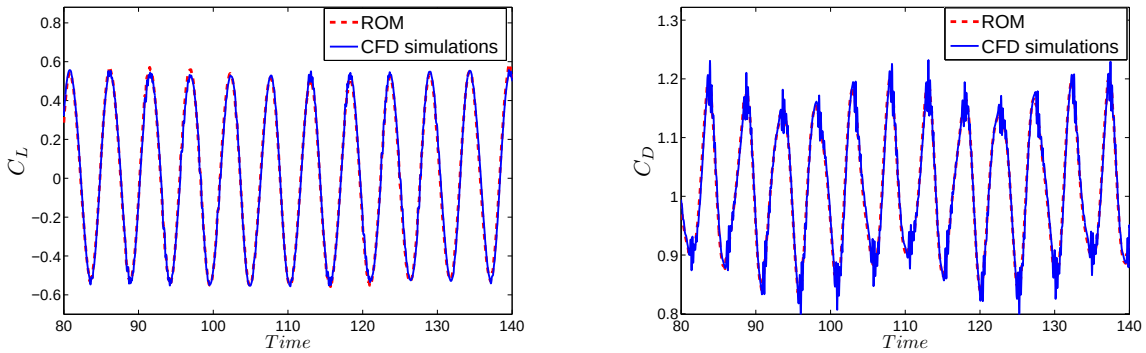

(a) Lift coefficient

(b) Drag coefficient

Figure 2.12: Lift and drag coefficients for the unsteady inflow: reduced-order model (ROM) vs direct numerical simulation (CFD).

inflow on force coefficients acting on a circular cylinder using POD modes from steady flow simulations is developed. The approach is based on combining POD and LSE techniques. In particular, the use of POD is extended to cover unsteady flows. Then, to overcome the difficulty of developing a ROM using Poissons equation (this methodology works well only for low Reynolds number and cannot cover unsteady mean flow cases as reported by Akhtar et al. (42)), the pressure field is related to the velocity field through a mapping function based on LSE. For both steady and unsteady cases, the final outcome is a representation of the lift and drag coefficients in terms of velocity and pressure temporal coefficients. Such a representation could serve as the basis for implementing control strategies or conducting uncertainty quantification analyses.

2.2 Example 2: Normal Form Representation of The Aeroelastic Response of The Goland Wing

In this section [2], the usefulness and effectiveness of low-dimensional representations of aeroelastic systems to characterize their physical behaviors and perform rapid sensitivity analysis are shown. To this end, the aeroelastic response of the Goland wing is considered and two approaches to derive its normal form are followed. Such a form constitutes an effective tool to model the main physical behaviors of aeroelastic systems and, as such, can be used for developing a phenomenological reduced-order model.

Beran (56) used perturbation techniques to study limit cycle oscillations (LCO) dynamics of a structurally supported airfoil with a flap. The typical airfoil section is free to translate vertically, rotate about the elastic axis, and can undergo flap deflection about a hinge point. The governing aerodynamic equations are the Euler equations. The method of multiple scales (MMS) was applied on the combined fluid and structure equations to derive the normal form that provides an explicit description of the amplitude and frequency of LCO. The direct analysis showed capability to predict accurately LCO and more efficiently in terms

[2] Nayfeh, A.H., Ghommem, M., and Hajj, M.R., 2011, Normal Form Representation of The Aerodynamic Response of The Goland Wing, *Nonlinear Dynamics*. DOI: 10.1007/s11071-011-0111-6.

of computational cost than the approach based on time integration. However, particular care was taken in the numerical estimation of high-order derivatives needed in the LCO computation procedure when using MMS. Direct tools based on Hopf bifurcation analysis for flutter prediction were also developed by Morton and Beran (57) and tested for a pitch-and-plunge airfoil at transonic Mach number conditions. These tools were extended later by Badcock et al. (58) who used direct approach, based on establishing a nonlinear set of algebraic equations, for prediction of flutter onset. Woodgate and Badcock (59) followed an approach based on the center manifold theory for reducing a large dimensional model of a three-dimensional aeroelastic system, governed by the Euler equations, to its essential dynamics. Their analysis was limited to computing the damping as needed for the prediction of flutter onset and did not cover the post-bifurcation behavior (i.e. LCOs). Dimitriadis et al. (60) applied the center manifold theorem to a nonlinear aeroelastic system in order to reduce its dimensionality and predict its bifurcation and post-bifurcation behavior. In particular, an extended version of the center manifold representation was introduced to allow for an accurate prediction of the aeroelastic behavior away from the flutter onset. Leng (61) used the method of averaging to derive a reduced-order model for a nonlinear aeroelastic system. The model was used to conduct bifurcation analysis and showed a capability to perform a nonlinear analysis for such systems.

In this work, two approaches are followed to derive the normal form of the dynamics of the Goland wing. In the first approach, an approximation of the wing's response near the Hopf bifurcation is constructed by directly applying the method of multiple scales to the two coupled partial-differential equations of motion. In the second approach, the same method is applied to a Galerkin discretized model that is based the mode shapes of a cantilever beam. The perturbation results from both approaches are verified by comparison with results from numerical integration of the discretized equations.

2.2.1 Problem formulation

The dynamics of the Goland wing in an air stream is considered, as shown in Figure 2.13. The geometric and physical properties of the aeroelastic system are similar to the ones considered by Beran et al. (62) and are provided in Table 2.2. The wing is assumed to undergo bending

around the x axis and twisting around the y axis. Moreover, the case in which the wing is inextensional is considered. To derive the governing equations and boundary conditions, the extended Hamilton principle is used

$$\int_{t_1}^{t_2} (\delta T_w - \delta V + \delta W_{nc}) dt = 0. \tag{2.15}$$

where, T_w is the total kinetic energy of the wing; V is the total elastic energy of the wing; and the variation of the nonconservative energy, δW_{nc}, is due to damping and applied aerodynamic (lift and moment) loads.

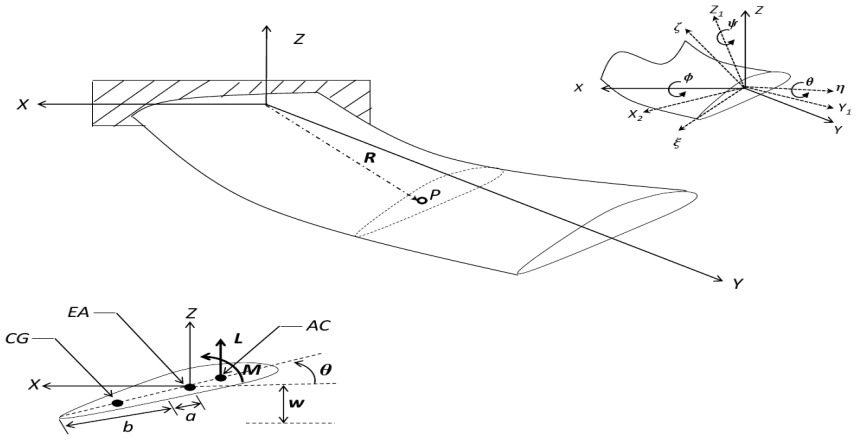

Figure 2.13: A Cantilever Wing Geometry.

Kinematics

To calculate the kinetic and elastic energies, two coordinate systems are introduced: the Cartesian coordinate system XYZ that describes the undeformed configuration, and the orthogonal curvilinear coordinate system $\xi\eta\zeta$ that describes the deformed geometry. u, v, and w denote the displacements of the reference point on the observed cross–section along the the X, Y, and Z directions, respectively; s denotes the undeformed length from the root of the wing to the reference point; $\mathbf{i}_X$, $\mathbf{i}_Y$, and $\mathbf{i}_Z$ denote the unit vectors along the x, y, and z directions, respectively; and $\mathbf{i}_1$, $\mathbf{i}_2$, and $\mathbf{i}_3$ denote the unit vectors along the ξ, η, and ζ axes, respectively. In terms of the (1-3-2) Euler angles (ϕ, ψ, θ), the two unit vectors are related

as follows:

$$\begin{Bmatrix} \mathbf{i}_1 \\ \mathbf{i}_2 \\ \mathbf{i}_3 \end{Bmatrix} = [T] \begin{Bmatrix} \mathbf{i}_X \\ \mathbf{i}_Y \\ \mathbf{i}_Z \end{Bmatrix} \tag{2.16}$$

where

$$[T] = \begin{bmatrix} \cos\theta\cos\psi & \cos\theta\sin\psi\cos\phi + \sin\theta\sin\phi & \cos\theta\sin\psi\sin\phi - \sin\theta\cos\phi \\ -\sin\psi & \cos\phi\cos\psi & \sin\phi\cos\psi \\ \sin\theta\cos\psi & \sin\theta\sin\psi\cos\phi - \cos\theta\sin\phi & \sin\theta\sin\psi\sin\phi + \cos\theta\cos\phi \end{bmatrix} \tag{2.17}$$

The bending curvature ρ_1 about the ξ axis, the twisting curvature ρ_2 about the η axis, and the bending curvature ρ_3 about the ζ axis are given by

$$\rho_1 = \phi' \cos\theta\cos\psi - \psi'\sin\theta \tag{2.18}$$

$$\rho_2 = -\phi'\sin\psi + \theta' \tag{2.19}$$

$$\rho_3 = \phi'\sin\theta\cos\psi + \psi'\cos\theta \tag{2.20}$$

where the prime indicates the derivative with respect to y. It follows that the Euler angles ϕ and ψ are related to the u, v, and w displacements as

$$\cos\phi = \frac{1+v'}{\sqrt{(1+v')^2 + w'^2}} \quad \text{and} \quad \sin\phi = \frac{w'}{\sqrt{(1+v')^2 + w'^2}} \tag{2.21}$$

$$\cos\psi = \frac{\sqrt{(1+v')^2 + w'^2}}{\sqrt{(1+v')^2 + u'^2 + w'^2}} \quad \text{and} \quad \sin\psi = \frac{-u'}{\sqrt{(1+v')^2 + u'^2 + w'^2}} \tag{2.22}$$

Moreover, the axial strain e is given by

$$e = \sqrt{(1+v')^2 + u'^2 + w'^2} - 1 \tag{2.23}$$

Because the wing is assumed to be inextensional, $e = 0$ and, Equation (2.23) is rewritten as:

$$v' = -\frac{1}{2}(u'^2 + w'^2) + \cdots$$

Moreover, for a wing undergoing bending about the x axis only, $u = 0$, which yields

$$v' = -\frac{1}{2}w'^2 + \cdots \quad \text{or} \quad v = -\frac{1}{2}\int_0^s w'^2 \, ds \tag{2.24}$$

With these assumptions, the kinetic and elastic energies of the wing are developed as shown below.

Kinetic energy

It follows from Figure 2.13 that the deformed position vector $\mathbf{R}$ of an arbitrary point $(0, s, 0)$ on the elastic axis of the observed cross–section in the XYZ frame is given by

$$\mathbf{R} = u\mathbf{i}_X + (s+v)\mathbf{i}_Y + w\mathbf{i}_Z + \xi\mathbf{i}_1 + 0\mathbf{i}_2 + \zeta\mathbf{i}_3 \tag{2.25}$$

Therefore, the kinetic energy density of the wing is given by

$$T_w = \frac{1}{2}\int_0^L \int_A \rho_w \dot{\mathbf{R}} \cdot \dot{\mathbf{R}}\, dA\, dy \tag{2.26}$$

where ρ_w is the wing material density, the overdot denotes the derivative with respect to t, L is the wing span, and A is the cross–section area of the wing. Using the transformation matrix T and taking the derivative of Equation (2.25) with respect to t yields

$$\dot{\mathbf{R}} = (\dot{u} + \xi\dot{T}_{11} + \zeta\dot{T}_{31})\mathbf{i}_X + (\dot{v} + \xi\dot{T}_{12} + \zeta\dot{T}_{32})\mathbf{i}_Y + (\dot{w} + \xi\dot{T}_{13} + \zeta\dot{T}_{33})\mathbf{i}_Z \tag{2.27}$$

where the T_{ij} are the components of the matrix T. Using Equation (2.17), Equation (3.13) is rewritten as

$$\begin{aligned}\dot{\mathbf{R}} \quad &= (-\xi\sin\theta + \zeta\cos\theta)\dot{\theta}\mathbf{i}_X + \Big[\dot{v} + (\xi\cos\theta + \zeta\sin\theta)\,\dot{\theta}\sin\phi + (\xi\sin\theta - \zeta\cos\theta)\dot{\phi}\cos\phi\Big]\mathbf{i}_Y \\ &+ \Big[\dot{w} - (\xi\cos\theta + \zeta\sin\theta)\dot{\theta}\cos\phi + (\xi\sin\theta - \zeta\cos\theta)\dot{\phi}\sin\phi\Big]\mathbf{i}_Z \end{aligned} \tag{2.28}$$

Substituting Equation (2.28) into Equation (2.26), using Equations (2.21) and (2.24), and expanding the result for small θ and w, one obtains

$$T_w = \frac{1}{2}\int_0^L \Big[m\dot{v}^2 + m\dot{w}^2 - 2me_x\dot{w}\dot{\theta} + J_y\dot{\theta}^2 + J_x\dot{w}'^2\Big]\, dy + \cdots \tag{2.29}$$

where

$$m = \int_A \rho_w\, dA, \quad me_x = \int_A \rho_w\xi\, dA, \quad J_x = \int_A \rho_w\xi^2\, dA, \quad J_y = \int_A \rho_w(\xi^2+\zeta^2)\, dA \tag{2.30}$$

Here, m is the mass per unit span and e_x denotes the distance from the centroidal axis to the elastic axis. The nonlinear terms involving e_x have been neglected under the assumption that it is much smaller than the wing span L. Similar terms involving J_x and J_y have also been neglected because their contributions to the kinetic energy are small in comparison to contributions by terms involving stiffness coefficients.

Elastic energy

The total elastic energy of the wing span is given by

$$V = \frac{1}{2}\int_0^L \left(D_x\rho_1^2 + D_y\rho_2^2 + D_z\rho_3^2\right) dy \tag{2.31}$$

where D_x, D_z, and D_y are the bending and torsional stiffnesses. Substituting Equations (2.18)–(2.20) into Equation (2.31), using Equations (2.21) and (2.24), and expanding the result for small θ and w, one obtains

$$V = \frac{1}{2}\int_0^L \left[D_y\theta'^2 + D_x w''^2 - D_x\theta^2 w''^2 + D_z\theta^2 w''^2 + D_x w'^2 w''^2\right] dy + \cdots \tag{2.32}$$

Nonconservative work

The nonconservative work is due to the aerodynamic loads. The quasi-steady model (63) is used to estimate these loads

$$L = \quad \pi\rho U b^2\dot{\theta} + 2\pi\rho U^2 b\left(\alpha_e - C_e\,\alpha_e^3\right) \tag{2.33}$$

$$M = \quad -\pi\rho U b^3\left(\frac{1}{2} - a\right)\dot{\theta} + 2\pi\rho U^2 b^2\left(\frac{1}{2} + a\right)\left(\alpha_e - C_e\,\alpha_e^3\right) \tag{2.34}$$

where ρ is the air density, b is the half wing chord length, U is the air speed, a is the location of the elastic axis relative to the midchord, C_e is a nonlinear coefficient to model stall, and α_e is the effective angle of attack given by

$$\alpha_e = \quad \theta - \frac{\dot{w}}{U} + \frac{b}{U}\left(\frac{1}{2} - a\right)\dot{\theta} \tag{2.35}$$

The nonconservative work is written as:

$$W_{nc} = L\ w\ +\ M\ \theta \tag{2.36}$$

Equations of motion and boundary conditions

Substituting Equations (2.29), (2.32), and (2.36) into Equation (2.15), integrating the outcome by parts, assuming that $\delta\theta(y,t_1) = \delta\theta(y,t_2) = 0$ and $\delta w(y,t_1) = \delta w(y,t_2) = 0$, and

using the boundary conditions $w(0,t)=0$, $w'(0,t)=0$, and $\theta(0,t)$, one obtains

$$\begin{aligned}
\int_{t_1}^{t_2}\int_0^L \Bigg\{ \Bigg[& -J_y\ddot{\theta} + me_x\ddot{w} + D_y\theta'' - (D_z-D_x)\theta w''^2 + M \Bigg]\delta\theta \\
& -\Bigg[m\ddot{w} - me_x\ddot{\theta} - J_x\ddot{w}'' + D_x w^{iv} + (D_z-D_x)(\theta^2 w'')'' + \\
& D_x\left(w'(w'w'')'\right)' + \frac{1}{2}m\left(w'\int_L^y \frac{\partial^2}{\partial t^2}\left[\int_0^s w'^2 ds\right] ds\right)' - L\Bigg]\delta w \Bigg\}\, dy\, dt \\
& -\int_{t_1}^{t_2}\Bigg[D_y\theta'\,\delta\theta + \left(D_x w'' + (D_z-D_x)\theta^2 w'' + D_x w'^2 w''\right)\delta w' \\
& \quad +\left(D_x w''' + D_x(w'w''^2 + w'^2 w''') + (D_z-D_x)(\theta^2 w'')'\right)\delta w\Bigg]_0^L dt = 0
\end{aligned} \tag{2.37}$$

It follows from Equations (2.37) and (2.33)–(2.35) that the equations describing the bending and twisting motions of the wing are given by

$$\begin{aligned}
m\ddot{w} - me_x\ddot{\theta} + D_x w^{iv} - J_x\ddot{w}'' - 2\pi\rho U b\left[b(1-a)\dot{\theta} - \dot{w} + U\theta\right] = \\
(D_x-D_z)(\theta^2 w'')'' - D_x\left(w'(w'w'')'\right)' - \frac{1}{2}m\left[w'\int_L^y \frac{\partial^2}{\partial t^2}\left(\int_0^s w'^2 ds\right) ds\right]' \\
- 2\pi\rho U^2 b C_e\left[\theta - \frac{\dot{w}}{U} + \frac{b}{U}\left(\frac{1}{2}-a\right)\dot{\theta}\right]^3
\end{aligned} \tag{2.38}$$

$$\begin{aligned}
J_y\ddot{\theta} - me_x\ddot{w} - D_y\theta'' - \pi\rho U b^2\left[ba(1-2a)\dot{\theta} + (1+2a)\left(U\theta - \dot{w}\right)\right] = \\
(D_x-D_z)\theta w''^2 - \pi\rho U^2 b^2\left(1+2a\right) C_e\left[\theta - \frac{\dot{w}}{U} + \frac{b}{U}\left(\frac{1}{2}-a\right)\dot{\theta}\right]^3
\end{aligned} \tag{2.39}$$

and the boundary conditions are

$$w = 0, \qquad w' = 0, \qquad \theta = 0 \qquad \text{at} \quad y = 0 \tag{2.40}$$

$$D_y\theta' = 0 \qquad \text{at} \quad y = L \tag{2.41}$$

$$w'' = 0 \qquad \text{at} \quad y = L \tag{2.42}$$

$$D_x w''' = (D_x-D_z)\theta^2 w''' - D_x w'^2 w''' \ \text{ at } \ y = L \tag{2.43}$$

For convenience, the nondimensional variables (denoted by hats) are introduced

$$\hat{w} = \frac{w}{L},\ \hat{y} = \frac{y}{L},\ \hat{e}_x = \frac{e_x}{L},\ \hat{b} = \frac{b}{L},\ \hat{J}_x = \frac{J_x}{mL^2},\ \hat{J}_y = \frac{J_y}{mL^2},\ \hat{t} = \frac{t}{\tau},$$
$$\hat{U} = \frac{U\tau}{L},\ \tau = L^2\sqrt{\frac{m}{D_x}},\ S = \frac{\pi\rho L^2}{m},\ D_{31} = \frac{D_z}{D_x},\ D_{21} = \frac{D_y}{D_x} \tag{2.44}$$

into Equations (2.38)–(2.43). Dropping the hat to simplify the notation, the following nondimensional equations of motion and boundary conditions are obtained

$$\begin{aligned} \ddot{w} \quad - \quad & e_x\ddot{\theta} + w^{iv} - J_x\ddot{w}'' - 2SUb\left[b(1-a)\dot{\theta} - \dot{w} + U\theta\right] = \\ & (1-D_{31})(\theta^2 w'')'' - \left(w'(w'w'')'\right)' - \frac{1}{2}\left[w'\int_1^y \frac{\partial^2}{\partial t^2}\left(\int_0^s w'^2 ds\right) ds\right]' \\ & -2SU^2 bC_e\left[\theta - \frac{\dot{w}}{U} + \frac{b}{U}\left(\frac{1}{2} - a\right)\dot{\theta}\right]^3 \end{aligned} \tag{2.45}$$

$$\begin{aligned} J_y\ddot{\theta} \quad - \quad & e_x\ddot{w} - D_{21}\theta'' - SUb^2\left[ba(1-2a)\dot{\theta} + (1+2a)\left(U\theta - \dot{w}\right)\right] = \\ & (1-D_{31})\theta w''^2 - SU^2b^2\left(1+2a\right)C_e\left[\theta - \frac{\dot{w}}{U} + \frac{b}{U}\left(\frac{1}{2} - a\right)\dot{\theta}\right]^3 \end{aligned} \tag{2.46}$$

$$w = 0, \qquad w' = 0, \qquad \theta = 0 \qquad \text{at} \quad y = 0 \tag{2.47}$$

$$D_{21}\theta' = 0 \qquad \text{at} \quad y = 1 \tag{2.48}$$

$$w'' = 0 \qquad \text{at} \quad y = 1 \tag{2.49}$$

$$w''' = (1-D_{31})\theta^2 w''' - w'^2 w''' \ \text{ at } \ y = 1 \tag{2.50}$$

As shown above, cubic nonlinearities in the governing equations include geometric, inertia and aerodynamic contributions. Due to the inherent nonlinearity, approaching these equations using numerical techniques to characterize the physical behavior of the wing under varying conditions and parameters would be an expensive and hard task. To overcome this issue, perturbation techniques are used to derive the normal form which allows for a simplified representation of the dynamics of the wing near the onset of flutter.

2.2.2 Analysis

For small air speeds, the wing is stable, in the sense that any disturbances would decay with time. As this speed increases, the trivial state loses stability with two complex–conjugate

Table 2.2: Geometric and physical properties of the Goland wing.

Parameter	Value
Mass per unit span, m (slug/ft)	11.249
Bending stiffness, D_x (lb/ft^2)	23.647$\times 10^6$
Torsional stiffness, D_y (lb/ft^2)	2.3899$\times 10^6$
Air density, ρ (slug/ft^3)	0.00238
Half wing chord, b (ft)	6
Wing span, L (ft)	20
Nondimensional distance of the elastic axis relative to the midchord, a	-1/3
e_x from leading edge(ft)	2
Wing mass moments of inertia/span about the x axis, J_x (slug-ft^2/ft)	0.24921
Wing mass moments of inertia/span about the y axis, J_y (slug-ft^2/ft)	25.170

eigenvalues of the linearized system transversely exiting from the left–half to the right–half of the complex plane. This indicates the onset of a Hopf bifurcation. Next, two approaches to determine the aerodynamic response of the wing near this bifurcation are presented.

Direct approach

Here, the partial differential equations (2.45)–(2.50) are directly tackled. The method of multiple scales (64; 65) is used to determine the normal form of the wing dynamics near the flutter boundary. To this end, a nondimensional small parameter ϵ as a bookkeeping device, a small detuning U_δ of the flutter speed U_f in the form $U = U_f + \epsilon^2 U_\delta$ are introduced, and an approximate solution of Equations (2.45)–(2.50) is sought in the form

$$w(y,t;\epsilon) = \epsilon w_1(y,T_0,T_2) + \epsilon^3 w_3(y,T_0,T_2) + \cdots \quad (2.51)$$

$$\theta(y,t;\epsilon) = \epsilon \theta_1(y,T_0,T_2) + \epsilon^3 \theta_3(y,T_0,T_2) + \cdots \quad (2.52)$$

where $T_0 = t$ and $T_2 = \epsilon^2 t$. Because the rotary inertia is small, J_x is scaled as $\epsilon^2 J_x$. Substituting Equations (2.51) and (2.52) into Equations (2.45)–(2.50) and equating coefficients of like powers of ϵ, one obtains

Order ϵ

$$\mathcal{L}_1(w_1,\theta_1) = D_0^2 w_1 - e_x D_0^2\theta_1 + w_1^{iv} - 2SU_f b\left[b(1-a)D_0\theta_1 - D_0 w_1 + U_f\theta_1\right] = 0 \tag{2.53}$$

$$\mathcal{L}_2(w_1,\theta_1) = J_y D_0^2\theta_1 - e_x D_0^2 w_1 - D_{21}\theta_1'' - SU_f b^2\left[ba(1-2a)D_0\theta_1 + (1+2a)\left(U_f\theta_1 - D_0 w_1\right)\right] = 0 \tag{2.54}$$

$$w_1 = 0, \qquad w_1' = 0, \qquad \theta_1 = 0 \qquad \text{at} \quad y = 0 \tag{2.55}$$

$$D_{21}\theta_1' = 0 \qquad \text{at} \quad y = 1 \tag{2.56}$$

$$w_1'' = 0 \qquad \text{at} \quad y = 1 \tag{2.57}$$

$$w_1''' = 0 \quad \text{at} \quad y = 1 \tag{2.58}$$

Order ϵ^3

$$\begin{aligned}
\mathcal{L}_1(w_3,\theta_3) &= -2D_0D_2w_1 + 2e_xD_0D_2\theta_1 + J_xD_0^2w'' + 2SU_fb\Big[b(1-a)D_2\theta_1 - D_2w_1\Big] \\
&+ 2SU_\delta b\Big[b(1-a)D_0\theta_1 - D_0w_1 + 2U_f\theta_1\Big] + (1-D_{31})(\theta_1^2w_1'')'' \\
&- \left(w_1'(w_1'w_1'')'\right)' - \frac{1}{2}\left[w_1'\int_1^y D_0^2\left(\int_0^s {w_1'}^2 ds\right)ds\right]' \\
&- 2SU_f^2bC_e\left[\theta_1 - \frac{D_0w_1}{U_f} + \frac{b}{U_f}\left(\frac{1}{2}-a\right)D_0\theta_1\right]^3
\end{aligned} \tag{2.59}$$

$$\begin{aligned}
\mathcal{L}_2(w_3,\theta_3) &= -2J_yD_0D_2\theta_1 + 2e_xD_0D_2w_1 + SU_fb^2\Big[ba(1-2a)D_2\theta_1 - (1+2a)D_2w_1\Big] \\
&+ SU_\delta b^2\Big[ba(1-2a)D_0\theta_1 + (1+2a)\left(2U_f\theta_1 - D_0w_1\right)\Big] + (1-D_{31})\theta_1w_1''^2 \\
&- SU_f^2b^2(1+2a)C_e\left[\theta_1 - \frac{D_0w_1}{U_f} + \frac{b}{U_f}\left(\frac{1}{2}-a\right)D_0\theta_1\right]^3
\end{aligned} \tag{2.60}$$

$$w_3 = 0, \qquad w_3' = 0, \qquad \theta_3 = 0 \qquad \text{at} \quad y = 0 \tag{2.61}$$

$$D_{21}\theta_3' = 0 \qquad \text{at} \quad y = 1 \tag{2.62}$$

$$w_3'' = 0 \qquad \text{at} \quad y = 1 \tag{2.63}$$

$$w_3''' = (1-D_{31})\theta_1^2w_1''' - w_1'^2w_1''' \qquad \text{at} \quad y = 1 \tag{2.64}$$

The eigenvalue problem consisting of Equations (2.53)–(2.58) has an infinite number of eigenvalues, all of them lie in the left–half of the complex plane when $U = U_f$ except for a

purely complex–conjugate pair. Therefore, all of the eigensolutions decay with time except those corresponding to the purely imaginary pair. Consequently, the long time dynamics of the system can be expressed as

$$w_1 = A(T_2)\Phi(y)e^{i\omega_c T_0} + \bar{A}(T_2)\bar{\Phi}(y)e^{-i\omega_c T_0} \tag{2.65}$$

$$\theta_1 = A(T_2)\Psi(y)e^{i\omega_c T_0} + \bar{A}(T_2)\bar{\Psi}(y)e^{-i\omega_c T_0} \tag{2.66}$$

where $\pm i\omega_c$ are the purely imaginary eigenvalues. Substituting Equations (2.65) and (2.66) into Equations (2.59)–(2.64) yields

$$\begin{aligned}
\mathcal{L}_1(w_3,\theta_3) &= -\omega_c^2 J_x \Phi'' A e^{i\omega_c T_0} + \Big[2i\omega_c(e_x\Psi - \Phi) + 2SU_f b\,[b(1-a)\Psi - \Phi]\Big]A' e^{i\omega_c T_0} \\
&+ 2SU_\delta b\,[i\omega_c b(1-a)\Psi - i\omega_c\Phi + 2U_f\Psi]\,A e^{i\omega_c T_0} + \Big\{(1-D_{31})(\Psi^2\bar{\Phi}'' + 2\Phi''\Psi\bar{\psi})'' \\
&- \Big[\Phi'\left(\bar{\Phi}'\Phi'' + \Phi'\bar{\Phi}''\right)' + \bar{\Phi}'(\Phi'\Phi'')'\Big]' + 2\omega_c^2\left[\bar{\Phi}'\int_1^y\left(\int_0^s \Phi'^2 ds\right)ds\right]' \\
&- 6SU_f^2 bC_e\left[\Psi - \frac{i\omega_c\Phi}{U_f} + \frac{ib(1-2a)\omega_c\Psi}{2U_f}\right]^2\left[\bar{\Psi} + \frac{i\omega_c\bar{\Phi}}{U_f} - \frac{ib(1-2a)\omega_c\bar{\Psi}}{2U_f}\right]\Big\}A^2\bar{A}e^{i\omega_c T_0} \\
&+ cc + NST
\end{aligned} \tag{2.67}$$

$$\begin{aligned}
\mathcal{L}_2(w_3,\theta_3) &= \Big[2i\omega_c(e_x\Phi - J_y\Psi) + SU_f b^2\,[ba(1-2a)Psi - (1+2a)\Phi]\Big]A' e^{i\omega_c T_0} \\
&- SU_\delta b^2\Big[-i\omega_c ba(1-2a)\Psi - (1+2a)\,(2U_f\Psi - i\omega_c\Phi)\Big]A e^{i\omega_c T_0} \\
&+ \Big\{(1-D_{31})(\bar{\Psi}\Phi''^2 + 2\Psi\Phi''\bar{\Phi}'') - 3SU_f^2 b^2(1+2a)C_e\Big[\Psi - \frac{i\omega_c\Phi}{U_f} \\
&+ \frac{ib(1-2a)\omega_c\Psi}{2U_f}\Big]^2\Big[\bar{\Psi} + \frac{i\omega_c\bar{\Phi}}{U_f} - \frac{ib(1-2a)\omega_c\bar{\Psi}}{2U_f}\Big]\Big\}A^2\bar{A}e^{i\omega_c T_0} + cc + NST
\end{aligned} \tag{2.68}$$

$$w_3 = 0, \qquad w_3' = 0, \qquad \theta_3 = 0 \qquad \text{at} \quad y = 0 \tag{2.69}$$

$$D_{21}\theta_3' = 0 \ \text{ at } \ y = 1 \tag{2.70}$$

$$w_3'' = 0 \qquad \text{at} \quad y = 1 \tag{2.71}$$

$$w_3''' = \Big[(1-D_{31})(\Psi^2\bar{\Phi}''' + 2\Psi\bar{\Psi}\Phi''') - (\Phi'^2\bar{\Phi}''' + 2\Phi'\bar{\Phi}'\Phi''')\Big]A^2\bar{A}e^{i\omega_c T_0} + cc + NST \ \text{ at } \ y = 1 \tag{2.72}$$

It is noted that the homogeneous part of Equations (2.67)–(2.72) is the same as Equations (2.53)–(2.58) and that the latter has a nontrivial solution. Hence, the nonhomogeneous Equations (2.67)–(2.72) have a solution only if a solvability condition is satisfied (64). To determine this solvability condition, a particular solution of Equations (2.67)–(2.72) that results from the terms proportional to $e^{i\omega_c T_0}$ is sought in the form

$$w_3(y,T_0,T_2) = \mathbf{W}(y,T_2)e^{i\omega_c T_0} \quad \text{and} \quad \theta_3(y,T_0,T_2) = \Theta(y,T_2)e^{i\omega_c T_0} \tag{2.73}$$

and obtain

$$\mathbf{W}^{iv} - \omega_c^2\mathbf{W} + \omega_c^2 e_x\Theta - 2SU_f b\left[i\omega_c b(1-a)\Psi - i\omega_c\mathbf{W} + U_f\Theta\right] = R_1 \tag{2.74}$$

$$D_{21}\Psi'' + \omega_c^2 J_y\Psi - \omega_c^2 e_x\mathbf{W} + SU_f b^2\left[i\omega_c ba(1-2a)\Psi + (1+2a)\left(U_f\Psi - i\omega_c\mathbf{W}\right)\right] = -R_2 \tag{2.75}$$

$$\mathbf{W} = 0, \qquad \mathbf{W}' = 0, \qquad \Psi = 0 \qquad \text{at} \quad y = 0 \tag{2.76}$$

$$D_{21}\Theta' = 0 \ \text{ at } \ y = 1 \tag{2.77}$$

$$\mathbf{W}'' = 0 \qquad \text{at} \quad y = 1 \tag{2.78}$$

$$\mathbf{W}''' = B \ \text{ at } \ y = 1 \tag{2.79}$$

where R_1 and R_2 are, respectively, the coefficients of $e^{i\omega_c T_0}$ of the right-hand sides of Equations (2.67) and (2.68) and B is the coefficient of $e^{i\omega_c T_0}$ of the right-hand sides of Equation (2.72). Therefore, determining the solvability condition of Equations (2.67)–(2.72) has been transformed into determining the solvability condition of Equations (2.74)–(2.79).

To determine the solvability condition of Equations (2.74)–(2.79), Equation (2.74) is multiplied with Φ^* and Equation (2.75) with $-\Psi^*$, add the results, integrate the outcome by parts over the interval [0 1] to transfer the derivatives from $\mathbf{W}$ and Θ to Φ^* and Ψ^*, and

obtain

$$\begin{aligned}
&\int_0^1 \mathbf{W}\Big[\Phi^{*iv} - \omega_c^2\Phi^* + \omega_c^2 e_x\Psi^* + i\omega_c SU_f b\big(2\Phi^* - (1+2a)b\Psi^*\big)\Big]dy \\
+ &\int_0^1 \Theta\Bigg[- D_{21}\Psi^{*\prime\prime} - \omega_c^2 J_y\Psi^* + \omega_c^2 e_x\Phi^* - SU_f b^2\big[\,(2i\omega_c b(1-a) + U_f)\,\Phi^* \\
&\qquad\qquad - (i\omega_c ba(1-a) + (1+2a)U_f)\,\Psi^*\big]\Bigg]dy \\
+ &\Big[\Phi^*\mathbf{W}''' - \Phi^{*\prime}\mathbf{W}'' + \Phi^{*\prime\prime}\mathbf{W}' - \Phi^{*\prime\prime\prime}\mathbf{W} - D_{21}(\Theta'\Psi^* - \Theta\Psi^{*\prime})\Big]_0^1 \\
= &\int_0^1 (R_1\Phi^* + R_2\Psi^*)dy
\end{aligned} \tag{2.80}$$

Therefore, the equations governing the adjoint Φ^* and Ψ^* are obtained by setting each of the coefficients of $\mathbf{W}$ and Θ in the integrand in Equation (2.80) equal to zero. The result is

$$\Phi^{*iv} - \omega_c^2\Phi^* + \omega_c^2 e_x\Psi^* + i\omega_c SU_f b\big(2\Phi^* + (1+2a)b\psi^*\big) = 0 \tag{2.81}$$

$$\begin{aligned}
D_{21}\Psi^{*\prime\prime} + \omega_c^2 J_y\Psi^* - \omega_c^2 e_x\Phi^* \quad + \quad & SU_f b^2\Big[\,(2i\omega_c b(1-a) + U_f)\,\Phi^* \\
+ \quad & (i\omega_c ba(1-a) + (1+2a)U_f)\,\Psi^*\Big] = 0
\end{aligned} \tag{2.82}$$

To determine the adjoint boundary conditions, the homogeneous case is considered; that is, $R_1 = 0$, $R_2 = 0$, and $B = 0$. Then, substituting Equations (2.76)–(2.79) into Equation (2.80) yields

$$-\Big[\mathbf{W}\Phi^{*\prime\prime\prime} - \mathbf{W}'\Phi^{*\prime\prime} - \Theta D_{21}\Psi^{*\prime}\Big]_{y=1} + \Big[\mathbf{W}'''\Phi^* - \Theta''\Phi^{*\prime} - D_{21}\Psi'\psi^*\Big]_{y=0} = 0 \tag{2.83}$$

Because $\mathbf{W}'''(0,T_2)$, $\mathbf{W}''(0,T_2)$, $\Theta'(0,T_2)$, $\mathbf{W}'(1,T_2)$, $\mathbf{W}(1,T_2)$, and $\Theta(1,T_2)$ are not constrained, there respective coefficients in Equation (2.83) must vanish, leading to the following adjoint boundary conditions:

$$\Phi^* = 0, \quad \Phi^{*\prime} = 0, \quad \Psi^* = 0 \quad \text{at} \quad y = 0 \tag{2.84}$$

$$\Phi^{*\prime\prime\prime} = 0 \quad \text{at} \quad y = 1 \tag{2.85}$$

$$\Phi^{*\prime\prime} = 0 \quad \text{at} \quad y = 1 \tag{2.86}$$

$$D_{21}\Psi^{*\prime} = 0 \quad \text{at} \quad y = 1 \tag{2.87}$$

Having defined the adjoint, returning to Equation (2.80), and using Equations (2.76),(2.79), (2.81), (2.82), and (2.84)-(2.86) yield the solvability condition

$$\Big[\Phi^* B\Big]_{y=1} = \int_0^1 (R_1\Phi^* + R_2\Psi^*)\, dy \tag{2.88}$$

Recalling the definitions of R_1, R_2, and B, one obtains from Equation (2.88) the complex-valued normal form for the Hopf bifurcation

$$\Gamma A' = \Lambda_1 U_\delta A + \Lambda_3 A^2 \bar{A} \tag{2.89}$$

where

$$\begin{aligned}\Gamma = \int_0^1 \Bigg\{ & \quad \Phi^*\Big[2i\omega_c(e_x\Psi - \Phi) + 2SU_f b\Big(b(1-a)\Psi - \Phi\Big)\Big] \\ & + \quad \Psi^*\Big[2i\omega_c(e_x\Phi - J_y\Psi) + SU_f b^2\Big(ba(1-2a)\Psi - (1+2a)\Phi\Big)\Big]\Bigg\}\, dy\end{aligned} \tag{2.90}$$

$$\begin{aligned}\Lambda_1 = \int_0^1 \Bigg\{ & \quad 2Sb\Phi^*\Big[i\omega_c b(1-a)\Psi - i\omega_c\Phi + 2U_f\Psi\Big] \\ & + \quad Sb^2\Psi^*\Big[i\omega_c ba(1-2a)\Psi + (1+2a)\left(2U_f\Psi - i\omega_c\Phi\right)\Big]\Bigg\}\, dy\end{aligned} \tag{2.91}$$

$$\begin{aligned}\Lambda_3 = \int_0^1 \Bigg\{ & \quad \Phi^*\Bigg[(1-D_{31})(\psi^2\bar{\Phi}'' + 2\Phi''\Psi\bar{\Psi})'' - \Big[\Phi'\left(\bar{\Phi}'\Phi'' + \Phi'\bar{\Phi}''\right)' + \bar{\Phi}'(\Phi'\Phi'')'\Big]' \\ & + \quad 2\omega_c^2\left[\bar{\Phi}'\int_1^y\left(\int_0^s \Phi'^2 ds\right) ds\right]'\Bigg] \\ & + \quad \Psi^*(1-D_{31})(\bar{\Psi}\Phi''^2 + 2\Psi\Phi''\bar{\Phi}'') - 3SU_f^2 bC_e\Big(2\Phi^* + b(1+2a)\Psi^*\Big) \\ & \times\Big[\Psi - \frac{i\omega_c\Phi}{U_f} + \frac{ib(1-2a)\omega_c\Psi}{2U_f}\Big]^2\Big[\bar{\Psi} + \frac{i\omega_c\bar{\Phi}}{U_f} - \frac{ib(1-2a)\omega_c\bar{\Psi}}{2U_f}\Big]\Bigg\}\, dy \\ & - \Bigg\{ \quad \Phi^*\Bigg[(1-D_{31})(\Psi^2\bar{\Phi}''' + 2\Psi\bar{\Psi}\Phi''') - (\Phi'^2\bar{\Phi}''' + 2\Phi'\bar{\Phi}'\Phi''')\Bigg]\Bigg\}_{y=1}\end{aligned} \tag{2.92}$$

Introducing the polar form

$$A = \frac{1}{2} r e^{i\beta} \tag{2.93}$$

into Equation (2.89) and separating real and imaginary parts, one obtain the real-valued normal form

$$\dot{r} = \gamma_r U_\delta r + \chi_r r^3 \tag{2.94}$$

$$\dot{\beta} = \gamma_i U_\delta + \chi_i r^2 \tag{2.95}$$

where

$$\gamma_r + i\gamma_i = \frac{\Lambda_1}{\Gamma} \quad \text{and} \quad \chi_r + i\chi_i = \frac{\Lambda_3}{4\Gamma} \tag{2.96}$$

It is noted that r is the amplitude and $\dot{\beta}$ is the shift in the frequency of the periodic solution (LCO) that is created due to Hopf bifurcation. The type of dynamic instability depends on the sign of χ_r. If $\chi_r > 0$ the system undergoes subcritical instability, catastrophic behavior, and if $\chi_r < 0$, supercritical instability (moderate behavior) takes place. Based on the normal form, one could predict analytically the amplitude and frequency of LCO near Hopf bifurcation, study the sensitivity of the LCO response to variations in the different system's parameters, characterize the type of instability, and implement linear and nonlinear control to delay the occurrence of flutter and/or avoid the catastrophic behavior of the subcritical instability.

Discretization approach

Here, the discretization approach is followed to derive the normal form. The wing deflection w and torsion θ are approximated by

$$w(y,t) = \sum_{i=1}^{n_w} q_i(t)\phi_i(y) \;\text{ and }\; \theta(y,t) = \sum_{i=1}^{n_t} q_{i+n_w}(t)\psi_i(y) \tag{2.97}$$

where ϕ and ψ are the uncoupled bending and torsion mode shapes, respectively, and n_w and n_t are the number of bending and torsion modes, respectively. Multiplying Equation (2.45) by ϕ_i and Equation (2.46) by ψ_i, and integrating the outcome by parts over the interval [0 1], one obtains the following reduced-order model:

$$M\ddot{q}(t) - UD\dot{q}(t) + (K_s - K_e U^2)q(t) = C(q(t), \dot{q}(t), \ddot{q}(t)) \tag{2.98}$$

where the matrices are given by

$$M = \begin{pmatrix} M_{11} & M_{12} \\ M_{21} & M_{22} \end{pmatrix}, \; D = \begin{pmatrix} D_{11} & D_{12} \\ D_{21} & D_{22} \end{pmatrix}, \; K_s = \begin{pmatrix} K_{s11} & K_{s12} \\ K_{s21} & K_{s22} \end{pmatrix}, \text{ and } K_e = \begin{pmatrix} K_{e11} & K_{e12} \\ K_{e21} & K_{e22} \end{pmatrix}$$

$$M_{11_{ij}} = \int_0^1 \phi_i(\phi_j - J_x\phi_j'')\, dy, \;\; M_{12_{ij}} = -e_x \int_0^1 \phi_i\, \psi_j\, dy, \;\; M_{21_{ij}} = -e_x \int_0^1 \phi_j\, \psi_i\, dy$$

$$M_{22_{ij}} = -J_y \int_0^1 \psi_i\, \psi_j\, dy$$

$$D_{11_{ij}} = -2Sb \int_0^1 \phi_i(\phi_j - J_x\phi_j'')\, dy, \;\; D_{12_{ij}} = 2Sb^2(1-a) \int_0^1 \phi_i\, \psi_j\, dy,$$

$$D_{21_{ij}} = -Sb^2(1+2a) \int_0^1 \phi_j\, \psi_i\, dy, \;\; \text{and} \;\; D_{22_{ij}} = Sb^3 a(1-2a) \int_0^1 \psi_i\, \psi_j\, dy$$

$$K_{s11_{ij}} = \int_0^1 \phi_i''\phi_j''\, dy, \;\; K_{s12_{ij}} = 0, \;\; K_{s21_{ij}} = 0, \;\; \text{and} \;\; K_{s22_{ij}} = D_{12} \int_0^1 \psi_i'\, \psi_j'\, dy$$

$$K_{e11_{ij}} = 0, \;\; K_{e12_{ij}} = 2Sb \int_0^1 \phi_i\psi_j, \;\; K_{e21_{ij}} = 0, \;\; \text{and} \;\; K_{e22_{ij}} = Sb^2(1+2a) \int_0^1 \psi_i\, \psi_j\, dy$$

Equations (2.98) represent the level of reduced-order modeling ROM I in the schematic shown in Figure 1.1. For subsequent analyses, the cubic vector function of the sate variables $q's$ is written as follows:

$$C(q, \dot{q}, \ddot{q}) = C^s(q, q, \ddot{q}) + C^a(q, \dot{q}, q) \tag{2.99}$$

where $(.)^s$ and $(.)^a$ stand for the structural and aerodynamic contributions, respectively, and

$$\begin{aligned}
C_i^s(q, q, \ddot{q}) =& \Big(1 - D_{31}\Big) \int_0^1 \Big[\Big(\sum_{j=1}^{n_t} q_j(t)\psi_j\Big)^2 \sum_{j=1}^{n_w} q_j(t)\phi_j''\Big]'' \phi_i\, dy \\
&- \int_0^1 \Big[\sum_{j=1}^{n_w} q_j(t)\phi_j' \Big((\sum_{j=1}^{n_w} q_j(t)\phi_j')(\sum_{j=1}^{n_w} q_j(t)\phi_j'')\Big)'\Big]' \phi_i\, dy \\
&- \frac{1}{2} \int_0^1 \Big[\sum_{j=1}^{n_w} q_j(t)\phi_j' \int_1^y (\int_0^s (\sum_{j=1}^{n_w} \ddot{q}_j(t)\phi_j')^2 ds) ds\Big]' \phi_i\, dy \\
&- (1 - D_{31})\Big[\Big(\sum_{j=1}^{n_t} q_j(t)\psi_j(1)\Big)^2 \sum_{j=1}^{n_w} q_j(t)\phi_j(1)'''\Big]\phi_i(1) \\
&+ \Big[\Big(\sum_{j=1}^{n_w} q_j(t)\phi_j'(1)\Big)^2 \sum_{j=1}^{n_w} q_j(t)\phi_j'''(1)\Big]\phi_i(1) \quad \text{for} \quad i = 1, 2, ..., n_w
\end{aligned}$$

and

$$C_i^s(q,q,\ddot{q}) = \Big(1 - D_{31}\Big) \int_0^1 \Big[\Big(\sum_{j=1}^{n_t} q_j(t)\psi_j\Big)\Big(\sum_{j=1}^{n_w} q_j(t)\phi_j''\Big)^2\Big]\psi_i \, dy \quad \text{for } \; i = n_w+1, ..., n_w+n_t$$

Similarly,

$$C_i^a(q,\dot{q},q) = - \quad 2SU^2bC_e \int_0^1 \Big[\sum_{j=1}^{n_t} q_j(t)\psi_j - \frac{1}{U}\sum_{j=1}^{n_w}\dot{q}_j(t)\phi_j + \frac{b}{U}(\frac{1}{2}-a)\sum_{j=1}^{n_w}\dot{q}_j(t)\psi_j\Big]^3\phi_i \, dy$$

$$\text{for} \qquad i = 1, 2, ..., n_w$$

and

$$C_i^a(q,\dot{q},q) = - \quad SU^2b^2(1+2a)C_e \int_0^1 \Big[\sum_{j=1}^{n_t} q_j(t)\psi_j - \frac{1}{U}\sum_{j=1}^{n_w}\dot{q}_j(t)\phi_j + \frac{b}{U}(\frac{1}{2}-a)\sum_{j=1}^{n_t}\dot{q}_j(t)\psi_j\Big]^3\psi_i \, dy$$

$$\text{for} \qquad i = n_w+1, ..., n_w+n_t$$

An approximate solution is sought in the form

$$q(t) = \epsilon q_1(T_0, T_2) + \epsilon^3 q_3(T_0, T_2) + ..., \qquad T_m = \epsilon^m t \tag{2.100}$$

where ϵ is a nondimensional bookkeeping parameter. The deviation of the speed U from the flutter speed U_f is expressed as

$$U = U_f + \epsilon^2 U_\delta \tag{2.101}$$

Substituting Equations (2.100) and (2.101) into Equation (2.98) and collecting the coefficients of like powers of ϵ, one obtains

Order(ϵ)

$$M\frac{\partial^2 q_1}{\partial T_0^2} - U_f D\frac{\partial q_1}{\partial T_0} + (K_s - K_e U_f^2)q_1 = 0 \tag{2.102}$$

Order(ϵ^3)

$$M\frac{\partial^2 q_3}{\partial T_0^2} - U_f D\frac{\partial q_3}{\partial T_0} + (K_s - K_e U_f^2)q_3 = -2M\frac{\partial^2 q_1}{\partial T_0 \partial T_1} + U_f D\frac{\partial q_1}{\partial T_1} + U_\delta D\frac{\partial q_1}{\partial T_0}$$
$$+ 2U_f U_\delta K_e q_1 + C^s(q_1,q_1,q_1) + C^a(q_1,q_1,q_1) \tag{2.103}$$

The general solution of Equation (2.102) can be expressed as

$$q_1(T_0, T_2) = \sum_{m=1}^{n} c_m(T_2) v_m e^{\lambda_m T_0} \tag{2.104}$$

where the λ_m are solutions of the characteristic equation

$$Det\Big[\lambda^2 M - U_f \lambda D + (K_s - K_e U_f^2)\Big] = 0 \tag{2.105}$$

and the v_m are the eigenvectors

$$\Big[\lambda_m^2 M - U_f \lambda_m D + (K_s - K_e U_f^2)\Big] v_m = 0 \tag{2.106}$$

Retaining only nondecaying solutions yields

$$q_1(T_0, T_2) = A_{disc}(T_2) v_f e^{i\omega_f T_0} + \overline{A}_{disc}(T_2) \overline{v}_f e^{-i\omega_f T_0} \tag{2.107}$$

where $A_{disc}(T_2)$ is a complex-valued function describing the amplitude and frequency of the response. Substituting Equation (2.107) into Equation (2.103) yields,

$$M\frac{\partial^2 q_3}{\partial T_0^2} - U_f D\frac{\partial q_3}{\partial T_0} + (K_s - K_e U_f^2) q_3 = \Big[- \Big(2i\omega_c M - U_f D\Big) v_f A'_{disc} + \Big(i\omega_f D + 2U_f K_e\Big) v_f U_\delta A_{disc} + C^s(v_f, v_f, \overline{v}_f) + C^a(v_f, v_f, \overline{v}_f) A_{disc}^2 \overline{A}_{disc} \Big] e^{i\omega_c T_0} + cc + NST \tag{2.108}$$

It is noted that the homogeneous part of Equation (2.108) is the same as that of Equation (2.102) and that the latter has a nontrivial solution. Thus, Equation (2.108) has a solution only if a solvability condition is satisfied. This condition requires that

$$u_f^T \cdot [-\Big(2i\omega_c M - U_f D\Big) v_f A'_{disc} + \Big(i\omega_f D + 2U_f K_e\Big) v_f U_\delta A_{disc} + C^s(v_f, v_f, \overline{v}_f) + C^a(v_f, v_f, \overline{v}_f) A_{disc}^2 \overline{A}_{disc} \Big] = 0 \tag{2.109}$$

where

$$\Big[\lambda_m^2 M - U_f \lambda_m D + (K_s - K_e U_f^2)\Big]^T u_f = 0 \tag{2.110}$$

Expressing A in the polar form

$$A_{disc}(T_2) = \frac{1}{2} r_{disc}(T_2) e^{i\beta_{disc}(T_2)} \tag{2.111}$$

and substituting Equation (2.111) into Equation (2.109), and separating the outcome into real and imaginary parts, one obtains the alternate real-valued normal form of the system near the Hopf bifurcation

$$\begin{aligned} \frac{dr_{disc}}{dT_2} &= \gamma_r U_\delta r_{disc} + \chi_r r_{disc}^3 \\ \frac{d\beta_{disc}}{dT_2} &= \gamma_i U_\delta + \chi_i r_{disc}^2 \end{aligned} \tag{2.112}$$

where $()_r$ and $()_i$ stand for the real and imaginary parts, respectively, and

$$\gamma = \frac{u_f^T \cdot \Big(i\omega_f D + 2U_f K_e\Big) v_f}{u_f^T \cdot \Big(2i\omega_f M - U_f D\Big) v_f}$$

$$\begin{aligned}\chi &= \chi^s + \chi^a \\ &= \frac{1}{4}\frac{u_f^T \cdot C^s(v_f, v_f, \overline{v}_f)}{u_f^T \cdot \Big(2i\omega_c M - U_f D\Big) v_f} + \frac{1}{4}\frac{u_f^T \cdot C^a(v_f, v_f, \overline{v}_f)}{u_f^T \cdot \Big(2i\omega_c M - U_f D\Big) v_f}\end{aligned}$$

Equations (2.112) represent the level of reduced-order modeling ROM II in the schematic shown in Figure 1.1.

2.2.3 Results and discussion

Linear analysis

For the flutter analysis, the linearized problem given by Equations (2.53)–(2.58) is used. First, the discretized form of these equations given by Equation (2.102) is considered. The solutions λ_m of the characteristic equation (2.105) determine the stability of the trivial state. If the real parts of the eigenvalues λ_m are negative, the trivial state is stable and decay for any disturbance. On the other hand, if the real part of one or more eigenvalues are positive, the trivial solution is unstable. The flutter speed U_f is reached once two complex-conjugate eigenvalues transversely exit from the left–half to the right–half of the complex plane. One bending mode and one torsion mode are used. In Figure 2.14 the variations of the eigenvalues λ_m with the air speed in the complex plane are shown. It is observed that two complex-conjugate eigenvalues transversally cross the imaginary axis at $U_f = 230.22$ ft/s. At this speed, the aeroelastic system undergoes a Hopf bifurcation. The effect of the number of mode shapes to be considered in the approximate solution on the flutter speed prediction will be discussed later.

To validate the flutter speed prediction, an exact solution for the governing equations of the linear problem (Equations (2.53)–(2.58)) is determined. To this end, separation of variables is used to seek solutions in the form

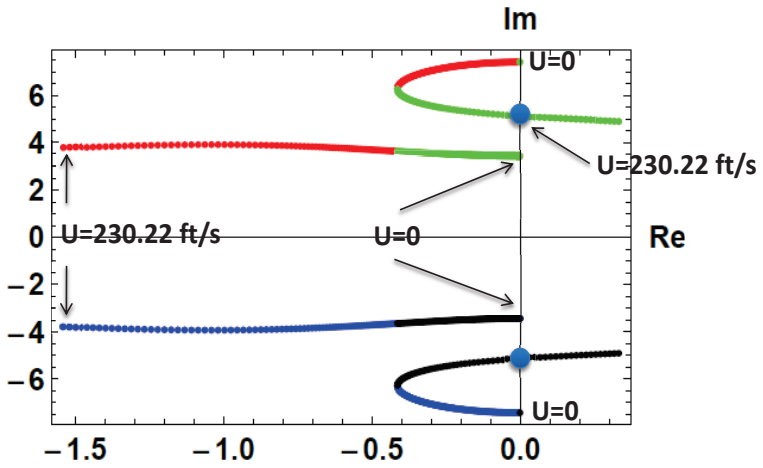

Figure 2.14: Variations of the eigenvalues with the air speed in the complex plane.

$$w(y,t) = A_1 e^{\alpha t} e^{sy} \quad \text{and} \quad \theta(y,t) = A_2 e^{\alpha t} e^{sy} \tag{2.113}$$

Substituting Equations (2.113) into (2.53) and (2.54) yields two linear homogeneous algebraic equations in the unknown coefficients A_1 and A_2 and the parameters s and α which can be written in a matrix form as

$$F(\alpha, s, U) \begin{pmatrix} A_1 \\ A_2 \end{pmatrix} = \begin{pmatrix} 0 \\ 0 \end{pmatrix} \tag{2.114}$$

Equation (2.114) has nontrivial solutions if and only if the determinant of the matrix $F(\alpha, s, U)$ is equal to zero. Setting this determinant equal to zero, one obtains a polynomial equation which is of sixth order in s and fourth order in α. Thus, for a given α, one can solve it and obtain six values s_i. Equation (2.113) can be rewritten as

$$w(y,t) = \sum_{i=1}^{6} C_i A_{1_i} e^{s_i y} e^{\alpha t} \quad \text{and} \quad \theta(y,t) = \sum_{n=1}^{6} C_i A_{2_i} e^{s_i y} e^{\alpha t} \tag{2.115}$$

where $[A_{1_i} \; A_{2_i}]^T$ are the eigenvectors of $F(\alpha, s_i, U)$ corresponding to the zero eigenvalue and the C_i are constants. Substituting Equations (2.115) into Equations (2.55)–(2.58) leads to a linear system of six algebraic equations in the C_i which can be written in a matrix form as

$$\mathbf{M}_{6\times 6} \begin{pmatrix} C_1 & C_2 & \cdots & C_6 \end{pmatrix}^T = 0_{6\times 1}$$

This system has a nontrivial solution $\begin{pmatrix} C_1 & C_2 & \cdots & C_6 \end{pmatrix}^T$ if $Det(\mathbf{M})$ is equal to zero. Thus, to calculate the α's, the approach is based on starting with an initial guess the value given from the discretization approach and iterating on it using the Newton-Raphson method until $Det(\mathbf{M}) < \epsilon$, where ϵ is a small specified number. Further details of the computation of the flutter speed based from the exact solution are provided in (66).

Table 2.3 presents the flutter speed obtained using the exact and discretization approaches. Clearly, there is an excellent agreement between values of the flutter speed obtained from the discretization analysis (even with use of few number of modes) and the exact solution.

Table 2.3: Flutter speed using different approaches

Approach	U_f (ft/s)
Discretization approach	
One bending & one torsion modes	230.220
Two bending & two torsion modes	230.405
Three bending & three torsion modes	230.406
Exact approach	
	230.406

To check the capability of the discretization approach in predicting the aerodynamic response of the wing, a comparison of the real and imaginary parts of the complex-valued bending and torsion responses of the wing $\Phi(x)$ and $\Psi(x)$ (space functions of the solutions of the first-order problem as given in Equations (2.65) and (2.66)) at the onset of the Hopf bifurcation obtained from the direct and discretization approaches using different numbers of modes is shown in Figure 2.15. The use of only one bending and one torsion modes leads to a fairly good agreement with the exact solution. As expected, including the higher modes improves the estimation of the solution.

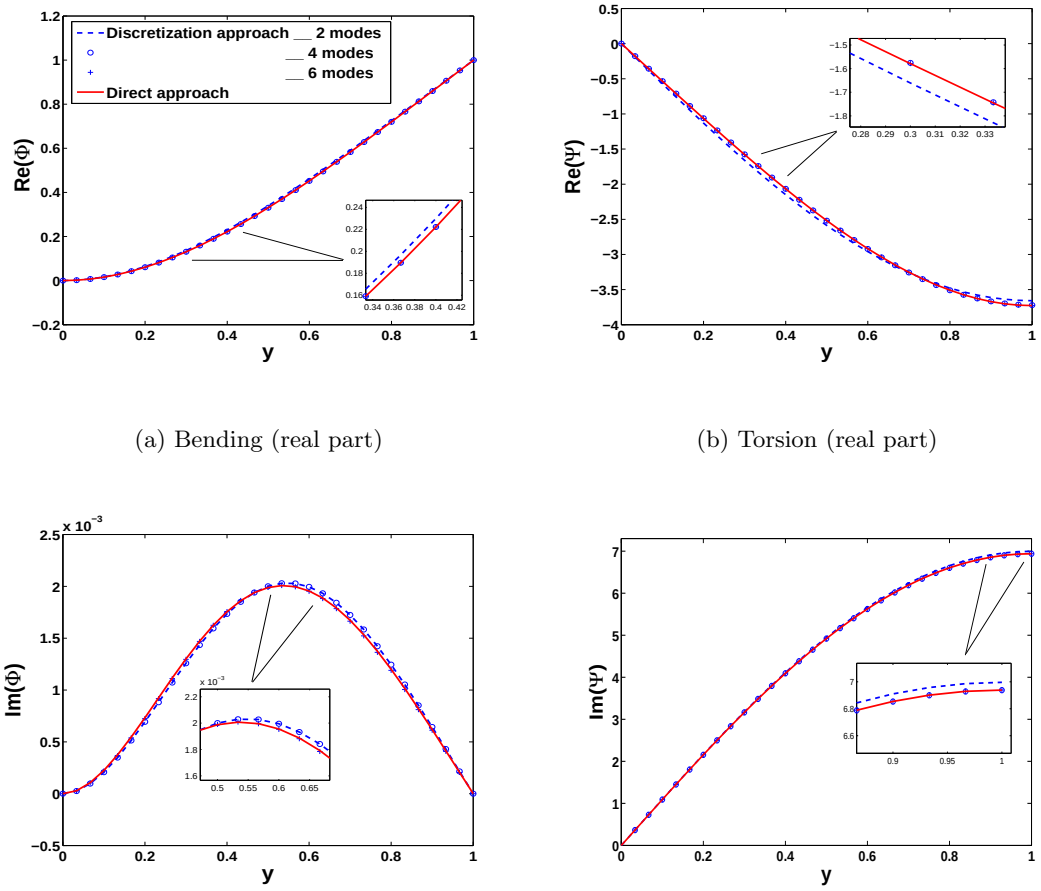

(a) Bending (real part)

(b) Torsion (real part)

(c) Bending (imaginary part)

(d) Torsion (imaginary part)

Figure 2.15: Complex-valued aerodynamic response at the Hopf bifurcation.

Nonlinear analysis

The principle of normal form yields a simplification of the dynamics of the aeroelastic system. Besides, as shown in Equations (2.112), the coefficients of the normal form are explicit functions of the system's parameters. This would enable an efficient investigation and analysis of the effect of system's parameters on the type of the dynamic instability and LCO that take place beyond flutter. Table 2.4 presents the linear and nonlinear coefficients of the normal form obtained from both Direct and Discretization approaches. Clearly, the use of one bending and one torsion modes produces accurate estimates of the linear coefficient χ.

However, more modes are needed to capture the effects of the system's nonlinearities. Results obtained from the direct and the discretization (using three bending and three torsion modes) approaches show an excellent agreement for both linear and nonlinear coefficients. Besides, for the specific values of the system's parameters given in Table 2.2, the structural nonlinearities are unfavorable ($\chi^s > 0$), whereas the aerodynamic nonlinearities are favorable ($\chi^a < 0$) in the sense that they lead to subcritical and supercritical instability, respectively.

Table 2.4: Normal Form: Direct vs. Discretized Solution

	γ	χ^s	χ^a
Discretization approach			
One bending & one torsion modes	$0.01787 - 0.01539\,i$	$9.2511 - 8.3697\,i$	$-363.087 + 73.438\,i$
Two bending & two torsion modes	$0.01788 - 0.01530\,i$	$10.040 - 9.5781\,i$	$-356.083 + 69.099\,i$
Three bending & three torsion modes	$0.01788 - 0.01530\,i$	$10.039 - 9.5666\,i$	$-356.451 + 69.153\,i$
Direct approach			
	$0.01788 - 0.01530\,i$	$10.033 - 9.5644\,i$	$-356.404 + 69.195\,i$

In order to check the accuracy of the analytical formulation given by the normal form in predicting the amplitude of LCO, Equations (2.98) are solved numerically and the bending and torsion responses at the wing tip are plotted in Figure 2.16. It is noted that the LCO prediction from the perturbation analysis is based on the first-order solution as given by Equation (2.107). A comparison between the solutions obtained numerically with those predicted from the normal form show an excellent agreement in the amplitudes of LCO near the bifurcation. This shows that the normal form representation has a great capability to predict accurately the response of the aeroelastic system.

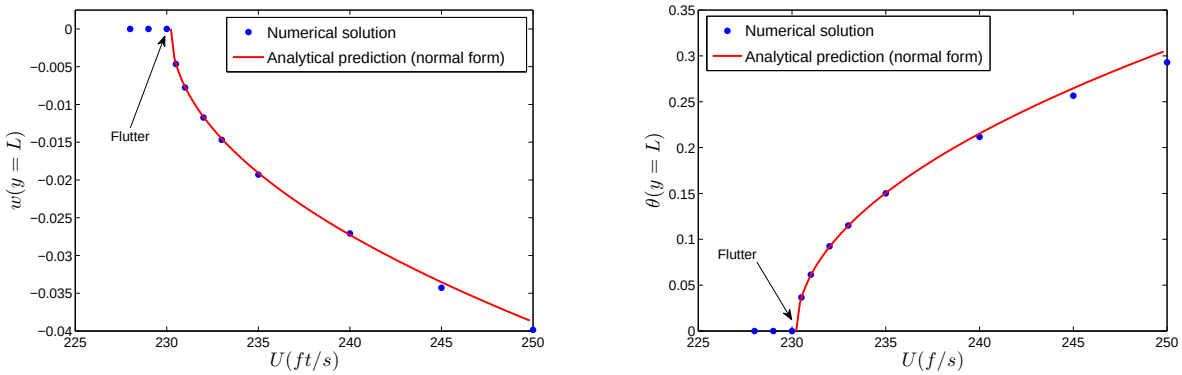

(a) Bending (b) Torsion

Figure 2.16: LCO amplitudes of bending and torsion motions at the wing tip.

2.2.4 Summary

In this effort, two approaches were followed to derive the normal form of the aeroelastic response of the Goland wing. Two approaches were followed to derive a normal form that characterizes the dynamic instability of an aeroelastic system. In the first approach, the method of multiple scales was applied directly to the partial-differential equations governing the motion to construct an approximation to its response near the Hopf bifurcation. In the second approach, the governing equations were first discretized using the Galerkin procedure yielding a set of nonlinear coupled ordinary-differential equations, and then the method of multiple scales was applied. The results, including flutter speed, type of instability, and limit cycle oscillations, obtained with both approaches show that the use of one bending mode and one torsion mode is good enough to predict the flutter speed. However, more modes are needed to capture the system's nonlinearities. The major finding of this work constitutes in the direct application of the method of multiple scales to the original governing equations of the aeroelastic response of the Goland wing which comprise a set of PDEs. Such approach cannot be handled when using CFD simulations to compute the aerodynamic variables.

2.3 Example 3: Uncertainty Analysis Near Bifurcation of an Aeroelastic System

The response of an aeroelastic system is governed by a combination of linear and nonlinear dynamics. When combined, the nonlinearities (geometric, inertia, free-play, damping, and/or aerodynamics) lead to different behaviors (67–69), including multiple equilibria, bifurcations, limit cycles, chaos, and various types of resonances (internal and super/subharmonic) (70). In particular, these nonlinear aspects that contribute to unstable responses could be either of the supercritical or subcritical type. In Figure 2.17, a qualitative sketch of the system behavior is showed. In the supercritical instability, the system response is stable to any disturbance below the flutter boundary. Beyond this boundary, nonlinearities yield LCO whose amplitude increases slowly with increasing flight speed. In the subcritical type, a sudden jump to a large-amplitude LCO takes place at or below the flutter speed, depending on the initial conditions. Uncertainties in the linear and nonlinear parameters may lower the flutter speed and lead to the undesirable subcritical behavior even if the deterministic design or solution exhibits supercritical behavior only. These effects are schematically illustrated by the arrows in Figure 2.17. Uncertainties of the linear parameters would cause the deterministic supercritical behavior represented by curve **A** to follow curve **A'**. Uncertainties in nonlinear parameters could cause the supercritical response represented by curve **A'** to become subcritical as represented by curve **A"**. Depending on the initial conditions, the system's response could exhibit subcritical behavior at speeds that are much lower than the flutter speed predicted with the deterministic approach.

To deal with these uncertainties, a common approach is to assign probabilistic distributions to certain input variables and structural parameters and use uncertainty propagation methods (sampling approaches such as Monte Carlo simulations (MCs) and Latin Hypercube Sampling (LHS) and response surface approaches, such as PCE, FCE (71; 72)) to obtain probability distributions functions (PDFs) of supercritical and subcritical responses. Following these approaches, one may obtain a range of variations of the LCO amplitude within a type of instability (73; 74), as shown in Figure 2.17. Since aeroelastic systems are usually not designed to operate beyond the flutter boundary, there is no need to quantify uncertain LCO

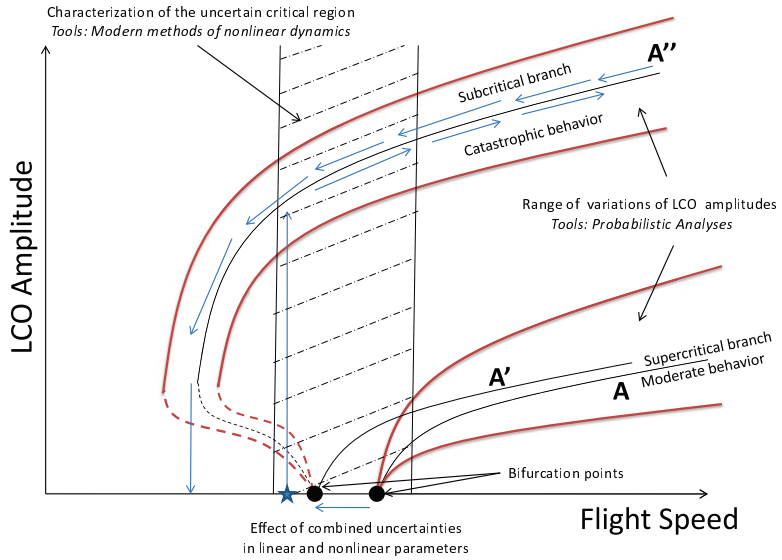

Figure 2.17: Schematic of LCO response of an aeroelastic system. Arrows denote path of system response that may occur due to uncertainty in structural or aerodynamic parameters: (→) increasing, (←) decreasing.

in those regions. Under these conditions, modern methods of nonlinear dynamics may be effectively implemented and used to perform the analysis near the bifurcation and especially capture the switch from the supercritical to the subcritical instability.

In this section [3], two approaches for determining the effects of variations in the linear and nonlinear spring coefficients of an aeroelastic system on its stability near a bifurcation point are assessed. In the first approach, the intrusive PCE is applied on the governing equations. This expansion yields a set of coupled equations that are numerically solved. In the second approach, modern methods of nonlinear dynamics are used to derive the normal form. A comparison of the usefulness and effectiveness of these approaches is shown by characterizing sensitivity of the response of the system to variations in its parameters.

[3]Ghommem, M., Hajj, M.R., and Nayfeh, A.H., 2010, Uncertainty Analysis near Bifurcation of an Aeroelastic System, *Journal of Sound and Vibration*, Vol. 329, 3335-3347.

2.3.1 Representation of the aeroelastic system

A common system that has been used to investigate the aeroelastic behavior and dynamic instabilities is a two-dimensional rigid airfoil undergoing pitch and plunge motions (75; 76) as presented in Figure 2.18. The wing is free to rotate about the elastic axis (pitch motion) and translate vertically (plunge motion). Denoting by h and α the plunge deflection and pitch angle, respectively, one can write the governing equations of this system as (70; 77)

$$\begin{pmatrix} m_T & m_W x_\alpha b \\ m_W x_\alpha b & I_\alpha \end{pmatrix} \begin{pmatrix} \ddot{h} \\ \ddot{\alpha} \end{pmatrix} + \begin{pmatrix} c_h & 0 \\ 0 & c_\alpha \end{pmatrix} \begin{pmatrix} \dot{h} \\ \dot{\alpha} \end{pmatrix} + \begin{pmatrix} k_h(h) & 0 \\ 0 & k_\alpha(\alpha) \end{pmatrix} \begin{pmatrix} h \\ \alpha \end{pmatrix} = \begin{pmatrix} -L \\ M \end{pmatrix}, \tag{2.116}$$

where m_T is the total mass of the wing and its support structure. m_W is the wing mass alone. I_α is the mass moment of inertia about the elastic axis. b is half chord length. $x_\alpha = r_{cg}/b$ is the nondimensional distance between the center of mass and the elastic axis. c_h and c_α are the plunge and pitch viscous damping coefficients, respectively. L and M are the aerodynamic lift and moment about the elastic axis, and k_h and k_α are the structural stiffnesses for the plunge and pitch motions, respectively. These stiffnesses are approximated in polynomial form by

$$\begin{aligned} k_\alpha(\alpha) &= k_{\alpha 0} + k_{\alpha 1}\alpha + k_{\alpha 2}\alpha^2 + ... \\ k_h(h) &= k_{h0} + k_{h1}h + k_{h2}h^2 + ... \end{aligned} \tag{2.117}$$

The aerodynamic loads are evaluated using a quasi-steady approximation with a stall model (77) and are written as

$$\begin{aligned} L &= \rho U^2 b c_{l_\alpha}(\alpha_{\text{eff}} - c_s \alpha_{\text{eff}}^3), \\ M &= \rho U^2 b^2 c_{m_\alpha}(\alpha_{\text{eff}} - c_s \alpha_{\text{eff}}^3), \end{aligned} \tag{2.118}$$

where U is the freestream velocity, c_{l_α} and c_{m_α} are the aerodynamic lift and moment coefficients, and c_s is a nonlinear parameter associated with stall. The effective angle of attack due to the instantaneous motion of the airfoil is given by (77)

$$\alpha_{\text{eff}} = \Big[\alpha + \frac{\dot{h}}{U} + (\frac{1}{2} - a)b\frac{\dot{\alpha}}{U}\Big], \tag{2.119}$$

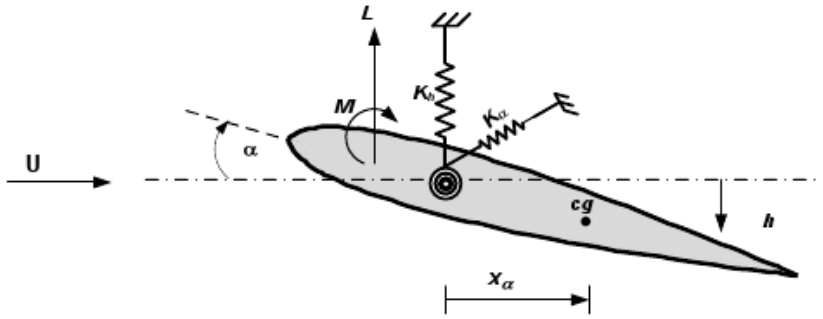

Figure 2.18: Sketch of a two-dimensional airfoil

where a is the nondimensional distance from the midchord to the elastic axis.

For the sake of simplicity, the state variables are defined

$$\mathbf{Y} = \begin{pmatrix} Y_1 \\ Y_2 \\ Y_3 \\ Y_4 \end{pmatrix} = \begin{pmatrix} h \\ \alpha \\ \dot{h} \\ \dot{\alpha} \end{pmatrix}.$$

and write the equations of motions in the form

$$\dot{\mathbf{Y}} = F(\mathbf{Y}, U), \tag{2.120}$$

where

$$F(\mathbf{Y}, U) = \begin{pmatrix} Y_3 \\ Y_4 \\ -p_h(Y_1)Y_1 - (k_1U^2 + p_\alpha(Y_2))Y_2 - c_1Y_3 - c_2Y_4 + g_{NL1}(Y) \\ -q_h(Y_1)Y_1 - (k_2U^2 + q_\alpha(Y_2))Y_2 - c_3Y_3 - c_4Y_4 + g_{NL2}(Y) \end{pmatrix}. \tag{2.121}$$

The relations of the new variables used in Equation (2.121) to the physical parameters are provided in Table 2.5. The original system, Equation (2.120), is then rewritten as

$$\dot{\mathbf{Y}} = A(U)\mathbf{Y} + Q(\mathbf{Y}, \mathbf{Y}) + C(\mathbf{Y}, \mathbf{Y}, \mathbf{Y}), \tag{2.122}$$

Table 2.5: System variables

$d = m_T I_\alpha - m_W^2 x_\alpha^2 b^2$
$k_1 = (I_\alpha \rho b c_{l_\alpha} + m_W x_\alpha \rho b^3 c_{m_\alpha})/d$
$k_2 = -(m_W x_\alpha \rho b^2 c_{l_\alpha} + m_T \rho b^2 c_{m_\alpha})/d$
$c_1 = [I_\alpha(c_h + \rho U b c_{l_\alpha}) + m_W x_\alpha \rho U b^3 c_{m_\alpha}]/d$
$c_2 = [I_\alpha \rho U b^2 c_{l_\alpha}(\frac{1}{2} - a) - m_W x_\alpha b c_{l_\alpha} + m_W x_\alpha \rho U b^4 c_{m_\alpha}(\frac{1}{2} - a)]/d$
$c_3 = [-m_W x_\alpha b(c_h + \rho U b c_{l_\alpha}) - m_T x_\alpha \rho U b^2 c_{m_\alpha}]/d$
$c_4 = [m_T(c_\alpha - \rho U b^3 c_{m_\alpha}(\frac{1}{2} - a)) - m_W x_\alpha \rho U b^3 c_{l_\alpha}(\frac{1}{2} - a)]/d$
$p_\alpha(\mathbf{Y}) = -m_W x_\alpha b k_\alpha(\mathbf{Y})/d$
$q_\alpha(\mathbf{Y}) = m_T k_\alpha(\mathbf{Y})/d$
$p_h(\mathbf{Y}) = I_\alpha k_h(\mathbf{Y})/d$
$q_h(\mathbf{Y}) = -m_W x_\alpha b k_h(\mathbf{Y})/d$
$g_{NL1}(\mathbf{Y}) = (c_s \rho U^2 b)(c_{l_\alpha} I_\alpha + m_W x_\alpha b^2 c_{m_\alpha})\alpha_{\text{eff}}^3(\mathbf{Y})/d$
$g_{NL2}(\mathbf{Y}) = -(c_s \rho U^2 b^2)(c_{l_\alpha} m_W x_\alpha + m_T c_{m_\alpha})\alpha_{\text{eff}}^3(\mathbf{Y})/d$

where $Q(\mathbf{Y}, \mathbf{Y})$ and $C(\mathbf{Y}, \mathbf{Y}, \mathbf{Y})$ are, respectively, the quadratic and cubic vector functions of the state variables collected in the vector $\mathbf{Y}$.

To determine the system's stability, the linearized governing equations is considered, which are written in a first-order differential form as

$$\dot{\mathbf{Y}} = A(U)\mathbf{Y}, \tag{2.123}$$

where

$$A(U) = \begin{pmatrix} 0 & 0 & 1 & 0 \\ 0 & 0 & 0 & 1 \\ -I_\alpha k_{h0}/d & -(k_1 U^2 - m_W x_\alpha b k_{\alpha 0}/d) & -c_1 & -c_2 \\ m_W x_\alpha b k_{h0}/d & -(k_2 U^2 + m_T k_{\alpha 0}/d) & -c_3 & -c_4 \end{pmatrix}. \tag{2.124}$$

The 4×4 matrix $A(U)$ has a set of four eigenvalues, $\{\rho_j, j = 1, 2, ..., 4\}$. These eigenvalues determine the stability of the trivial solution of Equation (2.123). If the real parts of all of the ρ_j are negative, the trivial solution is asymptotically stable. On the other hand, if the real part of one or more eigenvalues are positive, the trivial solution is unstable. The flutter speed U_f, for which one or more eigenvalues have zero real parts, corresponds to the onset of

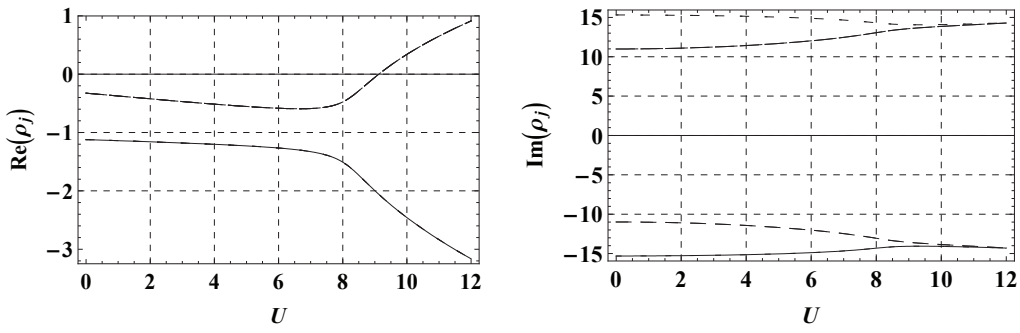

(a) (b)

Figure 2.19: Variations of (a) the real (dampings) and (b) imaginary (frequencies) parts of the ρ_j with the freestream velocity U (m/s).

linear instability. For the specific values given in Strganac et al. (77), Figures 2.19 (a) and (b) show, respectively, variations of the real and imaginary parts of the ρ_j with U. It is noted that two of the eigenvalues transversally cross the imaginary axis at $U_f = 9.1242$ m/s. At this speed, the aeroelastic system undergoes a Hopf bifurcation as indicated by the oscillatory solution ($Im(\rho) \neq 0$). The observed coalescence of the two aeroelastic modal frequencies is indicative of classical flutter.

2.3.2 Uncertainty quantification via intrusive polynomial chaos

In this section, the intrusive formulation of the polynomial chaos expansion (PCE) is implemented to quantify uncertainty in the flutter speed and the LCO of the aeroelastic system described above due to imprecision in the torsional stiffness. This formulation involves substitution of uncertain variables and parameters in the governing equations with polynomial expansions. The unknowns polynomial coefficients are then evaluated by projecting the resulting equations onto basis functions. Thus, the governing equations are reformulated to yield mode strengths (78) of the output.

Variations in the linear and cubic pitch stiffness coefficients $k_{\alpha 0}$ and $k_{\alpha 2}$ are described by

Gaussian distributions and expressed in standard forms:

$$k_{\alpha 0} = \overline{k}_{\alpha 0} + \sigma_1 \xi_1 \tag{2.125}$$

$$k_{\alpha 2} = \overline{k}_{\alpha 2} + \sigma_2 \xi_2 \tag{2.126}$$

The effects of randomness of these parameters on the flutter onset speed of the airfoil and LCO are determined using numerical analysis. For simplicity, variations in these two coefficients will be assumed to be independent. As such, their effects are discussed separately.

Effect of randomness of $k_{\alpha 0}$ on the flutter speed

In implementing the intrusive approach, the plunge displacement h and pitch angle α are considered as stochastic processes that are functions of the uncertain parameters. Their PCEs are then written as

$$\begin{aligned} h(t,\xi_1) &= \sum_{i=0}^{P} h_i(t)\Psi_i(\xi_1) \\ \alpha(t,\xi_1) &= \sum_{i=0}^{P} \alpha_i(t)\Psi_i(\xi_1) \end{aligned} \tag{2.127}$$

where $P+1 = \frac{(n+p)!}{n!p!}$ is the number of output modes, which is a function of the order of the polynomial chaos p and the number of random dimensions n. Here, the $h_i(t)$ and $\alpha_i(t)$ are the deterministic components, the amplitudes of the plunge and pitch fluctuation, respectively, and $\Psi_i(\xi_1)$ is the random basis function corresponding to the i^{th} mode. Many choices are possible for the basis functions, depending on the type of the probability distribution selected for the uncertainty of the random variable vector ξ_1 (79). For variables with Gaussian probability distributions, Hermite polynomials are used because they form an orthogonal set of basis functions (80). Taking $P = 1$ (i.e., keep only the linear terms) and substituting Equations (2.125) and (2.127) into Equation (2.123) yield

$$\dot{\mathbf{Y}} = \begin{pmatrix} 0 & 0 & 1 & 0 \\ 0 & 0 & 0 & 1 \\ -I_\alpha k_{h0}/d & -(k_1 U^2 - m_W x_\alpha b(\overline{k}_{\alpha 0} + \sigma_1\xi_1)/d) & -c_1 & -c_2 \\ m_W x_\alpha b k_{h0}/d & -(k_2 U^2 + m_T(\overline{k}_{\alpha 0} + \sigma_1\xi_1)/d) & -c_3 & -c_4 \end{pmatrix} \mathbf{Y} \tag{2.128}$$

where

$$\mathbf{Y} = \begin{pmatrix} h_0(t) + h_1(t)\xi_1 \\ \alpha_0(t) + \alpha_1(t)\xi_1 \\ \dot{h}_0(t) + \dot{h}_1(t)\xi_1 \\ \dot{\alpha}_0(t) + \dot{\alpha}_1(t)\xi_1 \end{pmatrix}$$

Multiplying both sides of Equation (2.128) by $\Psi_i(\xi_1)$, $i = 0, 1$ in sequence, using the orthogonality of the basis functions (Hermite polynomials), and taking the inner product with respect to the random variable, one obtains

$$\dot{Y}_s = A_s(U)Y_s \tag{2.129}$$

where

$$Y_s = \begin{pmatrix} h_0 & \alpha_0 & \dot{h}_0 & \dot{\alpha}_0 & h_1 & \alpha_1 & \dot{h}_1 & \dot{\alpha}_1 \end{pmatrix}^T,$$

$$A_s(U) = \begin{pmatrix} A(U) & D(\sigma_1) \\ D(\sigma_1) & A(U) \end{pmatrix}, \tag{2.130}$$

and

$$D(\sigma_1) = \begin{pmatrix} 0 & 0 & 0 & 0 \\ 0 & 0 & 0 & 0 \\ 0 & m_W x_\alpha b \sigma_1/d & 0 & 0 \\ 0 & -m_T \sigma_1/d & 0 & 0 \end{pmatrix} \tag{2.131}$$

The matrix $A_s(U)$ has a set of eigenvalues, $\{\rho_j, j = 1, 2, ..., 8\}$, which determine the stability of the system given by Equation (2.129). It is well-known that if the real parts of all ρ_j are negative, then the obtained solution is asymptotically stable. On the other hand, if one or more real parts of ρ_j are greater than zero, the solution is unstable. The flutter onset speed U_f is reached when one or more eigenvalues cross the imaginary axis into the right-half of the complex plane.

Figure 2.20 shows variation of the real parts of the ρ_j with the freestream velocity U. It shows the ranges of the onset flutter speed of the stochastic airfoil system for different values of σ_1. Figure 2.21 depicts the effect of the intensity of σ_1 on the upper U_{fu} and lower U_{fl} bounds of the onset flutter speed. Both bounds of the flutter speed vary linearly

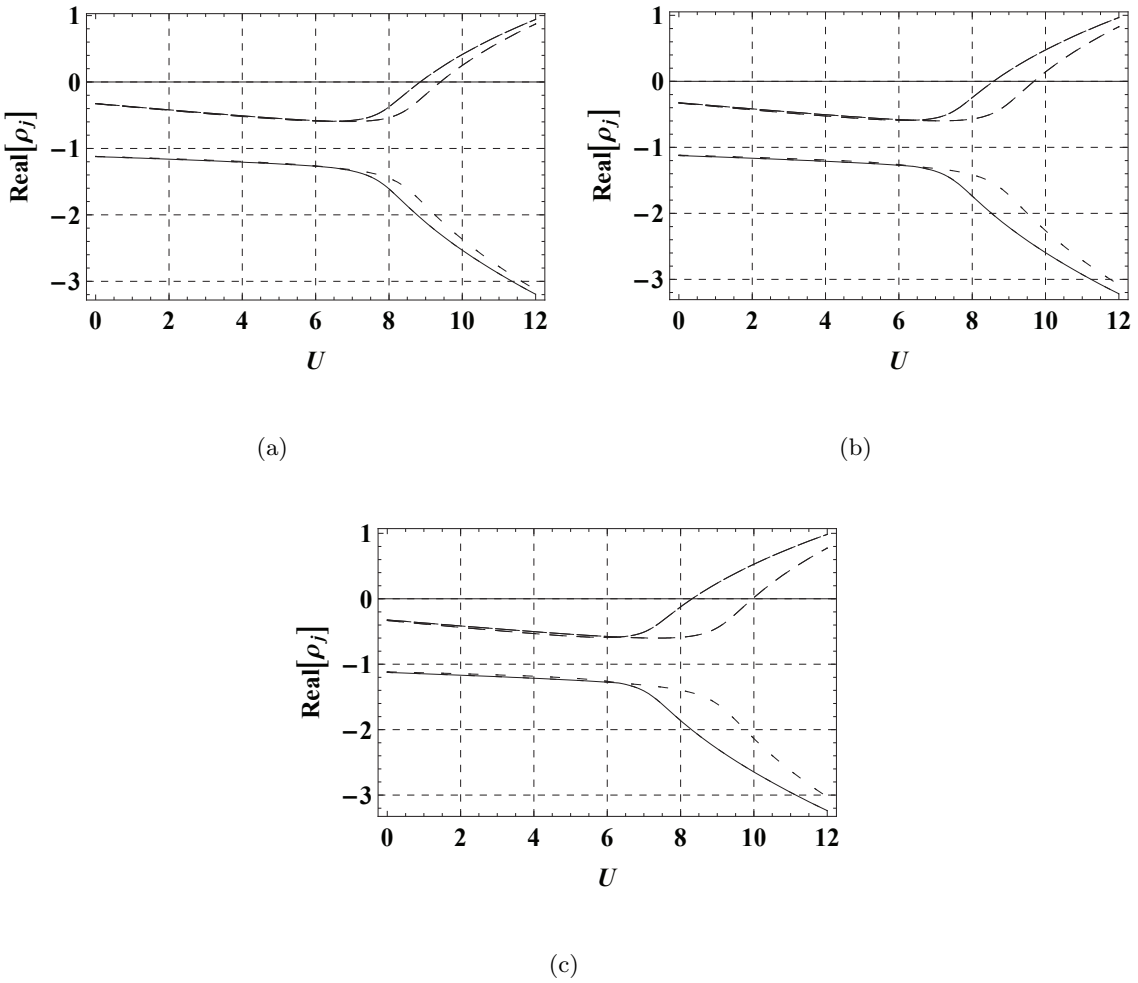

Figure 2.20: Variation of the real part of ρ_j with the freestream velocity U (m/s). (a) $\sigma_1 = 0.05\overline{k}_{\alpha 0}$ ($U_{fl} = 8.84929$, $U_{fu} = 9.40177$), (b) $\sigma_1 = 0.1\overline{k}_{\alpha 0}$ ($U_{fl} = 8.57824$, $U_{fu} = 9.68138$), and (c) $\sigma_1 = 0.15\overline{k}_{\alpha 0}$ ($U_{fl} = 8.31217$, $U_{fu} = 9.96227$)

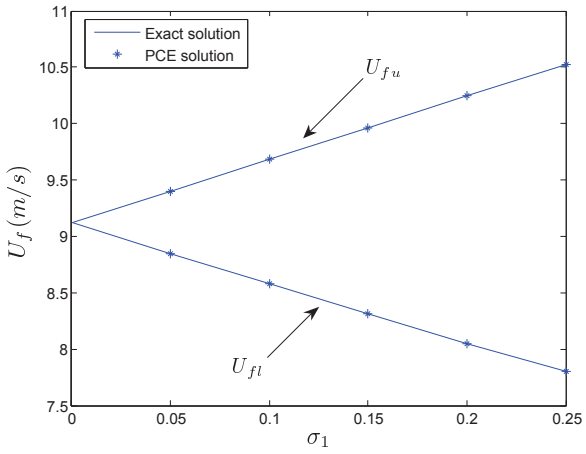

Figure 2.21: Variation of flutter onset speed U_f (m/s) with σ_1

with σ_1. A comparison between the flutter speeds obtained from the linearized system and the corresponding ones obtained from the PCE-based analysis shows that the first-order intrusive PCE produces coefficients that accurately estimate the sensitivity of the flutter speed to variations in structural stiffness.

Effect of randomness of $k_{\alpha 2}$ on LCO

In this case, the full nonlinear system is considered. For the sake of simplicity, the case in which structural nonlinearity is applied only in the pitch degree of freedom is considered; that is, $k_{h1} = k_{h2} = c_s = 0$, $\overline{k}_{\alpha 1} = 39.9967 N.m$, and $\overline{k}_{\alpha 2} = 67.685 N.m$. These values were selected to obtain a configuration that yields to a supercritical instability. $k_{\alpha 2}$ is considered as a random variable and $k_{\alpha 0}$ as deterministic (i.e., $\sigma_1 = 0$). Here, h and α are approximated by the following PCEs in terms of ξ_2:

$$\begin{aligned} h(t,\xi_2) &= \sum_{i=0}^{P} h_i(t)\Psi_i(\xi_2) \\ \alpha(t,\xi_2) &= \sum_{i=0}^{P} \alpha_i(t)\Psi_i(\xi_2) \end{aligned} \tag{2.132}$$

The intrusive approach relies on a Galerkin-projection reformulation of the original model equations to arrive at governing equations for the strengths of PCE modes of the model

output. The governing equations are rewritten by substituting Equations (2.126) and (2.132) into Equation (2.120); the result is

$$\begin{aligned}\sum_{i=0}^{P}\ddot{h}_i(t)\Psi_i(\xi_2) = &- (I_\alpha k_{h0}/d)\sum_{i=0}^{P}h_i(t)\Psi_i(\xi_2) - \Bigg[k_1U^2 - m_W x_\alpha b\Bigg(k_{\alpha0} + k_{\alpha1}\sum_{i=0}^{P}\alpha_i(t)\Psi_i(\xi_2)\\ &+ (\overline{k}_{\alpha2} + \sigma_2\xi_2)(\sum_{i=0}^{N}\alpha_i(t)\Psi_i(\xi_2))^2\Bigg)/d\Bigg]\sum_{i=0}^{P}\alpha_i(t)\Psi_i(\xi_2)\\ &- c_1\sum_{i=0}^{P}\dot{h}_i(t)\Psi_i(\xi_2) - c_2\sum_{i=0}^{P}\dot{\alpha}_i(t)\Psi_i(\xi_2) \qquad (2.133)\end{aligned}$$

$$\begin{aligned}\sum_{i=0}^{P}\ddot{\alpha}_i(t)\Psi_i(\xi_2) = &\quad (m_W x_\alpha b k_{h0}/d)\sum_{i=0}^{P}h_i(t)\Psi_i(\xi_2) - \Bigg[k_2U^2 + m_T\Bigg(k_{\alpha0} + k_{\alpha1}\sum_{i=0}^{P}\alpha_i(t)\Psi_i(\xi_2)\\ &+ (\overline{k}_{\alpha2} + \sigma_2\xi_2)(\sum_{i=0}^{P}\alpha_i(t)\Psi_i(\xi_2))^2\Bigg)/d\Bigg]\sum_{i=0}^{P}\alpha_i(t)\Psi_i(\xi_2)\\ &- c_3\sum_{i=0}^{P}\dot{h}_i(t)\Psi_i(\xi_2) - c_4\sum_{i=0}^{P}\dot{\alpha}_i(t)\Psi_i(\xi_2) \qquad (2.134)\end{aligned}$$

Using the orthogonality of the basis functions (Hermite polynomials) and projecting Equations (2.133) and (2.134) onto the $\Psi_l(\xi_2)$ yields the following stochastic version of the aeroelastic model:

$$\begin{aligned}\ddot{h}_l(t) = &- (I_\alpha k_{h0}/d)h_l(t) - (k_1U^2 - m_W x_\alpha b k_{\alpha0}/d)\alpha_l(t) + (m_W x_\alpha b k_{\alpha1}/d)\sum_{i=0}^{P}\sum_{j=0}^{P}\zeta_{ijl}\alpha_i(t)\alpha_j(t)\\ &+ (m_W x_\alpha b/d)\sum_{i=0}^{P}\sum_{j=0}^{P}\sum_{k=0}^{P}\alpha_i(t)\alpha_j(t)\alpha_k(t)(\overline{k}_{\alpha2}\varsigma_{ijkl} + \sigma_2\tau_{ijkl}) - c_1\dot{h}_l(t) - c_2\dot{\alpha}_l(t) \qquad (2.135)\end{aligned}$$

$$\begin{aligned}\ddot{\alpha}_l(t) = &\quad (m_W x_\alpha b k_{h0}/d)h_l(t) - (k_2U^2 + m_T/d)\alpha_l(t) - (m_T k_{\alpha1}/d)\sum_{i=0}^{P}\sum_{j=0}^{P}\zeta_{ijl}\alpha_i(t)\alpha_j(t)\\ &- (m_T/d)\sum_{i=0}^{P}\sum_{j=0}^{P}\sum_{k=0}^{P}\alpha_i(t)\alpha_j(t)\alpha_k(t)(\overline{k}_{\alpha2}\varsigma_{ijkl} + \sigma_2\tau_{ijkl}) - c_3\dot{h}_l(t) - c_4\dot{\alpha}_l(t) \qquad (2.136)\end{aligned}$$

where

$$\begin{aligned}&\zeta_{ijl} = <\Psi_i(\xi_2)\Psi_j(\xi_2), \Psi_l(\xi_2)>, \quad \varsigma_{ijkl} = <\Psi_i(\xi_2)\Psi_j(\xi_2)\Psi_k(\xi_2), \Psi_l(\xi_2)>,\\ &\tau_{ijkl} = <\Psi_i(\xi_2)\Psi_j(\xi_2)\Psi_k(\xi_2)\xi_2, \Psi_l(\xi_2)> \qquad (2.137)\end{aligned}$$

and $<,>$ denotes the inner product with the standard Gaussian distribution as a weighting function.

The PCE coefficients $h_l(t)$ and $\alpha_l(t)$ $(l = 0, 1, ..., P)$ can be then determined by numerical integration of the obtained set of nonlinear coupled ordinary-differential equations. The PCE coefficients directly yield estimates of the mean value and the variance. Furthermore, the first-order terms in these coefficients provide a measure of the sensitivity of the stochastic response to each of the uncertain parameters.

A first-order PCE (i.e, $P = 1$) is considered and the time histories of the pitch motion obtained from the deterministic model as well as from the stochastic one at $U = 9.8m/s$ for different variations of the uncertain parameter $k_{\alpha 2}$ are plotted in Figure 2.22. By integrating the dynamical system given by Equations (2.135) and (2.136), it is observed that the LCO response diverges from the physical limit cycle (obtained from the deterministic model) to a spurious limit cycle. It is also noted that, even with increasing the order of the PCE in attempt to improve the stochastic model, the solution still drifts to a nonphysical limit cycle. The occurrence of spurious limit cycles is due to the global nature of the basis functions in the PCE (73; 81). In fact, the global PCE expansion fails to reproduce the long-term characteristics of the stochastic response. It is noted that previous works (73; 81) have shown the failure of the PCE in predicting stochastic response of nonlinear aeroelastic systems that involve limit cycles and proposed modified basis as a potential remedy to the large-time inadequacy of the response. In Figure 2.22(b), a large variation of $k_{\alpha 2}$ is considered ($\xi_2 = 5$) to check if the PCE is capable of capturing the switch from the supercritical instability to the the subcritical one as would be detected using the normal form (see next section). It can be clearly seen that even for short-time integration, the PCE fails to predict the LCO for large variations of the uncertain cubic coefficient $k_{\alpha 2}$ of the torsional stiffness. Moreover, it cannot predict changes in the type of the instability. The intrusive formulation of the PCE shows weaknesses and lack of robustness in the modeling of stochastic oscillating aeroelastic systems characteristics.

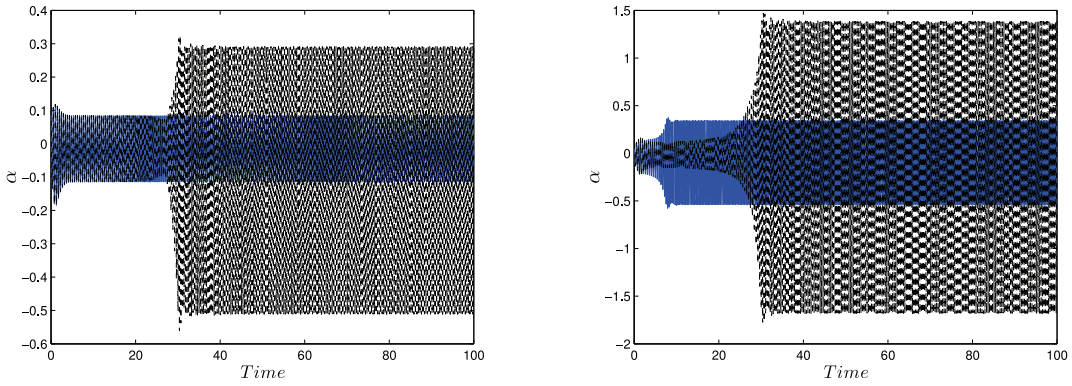

(a) (b)

Figure 2.22: Time histories of the pitch motion. The solid line represents the time history obtained by integrating numerically the deterministic model. The dashed line is from the stochastic model based on the 1^{st} order PCE. (a) $\xi_2 = 1$ and $\sigma_2 = 0.1\overline{k}_{\alpha 2}$ and (b) $\xi_2 = 5$ and $\sigma_2 = 0.1\overline{k}_{\alpha 2}$.

2.3.3 Uncertainty quantification via normal form of Hopf bifurcation

In this section, a second approach is followed, namely the normal form, to determine stochastic aspects of the response of aeroelastic systems as caused by variations in the system's parameters. To compute the normal form of the Hopf bifurcation of Equation (2.122) near $U = U_f$, Nayfeh and Balachandran (64) is followed and a small nondimensional parameter ϵ is introduced as a book keeping parameter and a third-order approximate solution of Equation (2.122) is sought in the form

$$\mathbf{Y}(t) = \epsilon \mathbf{Y}_1(T_0, T_2) + \epsilon^2 \mathbf{Y}_2(T_0, T_2) + \epsilon^3 \mathbf{Y}_3(T_0, T_2) + ... \tag{2.138}$$

where the time scales $T_m = \epsilon^m t$. As shown below, the secular term, arising from the nonlinear terms, appears at the third order and hence there is no dependence on the time scale T_1. Moreover, it is set $U = U_f + \epsilon^2 \sigma_U U_f$, $k_{\alpha 0} = \overline{k}_{\alpha 0} + \epsilon^2 \sigma_\alpha \overline{k}_{\alpha 0}$, and $k_{h0} = \overline{k}_{h0} + \epsilon^2 \sigma_h \overline{k}_{h0}$. The detunings are assumed to be $O(\epsilon^2)$ because secular term appears at $O(\epsilon^3)$.

The time derivative is expressed in terms of these scales as

$$\frac{d}{dt} = D_0 + \epsilon^2 D_2 + ... \tag{2.139}$$

where $D_m = \partial/\partial T_m$. Substituting Equations (2.138) and (2.139) into Equation (2.122) and equating coefficients of like powers of ϵ, one obtains

Order(ϵ)

$$D_0 \mathbf{Y}_1 - A(U_f)\mathbf{Y}_1 = 0 \tag{2.140}$$

Order(ϵ^2)

$$D_0 \mathbf{Y}_2 - A(U_f)\mathbf{Y}_2 = Q(\mathbf{Y}_1, \mathbf{Y}_1) \tag{2.141}$$

Order(ϵ^3)

$$D_0 \mathbf{Y}_3 - A(U_f)\mathbf{Y}_3 = -D_2\mathbf{Y}_1 + \sigma_U B_1 \mathbf{Y}_1 + \sigma_h B_2 \mathbf{Y}_1 + \sigma_\alpha B_3 \mathbf{Y}_1 + 2Q(\mathbf{Y}_1, \mathbf{Y}_2) + C(\mathbf{Y}_1, \mathbf{Y}_1, \mathbf{Y}_1) \tag{2.142}$$

where

$$B_1 = -2k_1 U_f^2 I_1 - 2k_2 U_f^2 I_2, \quad B_2 = -\frac{I_\alpha}{d} I_1 + \frac{m_W b x_\alpha}{d} I_2, \quad B_3 = \frac{m_W b x_\alpha}{d} I_1 - \frac{m_T}{d} I_2$$

$$I_1 = \begin{pmatrix} 0 & 0 & 0 & 0 \\ 0 & 0 & 0 & 0 \\ 0 & 1 & 0 & 0 \\ 0 & 0 & 0 & 0 \end{pmatrix}, \quad \textit{and} \quad I_2 = \begin{pmatrix} 0 & 0 & 0 & 0 \\ 0 & 0 & 0 & 0 \\ 0 & 0 & 0 & 0 \\ 0 & 1 & 0 & 0 \end{pmatrix} \tag{2.143}$$

The general solution of Equation (2.140) is the superposition of four linearly independent solutions corresponding to the four eigenvalues: two of these eigenvalues have negative real parts and the other two are purely imaginary ($\pm i\omega$). Because the two solutions corresponding to the two eigenvalues with negative real parts decay as $T_0 \to \infty$, one can retain only the nondecaying solutions and express the general solution of the first-order problem as

$$\mathbf{Y}_1(T_0, T_2) = \eta(T_2)\mathbf{p}e^{i\omega T_0} + \overline{\eta}(T_2)\overline{\mathbf{p}}e^{-i\omega T_0} \tag{2.144}$$

where $\eta(T_2)$ is determined by imposing the solvability condition (64) on the third-order level and $\mathbf{p}$ is the eigenvector of $A(U_f)$ corresponding to the eigenvalue $i\omega$; that is,

$$A(U_f)\mathbf{p} = i\omega\mathbf{p} \tag{2.145}$$

Substituting Equation (2.144) into Equation (2.141) yields

$$D_0\mathbf{Y}_2 - A(U_f)\mathbf{Y}_2 = Q(\mathbf{p},\mathbf{p})\eta^2 e^{2i\omega T_0} + 2Q(\mathbf{p},\overline{\mathbf{p}})\eta\overline{\eta} + Q(\overline{\mathbf{p}},\overline{\mathbf{p}})\overline{\eta}^2 e^{-2i\omega T_0} \tag{2.146}$$

The solution of Equation (2.146) can be written as

$$\mathbf{Y}_2 = \zeta_2\eta^2 e^{2i\omega T_0} + 2\zeta_0\eta\overline{\eta} + \overline{\zeta}_2\overline{\eta}^2 e^{-2i\omega T_0} \tag{2.147}$$

where

$$[2i\omega I - A(U_f)]\zeta_2 = Q(\mathbf{p},\mathbf{p}) \quad \text{and} \quad A(U_f)\zeta_0 = -Q(\mathbf{p},\overline{\mathbf{p}}) \tag{2.148}$$

Substituting Equations (2.144) and (2.147) into Equation (2.142), one obtains

$$\begin{aligned} D_0\mathbf{Y}_3 - A(U_f)\mathbf{Y}_3 = \; & - \; [D_2\eta\mathbf{p} - \sigma_U B_1\eta\mathbf{p} - \sigma_h B_2\eta\mathbf{p} - \sigma_\alpha B_3\eta\mathbf{p} - (4Q(\mathbf{p},\zeta_0) \\ & + \; 2Q(\overline{\mathbf{p}},\zeta_2) - 3C(\mathbf{p},\mathbf{p},\overline{\mathbf{p}}))\,\eta^2\overline{\eta}]\, e^{i\omega T_0} + cc + NST \end{aligned} \tag{2.149}$$

where cc stands for the complex conjugate of the preceding terms and NST stands for terms that do not produce secular terms. It is noted that the homogeneous part of Equation (2.149) is the same as Equation (2.140) and that the latter has nontrivial solutions. Therefore, the nonhomogeneous Equation (2.149) has a solution only if a solvability condition is satisfied. To determine this solvability condition, the left eigenvector $\mathbf{q}$ of $A(U_f)$ corresponding to the eigenvalue $i\omega$ is introduced; that is,

$$A(U_f)^T\mathbf{q} = i\omega\mathbf{q}$$

and normalize it so that $\mathbf{q}^T\mathbf{p} = 1$. Then, the solvability condition requires that terms proportional to $e^{i\omega T_0}$ in Equation (2.149) be orthogonal to $\mathbf{q}$. Imposing this condition, one obtains the following normal of the Hopf bifurcation:

$$\begin{aligned} D_2\eta \; = \; & [(0.433891 + 0.323942i)\sigma_U U_f - (4.1354 - 1.5023i)\sigma_h\overline{k}_{h0} \\ + \; & (2.3984 + 4.0114i)\sigma_\alpha\overline{k}_{\alpha 0}]\,\eta \\ + \; & [(0.0055995 + 0.0093651i)k_{\alpha 2} - (0.00072529 + 0.0011922i)k_{\alpha 1}^2 \\ - \; & (0.00083071 + 0.0013891i)k_{h1}k_{\alpha 1} \\ - \; & (2.19904\times 10^{-7} - 7.98847\times 10^{-8}i)k_{h2} - (1.04596\times 10^{-7} - 3.79928\times 10^{-8}i)k_{h1}^2 \\ - \; & (0.0779953 + 0.137028i)c_s]\,\eta^2\overline{\eta} \end{aligned} \tag{2.150}$$

The effects of all nonlinearities, including the higher-order spring coefficients (k_{h1}, k_{h2}, $k_{\alpha 1}$, and $k_{\alpha 2}$) and aerodynamic parameter c_s, are explicitly expressed through the last six terms of this normal form. For convenience, Equation (2.150) is written as

$$D_2\eta = \beta\eta + \Lambda\eta^2\overline{\eta} \tag{2.151}$$

where

$$\begin{aligned}
\Re(\beta) = \beta_r &= 0.433891\sigma_U U_f - 4.1354\sigma_h\overline{k}_{h0} + 2.3984\sigma_\alpha\overline{k}_{\alpha 0} \\
\Im(\beta) = \beta_i &= 0.323942\sigma_U U_f + 1.5023\sigma_h\overline{k}_{h0} + 4.0114\sigma_\alpha\overline{k}_{\alpha 0} \\
\Re(\Lambda) = \Lambda_r &= 0.0055995k_{\alpha 2} - 0.00072529k_{\alpha 1}^2 - 0.00083071k_{h1}k_{\alpha 1} \\
&- 2.19904\times 10^{-7}k_{h2} - 1.04596\times 10^{-7}k_{h1}^2 - 0.0779953c_s \\
\Im(\Lambda) = \Lambda_i &= 0.0093651k_{\alpha 2} - 0.0011922k_{\alpha 1}^2 - 0.0013891k_{h1}k_{\alpha 1} \\
&- 7.98847\times 10^{-8}k_{h2} - 3.79928\times 10^{-8}k_{h1}^2 - 0.137028c_s
\end{aligned} \tag{2.152}$$

and $\Re$ and $\Im$ stand for the real and imaginary parts, respectively.

Letting $\eta = \frac{1}{2}a\exp(i\theta)$ and separating the real and imaginary parts in Equation (2.151), one obtains the following alternate normal form of the Hopf bifurcation:

$$\dot{a} = \beta_r a + \frac{1}{4}\Lambda_r a^3 \tag{2.153}$$

$$\dot{\theta} = \beta_i + \frac{1}{4}\Lambda_i a^2 \tag{2.154}$$

where a is the amplitude and $\dot{\theta}$ is the shift in frequency of the periodic solution that is created due to Hopf bifurcation. It is noted that, because the a component is independent of θ, the problem is reduced to studying the stability of the fixed points of the one-dimensional system (2.153). Assuming that $\Lambda_r \neq 0$, Equation (2.153) admits three steady-state solutions, namely

$$a = 0, \quad a = \pm\sqrt{\frac{-4\beta_r}{\Lambda_r}} \tag{2.155}$$

The trivial fixed point of Equation (2.153) corresponds to the fixed point $(0, 0)$ of Equation (2.122), and a nontrivial fixed point (i.e, $a \neq 0$) of Equation (2.153) corresponds to a periodic solution of Equation (2.153). The origin is asymptotically stable for $\beta_r < 0$, unstable for $\beta_r > 0$, unstable for $\beta_r = 0$ and $\Lambda_r > 0$, and asymptotically stable for $\beta_r = 0$ and $\Lambda_r < 0$.

On the other hand, the nontrivial fixed points exist when $-\beta_r\Lambda_r > 0$. They are stable for $\beta_r > 0$ and $\Lambda_r < 0$ (supercritical Hopf bifurcation) and unstable for $\beta_r < 0$ and $\Lambda_r > 0$ (subcritical Hopf bifurcation). It is noted that a stable nontrivial fixed point of Equation (2.153) corresponds to a stable periodic solution of Equation (2.122). Likewise, an unstable nontrivial fixed point of Equation (2.151) corresponds to an unstable periodic solution of Equation (2.122).

Case study

In order to check the accuracy of the analytical formulation given by the normal form in predicting the amplitude of LCO, the case in which structural nonlinearity is applied only in the pitch degree of freedom is considered; that is, $k_{h1} = k_{h2} = c_s = 0$, $k_{\alpha 1} = 29.9967N.m$, and $k_{\alpha 2} = 67.685N.m$. This configuration corresponds to a supercritical instability ($\Lambda_r < 0$). To determine the amplitude of LCO associated with the pitch and plunge motions from the normal form, the first-order solution given by Equation (2.144) is considered. The amplitude of plunge and pitch LCO, A_h and A_α, respectively, are given by

$$\begin{aligned} A_h &= a\sqrt{\mathbf{p1}_r^2 + \mathbf{p1}_i^2} \\ A_\alpha &= a\sqrt{\mathbf{p2}_r^2 + \mathbf{p2}_i^2} \end{aligned} \tag{2.156}$$

where $\mathbf{pj}_r$ and $\mathbf{pj}_i$ denote the real and imaginary part of the j^{th} component of the vector $\mathbf{p}$, respectively. The LCO amplitudes for both pitch and plunge motions obtained by integrating the original system and those predicted from the normal form are plotted in Figure 2.23. The results show a good agreement in the amplitudes of LCO near the bifurcation.

To see the effect of the linear and nonlinear parameters on the system's behavior, $k_{\alpha 0}$ by 10%, $k_{\alpha 1}$ and $k_{\alpha 2}$ are varied by 20%. Variations of LCO amplitudes with the freestream velocity for the two configurations are plotted in Figure 2.24 . Clearly, the effect of combined uncertainties in linear and nonlinear parameters may cause the flutter to occur at speeds that are much lower than the flutter speed predicted by the linear model. Furthermore, they can cause a switch from a supercritical instability to a subcritical one.

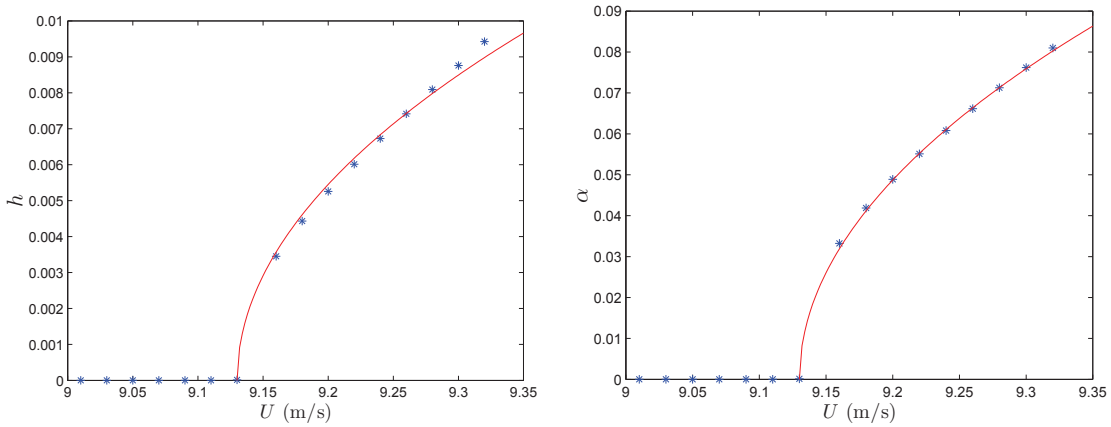

(a) (b)

Figure 2.23: LCO amplitudes of plunge and pitch motions: -, analytical prediction, $*$, numerical integration. (a) plunge motion and (b) pitch motion.

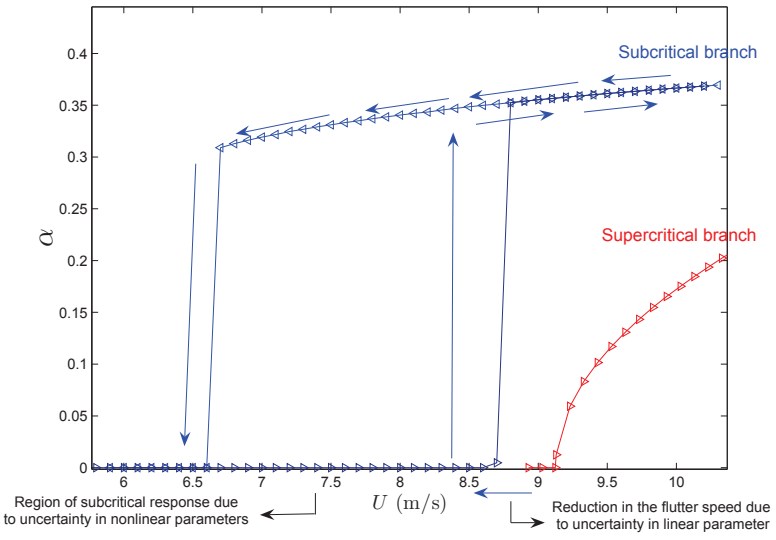

Figure 2.24: LCO amplitudes of pitch motion. Arrows show path of system response that may occur due to the effect of combined uncertainties in linear and nonlinear parameters: ($\rightarrow$) increasing, ($\leftarrow$) decreasing.

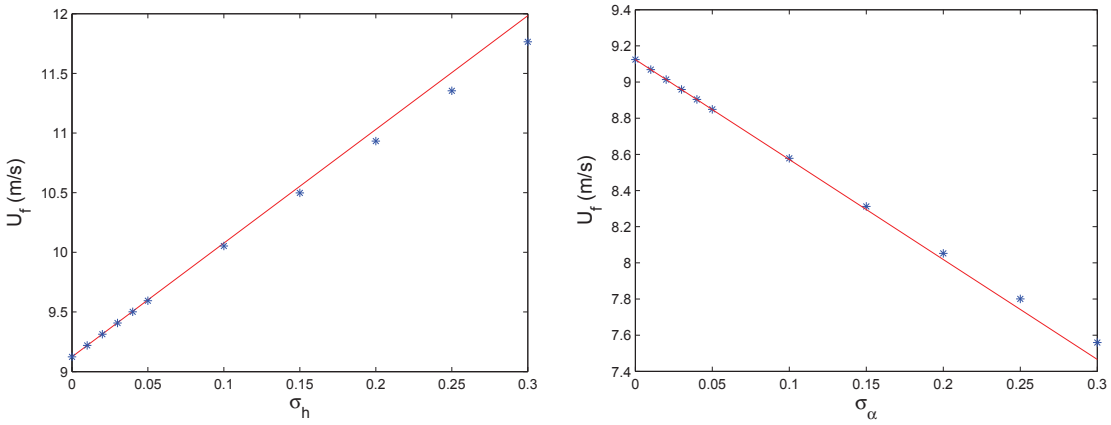

(a) (b)

Figure 2.25: Sensitivity of the flutter speed to variations in the structural stiffnesses. The solid line represents the flutter speed obtained from the perturbation analysis. The stars represent the exact flutter speed. (a) plunge structural stiffness and (b) pitch structural stiffness.

Sensitivity analysis

The effects of the structural stiffnesses and aerodynamic nonlinearity on the system behavior can be determined from the normal form. In fact, by setting β_r equal to zero, one can easily assess sensitivity of the flutter speed to variations in the structural pitch and plunge stiffnesses. For the specific values of the airfoil geometry (77), it is observed that

1. Variations in $k_{\alpha 0}$ and k_{h0} have opposite effects on the flutter speed as determined from the signs in Equation (2.151).

2. The effect of variations of k_{h0} is twice that of $k_{\alpha 0}$ as determined from the slopes in Figure 2.25.

3. The perturbation analysis is valid for small fluctuations of k_{h0} and $k_{\alpha 0}$ around their mean values, (see Figure 2.25).

As shown in Equation (2.152), the different nonlinearities may be favorable or unfavorable. For example, for the specific values of the system parameters (77), it is concluded that

1. In absence of the plunge stiffness nonlinearity, the pitch stiffness nonlinearity, even in the presence of the aerodynamic nonlinearity, may lead to large-amplitude LCO when transitioning through the Hopf bifurcation and also induce LCO even below the nominal flutter velocity if the disturbances to the system are sufficiently large (subcritical Hopf bifurcation).

2. The nonlinearity in the plunge stiffness (i.e., $k_{h1} \neq 0$ and $k_{h2} \neq 0$) is favorable in the sense that it inhibits the occurrence of LCO below the flutter boundary and limits the exponentially growing oscillations predicted by the linear model to a periodic response whose amplitude increases slowly with increasing freestream velocity (supercritical Hopf bifurcation).

3. Variations in the different system parameters, such as linear and nonlinear stiffnesses, can lead to a subcritical instability even if the deterministic problem does not exhibit that behavior.

These observations are based on the assumptions that all springs are of the hardening type. For softening springs, the analysis would yield other responses.

To gain more insight into the combined effect of the cubic and quadratic pitch stiffness coefficients $k_{\alpha 1}$ and $k_{\alpha 2}$ on the type of instability, a contour plot showing variations of Λ_r with $k_{\alpha 1}$ and $k_{\alpha 2}$ is generated (see Figure 2.26). It is noted that only the pitch stiffness nonlinearity is considered; that is, $k_{h1} = k_{h2} = c_s = 0$. This plot reveals the effect of the pitch stiffness nonlinearity on the type of instability as well as the amplitude of LCO using Equations (2.155) and (2.156).

2.4 Example 4: Control of Limit Cycle Oscillations of a Two-Dimensional Aeroelastic System

Different methods have been proposed to control bifurcations and achieve desirable nonlinear effects in complex systems. Abed and Fu (82; 83) proposed a nonlinear feedback control to suppress discontinuous bifurcations of fixed points, such as subcritical Hopf bifurcations,

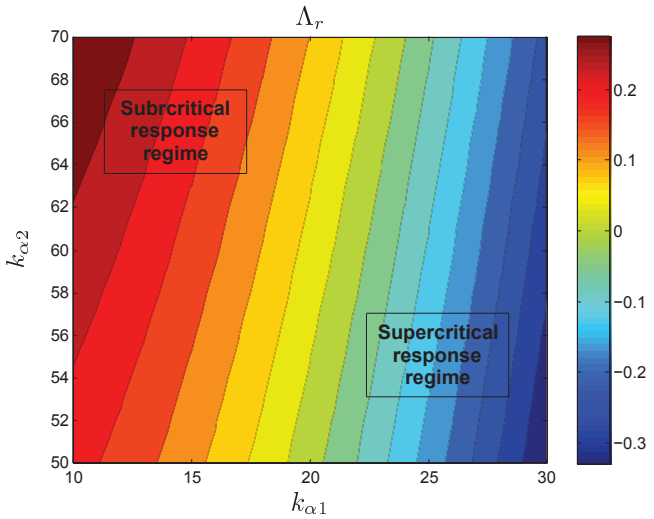

Figure 2.26: Variation of Λ_r with $k_{\alpha 1}$ and $k_{\alpha 2}$: effect of the pitch stiffness nonlinearity on the type of instability.

which can result in loss of synchronism or voltage collapse in power systems. For the pitch-plunge airfoil, Strganac et al. (77) used a trailing edge flap to control a two-dimensional nonlinear aeroelastic system. They showed that linear control strategies may not be appropriate to suppress large-amplitude LCO and proposed a nonlinear controller based on partial feedback linearization to stabilize the LCO above the nominal flutter velocity. Librescu et al. (84) implemented an active flap control for 2-D wing-flap systems operating in an incompressible flow field and exposed to a blast pulse and demonstrated its performances in suppressing flutter and reducing the vibration level in the subcritical flight speed range. Kang (85) developed a mathematical framework for the analysis and control of bifurcations and used an approach based on the normal form to develop a feedback design for delaying and stabilizing bifurcations. His approach involves a preliminary state transformation and center manifold reduction.

In this section, the aeroelastic system presented in Section 2.3.1 is considered to show the use of normal form to manage the Hopf bifurcation and achieve desirable nonlinear dynamics.

2.4.1 Static feedback control

To the system given by Equation (2.120), a static feedback $\mathbf{u}(\mathbf{Y})$ is added. This includes linear, $L_u\mathbf{Y}$, quadratic $Q_u(\mathbf{Y},\mathbf{Y})$, and cubic $C_u(\mathbf{Y},\mathbf{Y},\mathbf{Y})$ components; that is,

$$\mathbf{u}(\mathbf{Y}) = L_u\mathbf{Y} + Q_u(\mathbf{Y},\mathbf{Y}) + C_u(\mathbf{Y},\mathbf{Y},\mathbf{Y}) \tag{2.157}$$

where

$$\mathbf{Y} = \begin{pmatrix} Y_1 \\ Y_2 \\ Y_3 \\ Y_4 \end{pmatrix} = \begin{pmatrix} h \\ \alpha \\ \dot{h} \\ \dot{\alpha} \end{pmatrix}.$$

Hence, the controlled system takes the form

$$\dot{\mathbf{Y}} = F(\mathbf{Y},U) + \mathbf{u}(\mathbf{Y}), \tag{2.158}$$

Following similar approach as described in Section 2.3.3, he following modified normal form of the Hopf is obtained bifurcation:

$$D_2\eta = \hat{\beta}\eta + \hat{\Lambda}\eta^2\overline{\eta} \tag{2.159}$$

where

$$\hat{\beta} = \beta + \beta_u, \qquad \text{with} \quad \beta_u = \mathbf{q}^T L_u \mathbf{p}, \tag{2.160}$$

and

$$\hat{\Lambda} = \Lambda + \Lambda_u, \tag{2.161}$$

with

$$\Lambda_u = 4\mathbf{q}^T Q_u(\mathbf{p},\zeta_0) + 2\mathbf{q}^T Q_u(\overline{\mathbf{p}},\zeta_2) + 3\mathbf{q}^T C_u(\mathbf{p},\mathbf{p},\overline{\mathbf{p}}) + 4\mathbf{q}^T Q(\mathbf{p},\zeta_{0u}) + 2\mathbf{q}^T Q(\overline{\mathbf{p}},\zeta_{2u}) \tag{2.162}$$

Again, letting $\eta = \frac{1}{2}a\exp(i\theta)$ and separating the real and imaginary parts in Equation (2.159), the following alternate normal form of the Hopf bifurcation is obtained

$$\dot{a} = \hat{\beta}_r a + \frac{1}{4}\hat{\Lambda}_r a^3 \tag{2.163}$$

$$\dot{\theta} = \hat{\beta}_i + \frac{1}{4}\hat{\Lambda}_i a^2 \tag{2.164}$$

To delay the occurrence of Hopf bifurcation (i.e., stabilize the aeroelastic system at speeds higher than the flutter speed), one needs to set the real part of $\hat{\beta}$ to a negative value by appropriately managing the linear control represented by L_u in Equation (2.157). To eliminate subcritical instabilities and limit LCO amplitudes to small values at speeds higher than the flutter speed (supercritical Hopf bifurcation which is a favorable instability for such systems), the nonlinear feedback control given by $Q_u(\mathbf{Y},\mathbf{Y}) + C_u(\mathbf{Y},\mathbf{Y},\mathbf{Y})$ should be chosen so that $\text{Real}(\Lambda + \Lambda_u) < 0$.

2.4.2 Case study

To demonstrate the linear and nonlinear control strategies, an uncontrolled case (i.e., $\mathbf{u}(\mathbf{Y}) = 0$) in which only the pitch structural nonlinearity is taken into account is considered; that is, $k_{h1} = k_{h2} = c_s = 0$, $k_{\alpha 1} = 10$ N.m, and $k_{\alpha 2} = 167.68$ N.m. The hysteretic response as a function of the freestream velocity, obtained through the numerical integration of Equation (2.120) for these parameters, is presented in Figure 2.27. The onset of flutter takes place at $U_f = 9.12$ m/s and is characterized by a jump to a large-amplitude LCO when transitioning through the Hopf bifurcation. As the speed is increased beyond the flutter speed, the LCO amplitudes of both of the pitch and plunge motions increase. Furthermore, LCO take place at speeds lower than U_f if the disturbances to the system are sufficiently large. Clearly, this configuration exhibits a subcritical instability $\text{Real}(\Lambda) > 0$.

For linear control, the matrix L_u defined in Equation (2.157) is considered in the form of

$$L_u = \begin{pmatrix} -k_l & 0 & 0 & 0 \\ 0 & 0 & 0 & 0 \\ 0 & 0 & 0 & 0 \\ 0 & 0 & 0 & 0 \end{pmatrix}$$

where k_l is the linear feedback control gain. Then, for the specific values of the system parameters given in (77), one obtains

$$\hat{\beta} = (0.433891\sigma_U U_f - 0.110363 k_l) + \imath(0.323942\sigma_U U_f - 0.303804 k_l)$$

where σ_U is the velocity perturbation defined as a ratio of the flutter speed. To guarantee damped oscillations of the airfoil at speeds higher than the flutter speed, one needs to set k_l

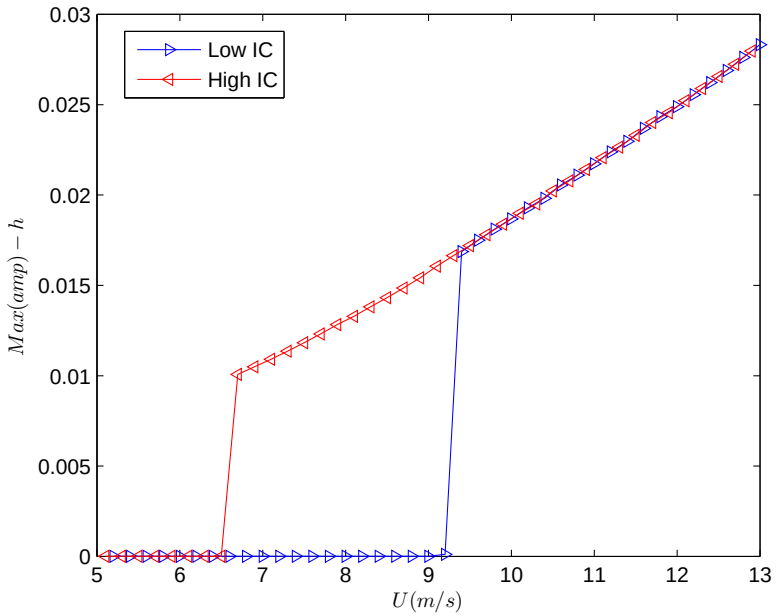

(a) Plunge motion

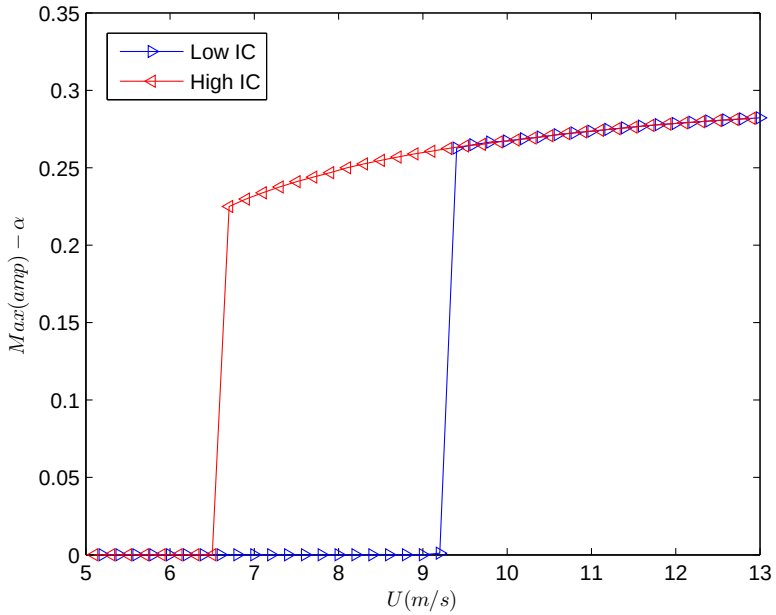

(b) Pitch motion

Figure 2.27: Hysteretic response of the aeroelastic system (subcritical instability). The steady-state amplitudes are plotted as a function of U.

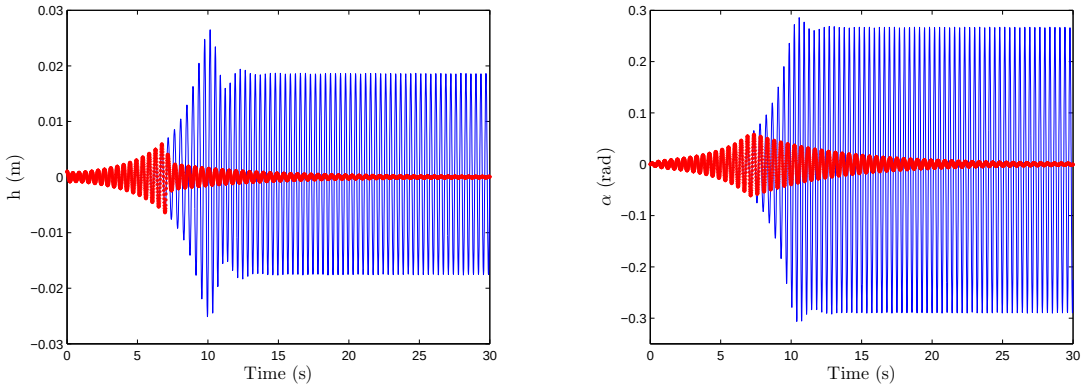

(a) Plunge motion

(b) Pitch motion

Figure 2.28: Measured pitch and plunge responses: blue line, without linear control, red stars, with linear control.

to a value such that Real$(\hat{\beta}) < 0$. Using a gain of 10, the plunge and pitch displacements for a freestream velocity of $U = 10$ m/s with and without linear control are plotted in Figure 2.28. Clearly, linear control damps the LCO of the controlled system. It is noted that, by increasing the linear feedback control gain k_l, the amplitudes of pitch and plunge decay more rapidly.

Although linear control is capable of delaying the onset of flutter in terms of speed and reducing the LCO amplitude, the system would require higher gains at higher speeds. Furthermore, it maintains its subcritical response. To overcome these difficulties and convert the subcritical instability to a supercritical one, the following nonlinear feedback control law is introduced

$$\mathbf{u}^T = -\begin{pmatrix} k_{nl1} & k_{nl2} & k_{nl3} & k_{nl4} \end{pmatrix} \dot{\alpha}^3 \tag{2.165}$$

where the k_{nli} are the nonlinear feedback control gains. For the specific airfoil's geometry given in (77), one obtains

$$\hat{\Lambda}_r = 0.866899 - (132.844k_{nl1} + 13.3643k_{nl2} + 2.9858k_{nl3} + 1.32415k_{nl4}) \tag{2.166}$$

This equation shows that applying gain to the plunge displacement is more effective than

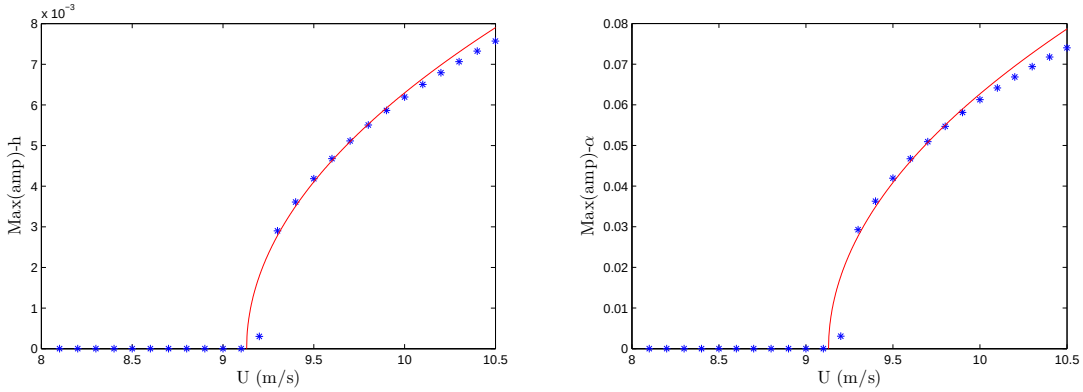

(a) Plunge motion

(b) Pitch motion

Figure 2.29: LCO amplitudes of plunge and pitch motions (controlled configuration): -, analytical prediction, $*$, numerical integration

applying it to the pitch displacement or plunge velocity or pitch velocity.

The subcritical instability takes place for positive values of $\hat{\Lambda}_r$. As such it can be eliminated by forcing $\hat{\Lambda}_r$ to be negative. This can be achieved by using nonlinear control gains $k_{nl1} = 0.02$ N.m ($k_{nl2} = k_{nl3} = k_{nl4} = 0$). The corresponding LCO amplitudes for both pitch and plunge motions obtained by integrating the original system and those predicted by the normal form are plotted in Figure 2.29. The results show good agreement in the LCO amplitudes only near the bifurcation. The subcritical Hopf bifurcation at U_f observed in Figure 2.27 has been transformed into the supercritical Hopf bifurcation of Figure 2.29. A comparison of the two figures shows that the unstable limit cycles observed over the freestream speed between $U = 6.5$ m/s and $U = 9.12$ m/s have been eliminated. Furthermore, the exponentially growing oscillations predicted by the linear model are limited to a periodic solution whose amplitude increases slowly with increasing freestream velocity. Moreover, increasing the value of k_{nl1} reduces the amplitude of the limit cycles created due to Hopf bifurcation.

A schematic to show possible physical implementation of the control mechanism is plotted in Figure 2.30. The control can be achieved as follows: an accelerometer is placed on the wing surface to measure the angular acceleration. The signal provided by the accelerometer

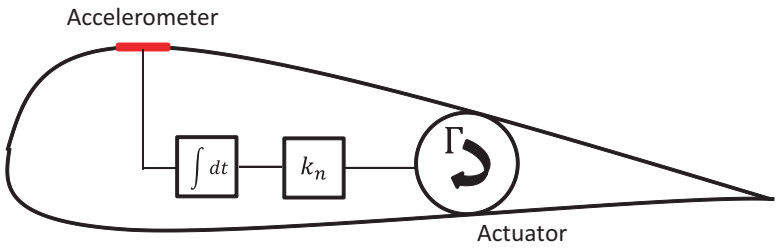

Figure 2.30: A schematic of the proposed controller.

is then sent to an integrator to convert it to the rate of the pitch angle $\dot{\alpha}$ which is cubed and multiplied by the nonlinear gain k_n. The signal is then used to apply a torque, Γ, to rotate the wing and achieve the desirable dynamics. Different actuation mechanisms to apply torques are reviewed in (86).

2.4.3 Summary

A methodology to convert subcritical bifurcations of aeroelastic systems into supercritical bifurcations is presented. This methodology involves the following steps: (i) reduction of the dynamics of the system into a two-dimensional dynamical system using the method of multiple scales and then (ii) designing a nonlinear feedback controller to convert subcritical to supercritical bifurcations and reduce the amplitude of any ensuing LCO.

Chapter 3

Stochastic Modeling of Incident Gust Effects on Aerodynamic Lift

Assessing upstream gust effects on flow quantities is required in many aeroelastic applications. This is particularly important for micro air vehicles (MAV) which are expected to operate in urban environments, where they will be subjected to varying turbulent or gust flows. Under these conditions, a quasi-steady approach would not yield correct aerodynamic forces as its temporal or length scale would be much larger than the ones in the range encountered by MAV. Consequently, upstream gust or turbulence should be modeled through many parameters, including turbulence intensities, integral length scales, relative energy content of large and small scales, and the aerodynamic roughness in the case of boundary layers. These parameters may not be known precisely or accurately. This is because they are statistics of flow quantities whose sampling distributions cannot be easily known a priori for the complex terrains in which MAV are expected to operate. Furthermore, since these parameters cannot be changed independently (87), it is difficult to perform a parametric assessment of their individual effects on different flow quantities (88; 89).

The influence of the likely range of gust statistics on unsteady aerodynamic loads can best be quantified through a broad sensitivity analysis. Comprehensive sampling-based simulations that make use of blind or wide variations of input parameters are inefficient for aeroelastic simulations which are already computationally expensive, even in the determinis-

tic sense. As such, an integrated approach that enables uncertainty propagation through the model would be more effective for performing sensitivity analysis of flow quantities to ranges of gust or turbulence parameters. The central role of sensitivity analysis in support of UQ is broadly recognized (90; 91). Formal uncertainty quantification (UQ) of unsteady aerodynamics and aeroelasticity has been an active area of research for at least the past 15 years. Pettit (92) summarized various UQ perspectives and methods in the context of aeroelasticity and surveyed the state of the field through 2004. Among the methods Pettit surveyed, series expansions of stochastic processes in terms of orthogonal functions of random variables were cited for their potential to integrate UQ with standard computational methods.

In this chapter, the intrusive formulation of the polynomial chaos expansion (PCE) is implemented in order to quantify the influence of imprecision in upstream gust parameters on aerodynamic loads on a rigid airfoil. This formulation involves the substitution of uncertain variables and parameters in the governing equations with polynomial expansions. The unknown polynomial coefficients are then evaluated by projecting the resulting equations onto basis functions. Thus, the governing equations are reformulated to yield mode strengths (78) of the output, which in this case is the unsteady lift coefficient. The aerodynamic model used in this effort is based on the unsteady vortex lattice method (UVLM). This relatively simple method, with linear assumptions, is chosen as a first step to implement the PCE approach in a nonlinear formulation of the deterministic problem, e.g. if the flow is modeled by Euler or Navier-Stokes equations.

3.1 Stochastic Gust Representation

Typically, turbulent fluctuations of the different velocity components of a flow field are compactly specified by frequency-domain power spectra (93; 94) such as the von Karman spectrum (95; 96). In this representation, the spectra of the velocity components are given by (96)

$$\begin{aligned} S_{uu}(\omega) &= \frac{2\sigma_u^2 L_u}{\pi V_\infty} \frac{1}{[1+(1.339 L_u \omega/V_\infty)^2]^{5/6}} \\ S_{vv}(\omega) &= \frac{2\sigma_v^2 L_v}{\pi V_\infty} \frac{1+\frac{8}{3}(2.678 L_v \omega/V_\infty)^2}{[1+(2.678 L_v \omega/V_\infty)^2]^{11/6}} \end{aligned} \tag{3.1}$$

where L_u and L_v, are respectively the integral length scales of the horizontal and vertical velocity fluctuations, and σ_u and σ_v, are used to denote the corresponding turbulence intensities.

In this work, stochastic gust fluctuations are obtained by superposing a finite set of sinusoidal components defined from their corresponding power spectra as follows,

$$\begin{aligned} u(t) &= \sum_{n=1}^{N_\omega} \sqrt{2S_{uu}(\omega_n)\Delta\omega_n(\omega_n)}\cos(\omega_n t + \phi_n), \text{ and} \\ v(t) &= \sum_{n=1}^{N_\omega} \sqrt{2S_{vv}(\omega_n)\Delta\omega_n(\omega_n)}\cos(\omega_n t + \phi_n). \end{aligned} \tag{3.2}$$

where the phase ϕ_n corresponding to each frequency component is a uniform random variable between 0 and 2π. It should be noted that for a particular group of spectral parameters, choosing a different set of phases ϕ_n will produce a different time history, but with the same long-term statistics because these are governed by the particular spectrum. In effect, this would introduce an additional N_ω random variables in the time integration problem that are not present in the frequency domain (97). These variables are not part of the random parameters considered in the subsequent analysis. Consequently, the set of phases ϕ_n is kept the same for all realizations. Additional details of the approach followed to represent fluctuations in atmospheric flows are provided by Paola (98) and Grigoriu (99).

3.2 2-D Unsteady Vortex Lattice Method Implementation

3.2.1 Formulation

The time-varying flow around the flat-plate airfoil is modeled using a two-dimensional unsteady vortex lattice method (UVLM). This method has been used extensively to determine aerodynamic loads and aeroelastic responses by (27; 100; 101). For instance, Nuhait and Mook (101) implemented an aeroelastic numerical model based on a two-dimensional vortex lattice method to compute the unsteady aerodynamic loads of a flat plate in a uniform flow and predict the flutter boundary. Their prediction for the flutter speed showed an excellent agreement with the one obtained based on Theodorsen's method. In this method, it is assumed that the flow field is inviscid everywhere except in the boundary layers and the wake.

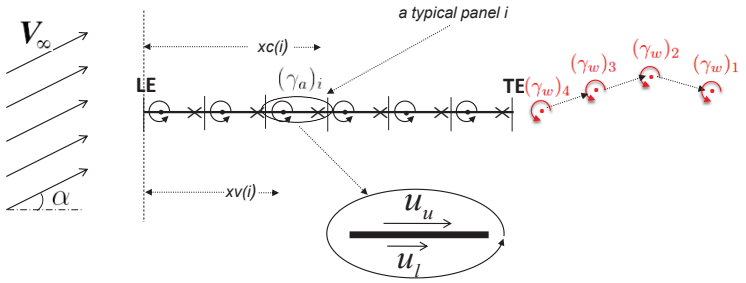

Figure 3.1: Representation of a model of a fixed flat plate with panels, each one has a concentrated vortex located at $xv(i)$, and a control point located at $xc(i)$.

A set of discrete vortices are placed on the plate to represent a viscous shear layer in the limit of the infinite Reynolds number. Highlights of this method are detailed below to show how the intrusive PCE can be conveniently implemented when using UVLM.

In this numerical model, the position of the wake and the distribution of circulation on the plate and in the wake are treated as unknowns. The plate is divided into N piecewise straight line segments or panels. In each panel, a point vortex with a circulation density $(\gamma_b)_i(t)$ is placed at the one-quarter chord position. The no-penetration condition is imposed at the three-quarter chord position, called the control point. Figure 3.1 shows a schematic of the flat plate with panels, each of them having a concentrated vortex located at $xv(i)$, and a control point located at $xc(i)$.

The time-varying gust is denoted by $\mathbf{V}_\infty(t) = [V_\infty + u(t), v(t)]^T$ and is introduced in the UVLM representation. The basic mathematical tool in this method is the expression derived from the Biot-Savart law that gives the velocity $\mathbf{V}$ at a point $\mathbf{r}$ associated with an individual vortex point located at $\mathbf{r}_0$ and having circulation $\gamma(t)$; that is,

$$\mathbf{V}(\mathbf{r},t) = -\frac{1}{2\pi}\mathbf{e}_z \times \gamma(t)\frac{\mathbf{r}-\mathbf{r}_0}{|\mathbf{r}-\mathbf{r}_0|^2} \tag{3.3}$$

where $\mathbf{e}_z$ is a unit vector perpendicular to the (x, y) plane so as to form a right-hand system with the basis vectors in the plane of the flow. Consequently, the normal component of the velocity at the control point of panel i, $xc(i)$, associated with the flow around the vortex in

panel j, $xv(j)$, is

$$\mathbf{u}_b(i,j)\cdot\mathbf{n} = u_{b_n}(i,j) = \frac{(\gamma_b)_j(t)}{2\pi}\Big[\frac{1}{xv(j)-xc(i)}\Big] = (\gamma_b)_j(t)L_1(i,j) \tag{3.4}$$

where $\mathbf{n}$ is the normal vector of the plate. The operator L_1 is used to denote the induced velocity obtained from the Biot-Savart law. The total normal component of the velocity at control point i attributed to the disturbance created by all bound vortices is then given by

$$u_{b_n}(i)\big|_{total} = \sum_{j=1}^{N} u_{b_n}(i,j) = \sum_{j=1}^{N}(\gamma_b)_j(t)L_1(i,j) \tag{3.5}$$

3.2.2 Wake development

The wake vorticity is introduced by shedding point vortices from the trailing edge, whose circulation is denoted by $(\gamma_w)_j(t)$. These vortices are convected downstream at each time step and their positions are denoted by $(\mathbf{r}_w)_j(t)$. The induced velocity at control point i that stems from all wake vortices is given by

$$\mathbf{u}_w(i) = -\frac{1}{2\pi}\mathbf{e}_z \times \sum_{j=1}^{N_w(t)} (\gamma_w)_j(t)\frac{\mathbf{r}_{c_i}-(\mathbf{r}_w)_j}{|\mathbf{r}_{c_i}-(\mathbf{r}_w)_j|^2} \tag{3.6}$$

where $\mathbf{r}_{c_i}$ is the position of the control point i in the global frame and $N_w(t)$ is the number of wake vortices. Additionally, there is the normal component of the freestream velocity, which, in this case, is the same for all control points $\mathbf{V}_\infty(t)\cdot\mathbf{n} = -L_3\mathbf{V}_\infty(t)$.

At every control point, the no-penetration condition applies and is written in the form

$$u_{b_n} = (-\mathbf{u}_w - \mathbf{V}_\infty)\cdot\mathbf{n} \tag{3.7}$$

In terms $\gamma_b(t)$, $\mathbf{r}_w(t)$, and $\gamma_w(t)$, this condition is written as

$$L_1\gamma_b(t) = L_2(\mathbf{r}_w(t))\gamma_w(t) + L_3\mathbf{V}_\infty(t) \tag{3.8}$$

where L_2 denotes a geometric operator that represents the induced velocity obtained form the Biot-Savart law and L_3 is an operator through which the fluctuations in the freestream velocity impact each control point.

At every time step, a vortex with circulation γ_{te} is shed from the trailing edge of the plate into the wake. The conservation of the total circulation yields

$$\sum_{i=1}^{N}(\gamma_b)_i(t) + \gamma_{te}(t) = -\sum_{j=1}^{N_w(t)}(\gamma_w)_j(t) \tag{3.9}$$

It is noted that vortices shed from the trailing edge retain their circulation values at all times. Thereafter, solving Equation (3.9) for given $(\gamma_b)_i(t)$ and $(\gamma_w)_j(t)$, and updating the vector of wake vortices yields

$$(\gamma_w)_1(t+1) = \gamma_{te}(t) \tag{3.10}$$

and

$$(\gamma_w)_{i+1}(t+1) = (\gamma_w)_i(t), \quad \text{for} \quad i = 1, 2, ..., N_w(t) \tag{3.11}$$

The steps described in Equations (3.9)-(3.11) are then summarized as:

$$\gamma_w(t+1) = L_4\gamma_w(t) + L_5(\mathbf{r}_w(t))\gamma_b(t) \tag{3.12}$$

where L_4 is a shift operator that updates the indices of the wake vortices at each time step as a new wake vortex is shed from the trailing edge and L_5 denotes geometric operator that represents the induced velocity obtained form the Biot-Savart law.

The path of wake particles is determined using the Euler integration scheme; that is,

$$(\mathbf{r}_w)_i(t+1) = (\mathbf{r}_w)_{i+1}(t) + \mathbf{u}_{w,i}((\mathbf{r}_w)_{i+1}(t), t)\Delta t \tag{3.13}$$

where $(\mathbf{r}_w)_i$ is the position of a given vortex in the wake and is calculated by convecting the downstream end point of segment $i-1$ found at previous time step and Δt is the time step. The velocity of the wake vortices $\mathbf{u}_w$ is then computed using the Biot-Savart law and combining the effects of the airfoil, the wake and the freestream on the wake. A major problem might occur in the system of point vortices when two vortices are convected close to each other. As such, the vortex blob concept is used to remove such singularity. More details of this concept are provided by Pettit et al. (81; 97). Equation (3.13) is then expressed as

$$\mathbf{r}_w(t+1) = L_6(\mathbf{r}_w(t))\gamma_w(t) + L_7(\mathbf{r}_w(t))\gamma_b(t) + L_8\mathbf{V}_\infty(t) \tag{3.14}$$

where L_6 and L_7 denote geometric operators that represent the induced velocity obtained form the Biot-Savart law and L_8 is an operator through which the fluctuations in the freestream

velocity are applied on each wake vortex location. The governing equations of the UVLM including gust effects are given by Equations (3.8), (3.12), and (3.14). These equations are used in the implementation of the intrusive PCE.

3.2.3 Aerodynamic lift

The computation of the aerodynamic lift is performed by multiplying the difference in the pressure across each panel by its length. These pressure differences are evaluated from the unsteady Bernoulli equation:

$$\frac{\partial \Phi_i}{\partial t} + \frac{p_i}{\rho} + \frac{1}{2} v_i^2 = H(t) \tag{3.15}$$

Rewriting Equation (3.15) in terms of a differential between a control point i on the body and a point in the far field lying on the same streamline, the pressure coefficient $(Cp)_i = \frac{p_i - p_\infty}{\frac{1}{2}\rho V_\infty^2}$ is given by

$$(Cp)_i = 1 - \big(\frac{v_i}{V_\infty}\big)^2 - \frac{2}{V_\infty^2}\frac{\partial \Phi_i}{\partial t} \tag{3.16}$$

The difference in the pressure coefficient across each panel i of the plate is

$$\Delta(Cp)_i = \big[\big(\frac{v_i}{V_\infty}\big)_u^2 - \big(\frac{v_i}{V_\infty}\big)_l^2\big] + \frac{2}{V_\infty^2}\big[\frac{\partial \Phi_i}{\partial t}|_u - \frac{\partial \Phi_i}{\partial t}|_l\big] \tag{3.17}$$

where $(.)_u$ and $(.)_l$ stand for the upper and lower surfaces of the plate, respectively. For convenience, $(\frac{v_i}{V_\infty})$ will be replaced by v_i. The first term in Equation (3.17) can be rewritten as

$$\begin{aligned}(v_i)_u^2 - (v_i)_l^2 &= \Big((v_i)_u + (v_i)_l\Big)\Big((v_i)_u - (v_i)_l\Big) \\ &= 2(v_i)_m \Delta v_i \\ &= 2\cos(\alpha)\Delta v_i \end{aligned} \tag{3.18}$$

where α is the angle of attack. The velocity difference across a panel surface Δv_i is obtained by dividing the vorticity circulation strength $(\gamma_b)_i$ by the panel length $(\Delta l)_i$.

The calculation of the unsteady portion of Equation (3.17) involves determining the rate of change of velocity potential Φ. The partial derivative is approximated through the first-order backward difference as

$$\frac{\partial \Phi}{\partial t} \approx \frac{\Phi(r,t) - \Phi(r, t - \Delta t)}{\Delta t} \tag{3.19}$$

Thus,

$$\frac{2}{V_\infty^2}\Big[\frac{\partial \Phi_i}{\partial t}|_u - \frac{\partial \Phi_i}{\partial t}|_l\Big] = \frac{2}{V_\infty^2 \Delta t}\Big[\Big((\Phi_i)_u(t) - (\Phi_i)_l(t)\Big) - \Big((\Phi_i)_u(t-\Delta t) - (\Phi_i)_l(t-\Delta t)\Big)\Big] \tag{3.20}$$

To calculate the difference in Φ across the panel surface in Equation (3.20), the definition of the velocity potential, $v = \nabla\Phi$, is manipulated to state $d\Phi = v \cdot dl$ or

$$(\Phi)_u - (\Phi)_l = \int_{l_l}^{l_u} v \cdot dl \tag{3.21}$$

Because the plate is considered as a body of zero thickness, the integration of Equation (3.21) is performed along a closed path. Using the definition of circulation,

$$\gamma = \oint_c v \cdot dl, \tag{3.22}$$

the value of the integral of Equation (3.21) is equal to the circulation associated with the vorticity encircled by that path. In this formulation, the circulation is simply the summation of individual strengths of vortices encountered along the path of integration. Consequently, the difference in the velocity potential is given by

$$(\Phi_i)_u(t) - (\Phi_i)_l(t) = \sum_{j=1}^{i} (\gamma_b)_j(t) \tag{3.23}$$

The aerodynamic lift is then calculated by integrating the pressure over the entire plate as follows

$$C_L(t) = \sum_{i=1}^{N} \Big[2\cos(\alpha)\frac{(\gamma_b)_i(t)}{(\Delta l)_i} + \frac{2}{V_\infty^2 \Delta t}\Big(\sum_{j=1}^{i}(\gamma_b)_j(t) - \sum_{j=1}^{i}(\gamma_b)_j(t-\Delta t)\Big)\Big]\Delta l\cos(\alpha) \tag{3.24}$$

3.3 Uncertainty Quantification

3.3.1 Background

A classical approach to determine the effect of parameter randomness or uncertainties on the system's response is Monte Carlo simulations (MC). In this approach, deterministic problems are solved for randomly varying parameter values. However, the relatively low convergence rate associated with this approach results in a large number of required samples. Therefore,

it remains impractical due to its high computational costs especially for problems which are already computationally intensive in the deterministic case. More sophisticated sampling strategies such as Latin Hypercube (102; 103) may improve the efficiency of MC to some extent.

The intrusive or Galerkin polynomial chaos (PC) method was first proposed by Ghanem and Spanos (80) in the context of structural mechanics as an efficient alternative to quantify system's uncertainties. Later applications of polynomial chaos in computational fluid dynamics problems can be found in (78; 104; 105). The polynomial chaos is based on the homogeneous chaos theory of Wiener (80). This approach is a spectral method in the probability space that approximates the model output by a polynomial expansion of uncertain parameters. The approximation is obtained by Galerkin projection on a basis of orthogonal polynomials. This projection leads to a coupled set of deterministic equations. However, solving these equations requires significant alterations to existing solvers of the deterministic problems. Thus, this approach may not be possible when the source code is unavailable (e.g. commercial software package) or when the deterministic equations are highly nonlinear. Consequently, the attention has been shifted to the non intrusive polynomial chaos approach which is based on constructing the polynomial approximation of the output by interpolating MC samples (78; 104; 105). In this method, the existing deterministic solver is used as a black box while reducing the number of deterministic solves in comparison with MC.

3.3.2 Polynomial chaos expansion

The spectral representation of uncertainty is based on the decomposition of the random function (or variable) into separable deterministic and stochastic components (104; 106). Thus, a random variable α^* is considered as a function of independent deterministic variables x and t and n-dimensional random variable vector $\xi = (\xi_{i_1}, ..., \xi_{i_n})$. It is expressed as

$$\alpha^*(x,t,\xi) = \sum_{m=0}^{\infty} \alpha_m(x,t)\Psi_m(\xi) \tag{3.25}$$

Here $\alpha_m(x,t)$ is the deterministic component, which is the amplitude of m^{th} fluctuation, and $\Psi_m(\xi)$ is the random basis function corresponding to the m^{th} mode. In practice, the finite-term summation should be limited by the highest order terms of the polynomials that yield

the required accuracy. Many choices are possible for the basis functions depending on the type of the probability distribution selected for the uncertainty of the random variable vector ξ (79). For variables with probability distributions that are Gaussian, Hermite polynomials are used because they are orthogonal with respect to the Gaussian measure (80). The Hermite polynomial of order n is defined as (80)

$$H_n(\xi_{i_1}, ..., \xi_{i_n}) = e^{\frac{1}{2}\xi^T\xi}(-1)^n \frac{\partial^n}{\partial\xi_{i_1}...\partial\xi_{i_n}} e^{-\frac{1}{2}\xi^T\xi}. \tag{3.26}$$

For ξ being a standard Gaussian distributed variable, the inner product has the form

$$< \Psi_i(\xi), \Psi_j(\xi) >= \frac{1}{\sqrt{(2\pi)^n}} \int_{-\infty}^{\infty} ... \int_{-\infty}^{\infty} \Psi_i(\xi)\Psi_j(\xi) e^{(-\frac{\xi^T\xi}{2})} d\xi, \tag{3.27}$$

with the density function of the n variate standard Gaussian distribution as a weighting function.

3.3.3 Gust uncertainties

For specified values of the spectral parameters (σ_u, L_u, σ_v and L_v), realizations for $u(t)$ and $v(t)$ are computed through Equations (3.1) and (3.2). Denoting the random vector composed of these parameters by Ξ and the corresponding random velocity components by $\mathbf{V}_\infty(t, \Xi) = [u_\infty(t, \Xi) = V_\infty + u(t, \Xi), v_\infty(t, \Xi)]^T$, this component is expanded as

$$\mathbf{V}_\infty(t, \Xi) \quad = \quad \sum_{m=0}^{P} \mathbf{V}_{\infty m}(t)\Psi_m(\Xi). \tag{3.28}$$

where $P + 1 = \frac{(n+p)!}{n!p!}$ is the number of output modes, which is a function of the order of the polynomial chaos p and the number of random dimensions n. The coefficients $\mathbf{V}_{\infty m}(t) = [u_{\infty m}(t) = V_\infty + u_m(t), v_{\infty m}(t)]^T$ are determined from a nonintrusive PCE procedure, i.e. by (i) generating samples of the uncertain spectral parameters using Latin Hypercube sampling (102; 103), (ii) constructing the time histories for the gust velocities for each sample using Equations (3.1) and (3.2), and (iii) using all samples to evaluate the PCE coefficients of the truncated expansion of $\mathbf{V}_\infty$ from

$$\mathbf{V}_{\infty m}(t) \approx \frac{\frac{1}{N}\sum_{n=1}^{N} \mathbf{V}_\infty(t, \xi_n)\Psi_m(\xi_n)}{< \Psi_m^2 >}, \tag{3.29}$$

where $\xi_\lambda = (\lambda - \mu_\lambda)/\sigma_\lambda$ and $\lambda \in \{\sigma_v, L_v, \sigma_u, L_u\}$.

To generate the samples, variations of the spectral parameters are obtained by assuming Gaussian distributions with 10% coefficients of variation and mean values that are computed from the specifications in MIL-HDBK-1797 (96).

For a micro air vehicle with an assumed flight speed of 25 ft/s at an elevation of 100 ft, the mean and standard deviations of the integral length scales and intensities of the stochastic gust are presented in Table 3.1. It is noted that, based on the assumed ranges of gust parameters, the fluctuation levels should not cause notable leading-edge separation.

Table 3.1: Mean values and assumed standard deviations of the von Karman spectrum parameters.

Parameter	Mean	Standard Deviation
σ_u	1.716 ft/s	0.1716 ft/s
L_u	505.2 ft	50.52 ft
σ_v	1.000 ft/s	0.1000 ft/s
L_v	50.00 ft	5.000 ft

The PCE coefficients of $\mathbf{V}_\infty$ are determined using 200 realizations of turbulent velocity components. The zero- and first-order polynomial chaos coefficients are shown in Figure 3.2. The zero-order coefficients are the estimated mean values of the stochastic gust. The first-order coefficients provide a measure of the sensitivity of the stochastic gust to each of the uncertain parameters ξ_1, ξ_2, ξ_3, and ξ_4 which correspond to the spectral parameters σ_v, L_v, σ_u, and L_u, respectively. These coefficients are the inputs of the stochastic version of the UVLM as will be shown in the following subsection. It should be noted that the time histories of the unsteady wind velocities are computed for a total physical time of 2 s on a flat plate airfoil with a chord of 0.5 ft. These parameters were chosen to ensure the inclusion of all gust wavelengths that cannot be modeled using quasi-steady aerodynamics.

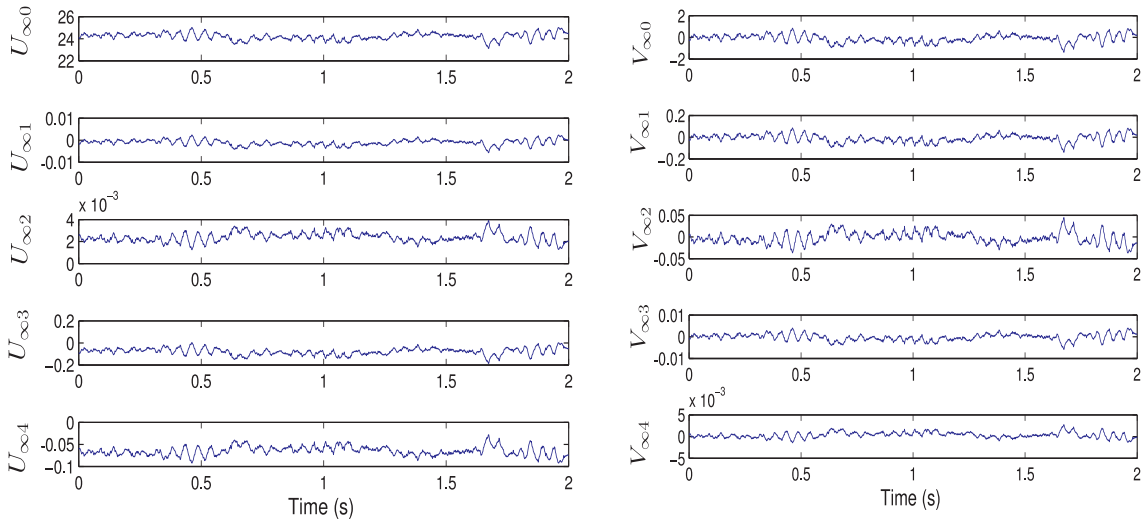

(a) $U_{\infty m}(t)$ (b) $V_{\infty m}(t)$

Figure 3.2: The PCE coefficients of the components of the random freestream flow speed. The zero-order coefficients are the estimated mean values of the stochastic gust. The first-order coefficient provide a measure of the sensitivity of the stochastic gust to each of the uncertain parameters.

3.3.4 Intrusive formulation

In the intrusive approach, spectral decomposition of the flow parameters, as described in the previous section, is introduced in the governing equations. In implementing the intrusive approach for the current work, the strengths of the bound and wake vortex elements for the fixed airfoil with wake vortex convection, $\gamma_b(t,\xi)$ and $\gamma_w(t,\xi)$, are considered as stochastic processes that are functions of the statistics of the upstream gust. Their PCE are then written as

$$\gamma_b(t,\Xi) = \sum_{m=0}^{P} \gamma_{bm}(t)\Psi_m(\Xi), \text{ and} \tag{3.30a}$$

$$\gamma_w(t,\Xi) = \sum_{m=0}^{P} \gamma_{wm}(t)\Psi_m(\Xi), \tag{3.30b}$$

For the sake of simplicity, the wake elements locations, $\mathbf{r}_w(t)$, are considered to be deterministic. The basis of this assumption is the result that ignoring effects of minor stochastic variations in the positions $\mathbf{r}_w(t)$ of the wake vortices does not significantly influence the airfoil loads (81).

The intrusive approach relies on a Galerkin projection of the original model equations to arrive at governing equations for the PC mode strengths of the model output (78; 80). The governing equations are rewritten by substituting Equations (3.28) and (3.30) in Equations (3.8), (3.12), and (3.14), i.e.,

$$\begin{aligned}
L_1 \sum_{m=0}^{P} \gamma_{bm}(t)\Psi_m(\xi) &= L_2(\mathbf{r}_w(t)) \sum_{m=0}^{P} \gamma_{wm}(t)\Psi_m(\xi) + L_3 \sum_{m=0}^{P} \mathbf{V}_{\infty m}\Psi_m(\xi) \\
\sum_{m=0}^{P} \gamma_{wm}(t+1)\Psi_m(\xi) &= L_4 \sum_{m=0}^{P} \gamma_{wm}(t)\Psi_m(\xi) + L_5(\mathbf{r}_w(t)) \sum_{m=0}^{P} \gamma_{bm}(t)\Psi_m(\xi), \\
\mathbf{r}_w(t+1) &= L_6(\mathbf{r}_w(t)) \sum_{m=0}^{P} \gamma_{wm}\Psi_m(\xi) + L_7(\mathbf{r}_w(t)) \sum_{m=0}^{P} \gamma_{bm}\Psi_m(\xi) \\
&\quad + L_8 \sum_{m=0}^{P} \mathbf{V}_{\infty m}\Psi_m(\xi).
\end{aligned} \tag{3.31}$$

Based on the orthogonality of the basis functions (Hermite polynomials), projecting Equation

(3.31) onto $\{\Psi_l(\xi)\}$ yields the stochastic version of the UVLM governing equations

$$\begin{aligned} L_1\gamma_{bl}(t) &= L_2(\mathbf{r}_w(t))\gamma_{wl}(t) + L_3\mathbf{V}_{\infty l}(t), \quad (l = 0, 1, ..., P), \\ \gamma_{wl}(t+1) &= L_4\gamma_{wl}(t) + L_5(\mathbf{r}_w(t))\gamma_{bl}(t), \quad (l = 0, 1, ..., P), \text{ and} \\ \mathbf{r}_w(t+1) &= L_6(\mathbf{r}_w(t))\gamma_{w0}(t) + L_7(\mathbf{r}_w(t))\gamma_{b0}(t) + L_8\mathbf{V}_{\infty 0}(t). \end{aligned} \tag{3.32}$$

The above system of $(2P + 3)$ equations is solved at each time step for the PCE coefficients γ_{bl} and γ_{wl}. The inputs are the PCE coefficients of the freestream flow speed $\mathbf{V}_{\infty m}(t) = [u_{\infty m}(t) = V_\infty + u_m(t), v_{\infty m}(t)]^T$ and the initial conditions at $t = 0$ that are $\gamma_w(0) = 0$ and $\mathbf{r}_w(0) = 0$ because no wake vortices exist yet. Note that, at each time step, a new vortex is shed from the airfoil's trailing edge, as in the deterministic UVLM.

3.4 Results and Discussion

3.4.1 Global sensitivity analysis

Considering the unsteady lift coefficient, $C_L(t, \xi)$ as a stochastic quantity, it is approximated by a truncated polynomial expansion of the form

$$C_L(t, \Xi) = \sum_{m=0}^{P} c_{l_m}(t)\Psi_m(\Xi). \tag{3.33}$$

Substituting Equation. (3.30a) and (3.33) into Equation (3.24), projecting the resulting equations onto $\Psi_m(\xi)$, one obtains the PCE coefficients of $C_L(t, \xi)$ given by the following:

$$c_{l_m}(t) = \sum_{i=1}^{N} \Big[2\cos(\alpha)\frac{(\gamma_{bm})_i(t)}{(\Delta l)_i} + \frac{2}{V_\infty^2 \Delta t}\Big(\sum_{j=1}^{i}(\gamma_{bm})_j(t) - \sum_{j=1}^{i}(\gamma_{bm})_j(t - \Delta t)\Big)\Big]\Delta l\cos(\alpha) \tag{3.34}$$

The computation of the PCE coefficients presents several advantages over performing a statistical analysis of the output data. In particular, the first-order terms in these coefficients provide a measure of the sensitivity of the stochastic process to each of the uncertain parameters. Figure 3.3 depicts the time histories of the zero-order polynomial chaos coefficient c_{l_0} and the first-order coefficients c_{l_1} through c_{l_4}. The zeroth-order term is the estimated ensemble mean value of the stochastic process, $C_L(t, \xi)$. The first order terms are the estimated

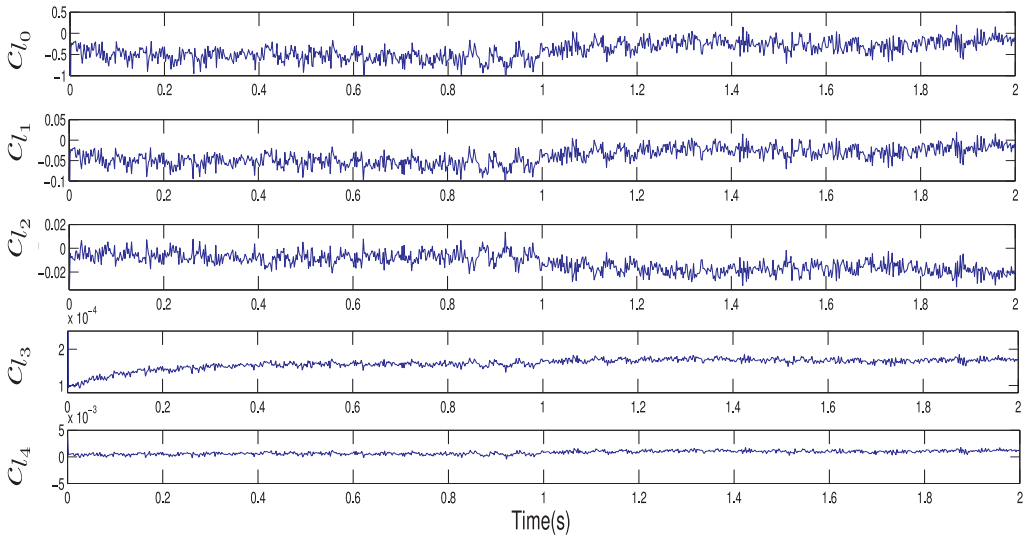

Figure 3.3: Time histories of the zeroth-order polynomial chaos coefficient, c_{l_0}, and the first-order coefficients, c_{l_1} through c_{l_4}, for the lift coefficient due to atmospheric turbulence.

linear coefficients for $\Psi_1 = \xi_1$ through $\Psi_4 = \xi_4$, which correspond to σ_v, L_v, σ_u and L_u, respectively. The relative importance of the linear dependence of the response on ξ_1 through ξ_4 can be inferred from relative magnitudes of these coefficients. Obviously, the magnitudes of c_{l_2}, c_{l_3}, and c_{l_4} are much smaller than that of c_{l_1}. This indicates that the $C_L(t)$ fluctuations are most sensitive to imprecision in the intensity of the vertical turbulence component σ_v. Then, in order of importance, the next is the imprecision in L_v which is the integral length scale of the vertical turbulence.

3.4.2 Validation

The sensitivity to each of the four random parameters can also be determined from the response at a given time as a function of each Ξ component. To this end, 200 realizations of lift coefficients were generated using the same uncertain spectral parameters of the generated flow field in the intrusive formulation. Variations of the lift coefficient with different ξ_i at t=1.0 s are plotted in Figure 3.4. The upper plots (I) present variations obtained from the 200 LHS realizations. The lower plots (II) and (III) show variations obtained from the

first-order and second-order intrusive PCE formulations, respectively. A linear regression analysis of the data in (I) plots is performed to determine the effectiveness of the intrusive PCE in measuring the first-order sensitivity to assumed randomness in the gust model's parameters. A comparison between the slopes obtained from the regression analysis and the corresponding PCE coefficient at $t = 1s$ is presented in Table 3.2. This comparison shows that the 1^{st}-order intrusive PCE produces coefficients that accurately represent the first-order sensitivity of the lift coefficient to imprecision in gust spectra. The 2^{nd}-order intrusive PCE produces coefficients that are relatively less accurate than their first order counterparts. Clearly, only linear expansion terms are required in the PC expansion and the inclusion of the nonlinear or cross-terms in the expansion leads to small errors in the estimated lift coefficient. Furthermore, the higher slope of C_L vs. ξ_{σ_v} is consistent with the expectation that the variations in the lift coefficient are linearly related to variations in the fluctuations of the vertical turbulence component.

Table 3.2: Comparison between the slope obtained from the regression analysis and the corresponding PCE coefficient at $t = 1.0s$. The 95% confidence intervals for the slopes are calculated for Monte Carlo simulations using the Bootstrap method.

	MC	1^{st}-order PCE	2^{nd}-order PCE	95% Conf. Interval
C_L vs. ξ_{σ_v}	-0.0427	-0.0425	-0.0467	$[-0.0428, -0.0427]$
C_L vs. ξ_{L_v}	-0.0121	-0.0120	-0.0130	$[-0.0121, -0.0118]$
C_L vs. ξ_{σ_u}	1.66×10^{-4}	1.65×10^{-4}	2.70×10^{-4}	$[0.612 \times 10^{-4}, 3.485 \times 10^{-4}]$
C_L vs. ξ_{L_u}	7.96×10^{-4}	7.91×10^{-4}	3.28×10^{-3}	$[7 \times 10^{-4}, 11 \times 10^{-4}]$

To analyze the statistics of the MC and intrusive PC methods quantitatively, the stochastic aerodynamic lift at four times ($t = 0.5$, 1, 1.5 and $2s$) are considered. Figure 3.5 shows empirical density functions of the lift coefficient at these times. The density functions are computed from 200 realizations based on both the original time histories (from the deterministic model) and those determined from the 1^{st} and 2^{nd}-order intrusive PCE. The results show an excellent match between the data obtained from the MC and 1^{st}-order PCE. The

PDF of the aerodynamic lift is nearly Gaussian when obtained from the MC and 1^{st}-order PCE but non-Gaussian and slightly skewed to the right when the 2^{nd}-order PCE terms are included.

The mean and standard deviation values of the stochastic aerodynamic lift obtained from the MC simulations combined with LHS as well as the intrusive PC methods are presented in Table 3.3. For the second-order PCE, the mean and standard deviations values are slightly different from those obtained with MC simulations, whereas, the first-order accurately yield the statistics of the stochastic aerodynamic lift. The results show that including quadratic terms in the PCE expansion cause errors in the estimation of the bound and wake vorticity circulation. In fact, the intrusive PCE is exact in an analytical sense, but the use of a non-intrusive PCE for $\mathbf{V}_\infty$ causes statistical estimation errors that corrupt the 2^{nd}-order terms and presumably the higher-order terms.

Table 3.3: The mean and standard deviation of the lift coefficient C_L obtained with intrusive PCE and MC combined with LHS.

		MC	1^{st}-order PCE	2^{nd}-order PCE
$t = 0.5s$	Mean	-0.620	-0.620	-0.621
	StD	0.062	0.0616	0.0765
$t = 1s$	Mean	-0.429	-0.429	-0.430
	StD	0.0444	0.0441	0.0552
$t = 1.5s$	Mean	-0.357	-0.357	-0.358
	StD	0.0383	0.038	0.0477
$t = 2s$	Mean	-0.215	-0.215	-0.216
	StD	0.0283	0.0280	0.0351

3.5 Summary

In this chapter, the intrusive polynomial chaos approach was implemented to determine uncertainty in gust loads on a rigid airfoil due to imprecision in an incoming gust characteristics.

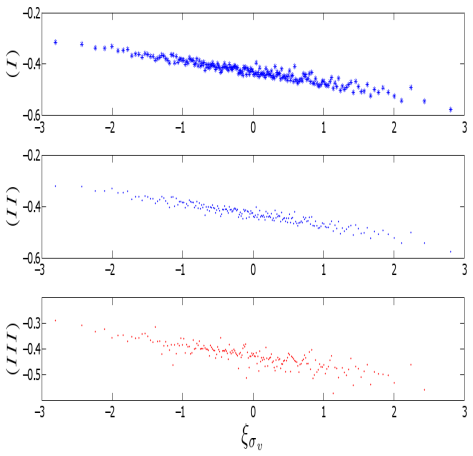

(a) $C_L(t = 1s, \xi) vs. \xi_{\sigma_v}$

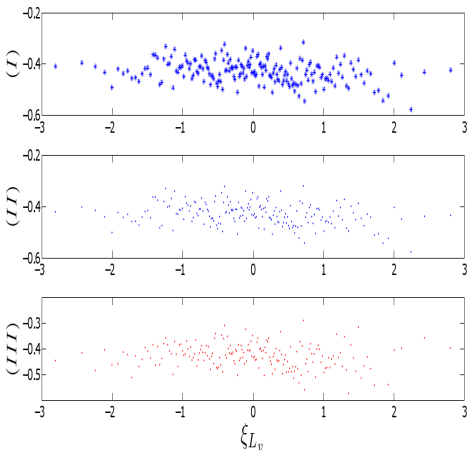

(b) $C_L(t = 1s, \xi) vs. \xi_{L_v}$

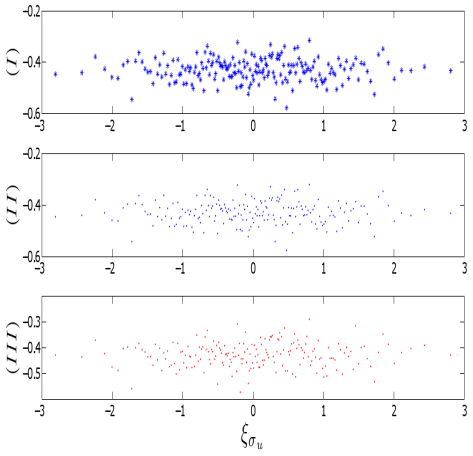

(c) $C_L(t = 1s, \xi) vs. \xi_{\sigma_u}$

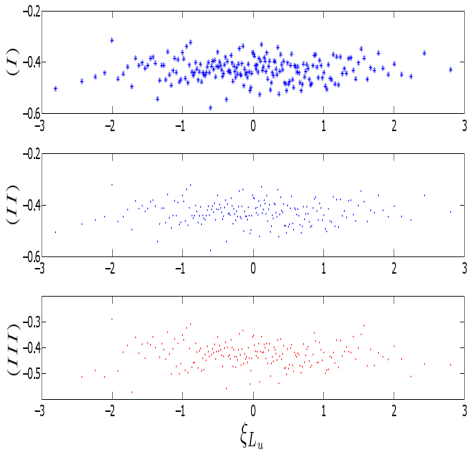

(d) $C_L(t = 1s, \xi) vs. \xi_{L_v}$

Figure 3.4: Lift coefficient at $t = 1s$ versus ξ_i. (I) depicts the original data, (II) and (III) show the same data simulated by the 1^{st}-order and 2^{nd}-order PCE, respectively. The results are plotted separately for ease of comparison.

The results yield the sensitivity of the lift coefficient, $C_L(t)$, to variations in the intensities and integral length scales of the gust fluctuations. Lift coefficient fluctuations about the mean at each time step were affected primarily by the intensity of the vertical fluctuations σ_v, which should be expected for an airfoil fixed at zero angle of attack. Second in order of importance was the integral length scale of the vertical velocity component, L_v. As might be expected, $C_L(t)$ was relatively insensitive to the streamwise gust parameters. Consequently, if the flow model and parameter ranges employed here are appropriate of the intended application, a stochastic analysis of the effects of gust on the lift coefficient of an airfoil would be satisfactory if the streamwise gusts were neglected. More generally, the analysis presented here provides a basis for exploring these and other parametric effects in a broad range of gust loads analyses. This successful implementation of the intrusive PCE provides guidance and a baseline for efforts to quantify uncertain gust loads on micro air vehicles (MAV) with higher fidelity models.

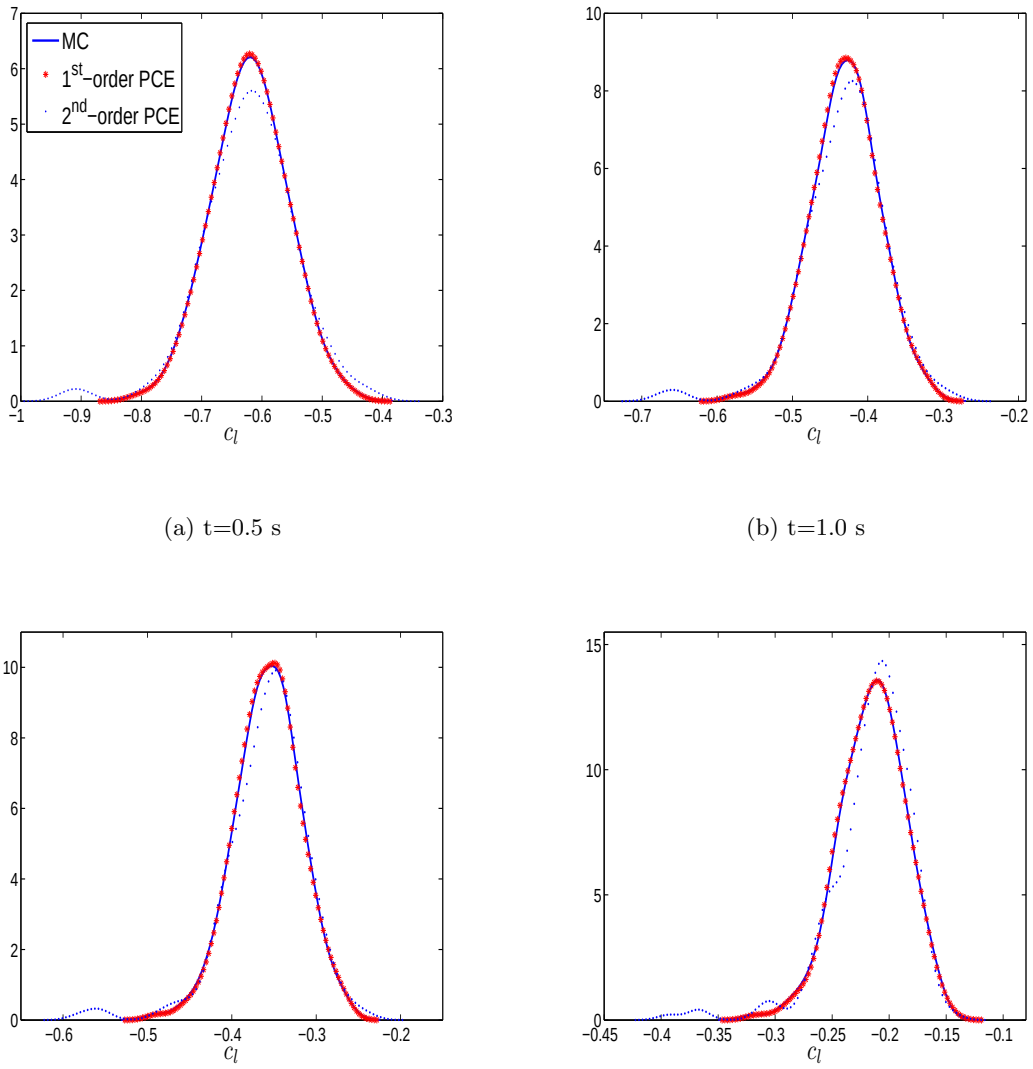

(a) t=0.5 s

(b) t=1.0 s

(c) t=1.5 s

(d) t=2.0 s

Figure 3.5: Empirical density functions for C_L at t=0.5, 1.0, 1.5 and 2.0 s. The solid blue lines is the estimated density function from the original time histories. The dashed red and blue line represent the estimated density function from the 1^{st}-order and 2^{nd}-order PCE, respectively.

Chapter 4

Optimization of Flapping Kinematics in Hovering Flights

In this chapter, an efficient search for optimal configurations of the kinematics of a flapping wing that minimize the aerodynamic power under lift constraint is performed. The flapping wing is chosen so that its chord length and flapping frequency match the morphological and flight properties of insects with different masses. The aerodynamic model is based on the unsteady vortex lattice method (UVLM). Unlike direct numerical simulation (DNS) methods that are very expensive in terms of computational resources, UVLM presents a good compromise between computational cost and fidelity. This aerodynamic tool is then combined with a hybrid of global and local optimization algorithms to perform a global search of stroke paths and avoid being trapped at local minimum points.

4.1 Aerodynamic Modeling of Hovering Flights

4.1.1 2-d unsteady vortex lattice method

In this analysis, the unsteady flow around a flat-plate airfoil is modeled using a two-dimensional unsteady vortex lattice method. This method has been used extensively to determine aerodynamic loads and aeroelastic responses (27; 100; 101).

In UVLM, it is assumed that the flow field is inviscid everywhere except in the boundary

layers and the wake. A set of discrete vortices are placed on the plate to represent a viscous shear (boundary) layer in the limit of infinite Reynolds number. The position of, and circulation around the vortices in the wake, and the circulations around the vortices on the plate are unknowns. The velocity field associated with these vortices is calculated according to Biot-Savart law. The plate is divided into a number of piecewise straight line segments or panels. In each panel, a point vortex is placed at the one-quarter chord position, and the no-penetration condition is imposed at the three-quarter chord position, called the control point. Figure 4.1 shows a schematic of the flat plate with panels, each of them having a concentrated vortex located at $xv(i)$, and a control point located at $xc(i)$. As shown in Figure 4.1 two coordinate systems are introduced to describe the motion of the plate: an inertial reference frame (X, Y) and a body-fixed frame (x, y). The body is assumed to translate along two directions and rotate about a pitch point E.

The vorticity is introduced into the wake by shedding point vortices from the trailing edge. To render the wake force-free, these vortices are moved with the fluid particle velocity and their individual circulations remain constant. These vortices influence the flowfield around the flat plate. Because they were generated previously in the motion, the flow around, and hence the aerodynamic loads on the plate, depend on the history of the motion, unlike the blade-element model which makes use of the quasisteady aerodynamics. The aerodynamic loads are computed by integrating the pressure difference, determined from the unsteady Bernoulli equation, over the whole plate surface. More details on the implementation of UVLM can be found in Section 3.2.

To test the capability of the aerodynamic tool, the cases of unsteady flows past plunging and pitching airfoils in uniform stream are considered and the results are compared with those obtained from previous works based on UVLM and two-dimensional Navier-Stokes simulations. Similar to Liang et al. (107), the airfoil plunge motion is prescribed as $Y(t) = h \cdot c \sin(2\pi f)$ where c is the chord length, h is the nondimensional plunge amplitude, and f is the frequency. The Strouhal number $Sr = 2\pi f hc/U_\infty$, where U_∞ is the freestream velocity, determines the degree of unsteadiness of the plunging motion. h and Sr are set equal to 0.12 and 1.5, respectively, and show in Figure 4.2(a) a comparison of the lift coefficient predicted from the current model, numerical simulations based on UVLM by Nuhait and Zedan (108),

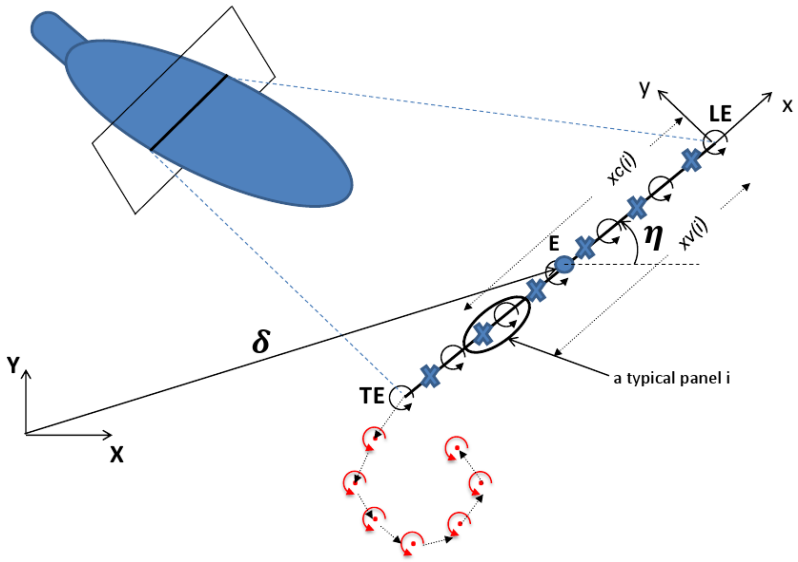

Figure 4.1: Representation of a model of a flat plate with panels, each one with a concentrated vortex located at $xv(i)$, and a control point located at $xc(i)$. Wake vortices are shown in red.

and that obtained by Liang et al. (107) using a high-order spectral difference method. Note that the numerical computations by Liang et al. (107) are performed on an airfoil at Re=1850. Both results agree fairly well. There is a small difference in the lift coefficient. The discrepancy between the two sets of data is most likely due to viscous effects (107) and airfoil thickness which have not been accounted for in this formulation of the UVLM model.

The position of the shed vorticity behind the plunging airfoil as obtained from the current UVLM and from Navier-Stokes simulations by Liang et al. [1] (107) is plotted in Figure 4.3(a). Similar vortical structures can be observed. Both plots show a deflected wake where counterrotating vortices (vortex strength is represented by different colors) are convected at an angle with respect to the freestream direction. In Figure 4.3(b), the position of the shed vorticity behind a pitching airfoil with an amplitude of 2° and a reduced frequency of $k = \pi f c/U_\infty = 6.68$ is plotted. The airfoil pitches about the quarter chord. Clearly, UVLM predicts well the main flow features behind the pitching airfoil.

[1] Reprinted with permission from Computers and Fluids. Copyright ©2010, Elsevier.

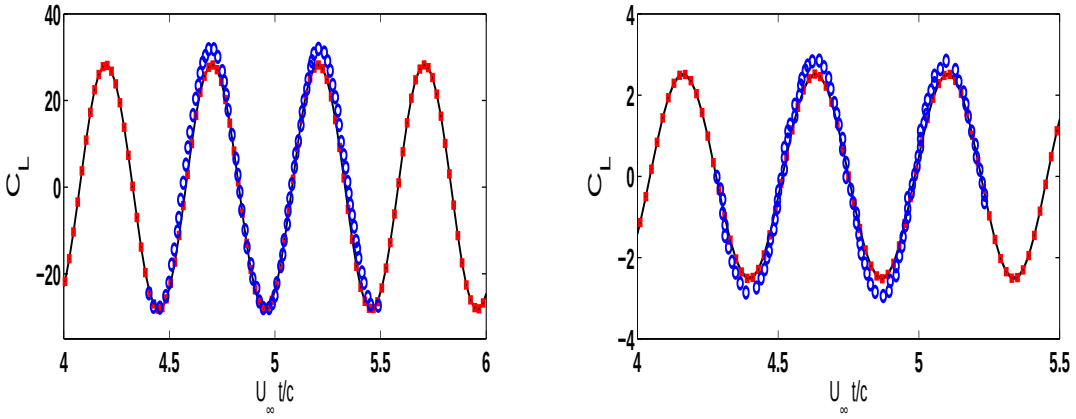

(a) (b)

Figure 4.2: Variations of the lift coefficient for (a) plunging and (b) pitching airfoils in a uniform stream. Comparison of current results -solid line with numerical results of Liang et al. (107) (N-S solver) -blue circles and Nuhait and Zedan 1993 (108) (UVLM) -red rectangles.

4.1.2 Flapping wing kinematics

Through a cycle, the motion of the flapping wing can be defined by a combination of translations and angular oscillations. In this work, the flapping motion is based on trigonometric functions given by (109):

$$\begin{aligned} \delta_x(t) &= A_x \sin(2\pi f t), \\ \delta_y(t) &= A_y \sin(2\pi f t + \psi_y), \\ \eta(t) &= A_\eta \frac{\tan^{-1}[\kappa \sin(2\pi f t + \psi_\eta)]}{\tan^{-1}(\kappa)} + \frac{\pi}{2}. \end{aligned} \tag{4.1}$$

This form of the trigonometric functions was obtained by fitting kinematic data determined from empirical studies performed on insects (110; 111). The translation motion consists of two half-strokes: the downstroke and the upstroke. At the end of each half-stroke, the rotational motion causes the plate to change its direction for the subsequent half-stroke. The stroke pattern involves seven control parameters: three amplitudes, one frequency, two phase angles, and one sharpness parameter. In the present study, the frequency will be assigned values of

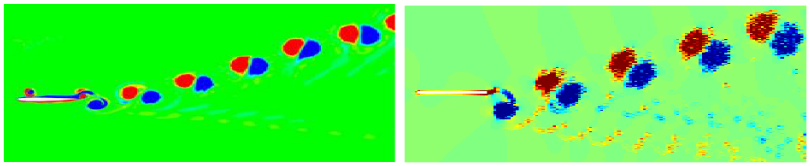

(a) Plunging airfoil ($h = 0.12 \cdot c$ and $Sr = 1.5$)

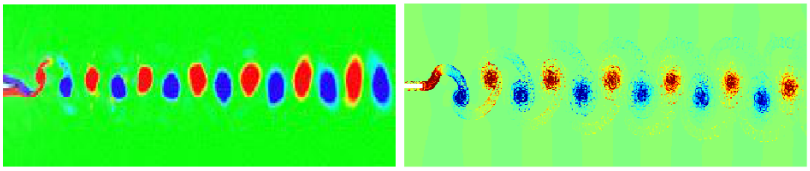

(b) Pitching airfoil ($A = 2^\circ$ and $k = 6.68$)

Figure 4.3: Vortical patterns for (a) plunging and (b) pitching airfoils in a uniform stream: (left plot) wake pattern obtained by Liang et al. (107), (right plot) wake pattern obtained from current UVLM.

26.1 Hz (hawkmoth) and 116 Hz (bumblebee); these frequencies were given in (14). The angle ψ_η specifies the timing of the rotation relative to the x-translation. For synchronized rotation (i.e. $\psi_\eta = 0^\circ$), the rotation occurs at the end of the x-translation cycle while setting ψ_η equal to a nonzero value causes the rotation to initiate either before or after the translation changes direction. The parameter κ represents the flipping of the plate between positive and negative inclinations at the ends of the flapping cycle. Larger values of κ provide a more sudden snap-like rotation.

Figure 4.4 shows the vorticity contours that develop with a flapping wing. This plot was generated by computing the velocity components at each of the grid points in the green shaded rectangular region. Along the two phases of the stroke, strong vortical structures of opposite signs form and drift vertically downward. This entrains the fluid between them which produces a downward jet flow that is responsible for lift.

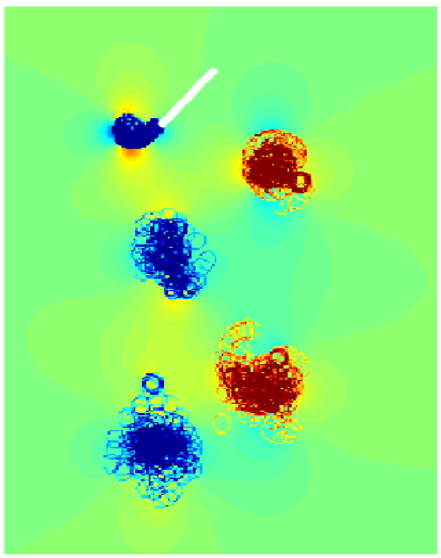

Figure 4.4: Vorticity contours over a flapping wing as computed with UVLM.

4.2 Kinematics Optimization

One important issue to be addressed is the identification of the optimal flapping wing kinematics to meet some aerodynamic performance specifications. In this study, a flapping airfoil in hover flight is considered and its chord length and flapping frequency are selected to match the morphological and flight properties of the hawkmoth and bumblebee as shown in Table 4.1. The two flying animals, whose masses and flapping frequencies vary by approximately two orders of magnitude, are chosen to analyze the effect of unsteady flow upon the flapping kinematics. Next, the aerodynamic tool (UVLM) is combined with global and local optimization algorithms to determine an optimal configuration that minimizes the required power to satisfy the lift constraint.

4.2.1 Problem formulation

One goal in MAV design is to use the minimum power to generate enough lift to support the weight and overcome harsh environmental conditions. To this end, the kinematic optimization problem subject to bound constraints that can be formulated as

Table 4.1: Morphological and kinematic parameters used for the analysis (5; 14).

	Mean chord length c_m (mm)	Aspect ratio AR	Mass M (g)	Flapping frequency f (Hz)
Hawkmoth	18.3	5.3	1.6	26.1
Bumblebee	4	6	0.175	116

$$\begin{aligned} &\text{Minimize} \quad \overline{P}(v), \\ \text{subject to} \quad & \\ &\overline{L}(v)/Mg = \overline{L}^*(v) \geq 1 \\ &v \in D, \end{aligned}$$

is solved. Here $P(v)$ is the aerodynamic power defined by the product of the pressure difference and the normal component of the velocity integrated over the wing surface and $L(v)$ is the lift force. M is the body's mass and g is the gravitational constant. The overline denotes a time-averaged quantity and v is the vector of control parameters consisting of amplitudes, phase angles, and sharpness parameter of the flapping motion, $D = \{v \in R^n \mid l \leq v \leq u\}$ is an n-dimensional bounding box as will be defined next. For the sake of simplicity, the lift and aerodynamic power predicted from the 2-D UVLM are multiplied by the span length corresponding to the wing of each of the mentioned insects.

To implement the lift constraint when performing the global search by VTDIRECT95 as will be discussed later, a penalty function approach is followed. The optimization problem is then rewritten as

$$\begin{aligned} &\text{Minimize} \quad \left[\overline{P} + \alpha\,(\overline{L}^* - 1)_-\right], \\ \text{subject to} \quad & \\ &v \in D, \end{aligned}$$

where α is a penalty parameter and set to 1000, and

$$X_- = \begin{cases} -X, & X < 0 \\ 0, & X \geq 0 \end{cases}$$

An alternative approach that avoids the use of penalty parameters is to simply set the aerodynamic power $\overline{P}$ equal to a high value whenever the constraint is violated.

The optimization procedure is based on a hybrid of two optimization algorithms: DIRECT and GCMMA. DIRECT (112–114) is a deterministic direct search global algorithm that does not require any knowledge of the objective function gradient. It uses information obtained from sampled points in the domain to decide where to search. In one iteration, DIRECT selects and subdivides subregions (boxes) of the feasible design space that are most likely to contain the global optimum point. Figure 4.5 shows the boxes produced and points sampled by DIRECT (as implemented in the Fortran 95 package VTDIRECT95) for a generic two-parameter problem over a square design space. DIRECT does not do a naive exhaustive search, but nevertheless finding a globally optimum point requires exploring every portion of D, and in high dimensions which can be very expensive.

GCMMA (115; 116) is a globally convergent (to a stationary point, not necessarily a global solution) method of moving asymptotes. It is a gradient-based method and employs conservative convex separable approximations for solving inequality constrained nonlinear programming problems (*minimization* problems with *less than* or *equal to* constraints). It searches by generating approximate subproblems at each iteration, in which both the objective and constraint functions are replaced by convex functions. The construction of these approximating functions is based mainly on gradient information at the current iteration point in the design space. GCMMA is a variant of the well-known sequential approximate optimization (SAO) widely used in aerospace engineering, and the standard sequential quadratic programming using in mathematical programming.

To carry out the optimization, a global search is first performed by VTDIRECT95 until one of the stopping conditions is reached. These conditions are a limit on the number of iterations and function evaluations and a minimum value for the change in the objective function. Then, a local search with GCMMA, using the best point found by VTDIRECT95 as a starting point, is carried out to accelerate the convergence to the optimal points.

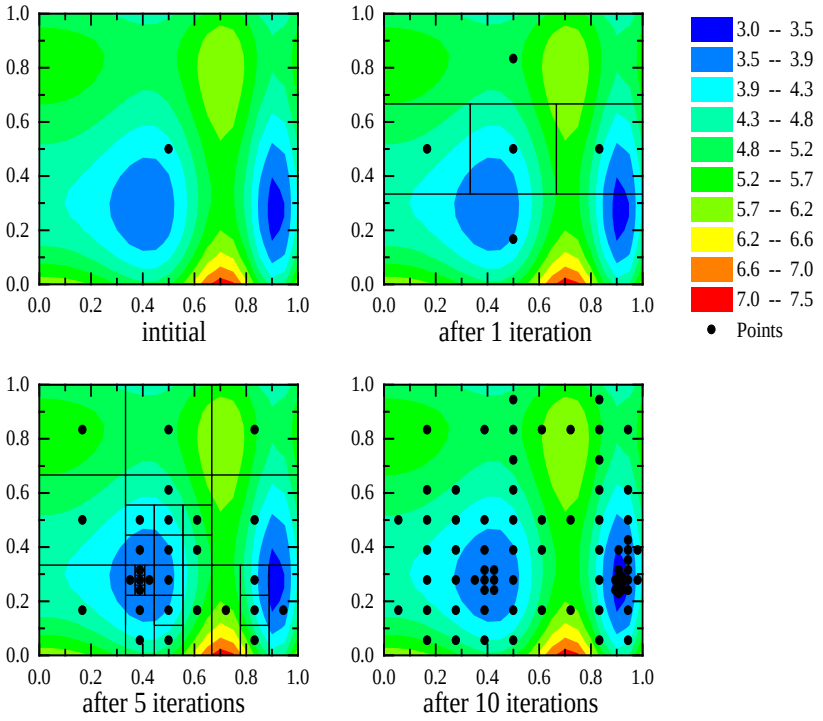

Figure 4.5: Boxes produced and points sampled by the code VTdirect (serial subroutine from VTDIRECT95) for a two-dimensional problem over a square design space.

4.2.2 Results and discussion

The variations of six parameters for the flapping-wing kinematics, namely A_x, A_y, A_η, ψ_y, ψ_η, and κ, are considered(the frequency f was assigned values as given in (14)). The upper and lower bounds are presented in Table 4.2.

Results for the kinematics, dimensionless lift force $\overline{L}^*$, and aerodynamic power for wings simulating the hawkmoth and bumblebee are given in Table 4.3. For both cases, the required power is strongly influenced by the selection of the parameters, especially, the phases and sharpness. Imposing a delay between the different oscillatory motions by appropriately specifying their phase angles and controlling the way through which the wing rotates at the end of each half stroke by varying the sharpness parameter κ minimize the required power to produce the desired aerodynamic forces. As expected, for all optimal cases the needed lift force

Table 4.2: Control variables constraints.

Parameter	Lower bound	Upper bound
A_x	$0 \cdot c$	$2 \cdot c$
A_y	$0 \cdot c$	$1 \cdot c$
A_η	20°	60°
ψ_y	-180°	180°
ψ_η	-180°	180°
κ	1	4

to support the mass of the insect is produced exactly. In fact, additional lift generation would require an increase in aerodynamic power, and so the lift constraint is always expected to be active. The orders of aerodynamic power in relation to the hover frequency as determined from the current optimizations are consistent with those predicted by Berman and Wang (14). In comparison to the 37.56 mW and 5.45 mW optimal aerodynamic powers for the hawkmoth and bumblebee, respectively, obtained in this work, Berman and Wang (14) found respective powers of 25.04 mW and 2.37 mW. To determine the effect of the wing shape on the generation of aerodynamic power, the following analysis is performed. The normal force applied on an infinitesimal slice of the wing is written as:

$$N(r) = \frac{1}{2}\rho V^2(r)c(r)C_N(\alpha)dr \tag{4.2}$$

where ρ is the fluid density, $c(r)$ is the chord length of the slice located at a distance r of away from the wing root, α is the angle of attack, V is the velocity of the wing, and C_n is the normal force coefficient. The aerodynamic power is given by

$$P(r) = N(r)V(r) \tag{4.3}$$

In hover flight, the velocity V is equal $r\dot{\phi}$. Here, ϕ is the stroke angle as will be defined in terms the x-translation below. Substituting Equation (4.2) into Equation (4.3) yields

$$P(r) = \frac{1}{2}\rho r^3 c(r)\dot{\phi}^3 C_N(\alpha)dr \tag{4.4}$$

Therefore,

$$P(r) \propto r^3 c(r) \tag{4.5}$$

For the elliptical wing, the chord length is assumed to vary like half-ellipse along the wing radius (14) i.e.

$$c(r) = \frac{4\overline{c}}{\pi}\sqrt{1 - \frac{r^2}{R^2}} \tag{4.6}$$

where $\overline{c}$ is the average chord length and R is the wing root to tip radius. For the rectangular wing, $c(r) = \overline{c}$. The wing shapes used in the present analysis and by Berman and Wang (14) are shown in Figure 4.6.

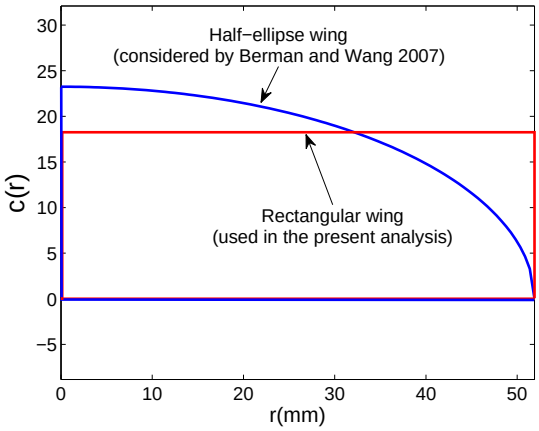

Figure 4.6: Elliptical vs. rectangular wing.

The location on the elliptical wing corresponding to $\overline{c}$ is given by $\overline{r} = R\frac{\sqrt{16-\pi^2}}{4}$. Assuming a rigid wing, that is ϕ and α are constant along the wing span, denoting by $\overline{P}$ the power per unit length computed at $\overline{r}$ and for a chord length $\overline{c}$, and using Equation (4.5) one can write

$$P(r) = \overline{P}\,\frac{r^3 c(r)}{\overline{r}^3 \overline{c}} \tag{4.7}$$

Considering a half-ellipse wing; that is

$$P_{ell} = 2\int_0^R \overline{P}\frac{r^3 c(r)}{\overline{r}^3 \overline{c}}\,dr \tag{4.8}$$

and using Equation (4.6), one obtains

$$\begin{aligned} P_{ell} &= \frac{2\overline{P}}{\overline{c}\frac{R^3}{64}(16-\pi^2)^{3/2}}\Big(\frac{2R^4}{15}\Big)\frac{4\overline{c}}{\pi} \\ &= \frac{512}{15\pi(16-\pi^2)^{3/2}}\,2R\overline{P} \end{aligned} \tag{4.9}$$

In terms of $\overline{P}$, the aerodynamic power for a rectangular wing is written as

$$P_{rect} = 2R\overline{P} \tag{4.10}$$

Using Equations (4.11) and (4.10), one obtains

$$P_{ell} = \frac{512}{15\pi(16-\pi^2)^{3/2}}\,P_{rect} = 0.715\,P_{rect} \tag{4.11}$$

Clearly, the aerodynamic power required to move a half-ellipse wing is about 71% of the power required to move a rectangular wing of the same area. As such, implementing the optimized kinematics on an elliptical wing instead of a rectangular wing will reduce the aerodynamic power from 37.56 mW and 5.45 mW to 26.86 mW and 3.9 mW for the hawkmoth and bumblebee, respectively. These values are close to the ones reported by Berman and Wang (14).

Table 4.3: Kinematics, dimensionless lift force $\overline{L}^*$, and aerodynamic power for optimized wing motions of the hawkmoth and bumblebee.

	A_x	A_y	A_η	ψ_y	ψ_η	κ	$\overline{L}^*$	P_{rect} (mW)	P_{ell} (mW)
Hawkmoth	$0.9\cdot c$	$0\cdot c$	47.34°	0°	90.87°	2	1	37.56	26.86
Bumblebee	$1.64\cdot c$	$0.177\cdot c$	57.09°	65.10°	87.07°	3.49	1.005	5.45	3.9

Figures 4.7 (a) and (b) show the progress that the local optimizer GCMMA makes in minimizing the aerodynamic power when started from different points. In other applications (as will be shown in Chapter 5), it is found that the final optimal result was independent of the starting point, but this is not the case here. This indicates that the design space associated with the flapping kinematics in hovering flights is complex and contains many local

minimum points. It is interesting to note that these minimum points are more separated for the bumblebee case. Furthermore, convergence for the bumblebee case is not as rapid as that of the hawkmoth, indicating a more complicated design space. In Figures 4.7 (c) and (d), the lift convergence histories show that the lift constraint is active for all cases and emphasizes the fact that GCMMA may converge to a lift-feasible power local minimum point, which in general may be quite inefficient compared to other optimum points. For both optimization cases, initiating the local search using the design points predicted from the global optimizer VTDIRECT95 leads to points with the lowest required aerodynamic power and in addition uses far fewer function evaluations (the optimizer found a solution in approximately ten iterations for the hawkmoth case and forty iterations for the bumblebee case). The hybrid of the two optimization algorithms speeds up and improves the search for the optimal point. In fact, VTDIRECT95 can accurately home in on the global optimum point if small enough boxes are used, however, this typically requires a relatively long time. On the other hand, there is no guarantee that GCMMA will home in on the global optimum, but the present hybrid procedure efficiently finds the global optimum point in a relatively short time.

The flapping motions that correspond to the optimal kinematics are shown in Figure 4.8. In (a) and (b), the results are from the present analysis and in (c) and (d) from Berman and Wang [2] (14). For both cases, a figure-8 motion is observed. For the hawkmoth, the optimal wing motion is qualitatively similar to that obtained by Berman and Wang (14). Smoother transitions between the two midstrokes are obtained. This is due to the absence of the translational motion along the y-direction in the current optimal configuration. This aspect would be of benefit when designing the actuation mechanism of a flapping wing. For the bumblebee case, a dissimilarity between the two sets of data is observed. This dissimilarity can be explained by the inability of the quasisteady model by Berman and Wang (14) to capture the unsteady wake effects which are more pronounced for flapping motions at higher frequencies. Larger x-translation amplitude A_x and higher pitching angle η are obtained for the bumblebee as shown in Table 4.3. Furthermore, the motion in the y-direction is more heavily utilized when considering problems with higher frequency and smaller size (bumblebee

[2]Reprinted with permission from Journal of Fluid Mechanics. Copyright ©2007, Cambridge University Press.

case). Clearly, based on the level of the unsteadiness associated with the flapping motion, specific kinematics need to be employed to control the flight performance and make it as efficient as possible.

Next, the optimized kinematics for the hawkmoth are compared against those obtained numerically by Berman and Wang (14) and experimentally by Willmott and Ellington (9). To this end, the translations used in the 2-d configuration are expressed in terms of the azimuthal (or stroke) angle ϕ and the elevation or deviation angle (the angle related to vertical displacement) θ. As shown in Table 4.3, the optimal value of the amplitude of the vertical translation A_y was found equal to zero. In this case, $\theta = 0^\circ$ and $\delta_x = r\phi$ where r is the location of the typical section of the wing under study. Figure 4.9 shows a comparison between the optimized hawkmoth hovering kinematics as determined by the present analysis, those obtained by Berman and Wang (14), and the observed data from Willmott and Ellington (9). It is noted that the typical section (simulated with UVLM) is considered to be located one chord length away from the wing root (i.e., $r = c$). It is interesting to note that the current optimized kinematics of the angles ϕ and η match better with the observed kinematics than those of Berman and Wang (14). This result indicates that the leading-edge vortex (unaccounted for in the UVLM model) may not be critical for the hawkmoth flight. As for the θ motion, the current analysis did not yield a translation in the y-direction which translates to a zero value for θ. It should be noted here that adding a small y-translation to the optimized results did not improve the performance in terms of aerodynamic power. Furthermore, the elevation angle θ observed in the experiments by Willmott and Ellington (9) could be attributed to the flexibility of wing which can be large at the wing tip. The flexibility issue has been considered by McClung et al. (117) who simulated hover flight of the Hawkmoth and examined the effect of spanwise wing deformation on the generation of the aerodynamic loads. They showed that out-of-plane bending increases the lift by 5% in comparison with the rigid case. This indicates that insects may utilize some sort of deformation to improve their flight performance. An optimization analysis that accounts for the coupled aerodynamic and structural response would shed more light on this point.

As for the bumblebee, the optimized kinematics obtained here did not match the optimized kinematics of Berman and Wang (14). It is noted that Berman and Wang (14) account for

LEV to some degree by introducing some empirical corrections for the translational and rotational lift coefficients. The fact that the level of agreement of optimized kinematics that are obtained from UVLM and quasisteady approaches (that account for LEV) depends on the hovering frequency implies that the impact of LEV depends on the hover frequency. This argument will be the topic of a future research effort.

4.3 Sensitivity Analysis of Optimized Kinematics

To gain a better understanding of the reasons for which the obtained optimized kinematics produce power-efficient lift, the impact of varying each of the kinematics parameters is examined. This is performed by perturbing the design parameters around the optimized kinematics obtained for the hawkmoth. Figure 4.10 shows the variations of the dimensionless lift L^* and aerodynamic power P with each of the kinematics parameters (A_x, A_η, ψ_η, and κ) while keeping all others constant and equal to their optimized values. As shown in Figure 4.10 (a), increasing the amplitude of x-translation A_x (i.e., augmenting the stroke angle ϕ) yields higher lift and aerodynamic power. Thus, given the optimization's constraint ($L^* \geq 1$), the optimizer identified a design point with the amplitude that enables to produce exactly the lift needed to support the mass (i.e., hits the lower bound of the lift constraint). Figure 4.10 (b) shows that the lift increases slightly with the amplitude of the pitch angle A_η to achieve a maximum near a value of 41°. On the other hand, the aerodynamic power decreases monotonically when A_η is increased over a small range near the optimal value. Hence, the optimal value of A_η corresponds to the smallest power that meets the lift constraint. Figure 4.10 (c) shows that the phase angle ψ_η plays an important role in the lift generation. The lift is the largest (a value greater than 1) when $\psi_\eta = 98°$. Furthermore, larger values of ψ_η yield higher aerodynamic powers. Thus, the smallest phase angle ψ_η that meets the lift constraint is picked by the optimizer.

As for the sharpness parameter κ, Figure 4.10 (d) shows that increasing its amplitude results in more lift production, but also yields more sudden rotation which requires more aerodynamic power.

To gain insight into the physics associated with variations of the sharpness parameter κ,

the flow field around the flapping wing is generated and plotted in Figure 4.11 for varying values of κ. Setting κ equal to 1 (lower than $\kappa = \kappa_{opt} = 2$) gives much lower lift than the required one without significant enhancement in terms of aerodynamic power. This can be explained by the deflected jet as shown in Figure 4.11 (a) while the flow is drifted more or less vertically downward in the optimal configuration (Figure 4.11 (b)). For $\kappa = 3$, similar features in the flow field are observed (Figure 4.11 (c)).

Figure 4.12 shows the velocity of x-translation (upper frame), angular velocity (second frame), dimensionless lift (third frame), and aerodynamic power (lower frame) for one flapping cycle. Results are presented for two different values of the sharpness parameter $\kappa = 2$, and 3. Two peaks are observed in both of the transient variations of lift and power. A major peak corresponds to the translational effects (reached when the magnitude of the translation velocity is maximum) and a secondary peak is associated with the rotational effects (reached near the maximum of the magnitude of the angular velocity). The secondary power peak is drastically affected by κ. As such, increasing the value of κ yields higher power peak as shown in Figure 4.12 (b) and then resulting in an increase in the aerodynamic power as can be seen in Figure 4.10 (d). This is expected since increasing κ leads to higher angular acceleration for the wing and consequently for the surrounding fluid (non-circulatory or added mass effects) which would require additional amount of power to accelerate the surrounding fluid.

4.4 Summary

In this work, the kinematics of a flapping wing in hover flight are optimized by combining the unsteady vortex lattice method with a hybrid of global and local optimization algorithms that accelerates the convergence to the global optimum point. The objective is to minimize the required aerodynamic power to produce enough lift to sustain hovering flight. The flapping wing is chosen so that its chord length and flapping frequency match the morphological and flight properties of insects with different masses. The analysis identified optimal kinematics that agree fairly well with the observed data, as well as previously published numerical results. Furthermore, two levels of unsteadiness associated with the flapping motion are considered to show that specific kinematics need to be employed to control the flight performance and

make it as efficient as possible. Finally, a sensitivity analysis is performed to gain a better understanding of the reasons for which the obtained optimized kinematics produce power-efficient lift.

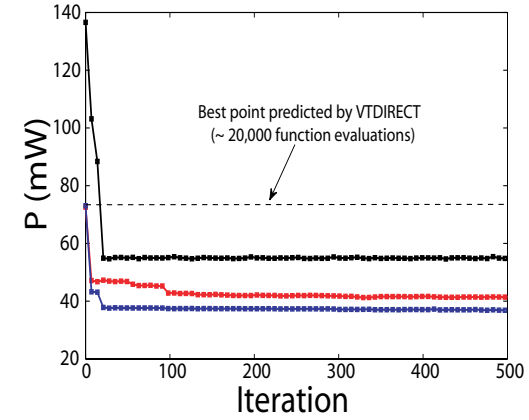

(a) Hawkmoth

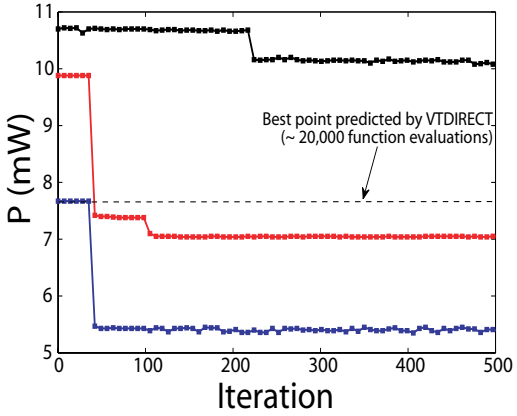

(b) Bumblebee

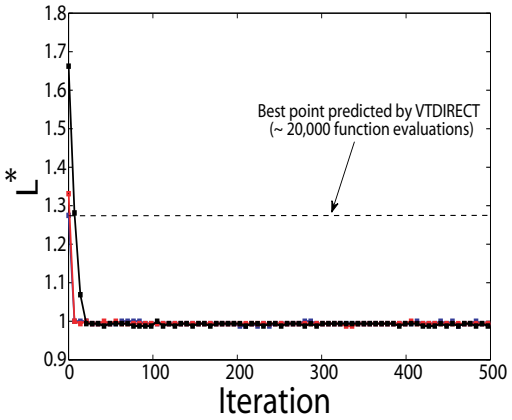

(c) Hawkmoth

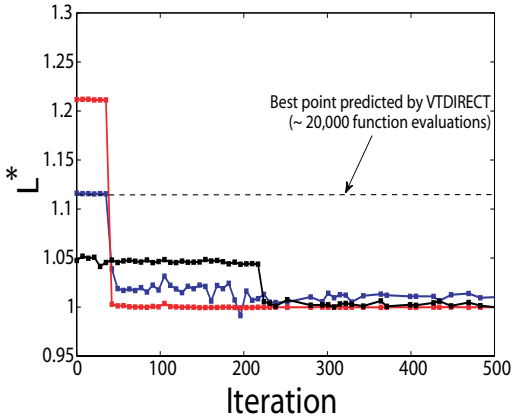

(d) Bumblebee

Figure 4.7: The aerodynamic power (upper plots) and normalized lift (lower plots) values at the best point found versus the number of evaluations for GCMMA using different initial conditions.

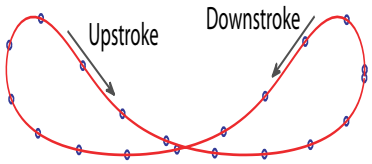

(a) Hawkmoth

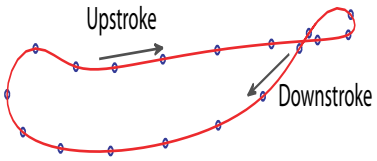

(b) Bumblebee

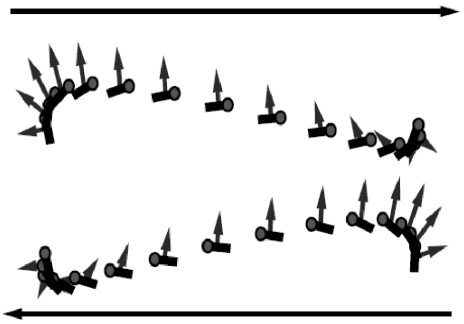

(c) Hawkmoth

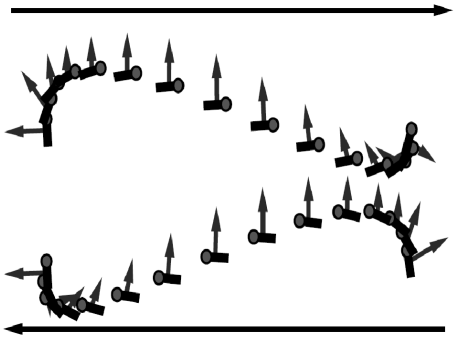

(d) Bumblebee

Figure 4.8: Optimal motions predicted from the present analysis (upper plots) and by Berman and Wang (14) (lower plots) for the hawkmoth and bumblebee cases. Circles represent the wing's leading edge. The arrows are introduced to show the sequence of the flapping motion and differentiate between the two midstrokes.

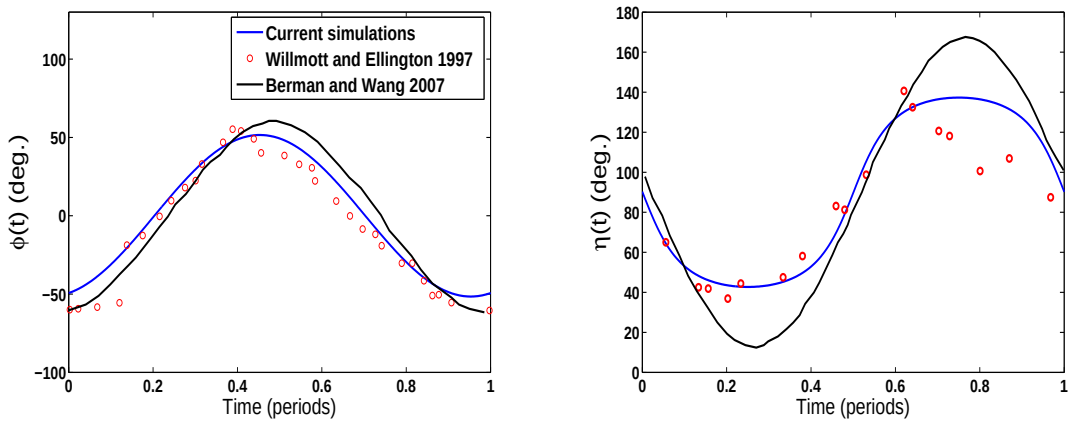

(a) Azimuthal angle ϕ

(b) Pitching angle η

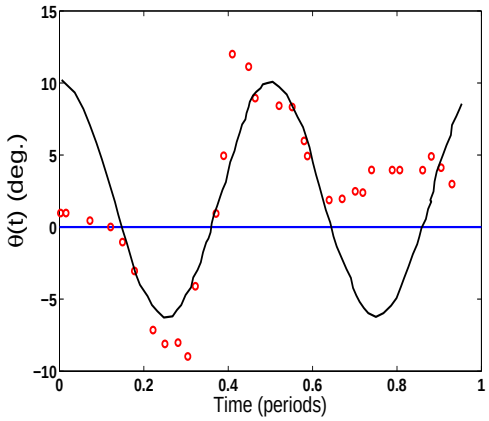

(c) Elevation angle θ

Figure 4.9: Optimized hawkmoth hovering kinematics: Comparison with Berman and Wang (14) and Willmott and Ellington (9).

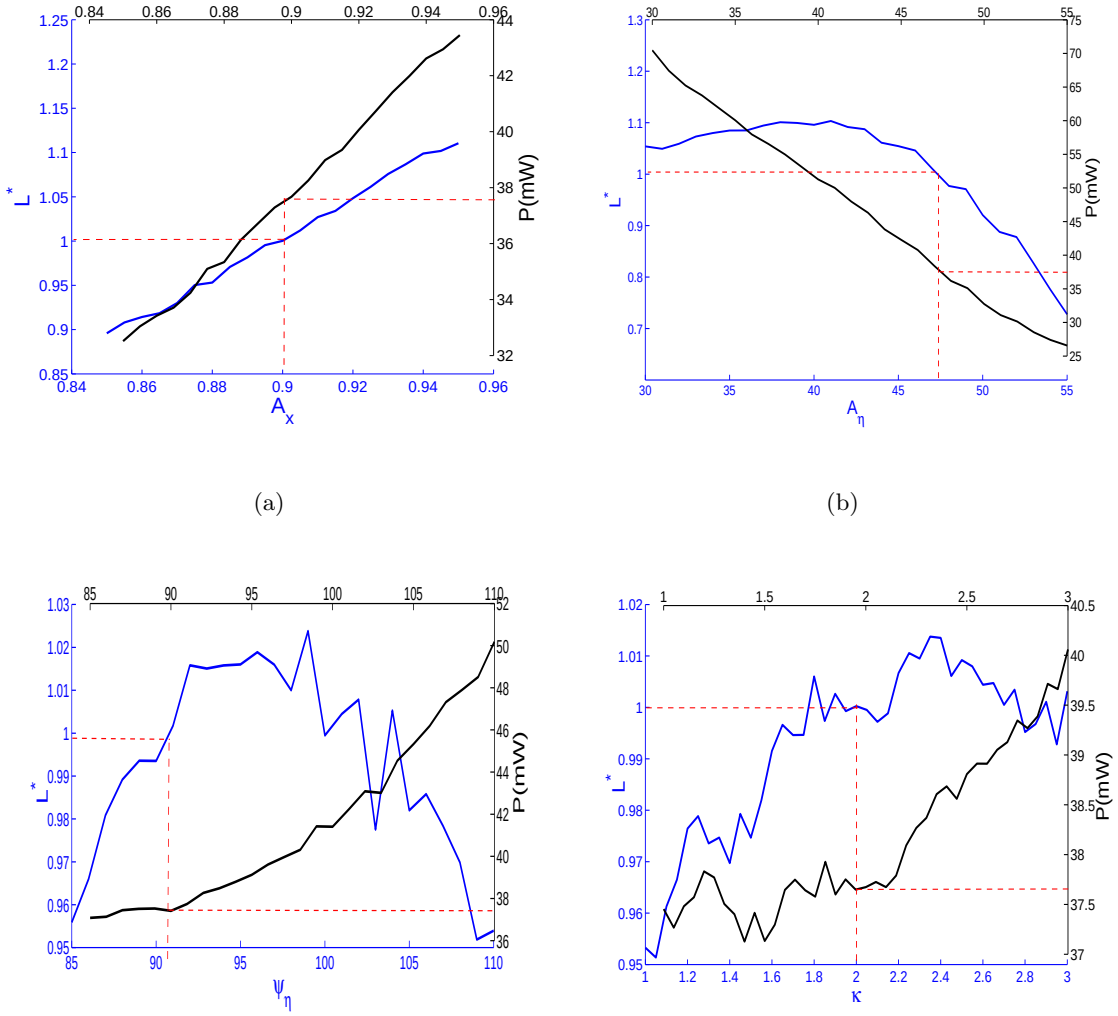

(a) (b)

(c) (d)

Figure 4.10: Sensitivity of the optimized configuration to disturbances in the kinematics parameters. The blue lines show the variations of the dimensionless lift L^* with each of the kinematics parameters and the black lines represent the variations of aerodynamic power P. The red dashed lines indicate the optimal solution for the parameter.

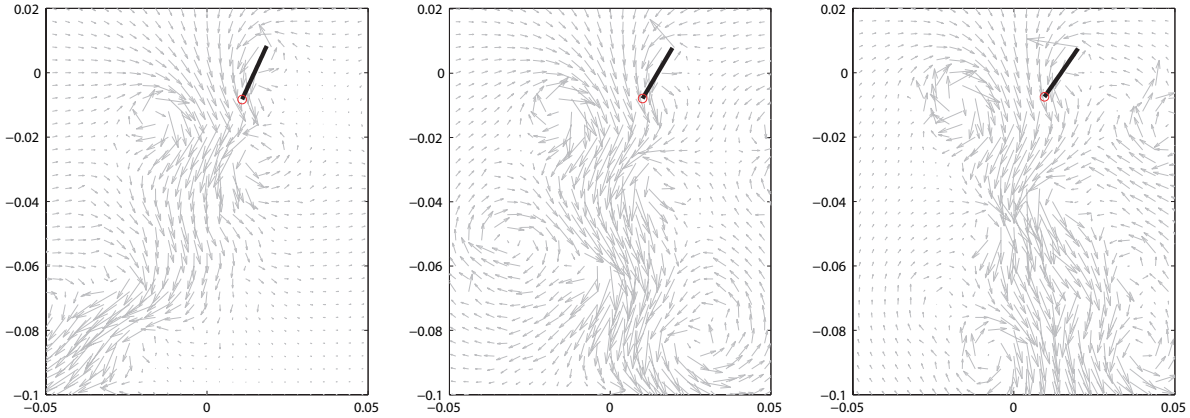

(a) $\kappa = 1$ (b) $\kappa = 2$ (optimal configuration) (c) $\kappa = 3$

Figure 4.11: Flow field around the flapping wing for different values of the sharpness parameter κ.

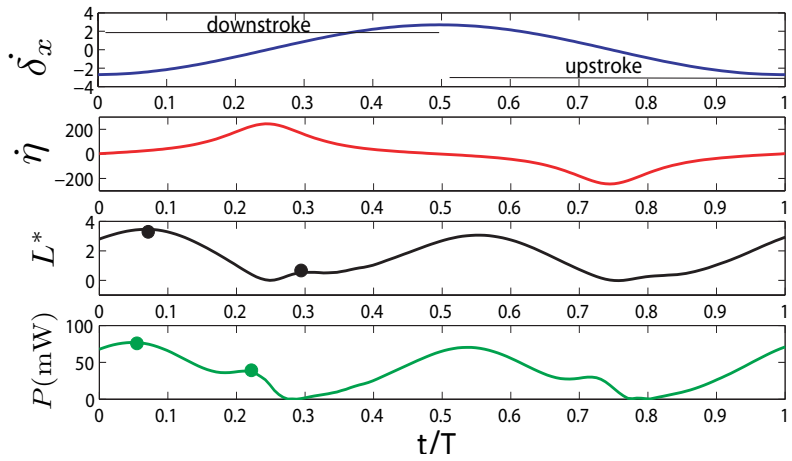

(a) $\kappa = 2$

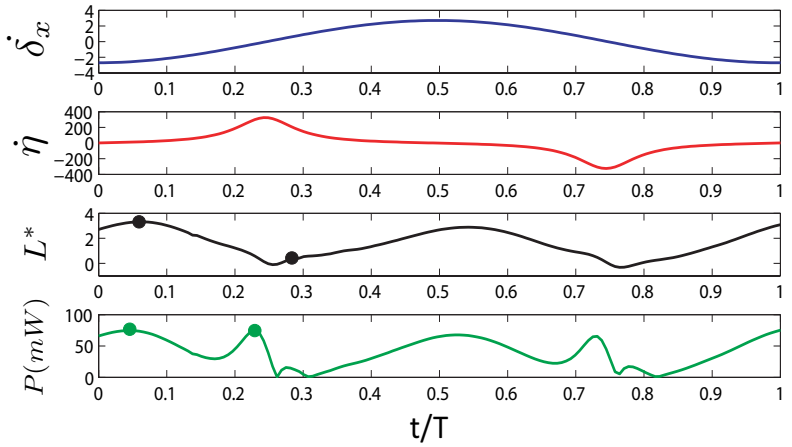

(b) $\kappa = 3$

Figure 4.12: x-translation velocity (upper frame), angular velocity (second frame), dimensionless lift (third frame), and aerodynamic power (lower frame) for different values of the sharpness parameter κ.

Chapter 5

Robust-based Analysis of Flapping Kinematics for Micro Air Vehicles

In this chapter, a three-dimensional version of the unsteady vortex lattice method (UVLM) is implemented to simulate the aerodynamic response of a plunging, flapping wing in forward flight. UVLM requires much less computational resources than methods based on solving the Navier-Stokes or Euler equations, but applies only to incompressible, inviscid flows where the separation lines are known a priori. The UVLM shows a great efficiency in terms of solution accuracy, memory requirement, and speed, which makes it suitable to tackle such aerodynamic problems (15; 28; 100).

A description of the model is first presented and some numerical examples for plunging-wing and flapping/twisting-wing are given to verify and demonstrate the capability of the model. Then, active shape morphing (prescribed wing deformation) is considered to optimize the flight performance of flapping wings. To this end, UVLM is combined with global and local optimization algorithms to identify the optimal kinematics that maximize the propulsive efficiency under lift and thrust constraints. Two types of morphing parametrization are investigated here – trigonometric and spline-based. The results show that the spline-based morphing, which requires specification of more design variables, yields a significant improvement in terms of propulsive efficiency. Furthermore, a sensitivity analysis of the optimal design points is performed to investigate the effects of perturbing various parameters on the

propulsive efficiency and solution feasibility. Finally, an innovative analysis is carried out to explain how birds morph (deform) their wings and employ specific wing shapes to control their flight performance, as well as to make it more efficient.

5.1 3-D Unsteady Vortex Lattice Method

When a lifting surface is suddenly set in motion, the fluid is set in motion too and boundary layers on the upper and lower surfaces are generated as a result of the no-slip boundary condition. These boundary layers are the source of vorticity in the flow. This vorticity is then shed along the wing tips and trailing edges and convected downstream. This shedding process forms the wake. As a result, all vorticity is confined to thin regions in the boundary layers that form on the lifting surface and in the wake shed behind it. Outside these regions, the flow is assumed to be irrotational. In the unsteady vortex-lattice method, both the lifting surface and its wake are represented by a sheet of vorticity. This sheet consists of two parts. The first part represents the lifting surface and has its position specified. It is called the bound vortex sheet and a pressure jump may exist across it. The second represents the wake, does not have its position given in advance and deforms freely into the force-free position. It is called the free vortex sheet and no pressure jump can exist across it. The bound and free vortex sheets are joined along the sharp edges where separation occurs and Kutta condition is imposed.

In the simulation, the entire bound and free vortex sheets are replaced with discrete vortex rings. Each vortex ring consists of four short straight vortex segments. The outcome is a lattice of vortex lines that divide the body surface into elements. The shape of each element is chosen to be rectangular. In previous studies (100; 118), it was pointed out that such elements are superior to other shapes in terms of accuracy and rate of convergence. Figure 5.1 shows a typical element of the aerodynamic grid. The points P_1, P_2, P_3, and P_4 form the corners of the element. The control point (centroid of the element) P_c is determined by taking the intersection of the vectors $\overrightarrow{P_1P_3}$ and $\overrightarrow{P_2P_4}$ and the outward normal $\mathbf{n}$ and tangential vector τ respectively, are computed as

$$\mathbf{n} = \overrightarrow{P_1P_3} \times \overrightarrow{P_2P_4} / \left| \overrightarrow{P_1P_3} \times \overrightarrow{P_2P_4} \right|, \text{and} \tag{5.1}$$

$$\tau = 0.5 \cdot \left(\overrightarrow{P_1P_3} + \overrightarrow{P_2P_4} \right) / \left| 0.5 \cdot \left(\overrightarrow{P_1P_3} + \overrightarrow{P_2P_4} \right) \right|. \tag{5.2}$$

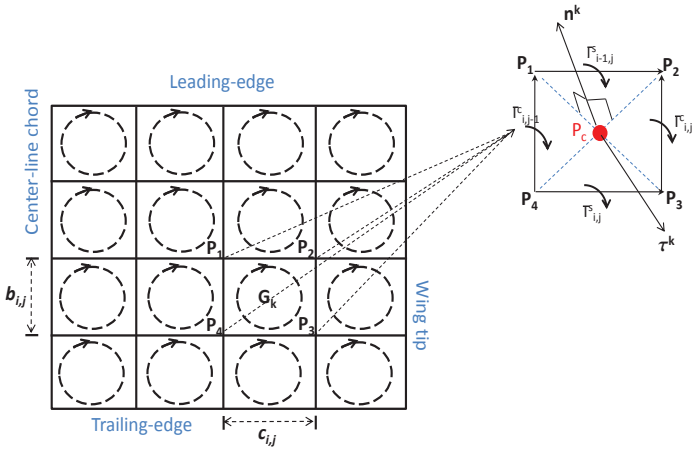

Figure 5.1: Wing discretization and an example of a typical vortex element.

The circulation is taken to be the same for all four segments of the same loop to ensure spatial conservation of circulation. Each vortex segment is shared by two adjoining loops, except the ones along the first and last rows and columns, and its strength is equal to the difference in the circulations of the two loops to which it belongs.

The absolute velocity induced by all discrete vortex segments is computed according to the Biot-Savart law given by

$$\mathbf{V}(r) = \frac{\Gamma}{2\pi h} \Big(\cos(\theta_1) - \cos(\theta_2) \Big) \, \mathbf{e}, \tag{5.3}$$

where, in Figure 5.2, $\mathbf{V}$ is the velocity at point P_c, $\mathbf{e}$ is the unit vector perpendicular to the plane formed by the three points P_1, P_2, and P_c. Points P_1 and P_2 lie at the ends of the straight vortex segment, h is the perpendicular distance from P_c to the vortex segment. Γ is the circulation strength of the vortex filament. The angles θ_1 and θ_2 are defined as shown in Figure 5.2. The Biot-Savart law is used intensively in this method and the corresponding script is the most called during a simulation.

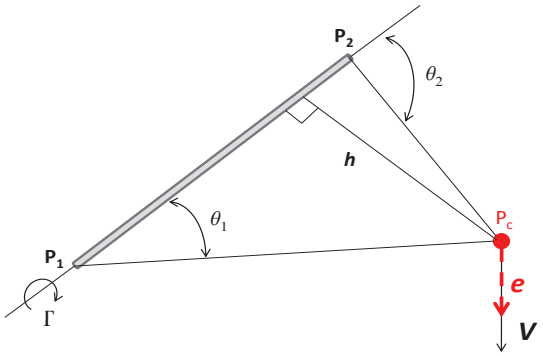

Figure 5.2: Velocity field induced by a straight vortex segment.

Because the induced velocity is computed according to the Biot-Savart law, the velocity field satisfies the continuity equation. Furthermore, the velocity decays as the distance from the vortex segment increases and assumes a zero value at infinity. To make the pressure continuous in the wake, vortex segments are convected and circulation around each segment remains constant after it is shed at the local fluid particle velocity as required by the Kelvin-Helmholtz theorem. The spatial conservation of circulation is satisfied by taking the circulation to be identical for all the discrete vortex segments of the same loop. The unsteady Kutta condition is satisfied by shedding all the vorticity formed along the sharp edges. The no-penetration boundary condition will be discussed next.

For convenience, all variables are written in dimensionless form by introducing the following characteristic velocity, length, time, and pressure:

- U_c is the freestream speed or a speed characterizing the forward motion of the lifting surface (wing).
- L_c is the physical length of the chordwise increment of the bound lattice, i.e. c/n_r, where c is the chord length.
- $t_c = L_c/U_c$ is the characteristic time. The computational time step is taken to be unity.
- $P_c = \rho U_c^2/2$ is the characteristic pressure, where ρ is the fluid density.

The dimesionless variables are then given by

$$U^* = \frac{U}{U_c}, \quad L^* = \frac{L}{L_c}, \quad t^* = \frac{t}{t_c}, \quad \text{and} \quad P^* = \frac{P}{P_c}. \tag{5.4}$$

The superscript $(.)^*$ is removed in the following equations.

The no-penetration boundary condition is imposed for each element, at the control point P_c as defined in Figure 5.1, and is written as

$$\left(\mathbf{V}_\infty + \mathbf{V}_{B_i} + \mathbf{V}_{W_i} - \mathbf{V}_{LS_i}\right) \cdot \mathbf{n}_i = 0, \tag{5.5}$$

where $\mathbf{V}_\infty$ is the freestream velocity, $\mathbf{V}_{B_i}$ is the disturbance velocity generated by bound vortices, and $\mathbf{V}_{W_i}$ is the velocity induced by the wake; $\mathbf{n}_i$ is the unit normal vector at the control point of the i^{th} element; and $\mathbf{V}_{LS_i}$ is the absolute velocity of the lifting surface at the control point of the i^{th} element and in general is a function of space and/or time, computed according to the following equation:

$$\mathbf{V}_{LS_i} \quad = \quad \mathbf{V}_A + \frac{d\mathbf{r}_i}{dt} + \omega \times \mathbf{r}_i, \tag{5.6}$$

where $\mathbf{r}_i$ is the position vector of the control point of the i^{th} element relative to the moving reference frame. $\mathbf{V}_A$ is the velocity of the moving frame with respect to the fixed inertial frame. ω is the angular velocity of the moving frame. Using Equation 5.5, the no-penetration condition is rewritten as

$$\sum_{j=1}^{N_{el}} A_{ij} G_j \quad = \quad \left(\mathbf{V}_{LS_i} - \mathbf{V}_{W_i}\right) \cdot \mathbf{n}_i \tag{5.7}$$

where N_{el} is the number of elements. A_{ij} represents the normal component of the velocity induced at the control point of the i^{th} element by the vortex ring, having a unit circulation, around element j. A is called the influence matrix and in general, is a function of space and/or time. G_j is the circulation of the vortex ring at element j.

In order to solve the no-penetration boundary condition, an initial condition must be prescribed that describes the wake by giving the position and vorticity distribution. One special case of interest is when the lifting surface is set into motion impulsively. At this instant, no wake yet exists; $\mathbf{V}_W$ is zero, and Equation (5.7) reduces to

$$\sum_{j=1}^{N_{el}} A_{ij} G_j \quad = \quad \mathbf{V}_{LS_i} \cdot \mathbf{n}_i. \tag{5.8}$$

The linear system given by Equation (5.8) is solved for the unknown loop circulations G_j. When the influence matrix, A, is constant, i.e., for fixed and rigid wings, it is inverted once. However, for flexible or rigid flapping wings, the matrix inversion operation is carried out at each time step. At the beginning of the first time step, $t = 0$, all the circulations in the bound and free portions of the vortex lattice are set to zero. At the end of the first time step, the circulations in the bound portion change and a vortex line is formed along the sharp edges. This is the starting vortex dictated by the requirement of spatial conservation of circulation.

At the beginning of the second time step, $t = \Delta t$, all the vorticity formed along the sharp edges is convected downstream at the local fluid particle velocity in order to satisfy the unsteady Kutta condition. This local fluid particle velocity $\mathbf{v}_k$ at a node k of the wake in the moving reference frame is computed by

$$\mathbf{v}_k = \mathbf{V}_\infty + \mathbf{V}_k - \mathbf{V}_A, \tag{5.9}$$

where $\mathbf{V}_k$ is the velocity induced by the lifting surfaces and its wake.

Despite the fact that each quantity in Equation (5.9) is a function of time, the quantities that are computed at the previous time step $t = 0$ are used. The justification is that computing the quantities at the present time step $t = \Delta t$ requires iterations, which in turn increases the computation time without any significant improvement in the accuracy of the method (although the iteration allows larger time steps Δt while maintaining stability) (30). The starting vortex is convected downstream and its circulation at the new position is the same as the circulation around the starting vortex at $t = 0$ to satisfy the temporal conservation of circulation. So, the wake stores the values of the loop circulations at previous time steps. As such, Preidikman (118; 119) describes the wake as the historian of the flow. In order to guarantee the spatial conservation of circulation, the starting vortices at the old and new positions are joined at the nodal points with connectors and the new position of the node k, $\mathbf{R}_k^w(t + \Delta t)$ is computed by following a first order Euler scheme; that is,

$$\mathbf{R}_k^w(t + \Delta t) = \mathbf{R}_k^w(t) + \mathbf{v}_k \Delta t \tag{5.10}$$

where $\mathbf{R}_k^w(t)$ is the old position of the node k and the wake is created as a result of shedding the starting vortices. The bound circulations are calculated at the second time step $t = \Delta t$

using Equation (5.7) and includes the effects of the wake. A second starting vortex forms along the sharp edges and is then shed and convected downstream to its new position as required by the unsteady Kutta condition. Simultaneously, the first starting vortex is convected to its new position and the wake keeps growing. The bound circulations are computed at the end of the third time step $t = 2\Delta t$ and a third starting vortex forms along the sharp edges. This process is repeated for any desired number of steps. Figure 5.3(a) plots a 4×5 lattice that models half a wing at $t = 0$. The flow is symmetric about the center chord plane of the wing. At that time, there is no wake vorticity yet. At $t = \Delta t$, the vorticity starts to shed from the wing tip and the trailing-edge as shown in Figure 5.3(b). The same shedding mechanism is carried out for the next time steps. Figure 5.3(c) shows the wing and the wake that has been formed at $t = 2\Delta t$.

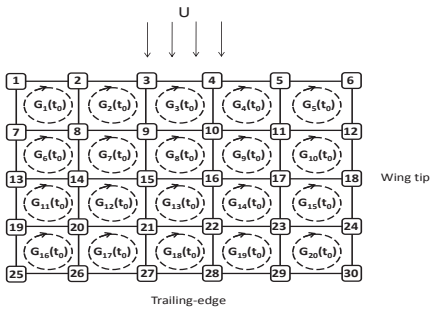

(a) $t = 0$

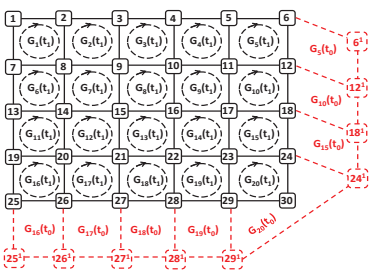

(b) $t = \Delta t$

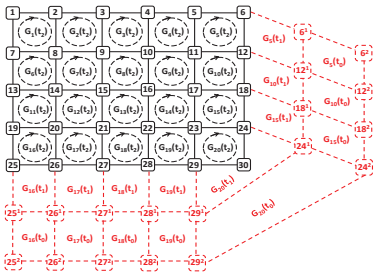

(c) $t = 2\Delta t$

Figure 5.3: Vortex lattice sheets that model the boundary layer at the lifting surface (wing) and its wake at the first three time steps.

5.2 Aerodynamic loads

To compute the aerodynamic loads, the approach given by Katz and Plotkin (30) is followed. This approach accounts for the leading-edge suction force. First, the local lift and drag contributions of each element are computed. Then, the elemental lift and drag are transformed to the inertial frame. Summing them and resolving the total force into three components yield the component parallel to the x-axis is the drag while the component parallel to the z-axis is the lift. Details of the force computation are given next.

The lift is the force component perpendicular to the flight direction; the panel k contribution is given by (15; 30)

$$\Delta L^k_{i,j} = \rho \cdot b_{i,j} \cdot \Big[\mathbf{V}^k_{i,j}(\Gamma^s_{i,j} - \Gamma^s_{i-1,j}) + c_{i,j} \cdot \frac{\partial}{\partial t}\Big(\frac{\Gamma^s_{i,j} + \Gamma^s_{i-1,j}}{2}\Big)\Big] \cdot \cos(\alpha^k). \tag{5.11}$$

The drag is the force component parallel to the flight direction; the panel k contribution is given by

$$\Delta D^k_{i,j} = \rho \cdot b_{i,j} \cdot \Big[\Big(\mathbf{V}_{ind} + \mathbf{V}_W\Big)^k_{i,j}(\Gamma^s_{i,j} - \Gamma^s_{i-1,j}) + c_{i,j} \cdot \frac{\partial}{\partial t}\Big(\frac{\Gamma^s_{i,j} + \Gamma^s_{i-1,j}}{2}\Big) \cdot \sin(\alpha^k)\Big], \tag{5.12}$$

and if the panel is located at the leading-edge, the lift and drag are given by

$$\Delta L^k_{i,j} = \rho \cdot b_{i,j} \cdot \Big[\mathbf{V}^k_{i,j}(\Gamma^s_{i,j}) + c_{i,j} \cdot \frac{\partial}{\partial t}\Big(\frac{\Gamma^s_{i,j}}{2}\Big)\Big] \cdot \cos(\alpha^k) \text{ and} \tag{5.13}$$

$$\Delta D^k_{i,j} = \rho \cdot b_{i,j} \cdot \Big[\Big(\mathbf{V}_{ind} + \mathbf{V}_W\Big)^k_{i,j}(\Gamma^s_{i,j}) + c_{i,j} \cdot \frac{\partial}{\partial t}\Big(\frac{\Gamma^s_{i,j}}{2}\Big) \cdot \sin(\alpha^k)\Big]. \tag{5.14}$$

where $\mathbf{V}^k_{i,j}$ is the velocity vector of panel k due to forward flight, flapping motion, and wing deformation (morphing). $\mathbf{V}_{ind}$ and $\mathbf{V}_W$ are the velocities induced by the wing's streamwise vortex lines and the wake, respectively. It is noted that $\mathbf{V}_{ind}$ is computed by summing the velocity induced by all the segments along the chordwise direction of the bound vortices. α^k is the angle of attack relative to the freestream direction of panel k and is computed as

$$\alpha^k = \arctan(\mathbf{V}^k_v/\mathbf{V}^k_h) \quad \text{where} \quad \mathbf{V}^k_v = \mathbf{V}^k \cdot \mathbf{n}^k \quad \text{and} \quad \mathbf{V}^k_h = \mathbf{V}^k \cdot \tau^k \tag{5.15}$$

The remaining parameters of Equations (5.11)–(5.14) are defined in Figure 5.1. It is noted that the quantities defined in Equations (5.11)–(5.14) are applied along the local lift vector $\mathbf{e}^k_{lift}$ and drag vector $\mathbf{e}^k_{drag}$ of the panel k as shown in Figure 5.4. So, to compute total lift and drag forces, the vector $\mathbf{q}^k$ and the transformation matrices T^k and T^k_α are first defined by

$$\mathbf{q}^k = \tau^k \times \mathbf{n}^k \tag{5.16}$$

$$T^k = \begin{pmatrix} \tau^k & \mathbf{n}^k & \mathbf{q}^k \end{pmatrix} \tag{5.17}$$

$$T^k_\alpha = \begin{pmatrix} \cos(\alpha^k) & \sin(\alpha^k) & 0 \\ -\sin(\alpha^k) & \cos(\alpha^k) & 0 \\ 0 & 0 & 1 \end{pmatrix} \tag{5.18}$$

The local lift and drag vectors then are given by

$$\begin{aligned} \mathbf{e}^k_{drag} &= T^k \cdot (T^k_\alpha)^T \cdot (T^k)^T \cdot \tau^k \\ \mathbf{e}^k_{lift} &= T^k \cdot (T^k_\alpha)^T \cdot (T^k)^T \cdot \mathbf{n}^k \end{aligned} \tag{5.19}$$

where the superscript $(.)^T$ denotes the transpose. Then, the total force vector is

$$\mathbf{F} = \sum_{k=1}^{N_{el}} \mathbf{F}^k = \sum_{k=1}^{N_{el}} \left(\Delta L^k \cdot \mathbf{e}^k_{lift} + \Delta D^k \cdot \mathbf{e}^k_{drag} \right) \tag{5.20}$$

The component of the force $\mathbf{F}$ parallel to the x-axis is the drag while the component parallel to the z-axis is the lift.

Similarly to (15), the power input P_{in} is considered as the aerodynamic power, that is,

$$P_{in} = \sum_{k=1}^{N_{el}} \Delta C_{P_k} \cdot A_k \cdot \mathbf{n}_k, \cdot \mathbf{V}^k_{motion}, \tag{5.21}$$

where

$$\Delta C_{P_k} = \left(\mathbf{F}^k \cdot \mathbf{n}_k \right) / A_k \tag{5.22}$$

It is noted that for this work the inertial power input required to flap and morph the wing is neglected. Shyy et al. (120) showed that this assumption is quite reasonable for forward

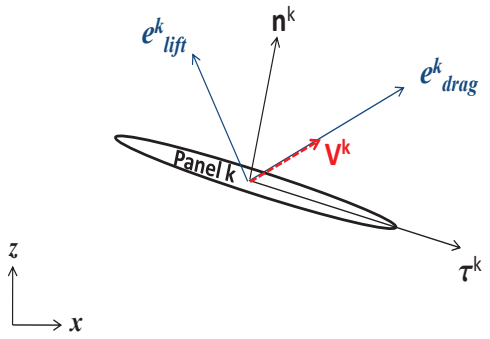

Figure 5.4: Local lift and drag vectors (for each panel).

flight. The power output P_{out} as the power used to move the wing in the forward direction, that is,

$$P_{out} = \left(\mathbf{F} \cdot i_x\right) \cdot U \tag{5.23}$$

The mean propulsive efficiency of the flapping wing is defined then as

$$\eta = \overline{P}_{out}/\overline{P}_{in} \tag{5.24}$$

where the overline denotes a time-averaged quantity over a flapping cycle.

5.3 Wing Kinematics

During forward flight, the wing displacement consists of four components: plunging $\gamma_z(t)$ (vertical translation motion), flapping $\phi(t)$ (rotation about the wing root) , twisting $\beta(\mathbf{X}, t)$ (rotation about the leading-edge of the wing), and bending $\gamma_b(\mathbf{X}, t)$ motions. It is noted here that the plunging and flapping are global motions (i.e., the entire wing moves as a whole), but twisting and bending are local motions (i.e., vary spatially).

To express the wing kinematics, two coordinate systems are introduced. A fixed coordinate system xyz describes the undeformed geometry, referred to as the ground reference frame, and a moving coordinate system $x_3y_3z_3$ that describes the deformed geometry, referred to as the body frame. Moreover, the x_3-axis is considered to point backward along the chordwise direction of the lifting surface toward the trailing-edge, the y_3-axis be coincident

with the spanwise direction, and z_3-axis be the normal to the lifting surface and pointing upward. i_x, i_y, and i_z denote the unit vectors along the x, y, and z axes, respectively, and i_{x_3}, i_{y_3}, and i_{z_3} denote the unit vectors along the x_3, y_3, and z_3 axes, respectively. Three consecutive angles β (twist angle), ϕ (flapping angle), and α (geometric angle of attack) are used to describe the motion of the wing.

The body frame $x_3y_3z_3$ is obtained as a result of a sequence of rotations about the axes in the following order. First, the xyz system is rotated through an angle β about the y-axis (a pitch-like rotation) to an intermediate coordinate system $x_1y_1z_1$ ($y = y_1$). The unit vectors of these two coordinate systems are related by

$$\begin{pmatrix} i_{x_1} \\ i_{y_1} \\ i_{z_1} \end{pmatrix} = \begin{pmatrix} \cos(\beta) & 0 & \sin(\beta) \\ 0 & 1 & 0 \\ -\sin(\beta) & 0 & \cos(\beta) \end{pmatrix} \begin{pmatrix} i_x \\ i_y \\ i_z \end{pmatrix}$$

Second, the $x_1y_1z_1$ system is rotated by an angle ϕ about the x_1-axis (a roll-like rotation) to a second intermediate coordinate system $x_2y_2z_2$ ($x_1 = x_2$).The unit vectors of these two coordinate systems are related by

$$\begin{pmatrix} i_{x_2} \\ i_{y_2} \\ i_{z_2} \end{pmatrix} = \begin{pmatrix} 1 & 0 & 0 \\ 0 & \cos(\phi) & \sin(\phi) \\ 0 & -\sin(\phi) & \cos(\phi) \end{pmatrix} \begin{pmatrix} i_{x_1} \\ i_{y_1} \\ i_{z_1} \end{pmatrix}$$

Finally, the $x_3y_3z_3$ coordinate system is obtained by rotating the system $x_2y_2z_2$ by a constant angle α about the y_2-axis (a second pitch-like rotation). Their unit vectors are related by

$$\begin{pmatrix} i_{x_3} \\ i_{y_3} \\ i_{z_3} \end{pmatrix} = \begin{pmatrix} \cos(\alpha) & 0 & \sin(\alpha) \\ 0 & 1 & 0 \\ -\sin(\alpha) & 0 & \cos(\alpha) \end{pmatrix} \begin{pmatrix} i_{x_2} \\ i_{y_2} \\ i_{z_2} \end{pmatrix}$$

Therefore, the unit vectors of the two coordinate systems xyz and $x_3y_3z_3$ are related by

$$\begin{pmatrix} i_{x_3} \\ i_{y_3} \\ i_{z_3} \end{pmatrix} = [T] \begin{pmatrix} i_x \\ i_y \\ i_z \end{pmatrix}$$

where

$$[T] = \begin{pmatrix} \cos(\alpha) & 0 & \sin(\alpha) \\ 0 & 1 & 0 \\ -\sin(\alpha) & 0 & \cos(\alpha) \end{pmatrix} \begin{pmatrix} 1 & 0 & 0 \\ 0 & \cos(\phi) & \sin(\phi) \\ 0 & -\sin(\phi) & \cos(\phi) \end{pmatrix} \begin{pmatrix} \cos(\beta) & 0 & \sin(\beta) \\ 0 & 1 & 0 \\ -\sin(\beta) & 0 & \cos(\beta) \end{pmatrix}$$

Using the transformation matrix defined above, the position vector $\mathbf{R}(\mathbf{X}_0, t)$ of an arbitrary point on wing is given by

$$\mathbf{R}(\mathbf{X}_0, t) = \gamma_z(t) i_z + [T] \cdot \Big(\mathbf{X}_0 + \gamma_b^c((\mathbf{X}_0, t)) i_y + \gamma_b((\mathbf{X}_0, t)) i_z \Big) \tag{5.25}$$

where γ_b^c is a displacement introduced along the spanwise direction in order to guarantee that the length of the wing from root to tip remains the same during the motion as considered in (15). $\mathbf{X}_0$ is the initial wing grid defined in the global reference frame. The motion of the wing is governed then by Equation (5.25).

5.3.1 Implementation of wing motion

The motion of the wing, over one cycle, can be defined by a combination of translational and angular oscillations. In this work, the flapping and plunging motions are based on sinusoidal functions, that is,

$$\begin{aligned} \phi(t) &= M_\phi + A_\phi \sin(\, 2\pi\, \omega_\phi t + \psi_\phi) \\ \gamma_z(t) &= M_{\gamma_z} + A_{\gamma_z} \sin(\, 2\pi\, \omega_{\gamma_z} t + \psi_{\gamma_z}) \end{aligned} \tag{5.26}$$

As defined above, the wing motion involves mean values, amplitudes, frequencies, and phase angles. Using the characteristic parameters defined in Equation (5.4), the dimensionless parameters are introduced

$$\begin{aligned} M^*_{\gamma_z} &= M_{\gamma_z}/L_c, \quad A^*_{\gamma_z} = A_{\gamma_z}/L_c, \\ k_\phi &= \omega_\phi\, (c/2)/U_c = \omega_\phi\, (L_c/U_c)\, (n_r/2), \quad \text{and} \\ k_{\gamma_z} &= \omega_{\gamma_z}\, (c/2)/U_c = \omega_{\gamma_z}\, (L_c/U_c)\, (n_r/2) \end{aligned} \tag{5.27}$$

where k_ϕ and k_{γ_z} are the reduced frequencies of the flapping and plunging motions, respectively. These parameters provide a measure of the degree of unsteadiness of the flapping motion and then, define the type of flight conditions (e.g., quasi-steady, unsteady, etc.).

5.3.2 Implementation of wing deformation (active shape morphing)

A prescribed deformation of the wing using bending and twisting mode shapes is assumed as followed by Stanford and Beran (15). The first two bending and twisting modes of each of the shapes are considered in this work and defined as

$$\begin{aligned} \beta(\mathbf{X}_0, t) &= \beta_1(t) \cdot F_1(\mathbf{X}_0) + \beta_2(t) \cdot F_2(\mathbf{X}_0) \\ \gamma_b(\mathbf{X}_, t) &= \gamma_{b_1}(t) \cdot G_1(\mathbf{X}_0) + \gamma_{b_2}(t) \cdot G_2(\mathbf{X}_0) \end{aligned} \tag{5.28}$$

where

$$\begin{aligned} F_1(\mathbf{X}_0) &= \mathbf{X}_0(2)/(s/2) \\ F_2(\mathbf{X}_0) &= -192 \times (\mathbf{X}_0(2)/s)^4 + 224 \times (\mathbf{X}_0(2)/s)^3 - 60 \times (\mathbf{X}_0(2)/s)^2 \\ G_1(\mathbf{X}_0) &= (\mathbf{X}_0(2)/s)^2 \\ G_2(\mathbf{X}_0) &= -192 \times (\mathbf{X}_0(2)/s)^4 + 224 \times (\mathbf{X}_0(2)/s)^3 - 60 \times (\mathbf{X}_0(2)/s)^2 \end{aligned} \tag{5.29}$$

where s is the span length. Figure 5.5 shows the wing mode shapes used in the active shape morphing. It is noted that imposing the wing deformation, usually referred to as active shape morphing, can be achieved by placing actuators (e.g., piezoelectric patches) on the wing surface (121) or connecting the wing with simple torque rods (122; 123). The purpose of introducing this dynamic shape deformation is to investigate how it would improve the flight performance of the wing.

5.4 Numerical Simulations and Validation

In order to demonstrate the ability of the UVLM to appropriately capture the flow around moving bodies and accurately predict the associated aerodynamic loads, different configurations for flows past wings are presented and analyzed. Results from these configurations are compared against those obtained from numerical and experimental efforts.

5.4.1 Flow past a plunging rectangular wing

A plunging rectangular wing with an aspect ratio equal to six and a chord of 0.1 m as studied by Heathcote et al. (36) and Stanford and Beran (15) is considered. The plunging

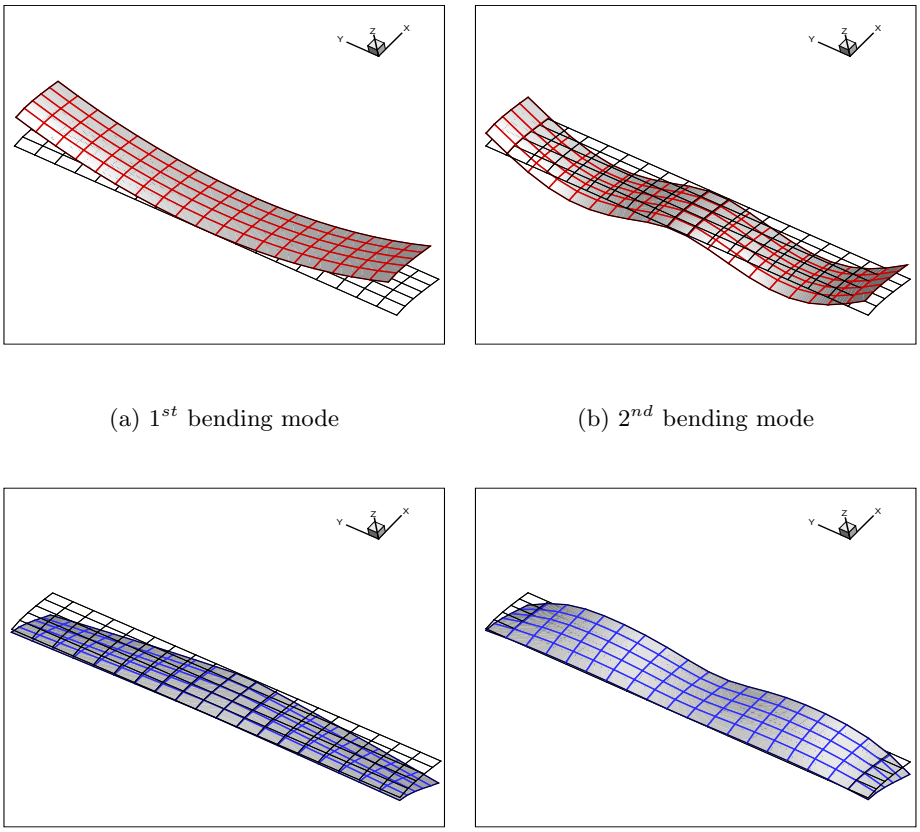

(a) 1^{st} bending mode

(b) 2^{nd} bending mode

(c) 1^{st} twisting mode

(d) 2^{nd} twisting mode

Figure 5.5: Wing mode shapes used in the active shape morphing.

amplitude is equal to 0.175 c. The experiments of Heathcote et al. (36) were performed on a wing at Re $= 30,000$. Figure 5.6 shows the thrust coefficient as a function of the reduced frequency k_{γ_z}. For the sake of comparison, two sets of results obtained from the current simulation are presented: with and without tip vorticity shedding. There is good match between data obtained from the current model, especially the results obtained when the tip vorticity shedding was excluded from the model, and those obtained by Stanford and Beran (15). Shedding vorticity from the tip yields slightly higher thrust at the higher reduced frequencies. Furthermore, both models capture fairly well the trend of the thrust variations when compared to the experimental results of Heathcote et al. (36). The discrepancy in the

thrust coefficient is most likely due to viscous effects which have not been accounted for in the formulation of UVLM models.

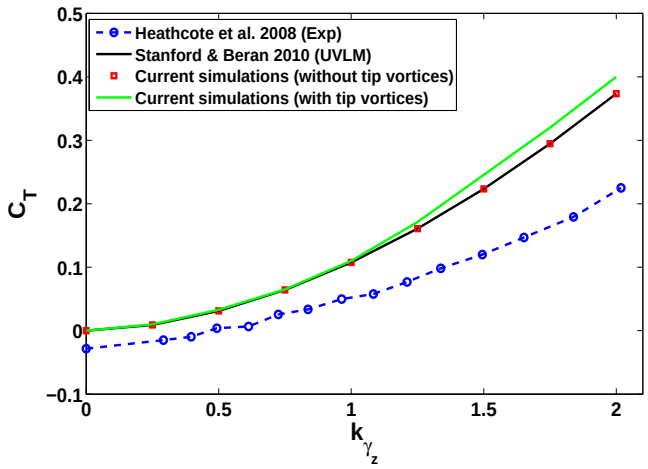

Figure 5.6: Variations of the averaged-value of the thrust coefficient with the reduced frequency. Comparison with the results of Stanford and Beran (15) and Heathcote et al. (36).

5.4.2 Flow past a flapping/twisting rectangular wing

Here, a test case for a flapping/twisting wing is considered. The flapping wing has a rectangular lifting surface with an aspect ratio of eight, a flapping amplitude of $A_\phi = 15°$, and a reduced frequency $k_\phi = 0.1$. The first twisting mode β_1 is used to deform the wing where the twisting angle β varies linearly along the spanwise direction, as in Equation (5.29), and the leading-edge is considered as the axis of rotation. The amplitude of the twisting motion at the wing tip ($\mathbf{X}_0(2) = s/2$) is equal to $A_\beta = 4°$ and the corresponding phase angle is equal to $\psi_\beta = 90°$. More details about the flapping/twisting configuration are given in (8). It is noted that the range of parameters for the combined flapping and twisting motions are selected so that the flow remains attached throughout the flapping cycle. Figure 5.7 shows a snapshot of the wing and its wake after one cycle for a flapping/twisting wing. It depicts the vortex lattices that simulate the bound and the wake. The roll-up of the starting, trailing, and tip vortices can be observed.

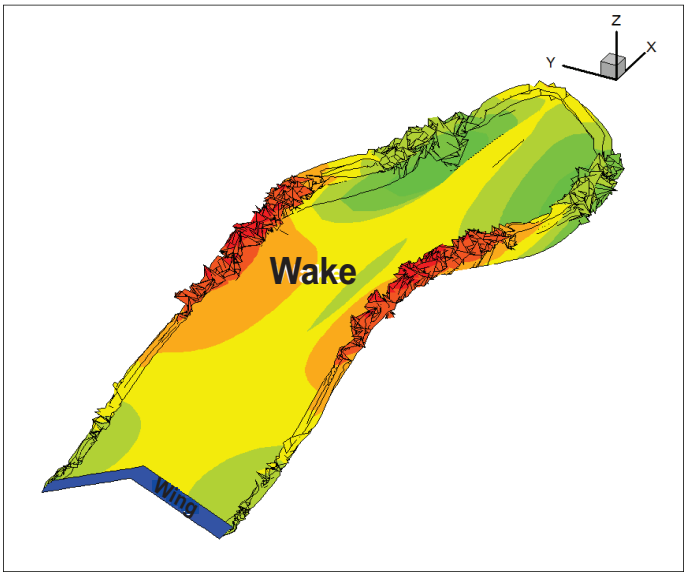

Figure 5.7: UVLM simulation of the wake of a flapping wing.

The results for the lift and thrust (negative drag) of the current vortex-lattice model are compared against previous work based on UVLM by Stanford and Beran (15) and Euler computations of Neef and Hummel (8). Here, two cases are considered: (1) the wing root is parallel to the freestream direction ($\alpha = 0°$) and (2) the wing root is turned with an angle of attack of $\alpha = 4°$. Again, for the sake of comparison, the variations of the lift and thrust for a flapping cycle obtained from the current method with and without tip vorticity shedding are plotted in Figure 5.8. As expected, the inclusion of tip vortices does not contribute much for a high-aspect ratio wing (AR = 8). The results from the current model, especially when excluding the tip vorticity shedding process, compare very well with those obtained by Stanford and Beran (15). The results are in good agreement as well with those of Neef and Hummel (8), except that the thrust is slightly overpredicted when the wing root is at an angle of attack during the upstroke (see Figure 5.8(b)). Stanford and Beran (15) associated this overprediction in the thrust to the wing tip vorticity shedding mechanism which was not considered in their model. However, the results show that including that mechanism does not significantly improve the thrust prediction. Based on the validation as presented in Figure 5.8, the UVLM shows great capability to appropriately predict the aerodynamic loads of a

flapping/twisting wing. However, one needs to be careful in the selection of the range of parameters and wing geometry by making sure that the assumptions of inviscid and attached flow regimes remain valid.

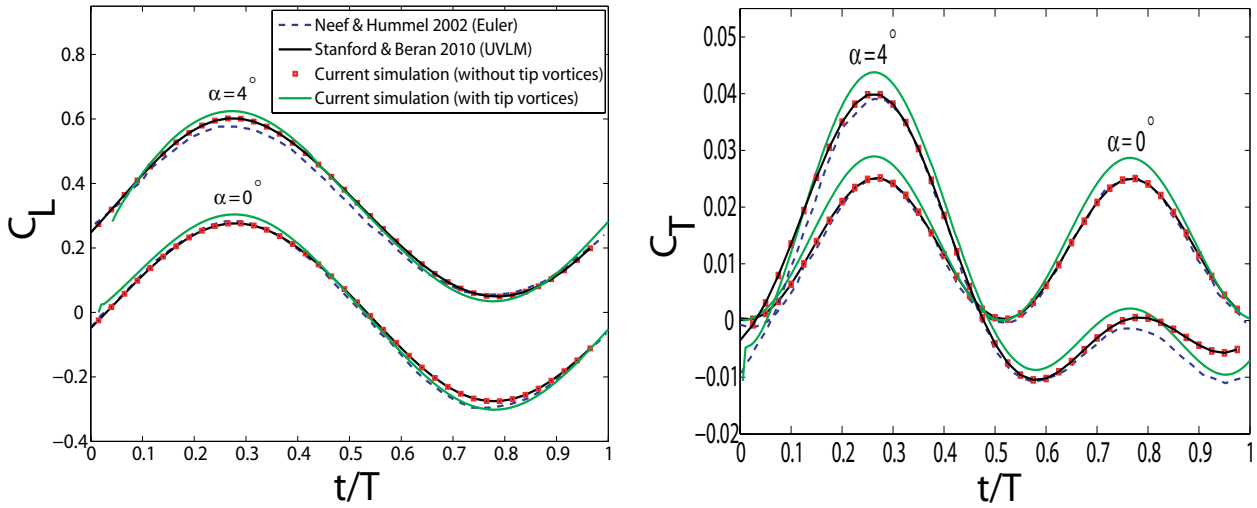

(a) Lift

(b) Thrust

Figure 5.8: Variations of the lift and thrust coefficients for a flapping/twisting wing. Comparison with numerical results of Neef and Hummel 2002 (8) (Euler solver) and Stanford and Beran 2010 (15) (UVLM).

5.4.3 Flow past a flapping cambered wing

Here, a wing geometry with an aspect ratio of eight and a NACA 83XX airfoil profile as studied by Vest and Katz (28) and Fejtek and Nehera (124) is considered. It is noted here that the last two digits of the NACA specification are denoted by "XX" since the airfoil thickness is not taken into consideration in the UVLM formulation. The motion of the wing is restricted to a flapping motion with a flapping angle equal to $A_\phi = 45°$ and a low reduced frequency ($k_\phi = 0.03082$). As reported by Vest and Katz (28), this configuration corresponds to a large bird traveling at high speeds.

Figures 5.9(a) and 5.9(b) show a comparison of the predicted lift and thrust coefficients by

the present model, the experimentally measured coefficients of Fejtek and Nehera (124) and the predicted coefficients by the potential flow model of Vest and Katz (28). In comparison with experimental results, the current model predicts the lift fairly well (within 5 to 10% error). In particular, excluding the tip vorticity yields a better prediction of the maximum lift. However, Figure 5.9(b) shows a discrepancy between the experimental and predicted thrust, especially, during some portions of the stroke where the flapping velocity is the greatest. As noted by Vest and Katz (28), this dissimilarity between the two sets of data is mostly due to flow separation which is not captured by both of the current model and the potential flow model of Vest and Katz (28).

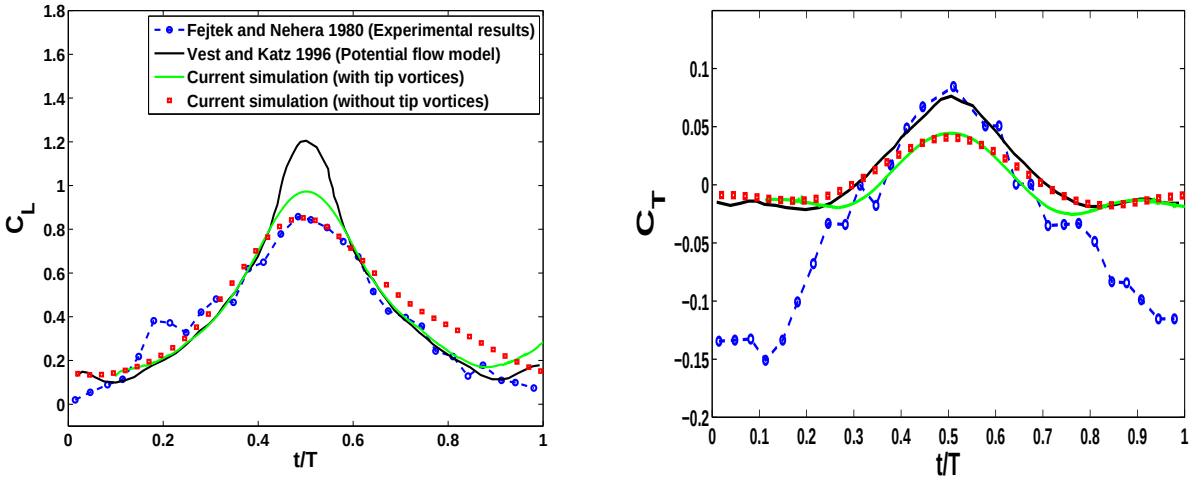

(a) Lift coefficient

(b) Thrust coefficient

Figure 5.9: Variations of the lift and thrust coefficients for one flapping cycle of a cambered wing. Comparison with numerical results of Vest and Katz (28) and experimental results of Fejtek and Nehera (124).

For the subsequent analysis, the numerical model excluding the shedding of wing tip vorticity is used. Furthermore, the wing geometry, the reduced frequency of the flapping motion and the range of variations of the kinematics parameters are selected so that the flow would remain attached.

5.5 Global Optimization

In this section, cambered and uncambered rectangular wings with an aspect ratio of six are considered. The cambered wing has a NACA 83XX cross-sectional profile as studied by Stanford and Beran (15). Details of the flapping configuration are given in Table 5.1. Table 5.2 presents results for baseline cases and a comparison with results obtained by Stanford and Beran (15). An excellent agreement between the two sets of data is obtained. Furthermore, it is observed that the use of a symmetric wing (NACA 00XX) leads to a significant improvement in terms of efficiency. This is accompanied, however, by a substantial decrease in the lift force. Thus, introducing camber to the wing allows for supporting heavier bodies at the price of loosing the wing's propulsive performance.

Table 5.1: Fixed Kinematics Parameters

Symbol	Description	Numerical values
A_ϕ	flapping angle	45.0°
M_ϕ	Mean value of flapping motion	0.0
k_ϕ	reduced frequency of flapping motion	0.1
ψ_ϕ	phase angle of flapping motion	0.0

The aim of this study is to investigate if the performance of flapping flight can be improved by introducing time-varying twist and bending as given by Equations (5.28) and (5.29). To this end, UVLM is combined with a deterministic global optimization algorithm VTdirect to determine an optimal kinematic configuration that maximizes the propulsive efficiency under lift and thrust constraints. VTdirect is a sampling algorithm. It does not require knowledge of the objective function gradient, but requires sampled points in the domain, and uses the information it has obtained about these points to decide where to search next based on the Lipschitz criteria. This algorithm is widely used in multidisciplinary engineering problems and is designed as an effective global optimization method that avoids being trapped at local optima (125–128). The search for globally-optimal points is performed through three main operations. These operations in each iteration are

1. Selection of "potentially optimal" boxes which are the regions that are most likely to contain the global optimum;

2. Point sampling within the potentially optimal boxes;

3. Subdividing the potentially optimal boxes.

A detailed description and implementation of the code is provided in He et al. (112–114). A distinctive characteristic of deterministic algorithms like VTdirect is their frugal use of function evaluations, compared to population based evolutionary algorithms (even if the latter use memory (129) and local approximations (130)).

Table 5.2: Baseline case results

Wing		$\overline{C}_L$	$\overline{C}_T$	$\overline{C}_P$	η
NACA 83XX	Current method	0.695	0.033	0.171	0.191
	Stanford and Beran (15)	0.695	0.033	0.171	0.191
NACA 00XX	Current method	0.29	0.0631	0.131	0.479

5.5.1 Problem formulation

The flapping motion and deformation of wings are the main mechanisms that ensure and control the flight of a MAV. Thus, the design of these mechanisms should satisfy some requirements. In particular, generating enough lift to support the body and thrust to sustain forward flight, and minimizing the aerodynamic power required to actuate the flapping and morphing mechanisms (equivalent to maximizing the efficiency) are highly desirable. Here, a global search is conducted to find a suitable kinematic configuration that satisfies the afore-

mentioned design specifications. Thus, the optimization problem is formulated as

$$\begin{aligned} &\max \quad \eta, \\ \text{subject to} \quad & \\ &\overline{C}_L \geq \overline{C}_{L_{bl}} \\ &\overline{C}_T \geq \overline{C}_{T_{bl}} \\ &v \in D, \end{aligned}$$

where v is the vector of control parameters consisting of parameters describing the twist and bending deformations, $D = \{v \in R^n \mid l \leq v \leq u\}$ is an n-dimensional bounding box, and $\overline{C}_{L_{bl}}$ and $\overline{C}_{T_{bl}}$ are the mean values of the lift and thrust obtained without shape morphing as given in Table 5.2.

For any sequential unconstrained minimization technique method, there are two choices for handling constraints: (1) use interior point barrier functions, or (2) define the objective function to be infinite at infeasible points. The latter option in known to work very well for direct search methods, and so the penalty function approach is used here to implement the lift and thrust constraints. The optimization problem is then rewritten as

$$\begin{aligned} &\max \quad \left[\eta - \alpha_L \cdot \left(\overline{C}_L - \overline{C}_{L_{bl}}\right)_- - \alpha_T \cdot \left(\overline{C}_T - \overline{C}_{T_{bl}}\right)_-\right], \\ \text{subject to} \quad & \\ &v \in D, \end{aligned}$$

where α_L and α_T are penalty parameters and set to 1000, and

$$X_- = \begin{cases} -X, & X < 0 \\ 0, & X \geq 0 \end{cases}$$

An alternative approach that avoids the use of penalty parameters is to simply set the efficiency η equal to zero whenever either of the constraints is violated.

5.5.2 Morphing parametrization

Two morphing parameterizations are considered. First, trigonometric functions are assumed for the time-varying bending and twisting modes. Thus, for example, the first twist mode is

written as

$$\beta_1(t) = A_{\beta_1} \sin(\, k_{\beta_1} t + \psi_{\beta_1}).$$

This leads to the design vector

$$v = \{A_{\beta_1}, \psi_{\beta_1}, A_{\beta_2}, \psi_{\beta_2}, A_{\gamma_{b_1}}, \psi_{\gamma_{b_1}}, A_{\gamma_{b_2}}, \psi_{\gamma_{b_2}}\}$$

It is noted that the frequencies of twist and bending are considered the same as the frequency of the flapping motion. The second parametrization is based on periodic splines. For this case, control points are specified to describe the time variations of the mode shape. Note that the last and first points must have the same value and slope to guarantee the time-periodicity. A cubic spline is used then to interpolate these points (see Figure 5.10). In this case, the vector of design variables is (16)

$$v = \{K^1_{\beta_1}, \cdots, K^m_{\beta_1}, K^1_{\beta_2}, \cdots, K^m_{\beta_2}, K^1_{\gamma_{b_1}}, \cdots, K^m_{\gamma_{b_1}}, K^1_{\gamma_{b_2}}, \cdots, K^m_{\gamma_{b_2}}\}$$

where, for example, $K^i_{\beta_1}$ is the value of the spline at i^{th} breakpoint used to define the first twisting mode and m is the total number of breakpoints for each mode. It is noted that the location of the spline in time is not a control variable.

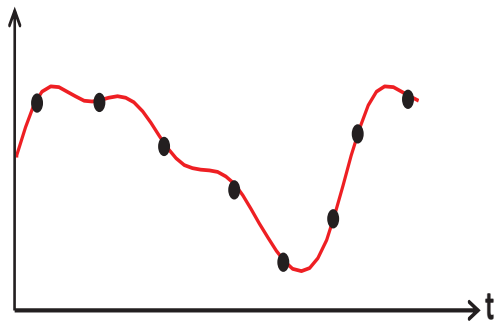

Figure 5.10: Spline-based description of the wing morphing.

Regarding the choice of design variables, parameterizing scheduled bending and twisting modes provides a MAV system which is immediately recognizable in practice. An elastic wing may be actively morphed in any number of ways during a flapping stroke for improved efficiency, or alternatively, the elastic wing may passively deform due to inertial and aerodynamic loads. In this case, the internal structure may be located such that the wing deforms

into the aerodynamically-efficient shapes as considered in the present work. In either case, this definition of the design parameterization and optimization problem constitutes an attempt to provide valuable insight into how either of these approaches may be realized in the design of micro air vehicles.

5.5.3 Results: optimization with a trigonometric morphing parametrization

Variations of the amplitudes and phase angles of the twisting and bending modes are considered. The upper and lower bounds of these parameters are presented in Table 5.3.

Table 5.3: Kinematic variables constraints

Wing morphing	Parameter	Lower bound	Upper bound
Twist deformation			
First mode	A_{β_1}	0°	45°
	ψ_{β_1}	-180°	180°
Second mode	A_{β_2}	0°	20°
	ψ_{β_2}	-180°	180°
Bending deformation			
First mode	$A_{\gamma_{b_1}}$	0	$0.7\ c$
	$\psi_{\gamma_{b_1}}$	-180°	180°
Second mode	$A_{\gamma_{b_2}}$	0	$0.3\ c$
	$\psi_{\gamma_{b_2}}$	-180°	180°

To carry out the optimization search, stopping conditions for VTdirect have been considered. These conditions serve as convergence criteria for the optimizer and basically limit the number of iterations and function evaluations, as well as the minimal value for the change in the objective function. For this type of morphing parametrization, Stanford and Beran (15) considered variations only in the amplitudes and phases of the first twist and bending modes, namely A_{β_1}, ψ_{β_1}, $A_{\gamma_{b_1}}$, and $\psi_{\gamma_{b_1}}$ and used the gradient-based algorithm to identify the

optimal design configuration that maximizes the efficiency under lift and thrust constraints. Thus, to assess the capability of the optimizer VTdirect, variations of the same parameters are considered. Table 5.8 provides a summary of the optimal results for the NACA 83XX wing as identified by VTdirect. Results include the kinematics parameters (A_{β_1}, ψ_{β_1}, $A_{\gamma_{b_1}}$, and $\psi_{\gamma_{b_1}}$) and averaged-values of the lift coefficient, $\overline{C}_L$, thrust coefficient, $\overline{C}_T$, power coefficient, $\overline{C}_P$, and efficiency η. These results show that morphing the wing shape using the first bending and twist modes yields a 11.5% increase in the propulsive efficiency. Furthermore, VTdirect found a different optimal design from that obtained by Stanford and Beran (15) who used gradient based optimization, with slightly higher efficiency. This exhibits the capability of VTdirect and confirms the existence of many local optimal points in the design space.

Table 5.4: Optimal kinematics results (four design variables) from VTdirect, NACA 83XX

Kinematic parameter	Optimal case (current method)	Optimal case (Stanford and Beran (15))
A_{β_1}	6.67°	8.94°
ψ_{β_1}	10.0°	− 0.45°
$A_{\gamma_{b_1}}$	0.607 c	0.693 c
$\psi_{\gamma_{b_1}}$	− 88.89°	− 89°
Performance measure		
$\overline{C}_L$	0.695	0.695
$\overline{C}_T$	0.0345	0.035
$\overline{C}_P$	0.1601	0.165
η	**0.2159**	**0.213**

Next, the second bending and twisting modes are incorporated. The optimal design results are presented in Table 5.5 for NACA 83XX and NACA 00XX wings. Providing more design variables enables a significant increase in the propulsive efficiency. As such, increases of 84% (from 0.191 to 0.353) for NACA 83XX and of 86% (from 0.479 to 0.89) for NACA

00XX have been achieved. The lift-thrust plots are shown in Figures 5.11(a) and 5.11(b) for both wings. Clearly, most of the useful lift and thrust is produced during the downstroke. Furthermore, it is observed that the lift remains positive during almost the entire stroke for the cambered wing while it reaches very low negative values during the upstroke for the uncambered wing. In Figures 5.12(a) and 5.12(b), the pressure distributions over the deformed wing for the optimal flight paths as predicted by VTdirect are plotted. For both wings, the highest pressure levels are obtained during the downstroke. This would explain the generation of the aerodynamic loads along the two phases of the stroke as reported in Figures 5.11(a) and 5.11(b). Furthermore, lower pressure levels are achieved for the uncambered wing and lead then to lower lift.

Table 5.5: Optimal kinematics results (eight design variables) from VTdirect

Kinematic parameter	NACA 83XX	NACA 00XX
A_{β_1}	15.3°	18.2°
ψ_{β_1}	44.4°	53.3°
A_{β_2}	7.28°	6.71°
ψ_{β_2}	57.8°	-44.4°
$A_{\gamma_{b_1}}$	$0.462\ c$	$0.431\ c$
$\psi_{\gamma_{b_1}}$	-40°	-40°
$A_{\gamma_{b_2}}$	$0.298\ c$	$0.299\ c$
$\psi_{\gamma_{b_2}}$	-147°	-156°
Performance measure		
$\overline{C}_L$	0.695	0.29
$\overline{C}_T$	0.0609	0.0632
$\overline{C}_P$	0.172	0.0727
η	**0.353**	**0.890**

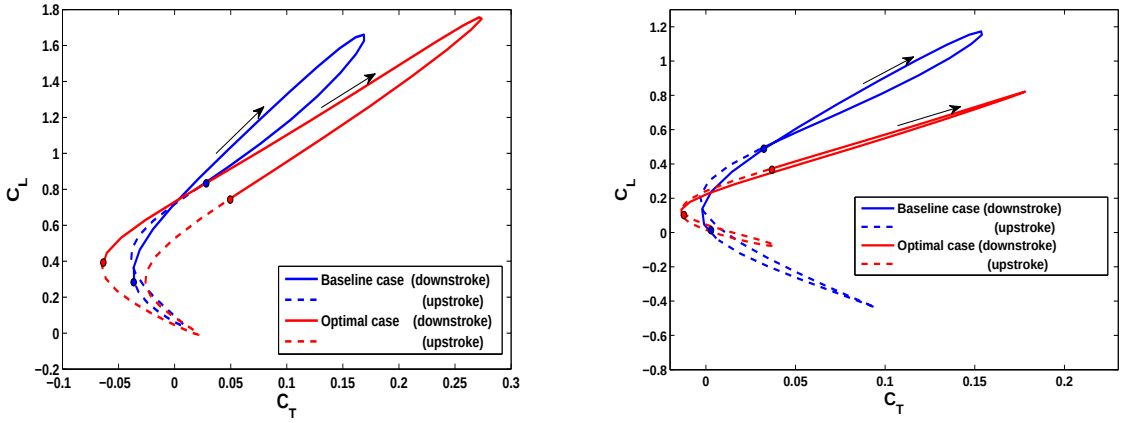

(a) NACA 83XX

(b) NACA 00XX

Figure 5.11: Lift coefficient vs. thrust coefficient for the optimal flight kinematics (trigonometric-based morphing).

5.5.4 Results: optimization with a spline-based morphing parametrization

The spline-based morphing parametrization requires specifying interpolation values for the spline describing the wing modes. Here, eight cubic spline breakpoints are considered for each mode. Their upper and lower bounds are taken the same as considered by Stanford and Beran (15) and are given in Table 5.6 (in this case seven (first and eighth are equal) values suffice to determine only a natural cubic spline). Considering only the first bending and twisting modes leads to a 46% increase in the efficiency (from 0.191 to 0.282) as shown in Table 5.7. A comparison of the optimal results with those obtained by Stanford and Beran (15) is reported also in Table 5.7. Again, the capability of VTdirect to identify the optimal design points is realized. The time variations of the bending and twist modes leading to maximum efficiency as predicted by VTdirect are given in Figure 5.13. These figures show that negative twist during the downstroke and large positive bending and twist during the upstroke are the probable causes of propulsive efficiency enhancement. The optimal bending and twist modes obtained by Stanford and Beran (15) are also plotted in Figure 5.13. Clearly, VTdirect found different kinematics than that of Stanford and Beran (15). This exhibits the

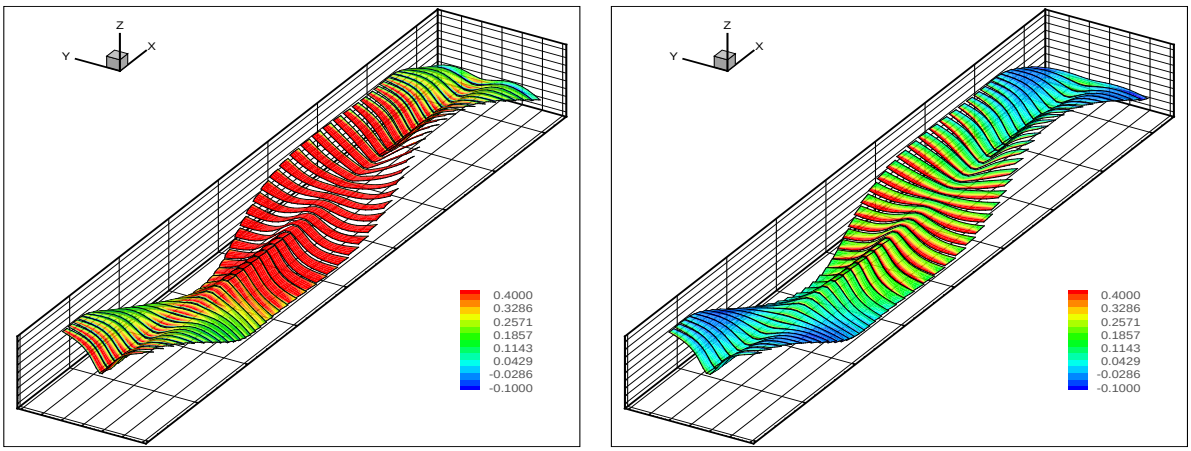

(a) NACA 83XX

(b) NACA 00XX

Figure 5.12: Flapping, morphing, and pressure distribution over the deformed wing for the optimal flight kinematics.

existence of many local optimal points in the design space.

By including the second modes (i.e., adding 14 design variables) in the global search of the optimal configuration, a higher efficiency as shown in Table 5.7 ($\eta = 0.421$) is obtained. This efficiency is close to that of Stanford and Beran (15). The time variations of the first and second bending and twist modes are plotted in Figure 5.14. Figure 5.15 shows lift-thrust phase plots for both the baseline case and the optimal design configurations as identified by VTdirect. Clearly, incorporating the second modes yields higher lift and thrust during the downstroke. However, in comparison with the baseline case where the lift remains positive during almost the entire stroke, the lift and thrust reach low negative values during the upstroke for the optimal case. This decrease in the aerodynamic loads is compensated by a significant increase along the downstroke and and results in the same averaged value for the lift and higher value for the thrust.

It is remarked that the average value of the lift coefficient in the optimized kinematics remained equal to the value in the baseline case. In fact, the optimizer would decrease the lift coefficient if it could, because that constraint is always active. So, there is a natural trade-off

Table 5.6: Kinematic variables constraints (spline-based morphing)

Wing morphing	Lower bound	Upper bound
β_1: first twisting mode	$-45°$	$45°$
β_2: second twisting mode	$-20°$	$20°$
γ_{b_1}: first bending mode	$-0.7\,c$	$0.7\,c$
γ_{b_2}: second bending mode	$-0.3\,c$	$0.3\,c$

Table 5.7: Optimal design results, NACA 83XX (spline-based morphing)

Wing morphing case		$\overline{C}_L$	$\overline{C}_T$	$\overline{C}_P$	η
First modes					
	Current method	0.695	0.0515	0.1826	**0.282**
	Stanford and Beran (15)	0.695	0.0460	0.1660	**0.281**
First and second modes					
	Current method	0.695	0.0818	0.1943	**0.421**
	Stanford and Beran (15)	0.695	0.0720	0.1630	**0.440**

between lift and efficiency, but not so for thrust and efficiency. This indicates that, in the optimized configuration, the morphing is used to improve thrust generation without affecting the lift. Moreover, activating the second modes in both twisting and bending increases the efficiency significantly.

As discussed in the previous subsections, VTdirect is a global optimizer that avoids being trapped at local optimal points. Through the present study, the capability of this tool to identify the optimal points has been shown. However, it should be mentioned that the global convergence came at the expense of a large and exhaustive search over the domain. In fact, thousands of function evaluations were required to obtain the reported results.

The kinematics modeling used here undoubtedly truncates several important parameters which may reside in the infinite-dimensional space. These kinematics (e.g., a third-order

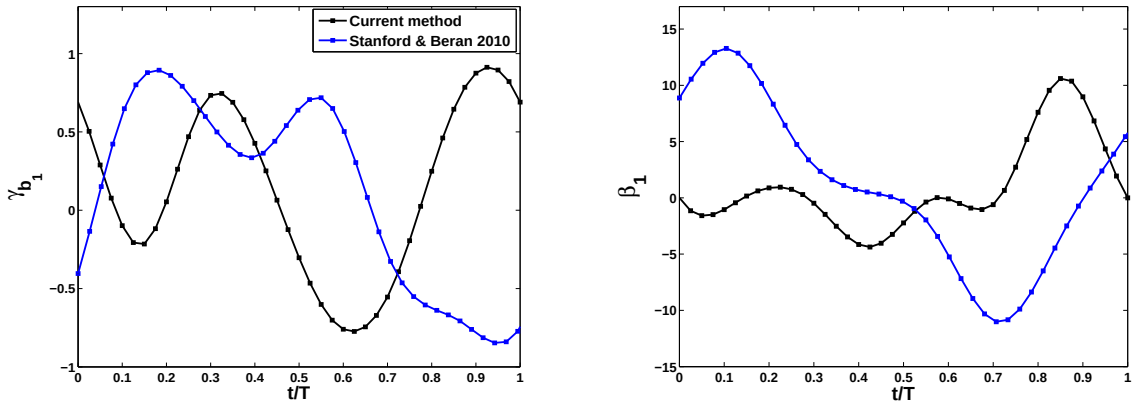

(a) Bending

(b) Twisting

Figure 5.13: Variations in time (spline-based) of the optimal wing morphing using the first bending and twisting modes. Comparison with variations of Stanford and Beran (15).

bending mode) are presumably too difficult to achieve in practice. It seems unlikely that the optimal-efficiency solution would ever converge as higher and higher morphing mode shapes are included (theoretically obtaining higher and higher efficiencies), but morphing feasibility requirements should constrain the optimum to lie within the first few mode shapes, which has been included in the present analysis.

5.6 Global vs. Local Optimization

To perform optimization, in addition to the global optimizer VTDIRECT, two gradient-based optimizers, namely GCMMA (globally convergent method of moving asymptotes) and FMINCON (Matlab function which uses sequential quadratic programming with a quasi-Newton approximation to the Hessian) are considered.

GCMMA is a gradient-based method and employs conservative convex separable approximations for solving inequality-constrained nonlinear programming problems (*minimization* problems with *less than* or *equal to* constraints). It performs the search for the optimal configuration by generating approximate subproblems at each iteration, in which the objective

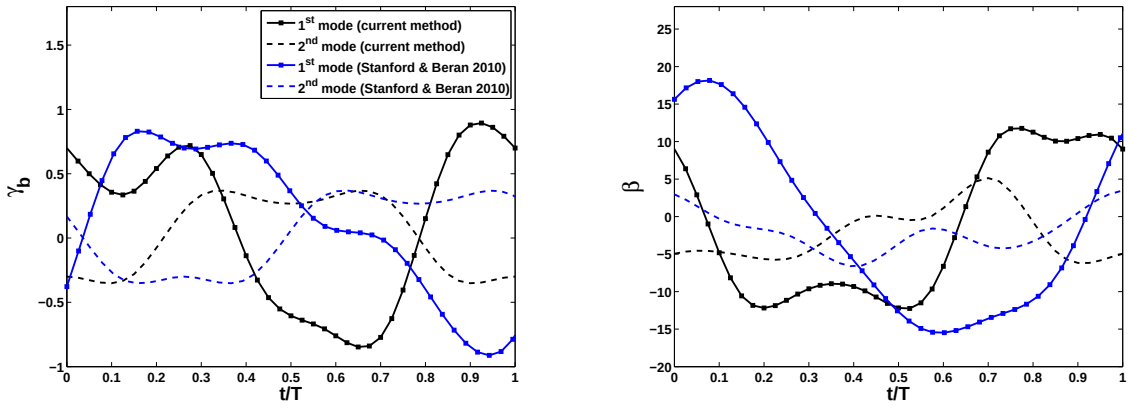

(a) Bending (b) Twisting

Figure 5.14: Variations in time (spline-based) of the optimal wing morphing using the first and second bending and twisting modes. Comparison with variations of Stanford and Beran (15).

and constraints functions are replaced by certain convex functions. The construction of these approximating functions is based mainly on gradient information at the current iteration point in the design space. Further details of the mathematical formulation of GCMMA are provided in (115; 116).

Several optimization runs are conducted with an increasing number of design variables. Table 5.8 provides a summary of the optimal results for the flapping wing as identified by different optimizers. The results show that the spline-based morphing, which requires specification of more design variables, yields a significant improvement in terms of propulsive efficiency, in particular when incorporating the second modes.

Figure 5.16 shows the progress that each optimizer made to converge to the optimal point for different morphing cases. It is remarked that the global optimizer VTDIRECT requires thousands of function evaluations to identify the optimal point while the local optimizers identify optimal design points with higher efficiency using much less function evaluations. Clearly, for the present problem, the local optimizers perform much better than the global

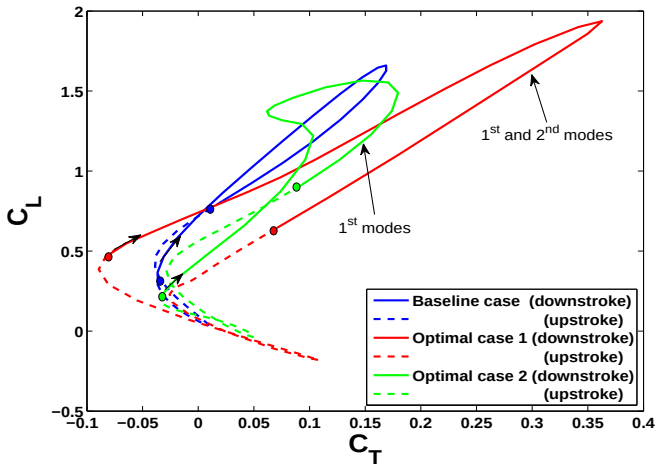

Figure 5.15: Lift coefficient vs. thrust coefficient for the optimal flight kinematics (spline-based morphing).

Table 5.8: Optimal results

	Morphing type	# of design variables	η_{opt} VTDIRECT	η_{opt} GCMMA	η_{opt} FMINCON
Case 1	Trigonometric-based First modes	4	0.2159	0.2174	0.2174
Case 2	Spline-based First modes	14	0.282	0.315	0.315
Case 3	Spline-based First & second modes	28	0.42	0.477	0.477

optimizer. As shown in Figure 5.16(c), results from the Matlab tool FMINCON show that if the no-morphing point is used as the initial guess, an efficiency of $\eta = 0.46$ is obtained while starting from the optimal point predicted by VTDIRECT yields a different point with higher efficiency ($\eta = 0.477$) and less number of function evaluations. This constitutes a

hybrid method where local and global optimizers are combined. When the optimization is performed with GCMMA, starting from different points leads to the same optimal point. This indicates that GCMMA is insensitive to the initial guess. To investigate further the efficiency

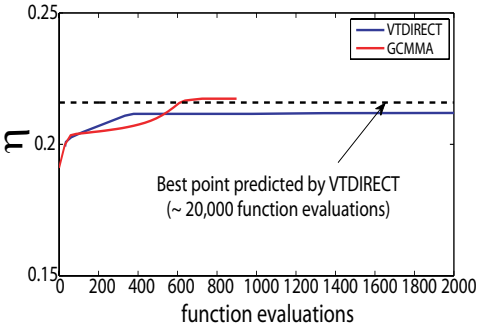

(a) Case 1

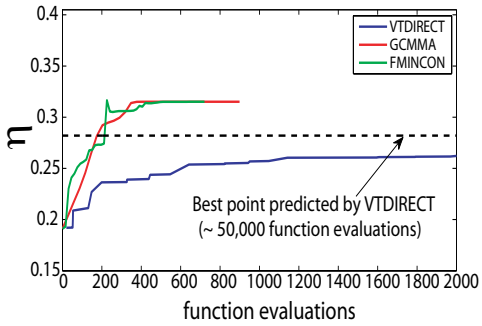

(b) Case 2

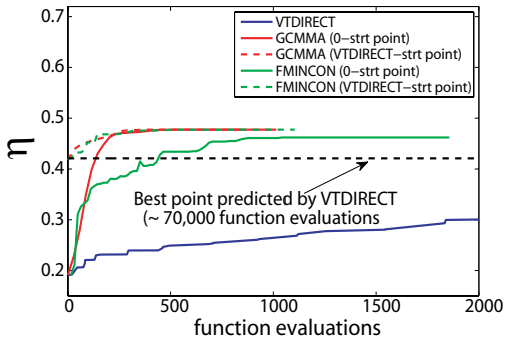

(c) Case 3

Figure 5.16: The objective function value at the best point found versus the number of evaluations for VTDIRECT, GCMMA, and FMINCON.

of the local optimizer GCMMA, a biomechanics problem (126) with 57 design variables is considered. This problem has many well separated local minima (126). VTDIRECT found an optimal point well away from the center with a value of 3048. Figure 5.17 shows the progress that GCMMA made to identify the optimal point. The final objective function is around 950000 and the optimal point is found near the center point (initial guess). Clearly,

GCMMA failed to find the optimal value. The reason behind showing this example is to point out that the efficiency of using a local or global optimizer depends on the nature of the problem and associated design space.

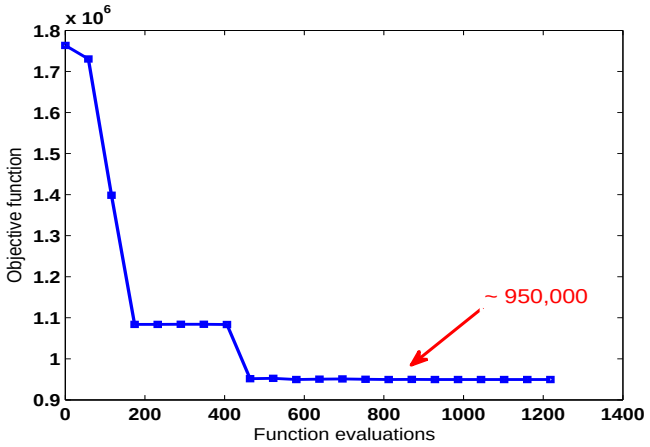

Figure 5.17: The objective function value at the best point found versus the number of evaluations for GCMMA.

5.7 Robustness of Optimal Points

To determine the sensitivity of the optimal flapping configuration predicted by GCMMA (as reflected in the propulsive efficiency) to local disturbances of the design variables, the design vectors obtained for the optimal cases are perturbed by introducing randomness following a uniform probability distribution function (±5%), and the objective function (propulsive efficiency) is evaluated at each of the perturbed vectors. The Latin hypercube sampling strategy (102; 103) is used to generate samples for these vectors. Histograms of the resulting objective function values are computed and shown in Figure 5.18. It is noted that 200 samples were used to generate the results shown in Figure 5.18. The set of samples that yield feasible design points (none of the constraints is violated) is represented by red bars. The histograms enable answers to the questions:

1. What percent of the perturbations is feasible?

A point with more nearby feasible points is a better engineering solution, since it is not desirable that moderate perturbations in system manufacturing or operating conditions result in an infeasible design.

2. Which optimal point has the largest percentage of perturbed values within, say, 1.5 % of the optimal value, and similarly for the feasible perturbed values?

For trigonometric-based morphing when considering the first modes, only 28% of the perturbed vectors are feasible. For spline-based morphing, this percentage is equal to 39% and 57.5% when considering only the first modes and both first and second modes, respectively. Clearly, the spline-based morphing, which requires specification of more design variables, yields optimal points with more nearby feasible points. Furthermore, in comparison with the other cases, the optimal point, obtained for the spline-based morphing when using the first and second modes, has the largest percentage of perturbed values remaining within 1.5% of the optimal value for both total and feasible perturbed vectors. Therefore, this point is considered as the most robust design point.

Next, case 3 is considered again, vary the number of samples, and determine the percentage of feasible perturbed vectors. As shown in Table 5.9, increasing the number of samples yields minor changes in this percentage. Then, to enable a more reasonable comparison of cases 2 and 3, only the variables defining the first modes are perturbed while keeping the remaining deterministic so that the number of design of variables would be the same for both cases. As would be expected, the percentage feasible perturbed vectors has increased from 57.5% to 61%. In fact, decreasing the number of uncertain parameters within design space would increase the level of robustness of the design point.

Table 5.9: Percentage of feasible perturbed vectors for different numbers of samples (Case 3).

Number of samples	200	1000	4000
Percentage of feasible perturbed vectors	57.5 %	56.7 %	56.77 %

5.8 How Wing Morphing Can Help in Thrust Generation?

Birds can fly by gliding (131; 132), soaring (133), or flapping (134; 135) depending on the atmospheric conditions and desired flight path. When gliding, the wings are held out to the side of the body and do not flap. The aerodynamic forces hold the bird up in the air and are similar to those generated on a fixed wing (136). Soaring differs from gliding flight in that the bird maintains its height relative to the ground and can even climb without flapping its wings. One way to perform this is to benefit from a rising air current. To generate sufficient aerodynamic forces for flight and overcome gust and turbulence in the incoming freestream, birds can also rely on flapping motion whereby they move their wings up and down in a reciprocating manner. The flapping motion consists of two half-strokes: the downstroke, which produces most of the useful lift and thrust, and the upstroke, which can also (depending on the geometric properties of the bird's wing) provide some thrust.

There is a general understanding of the physical aspects of the dynamics of bird flights (131–136). Most of this research has been based on experimental observations where results are usually interpreted using simplified aerodynamic models. Exploring the dynamics of birds' flight through higher fidelity numerical simulations of the flow and its interaction with the wing motions provides a more substantial characterization of the physics and dynamics associated with bird flights. This should facilitate better guidance for the design of engineered flying systems.

Birds have internal skeletons to which muscles are attached, permitting more localized actuation along the wing (active and passive wing morphing)(135). The three-dimensional version of the unsteady vortex lattice method is used again to simulate the flow over flapping wings that have the characteristics of two different birds, namely the *Giant petrel* and *Dove prion* (Table 5.10) to investigate the relation between morphing, aerodynamic forces and flight efficiency. For each bird, hypothetical rectangular and swept/tapered wings are considered to examine how wing geometry influences flight performance. The latter shape is based on the actual wings of the two birds, as shown in Figure 5.19.

Similarly to Stanford and Beran (15), a propulsive efficiency for bird kinematics is defined as the ratio of the power used to move the wing in the forward direction over the aerodynamic

Table 5.10: Bird characteristics and estimated aerodynamic forces. The wing camber ratio† is defined as the maximum deviation of the center of the wing from the line connecting leading and trailing edges relative to the chord length (132). Results are obtained from UVLM simulations of flapping rigid wing. The estimated mass‡ is computed based on $\overline{L}$/g where $\overline{L}$ is the average value of the lift and g is the acceleration due to gravity (g=9.81 m/s^2). The propulsive efficiency is defined as the ratio of the power used to move the wing in the forward direction over the aerodynamic power (15). The minus sign (-) indicates that the bird is unable to move forward.

Bird			*Giant petrel*	*Dove prion*
	Body mass (Kg)		**3.24**	**0.155**
	Wing span (m)		1.98	0.635
Bird characteristics(132; 134; 137; 138)	Wing area (m^2)		0.326	0.0469
	Wing camber ratio†		8%	6%
	Flapping frequency (Hz)		3.14	5.42
	Forward velocity (m/s)		15.2	11.1
		Wing root angle of attack		
	Estimated mass‡ (Kg)	$\alpha = 0°$	1.96	0.107
		$\alpha = 8°$	3.978	0.254
UVLM predictions	Thrust (N)	$\alpha = 0°$	0.506	0.01396
(rectangular wing)		$\alpha = 8°$	-0.613	-0.074
	Propulsive efficiency	$\alpha = 0°$	0.156	0.0948
		$\alpha = 8°$	(-)0.107	(-)0.2262
	Estimated mass‡ (Kg)	$\alpha = 0°$	2.027	0.112
		$\alpha = 8°$	4.1156	0.2632
UVLM predictions	Thrust (N)	$\alpha = 0°$	0.646	0.0149
(swept/tapered wing)		$\alpha = 8°$	-0.2669	-0.0894
	Propulsive efficiency	$\alpha = 0°$	0.213	0.117
		$\alpha = 8°$	(-)0.045	(-)0.247

power. The bird benefits from the wing taper and sweep to improve the performance of flight by generating more thrust that enables a higher propulsive efficiency (Table 5.10; Figure 5.20). The simulation of a flapping rigid (without morphing) wing also indicates (Figure 5.20) that to get enough lift to match the actual mass of the bird, the wing root should be placed at a specific angle of attack. To meet this requirement, the *Giant petrel* must flap its wing at an angle of attack of 4.7° when using a swept/tapered wing with a shape that approximates its physical shape. This is slightly smaller than the 5° angle required if a rectangular wing shape is assumed. For the *Dove prion*, these angles are 2.35° and 2.6° for swept/tapered and rectangular wings, respectively. Of interest is the fact that the thrust generated at those angles of attacks is very small or negative, depending on the bird wing shape. This indicates that each bird is utilizing some sort of of active wing twisting/bending to produce enough thrust for its forward motion.

Therefore, similar to the previous analysis, active shape morphing is considered to investigate its effect on the flight performance. The shape morphing is introduced using the first and second bending and twisting mode shapes to mimic each bird's wing deformations. These shapes are generated using the material and geometrical properties of the birds' wings. In-plane motions were not considered because previous results have shown that they do not need to be performed in forward flight. K. Dial (139) eliminated the neural control of certain muscle groups responsible for the change in the camber and in-plane planform motion and performed flight tests of Rock doves. He observed that the birds were capable of sustaining forward flight. However, they were incapable of performing take off and landing.

UVLM is combined with a gradient-based optimization algorithm (GCMMA) to identify the optimal kinematics (twisting and bending) that maximize the propulsive efficiency. For both birds, the results show that morphing the wing using the first bending and twisting modes yields a significant increase in the propulsive efficiency (Table 5.11). This efficiency is increased further when incorporating the second modes.

For the *Giant petrel*, morphing of the wing increases its thrust from 0.187 N to 0.38 N and its propulsive efficiency from 0.0459 to 0.38. For the *Dove prion*, morphing the wing increases its thrust from -0.00689 N to 0.059 N and its propulsive efficiency from (-)0.0442 to 0.147. The average value of the lift (represented as mass in Table 5.11) for the optimized kinematics

Table 5.11: Flight performance enhancement through morphing. Active shape morphing using first and second bending and twisting mode shapes is used to mimic local bird's wing deformations. These shapes are generated using the material and geometric properties of the birds wings (134; 140). Results are determined by combining UVLM with an optimization algorithm GCMMA(115; 116) (globally convergent method of moving asymptotes). The value of the wing root angle of attack α was chosen so that the average value of the lift $\overline{L}$ balances the weight of the bird for the base (no morphing) case.

Bird			*Giant petrel*	*Dove prion*
Rectangular wing				
	Wing root angle of attack (α)		5°	2.6°
	Mass (Kg)	Rigid wing	3.24	0.155
		Morphed wing (1^{st} modes)	3.24	0.155
		Morphed wing (1^{st} and 2^{nd} modes)	3.24	0.155
	Thrust (N)	Rigid wing	-0.108	-0.00808
		Morphed wing (1^{st} modes)	0.649	0.02031
		Morphed wing (1^{st} and 2^{nd} modes)	1.139	0.04051
	Propulsive efficiency	Rigid wing	(-)0.0256	(-)0.04298
		Morphed wing (1^{st} modes)	0.0864	0.06238
		Morphed wing (1^{st} and 2^{nd} modes)	0.15	0.12804
Swept/tapered wing				
	Wing root angle of attack (α)		4.7°	2.35°
	Mass (Kg)	Rigid wing	3.24	0.155
		Morphed wing (1^{st} modes)	3.24	0.155
		Morphed wing (1^{st} and 2^{nd} modes)	3.24	0.155
	Thrust (N)	Rigid wing	0.187	-0.00689
		Morphed wing (1^{st} modes)	2.52	0.03136
		Morphed wing (1^{st} and 2^{nd} modes)	2.59	0.059
	Propulsive efficiency	Rigid wing	0.0459	(-)0.0442
		Morphed wing (1^{st} modes)	0.32	0.09463
		Morphed wing (1^{st} and 2^{nd} modes)	0.38	0.1471

remains equal to its value for the baseline case (without morphing). This indicates that, in the optimized configuration, the morphing is used to improve thrust generation without affecting the lift.

Figure 5.21 shows the deformed wing for the optimal flight paths for the *Giant petrel* and *Dove prion* birds. To gain an insight into the wing deformation, the baseline flapping case is also shown so that the combined bending and twisting deformations of the wings are observed. The optimal kinematics for both birds are quite different. Clearly, based on the material and geometric properties of its wing, and the flapping frequency, each bird employs specific kinematics to control its flight performance to make it as efficient as possible.

To the best of my knowledge, there is no empirically-based parameterization (e.g., trigonometric or spline-based approximations) of the bird kinematics during forward flights. This is most likely due to the complex system of skeletal muscles actuating the wing motions and deformations. However, many attempts have been made to capture bird wing motions for different flight speeds with high-speed video cameras (10; 141–143). To this end, tapes were attached to some parts of the bird body and wing and were tracked during flights. The path traced by these tapes showed that bird wing kinematics are governed by a complex combination of vertical and horizontal motions along with bending and twisting. The experimental observations reported in (10; 141–143) demonstrated the significant influence of the wing shape, flight speed, and flapping frequency on the wing kinematics. In particular, they showed that significant differences exist between the bird species in terms wing kinematics as can be seen from the path of the wing tip during flapping cycle. For the magpie, the wing tip followed an elliptical path for different flight speeds. For the pigeon, the wing tip followed a figure-eight pattern at relatively low speeds, and an ellipse at higher speeds. Clearly, the wing tip paths as reported in (10; 141–143) are result of the combined flapping, twisting, and bending motions. These flight observations are consistent with results obtained from the present numerical analysis.

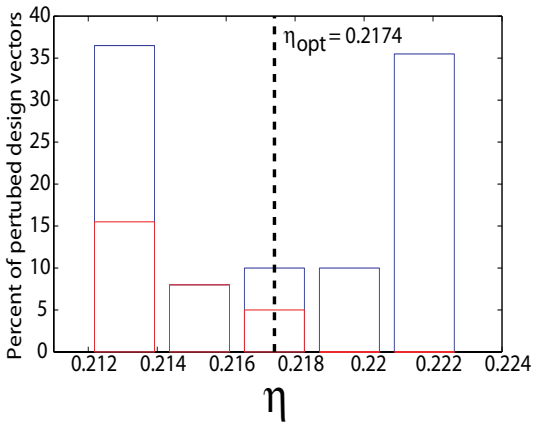

(a) Case 1

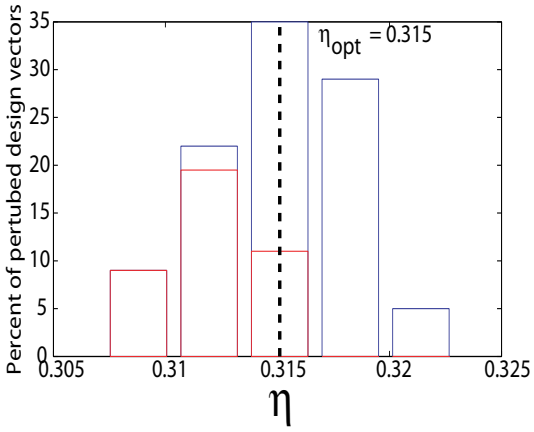

(b) Case 2

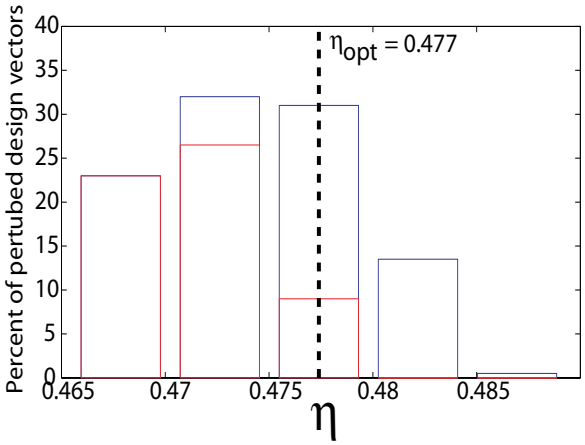

(c) Case 3

Figure 5.18: Histograms: sensitivity of optimal design points to perturbations in the design variables.

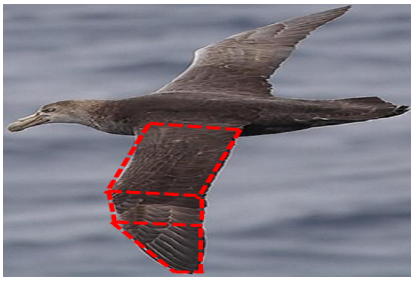

(a) *Giant petrel*

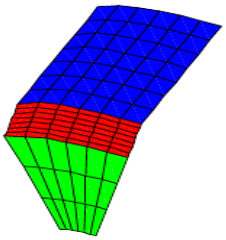

(b) Simulated wing

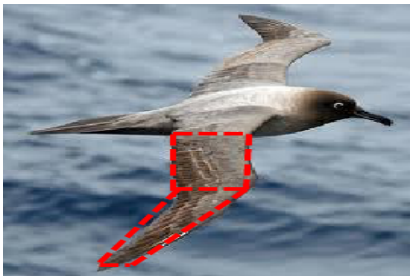

(c) *Dove prion*

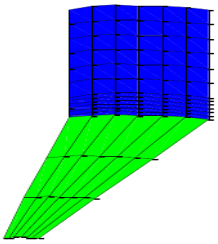

(d) Simulated wing

Figure 5.19: Simulated wing shapes of the *Giant petrel* and *Dove prion* birds. Sweep and taper are introduced in the wing geometry of each bird to reproduce its real shape.

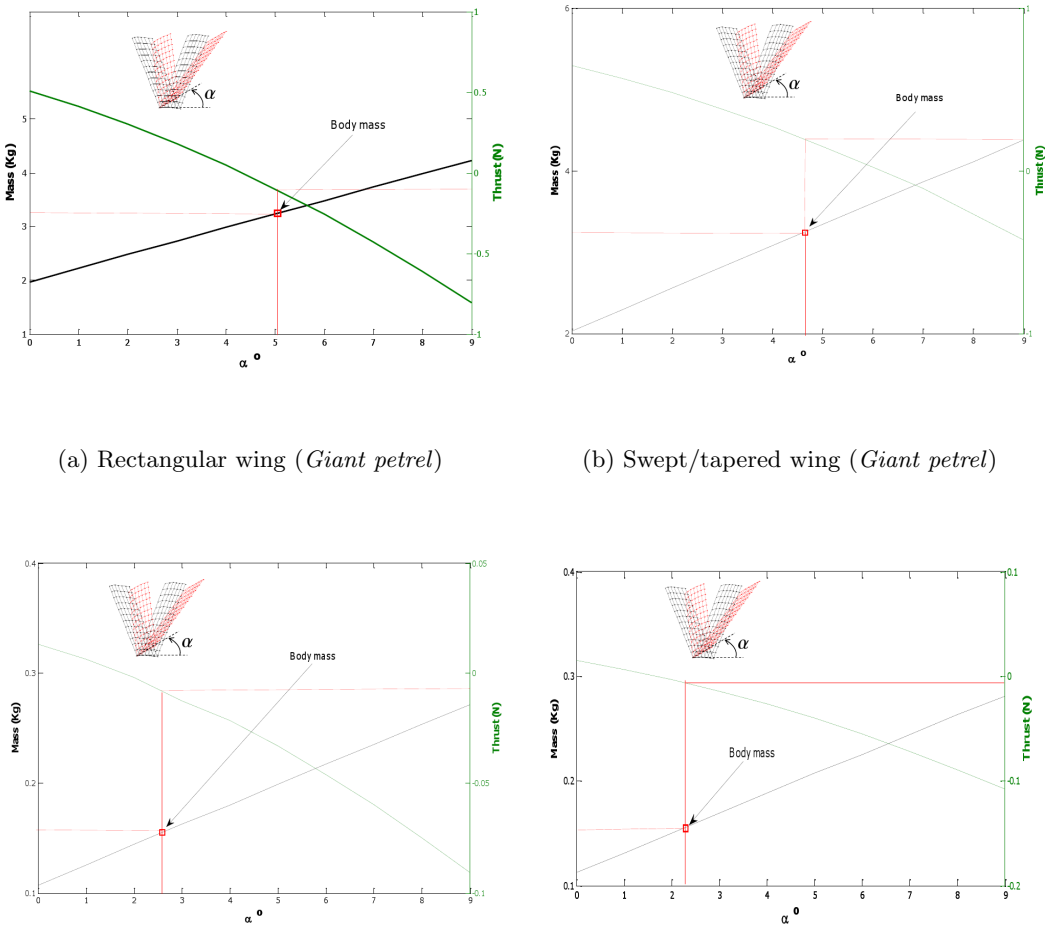

(a) Rectangular wing (*Giant petrel*)

(b) Swept/tapered wing (*Giant petrel*)

(c) Rectangular wing (*Dove prion*)

(d) Swept/tapered wing (*Dove prion*)

Figure 5.20: Variations of the estimated lift in terms of mass and thrust with the wing root angle of attack α for the *Giant petrel* and *Dove prion* bird (rigid wings). For each bird, rectangular and swept/tapered wings are considered to investigate how wing geometry affects flight performance. The latter shape is based on the actual wing shape as shown in Figure 5.19. Clearly, the bird benefits from the wing taper and sweep to improve the performance of flight (leading to higher thrust). The results also indicate that to get enough lift to match the actual mass of the bird, the wing root should be placed at specific angle of attack. However, the generated thrust is very small (or negative depending on the bird wing shape) indicating that the bird is utilizing some sort of active wing twisting/bending to produce enough thrust for forward motion.

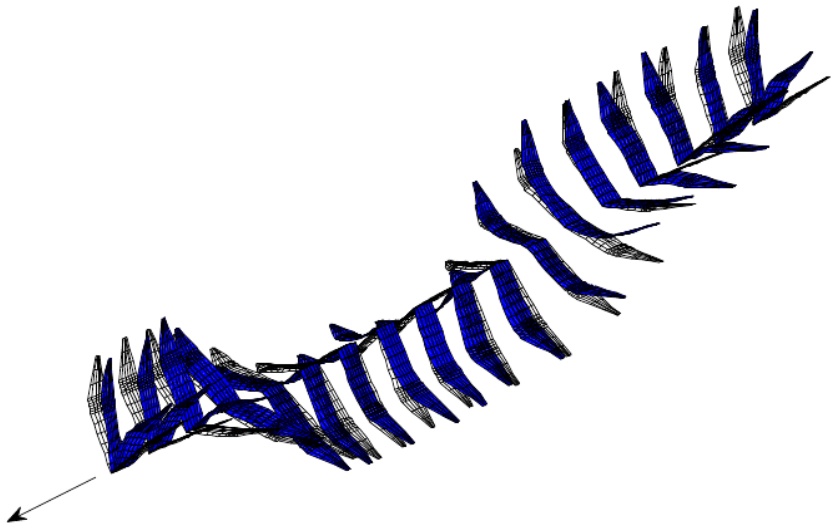

(a) *Giant petrel*

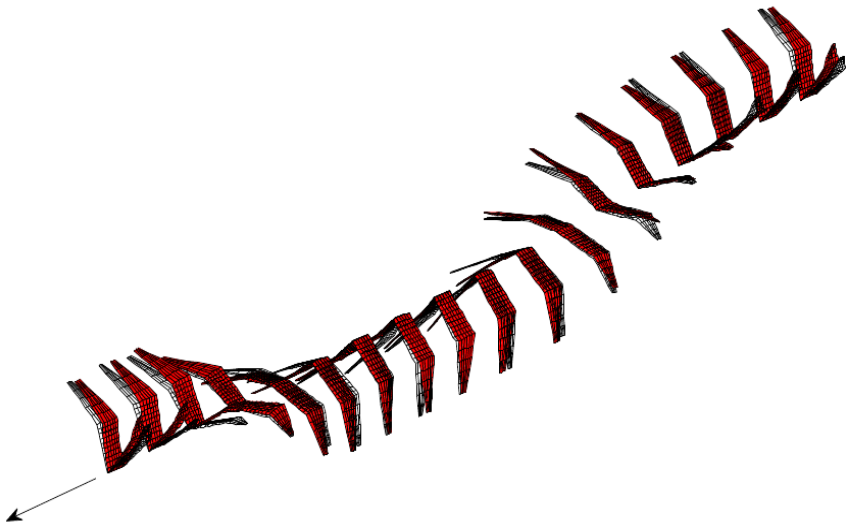

(b) *Dove prion*

Figure 5.21: Optimal flight paths of the swept/tapered wings: rigid (thin lines) and morphed shapes (colored surfaces). For the *Giant petrel*, the wing root angle of attack is set equal to 4.7°. Morphing the wing increases its thrust from 0.187 N to 0.38 N and its propulsive efficiency (Thrust power U/Aerodynamic power) from 0.0459 to 0.38. For the *Dove prion*, the wing root angle of attack is set equal to 2.35°. Morphing the wing increases its thrust from -0.00689 N to 0.059 N and its propulsive efficiency from (-)0.0442 to 0.147.

Chapter 6

Conclusions and Recommendations for Future Work

The research carried out in this thesis is mainly motivated by the need for reduced-order modeling and analysis of multidisciplinary systems. The contribution is to show, through studying different dynamical systems, how model reduction can be useful in characterizing the physics and dynamics associated with these systems, implementing control strategies to meet desirable responses, and performing rapid and reasonably accurate exploration of large design spaces as required for carrying out optimization and sensitivity analyses. All of these aspects are helpful in enhancing the performance of such systems. In this chapter, the main findings of the research are summarized and concluding remarks and recommendations for future work are presented.

6.1 Summary and Conclusions

It is shown that reduced-order models can be used to model and analyze different systems. In one example, a low-dimensional method to predict the effects of unsteadiness in the inflow on force coefficients acting on a circular cylinder has been developed. The approach was based on combining proper orthogonal decomposition (POD) and linear stochastic estimator technique (LSE). First, POD has been used to derive a reduced-order model of the velocity field. Then, to overcome the difficulty of developing a ROM using Poisson's equation, the

pressure field has been related to the velocity field through a mapping function based on LSE. Results for force coefficients obtained from this approach were verified by comparison with results from CFD simulations. This finding shows the capability of the developed tool to accurately predict the loads and then, could serve as the basis to apply additional analyses such as implementing control strategies.

In another example, the aeroelastic response of the Goland wing has been considered and two approaches have been followed to derive its normal form. Such a form constitutes an effective tool to model the main physical behaviors of aeroelastic systems. In the first approach, an approximation of the wing's response near the Hopf bifurcation was constructed by directly applying the method of multiple scales to the two coupled partial-differential equations of motion. In the second approach, the same method has been applied to a Galerkin discretized model that is based on the mode shapes of a cantilever beam. The perturbation results from both approaches were verified by comparison with results from numerical integration of the discretized equations.

Reduced-order models have been also used to determine the effects of variations in the linear and nonlinear spring coefficients of a rigid airfoil undergoing pitch and plunge motions on its stability near a bifurcation point. In the first approach, the intrusive polynomial chaos expansion (PCE) has been implemented on the governing equations. This expansion yielded a set of coupled equations that are numerically solved. In the second approach, modern methods of nonlinear dynamics have been used to derive the normal form. A comparison of the usefulness and effectiveness of these approaches was shown by characterizing sensitivity of the response of the system to variations in its parameters. The same aeroelastic system was used to present a methodology to convert subcritical bifurcations (dangerous) of aeroelastic systems into supercritical bifurcations (safe). This methodology involved the (i) reduction of the dynamics of the system into a one-dimensional dynamical system using the method of multiple scales and (ii) design of a nonlinear feedback controller to convert subcritical to supercritical bifurcations and reduce the amplitude of any ensuing LCO.

The focus has been also on the modeling, analysis, and optimization of the kinematics of flapping wings in the context of using them in micro air vehicles (MAVs). The intrusive PCE approach was implemented on a two-dimensional version of the unsteady vortex lattice

method to determine uncertainty in gust loads on a rigid airfoil due to imprecision in an incoming gust characteristics. The results yielded the sensitivity of the lift coefficient to variations in the intensities and integral length scales of the gust fluctuations. Lift coefficient fluctuations about the mean at each time step were affected primarily by the intensity of the vertical fluctuations, which should be expected for an airfoil fixed at zero angle of attack. Second in order of importance was the integral length scale of the vertical velocity component. As might be expected, the lift coefficient was relatively insensitive to the streamwise gust parameters. Consequently, if the flow model and parameter ranges employed in the analysis are appropriate of the intended application, a stochastic analysis of the effects of gust on the lift coefficient of an airfoil would be satisfactory if the streamwise gusts were neglected. More generally, the analysis presented here provides a basis for exploring these and other parametric effects in a broad range of gust loads analyses. This successful implementation of the intrusive PCE provides guidance and a baseline for efforts to quantify uncertain gust loads on MAVs with higher fidelity models.

The unsteady vortex lattice method has been also combined with a hybrid of global and local optimization algorithms to optimize the kinematics of flapping wings in hovering flights. The objective was to minimize the required aerodynamic power to produce enough lift to sustain hovering flight. The flapping wing was chosen so that its chord length and flapping frequency match the morphological and flight properties of insects with different masses. The analysis identified optimal kinematics that agree fairly well with the observed data, as well as previously published numerical results. Furthermore, two levels of unsteadiness associated with the flapping motion have been considered to show that specific kinematics need to be employed to control the flight performance and make it as efficient as possible. The present aerodynamic model can be extended to accurately treat arbitrary deforming planforms.

A global search has been performed to find the optimal flapping kinematics of forward flights that maximizes the propulsive efficiency under lift and thrust constraints. For that, a three-dimensional version of the unsteady vortex lattice method has been implemented to simulate the flow over a flapping wing in forward flight. Furthermore, active shape morphing of the wing was considered by introducing time-varying bending and twist. The aerodynamic tool and kinematics parametrization were then combined with global and local optimization

algorithms. Two types of morphing parameterizations have been investigated: trigonometric and spline-based. The use of a spline-based morphing parametrization, which requires the specification of more design variables, has enabled a significant improvement in the propulsion efficiency. Furthermore, it has been remarked that the average value of the lift coefficient in the optimized kinematics remained equal to the value in the baseline case. This indicates that morphing is most efficiently used to generate thrust and not increase lift beyond the basic value obtained by flapping only. The results showed also that activating the second modes in both twisting and bending increases the efficiency significantly. Moreover, a sensitivity analysis of the optimal design points has been performed to investigate the effects of perturbing various parameters on the propulsive efficiency and solution feasibility. Finally, an innovative analysis has been carried out to explain why birds morph (deform) their wings and employ specific wing shapes to control their flight performance, as well as to make it more efficient.

6.2 Recommendations for Future Work on Micro Air Vehicles

In the last component of the research presented here, the goal was to optimize the flapping kinematics that maximize the aerodynamic performance in the context of using them in MAVs. But, there was no investigation of the MAV controllability under this "aero-optimum" kinematics. In reality, both controllability and aerodynamic performance should be considered when deciding on the proper kinematics to be employed. Thus, a significant improvement to the current study on MAVs would be to add the controllability component in the optimization process while modeling the aerodynamics with the UVLM.

Using UVLM for control and optimization might require development of a phenomenological model in the form of differential equations that capture the effects of unsteady motions and that can be used for arbitrary wing kinematics and geometry. Current aerodynamic modeling tools employed in flight dynamics of flapping wing MAV's lack these aspects.

Bibliography

[1] Akhtar, I., Nayfeh, A. H., and Ribbens, C. J., "On the Stability and Extension of Reduced-Order Galerkin Models in Incompressible Flows: A Numerical Study of Vortex Shedding," *Theoretical and Computational Fluid Dynamics*, Vol. 23, 2009, pp. 213–237.

[2] Nayfeh, A. H., Owis, F., and Hajj, M. R., "A Model for the Coupled Lift and Drag on a Circular Cylinder," *Proceedings of DETC03 ASME 2003 Design Engineering Technical Conferences and Computers and Information in Engineering Conference*, DETC2003–VIB48455, 2003.

[3] Akhtar, I., Marzouk, O. A., and Nayfeh, A. H., "A van der Pol-Duffing Oscillator Model of Hydrodynamic Forces on Canonical Structures," *Journal of Computational and Nonlinear Dynamics*, Vol. 4, 2009, pp. 041006–1–9.

[4] Petricca, L., Ohlckers, P., and Grinde, C., "Micro- and Nano-Air Vehicles: State of the Art," *International Journal of Aerospace Engineering*, 2011, Article ID 214549, 17 pages, doi:10.1155/2011/214549.

[5] Shyy, W., Aono, H., Chimakurthi, S. K., Trizila, P., Kang, C. K., Cesnik, C. E. E., and Liu, H., "Recent Progress in Flapping Wing Aerodynamics and Aeroelasticity," *Progress in Aerospace Sciences*, 2010, pp. 284–327.

[6] Ansari, S. A., Zbikowski, R., and Knowles, K., "Aerodynamic Modelling of Insect-like Flapping Flight for Micro Air Vehicles," *Progress in Aerospace Sciences*, Vol. 42, 2006, pp. 129–172.

[7] Shyy, W., Lian, Y., Tang, J., Vileru, D., and Liu, H., *Aerodynamics of Low Reynolds Number Flyers*, Cambridge University Press, MA, 2008.

[8] Mueller, T. H., *Fixed and Flapping Wing Aerodynamics for Micro Air Vehicles Applications*, American Institute of Aeronautics and Astronautics, Inc, 2001.

[9] Willmott, A. P. and Ellington, C. P., "The Mechanics of Flight in the Hawkmoth Manduca Sexta," *Journal of Experimental Biology*, Vol. 200, 1997, pp. 2705–2745.

[10] Tobalske, B. W., Hedrick, T. L., and Biewener, A. A., "Wing Kinematics of Avian Flight Across Speeds," *Journal of Avian Biology*, Vol. 34, 2003, pp. 177–184.

[11] Wallace, L. D., Lawson, N. J., Harvey, A. R., Jones, J. D. C., and Moore, A. J., "High-Speed Photogrammetry System For Measuring the Kinematics of Insect Wings," *Applied Optics*, Vol. 45, 2006, pp. 349–4173.

[12] Sane, S. P., "The Aerodynamics of Insect Flight," *Journal of Experimental Biology*, Vol. 206, 2003, pp. 4191–4208.

[13] Yuan, W., Lee, R., Hoogkamp, E., and Khalid, M., "Numerical and Experimental Simulations of Flapping Wings," *International Journal of Micro Air Vehicles*, Vol. 2, 2010, pp. 181–209.

[14] Berman, G. J. and Wang, Z. J., "Energy-Minimizing Kinematics in Hovering Insect Flight," *Journal of Fluid Mechanics*, Vol. 582, 2007, pp. 153–168.

[15] Stanford, B. K. and Beran, P. S., "Analytical Sensitivity Analysis of an Unsteady Vortex-Lattice Method for Flapping-Wing Optimization," *Journal of Aircraft*, Vol. 47, 2010, pp. 647–662.

[16] Moore, J., Stanford, B. K., McClung, A., and Beran, P. S., "Variable-Fidelity Kinematic Optimization of a Two-Dimensional Hovering Wing," *Proceedings of the 49th AIAA Aerospace Science Meeting and Exhibit*, AIAA Paper No. 2011-1245, 2011.

[17] Jones, K. D., Dohring, C. M., and Platzer, M. F., "Experimental and Computational Investigation of the Knoller-Betz Effect," *AIAA Journal*, Vol. 36, 1998, pp. 1240–1246.

[18] Dickinson, M. H., Lehmann, F.-O., and Sane, S. P., "Wing Rotation and the Aerodynamics Basis of Insect Flight," *Science*, Vol. 284, 1999, pp. 1954–1960.

[19] Liu, H., "Integrated Modeling of Insect Flight: From Morphology, Kinematics to Aerodynamics," *Journal of Computational Physics*, Vol. 228, 2009, pp. 439–459.

[20] Street, C. L. and Hussaini, M. Y., "Uncovering the Physics of Flapping Flat Plates with Artificial Evolution," *Journal of Fluid Mechanics*, Vol. 53, 2005, pp. 403–409.

[21] Muijres, F. T., l. C. Johansson, Barfield, R., Spedding, G. R., and Hedenstrom, A., "Leading-Edge Vortex Improves Lift in Slow-Flying Bats," *Science*, Vol. 319, 2008, pp. 1250–1253.

[22] Anderson, J. D., *Fundamentals of Aerodynamics*, 3rd ed. McGraw-Hill, New York, 2001.

[23] Shyy, W., Trizila, P., Kang, C.-K., and Aono, H., "Can Tip Vortices Enhance Lift of a Flapping Wing?" *AIAA Journal*, Vol. 47, 2009, pp. 289–293.

[24] Sane, S. P. and Dickinson, M. H., "The Aerodynamics Effects of Wing Rotation and a Revised Quasi-steady Model of Flapping Flight," *Journal of Experimental Biology*, Vol. 205, 2002, pp. 1087–1096.

[25] Birch, J. M. and Dickinson, M. H., "The Influence of Wing Wake Interactions on the Production of Aerodynamic Forces in Flapping Flight," *Journal of Experimental Biology*, Vol. 206, 2003, pp. 2257–2272.

[26] Grodnitsky, D. L. and Morozov, P. P., "Vortex Formation during Tethered Flight of Functionally and Morphologically Two-Winged Insects," *Journal of Experimental Biology*, Vol. 182, 1993, pp. 11–40.

[27] DeLaurier, J. and Winfield, J., "Simple Marching-Vortex Model for Two-Dimensional Unsteady Aerodynamics," *Journal of Aircraft*, Vol. 27, 1990, pp. 376–378.

[28] Vest, M. S. and Katz, J., "Unsteady Aerodynamic Model of Flapping Wings," *AIAA Journal*, Vol. 34, 1996, pp. 1435–1440.

[29] Fritz, T. E. and Long, L. N., "Object-Oriented Unsteady Vortex Lattice Method for Flapping Flight," *Journal of Aircraft*, Vol. 41, 2004, pp. 1275–1290.

[30] Katz, J. and Plotkin, A., *Low-Speed Aerodynamics*, Cambridge University Press, MA, 2001.

[31] Palacios, R., Murua, J., and Cook, R., "Structural and Aerodynamic Models in Nonlinear Flight Dynamics of Very Flexible Aircraft," *AIAA Journal*, Vol. 48, 2010, pp. 2648–2658.

[32] Zdunich, P., "Separated-Flow Discrete Vortex Model for Nano-Scale Hovering Flapping Wings," *Proceedings of the 26th Applied Aerodynamics Conference*, AIAA Paper No. 2008-6245, 2008.

[33] Vanella, M., T. Fitzgerald, S. P., Balaras, E., and Balachandran, B., "Influence of Flexibility on the Aerodynamic Performance of a Hovering Wing," *Journal of Experimental Biology*, Vol. 212, 2009, pp. 95–105.

[34] Wu, J. H., Zhang, Y. L., , and Sun, M., "Hovering of model insects: simulation by coupling equations of motion with NavierStokes equations," *Journal of Experimental Biology*, Vol. 212, 2009, pp. 3313–3329.

[35] Willis, D. J., Person, P., Israeli, E. R., Peraire, J., Swartz, S. M., and Breuer, K. S., "Multifidelity Approaches for the Computational Analysis and Design of Effective Flapping Wing Vehicles," *Proceedings of the 47th AIAA Aerospace Science Meeting and Exhibit*, AIAA Paper No. 2008-518, 2008.

[36] Heathcote, S., Wang, Z., and Gursul, I., "Effect of Spanwise Flexibility on Flapping Wing Propulsion," *Journal of Fluids and Structures*, Vol. 24, 2008, pp. 183–199.

[37] Shyy, W., Lian, Y., Tang, J., Liu, H., Trizila, P., Stanford, B., bernal, L., Cesnik, C., Friedmann, P., and Ifju, P., "Computational Aerodynamics of Low Reynolds Number Plunging, Pitching and Flexible Wings for MAV Applications," *Proceedings of the 46th AIAA Aerospace Science Meeting and Exhibit*, AIAA Paper No. 2008-523, 2008.

[38] Weis-Fogh, T., "Quick Estimates of Flight Fitness in Hovering Animals, Including Novel Mechanisms for Lift Production," *Journal of Experimental Biology*, Vol. 59, 1973, pp. 169–230.

[39] Zhu, Q., "Numerical Simulation of a Flapping Foil with Chordwise or Spanwise Flexibility," *AIAA Journal*, Vol. 45, 2007, pp. 2448–2457.

[40] Stanford, B. K. and Beran, P. S., "Formulation of Analytical Design Derivatives for Nonlinear Unsteady Aeroelasticity," *AIAA Journal*, Vol. 49, 2011, pp. 598–610.

[41] Stanford, B. K. and Beran, P. S., "An Updated Lagrangian Shell and Vortex Lattice Aeroelastic Framework for Flapping Wings," *International Forum on Aeroelasticity and Structural Dynamics*, 2009.

[42] Akhtar, I., Nayfeh, A. H., and Ribbens, C. J., "On the Stability and Extension of Reduced-Order Galerkin Models in Incompressible Flows," *Theoretical and Computational Fluid Dynamics*, Vol. 23, 2009, pp. 213–237.

[43] Akhtar, I., *Parallel Simulations, Reduced-Order Modeling, and Feedback Control of Vortex Shedding using Fluidic Actuators*, Ph.D. thesis, Virginia Tech, Blacksburg, VA, 2008.

[44] Deane, A. E. and Mavriplis, C., "Low-dimensional description of the dynamics in separated flow past thick airfoils," *AIAA*, Vol. 6, 1994, pp. 1222–1234.

[45] Akhtar, I., Nayfeh, A. H., and Ribbens, C. J., "A Reduced-order Galerkin Model of the Pressure Field in Incompressible Flows," *Proceedings of the 46th Aerospace Sciences Meeting and Exhibit*, AIAA Paper No. 2008-611, 2008.

[46] Pettit, C. L. and Beran, P. S., "Application of proper orthogonal decomposition to the discrete Euler equations," *International Journal for Numerical Methods in Engineering*, Vol. 55, 2002, pp. 479–497.

[47] Anttonen, J. S. R., King, P. I., and Beran, P. S., "POD-Based Reduced-Order Models with Deforming Grids," *Mathematical and Computer Modelling*, Vol. 38, 2003, pp. 41–62.

[48] Anttonen, J. S. R., King, P. I., and Beran, P. S., "Applications of Multi-POD to a Pitching and Plunging Airfoil," *Mathematical and Computer Modelling*, Vol. 42, 2005, pp. 245–259.

[49] Sirovich, L. and Kirby, M., "Low-Dimensional Procedure for the Characterization of Human Faces," *Journal of Optical Society of America A*, Vol. 4, 1987, pp. 529–524.

[50] Burkardt, J., Du, Q., Gunzburger, M. D., and Lee, H. C., "Reduced order modeling of complex systems," *Biennal Conferences on Numerical Analysis*, University of Dundee, Scotland, UK., 2002.

[51] Noack, B. R., Papas, P., and Monkewitz, P. A., "The Need for a Pressure-Term Representation in Empirical Galerkin Models of Incompressible Shear Flows," *Journal of Fluid Mechanics*, Vol. 523, 2005, pp. 339–365.

[52] Ma, X. and Karniadakis, G., "A Low-Dimensional Model for Simulating Three-Dimensional Cylinder Flow," *Journal of Fluid Mechanics*, Vol. 458, 2002, pp. 181–190.

[53] Akhtar, I. and Nayfeh, A. H., "Model Based Control of Laminar Wake Using Fluidic Actuation," *Journal of Computational and Nonlinear Dynamics*, Vol. 5, 2010, pp. 04105–1–04105–9.

[54] Taylor, J. A. and Glauser, "Towards Practical Flow Sensing and Control via POD and LSE Based Low-Dimensional Tools," *Journal of Fluids Engineering*, Vol. 126, 2004, pp. 337–345.

[55] Ausseur, J. M., Pinier, J. T., Glausser, M. N., and Higuchi, H., "Experimental Development of a Reduced-Order Model for Flow Separation Control," *Proceedings of the AIAA 30th Aerospace Sciences Meeting and Exhibit*, AIAA Paper No. 2006-1251, 2006.

[56] Beran, P. S., "Computation of Limit-Cycle Oscillation Using a Direct Method," *Proceedings of the 40th AIAA/ASME/ASCE/AHS/ASC Structures, Structural Dynamics, and Materials Conference*, AIAA Paper No. 99-24933, 1999.

[57] Morton, S. A. and Beran, P. S., "Hopf-Bifurcation Analysis of Airfoil Flutter at Transonic Speeds," *AIAA Journal*, Vol. 36, 1999, pp. 421–429.

[58] Badcock, K., Woodgate, M., and Richards, B., "Hopf Bifurcation Calculations for a Symmetric Airfoil in Transonic Flow," *AIAA Journal*, Vol. 42, 2004, pp. 883–892.

[59] Woodgate, M. and Badcock, K., "A Reduced Order Model for Damping Derived from CFD Based Aeroelastic Simulations," *Proceedings of the 47th AIAA/ASME/ASCE/AHS/ASC Structures, Structural Dynamics, and Materials Conference*, AIAA Paper No. 2006-2021, 2006.

[60] Dimitriadis, G., Vio, G. A., and Cooper, J. E., "Stability and Limit Cycle Oscillations Amplitude Prediction for Simple Nonlinear Aeroelastic Systems," *Proceedings of the 45th AIAA/ASME/ASCE/AHS/ASC Structures, Structural Dynamics, and Materials Conference*, AIAA Paper No. 2004-1693, 2004.

[61] Leng, G., "Reduced-Order Nonlinear Analysis of Aircraft Dynamics," *Journal of Guidance, Control, and Dynamics*, Vol. 18, 1995, pp. 361–364.

[62] Lucia, D. J., Beran, P. S., and Silva, W. A., "Reduced-Order Modeling: New Approaches for Computational Physics," *Progress in Aerospace Sciences*, Vol. 40, 2004, pp. 51–117.

[63] Kim, K. and Strganac, T. W., "Nonlinear Response of a Cantilever Wing with an External Store," *Proceedings of the 40th AIAA/ASME/ASCE/AHS/ASC Structures, Structural Dynamics, and Materials Conference and Exhibit*, AIAA Paper No. 2003-1708, 2003.

[64] Nayfeh, A. H. and Balachandran, B., *Applied Nonlinear Dynamics: Analytical, Computational, and Experimental Methods*, Wiley, New York, 1995.

[65] Nayfeh, A. H., *Introduction to Perturbation Techniques*, Wiley, New York, 1981.

[66] Nayfeh, A. H., Hammad, B. K., and Hajj, M. R., "Discretization Effects on Flutter Aspects and Control of Wing/Store Configurations," *Journal of Vibration and Control*, 2011, doi:10.1177/1077546311408468.

[67] Dowell, E. H. and Tang, D., "Nonlinear Aeroelasticity and Unsteady Aerodynamics," *AIAA Journal*, Vol. 40, 2002, pp. 1697–1707.

[68] Raghothama, A. and Narayanan, S., "Non-Linear Dynamics of a Two-Dimensional Airfoil by Incremental Harmonic Balance Method," *Journal of Sound and Vibration*, Vol. 226, 1999, pp. 493–517.

[69] Liu, L., Wong, Y. S., and Lee, B. H. K., "Application of the Center Manifold Theory in Non-Linear Aeroelasticity," *Journal of Sound and Vibration*, Vol. 234, 2000, pp. 641–659.

[70] Gilliatt, H. C., Strganac, T. W., and Kurdila, A. J., "An investigation of Internal Resonance in Aeroelastic Systems," *Nonlinear Dynamics*, Vol. 31, 2003, pp. 1–22.

[71] Allen, M. S. and Camberos, J. A., "Comparison of Uncertainty Propagation/Response Surface Techniques for Two Aeroelastic Systems," *Proceedings of the 50th AIAA/ASME/ASCE/AHS/ASC Structures, Structural Dynamics, and Materials Conference*, AIAA Paper No. 2009-2269, 2009.

[72] Witteveen, J. A. S., *Uncertainty Quantification Methods for Flow and Fluid-Structure Interaction Simulations*, Ph.D. thesis, Delft University of Technology, The Netherlands, 2008.

[73] Millman, D. R., King, P. I., and Beran, P. S., "Airfoil Pitch-and-Plunge Bifurcation Behavior with Fourier Chaos Expansions," *Journal of Aircraft*, Vol. 42, 2005, pp. 376–384.

[74] Chassaing, J.-C. and Lucor, D., "Stochastic Aeroelastic Analysis of a Pitching and Plunging Airfoil in an Incompressible Flow," *International Forum on Aeroelasticity and Structural Dynamics*, 2009.

[75] Lee, B. H. K., Jiang, L. Y., and Wong, Y. S., "Flutter of an Airfoil with a Cubic Restoring Force," *Journal of Fluids and Structures*, Vol. 13, 1999, pp. 75–101.

[76] Chabalko, C. C., Hajj, M. R., Mook, D. T., and Silva, W. A., "Characterization of the LCO Response Behaviors of the NATA Model," *Proceedings of the 47th AIAA/ASME/ASCE/AHS/ASC Structures, Structural Dynamics, and Materials Conference*, AIAA Paper No. 2006-1852, 2006.

[77] Strganac, T. W., J. Ko, J., and Thompson, D. E., "Identification and Control of Limit Cycle Oscillations in Aeroelastic Systems," *Proceedings of the 40th AIAA/ASME/ASCE/AHS/ASC Structures, Structural Dynamics, and Materials Conference and Exhibit*, AIAA Paper No. 99-1463, 1999.

[78] Najm, H. N., "Uncertainty Quantification and Polynomial Chaos Techniques in Computaional Fluid Dynamics," *The Annual Review of Fluid Mechanics*, Vol. 41, 2009, pp. 35–52.

[79] Xiu, D. and Karniadakis, G. E., "Modeling Uncertainty in Flow Simulations via Generalized Polynomial Chaos," *Journal of Computational Physics*, Vol. 187, 2003, pp. 137–167.

[80] Ghanem, R. and Spanos, P. D., *Stochastic Finite Elements: A Spectral Approach*, Dover, New York, 2003.

[81] Pettit, C., Hajj, M. R., and Beran, P. S., "Gust Loads with Uncertainty Due to Imprecise Gust Velocity Spectra," *48th AIAA/ASME/ASCE/AHS/ASC Structures, Structural Dynamics, and Materials Conference*, AIAA Paper No. 2007-1965, 2007.

[82] Abed, E. H. and Fu, J. H., "Local Feedback Stabilization and Bifurcation Control. I. Hopf Bifurcation," *Systems & Control Letters*, Vol. 7, 1986, pp. 11–17.

[83] Abed, E. H. and Fu, J. H., "Local Feedback Stabilization and Bifurcation Control. II. Stationary Bifurcation," *Systems & Control Letters*, Vol. 8, 1987, pp. 467–473.

[84] Librescu, L., Na, S., Marzocca, P., Chung, C., and Kwak, M. K., "Active Aeroelastic Control of 2-D Wing-Flap Systems Operating in an Incompressible Flowfield and Impacted by a Blast Pulse," *Journal of Sound and Vibration*, Vol. 283, 2005, pp. 685–706.

[85] Kang, W., "Bifurcation Control via State Feedback for Systems with a Single Uncontrollable Mode," *SIAM Journal on Control and Optimization*, Vol. 38, 2000, pp. 1428–1452.

[86] Gomez, J. C. and Garcia, E., "Morphing Unmanned Aerial Vehicles," *Smart Materials and Structures*, 2011, doi:10.1088/0964-1726/20/10/103001.

[87] Tieleman, H. W., Ge, Z., Hajj, M. R., and Reinhold, T. A., "Wind Tunnel Simulation of Time Variations of Turbulence and Effects on Pressure on Surface-Mounted Prisms," *Journal of Wind Engineering and Industrial Aerodynamics*, Vol. 88, 2003, pp. 197–212.

[88] Tieleman, H. W., "Universality of Velocity Spectra," *Journal of Wind Engineering and Industrial Aerodynamics*, Vol. 56, 1995, pp. 55–69.

[89] Pagnini, L. C. and Solari, G., "Gust Buffeting and Turbulence Uncertainties," *Journal of Wind Engineering and Industrial Aerodynamics*, Vol. 90, 2002, pp. 441–459.

[90] Saltelli, A., Chan, K., and Scott, E. M., editors, *Sensitivity Analysis*, Wiley, New York, 2000.

[91] Saltelli, A., *Global Sensitivity Analysis: The Primer*, Wiley, Chichester, England, 2008.

[92] Pettit, C. L., "Uncertainty Quantification in Aeroelasticity: Recent Results and Research Challenges," *Journal of Aircraft*, Vol. 41, 2004, pp. 1217–1229.

[93] Tennekes, H. and Lumley, J., *A First Course in Turbulence*, The MIT Press, Ma, 1972.

[94] Frisch, U., *Turbulence: The Legacy of A, N. Kolmogorov*, Cambridge University Press, England, 1995.

[95] Hoblit, F. M., *Gust Loads on Aircraft: Concepts and Applications*, AIAA Education Series, 1988.

[96] MIL, *U.S. Military Handbook MIL-HDBK-1797*, 1997.

[97] Pettit, C. L., Hajj, M. R., and Beran, P. S., "A Stochastic Approach for Modeling Incident Gust Effects on Flow Quantities," *Probabilistic Engineering Mechanics*, Vol. 25, 2010, pp. 153–162.

[98] Paola, M. D., "Digital Simulation of Wind Field velocity," *Journal of Wind Engineering and Industrial Aerodynamics*, Vol. 74-76, 1998, pp. 91–109.

[99] Grigoriu, M., *Stochastic Calculus: Applications in Science and Engineering*, Cambridge University Press, New York, 2002.

[100] Wang, Z., *Time-Domain Simulations of Aerodynamic Forces on Three-Dimensional Configurations, Unstable Aeroelastic Responses, and Control by Network Systems*, Ph.D. thesis, Virginia Tech, Blacksburg, VA, 2004.

[101] Nuhait, A. O. and Mook, D. T., "Aeroelastic Behavior of Flat Plates Moving Near the Ground," *Journal of Aircraft*, Vol. 47, 2010, pp. 464–474.

[102] Helton, J. C. and Davis, F. J., *Sampling-Based Methods*, Wiley, New York, 2000.

[103] Helton, J. C. and Davis, F. J., "Latin Hypercube Sampling and the Propagation of Uncertainty in Analyses of Complex Systems," *Reliability Engineering and System Safety*, Vol. 81, 2003, pp. 23–69.

[104] Hosder, S., Walters, R. W., and Rafael, P., "A Non-Intrusive Polynomial Chaos Method for Uncertainty Propagation in CFD Simulations," *Proceedings of the 44th AIAA Aerospace Sciences Meeting and Exhibit*, AIAA Paper No. 2006-891, 2006.

[105] Mola, A., Ghommem, M., and Hajj, M. R., "Sensitivity Analysis of Olympic Boat Dynamics," *Proceedings of the 13th AIAA/ISSMO Multidisciplinary Analysis Optimization Conference*, AIAA Paper No. 2010-9395, 2010.

[106] Reagan, M., Najm, H. N., Ghanem, R. G., and Knio, O. M., "Uncertainty Quantification in Reacting Flow Simulations through Non-Intrusive Spectral Projection," *Combustion and Flame*, Vol. 132, 2003, pp. 545–555.

[107] Liang, C., Ou, K., Premasuthan, S., Jameson, A., and Wang, Z. J., "High-order Accurate Simulations of Unsteady Flow Past Plunging and Pitching Airfoils," *Computers and Fluids*, Vol. 40, 2010, pp. 236–248.

[108] Nuhait, A. O. and Zedan, M. F., "Numerical Simulation of Unsteady Flow Induced by a Flat Plate Moving Near Ground," *Journal of Aircraft*, Vol. 30, 1993, pp. 611–617.

[109] Chabalko, C. C., Snyder, R. D., Beran, P. S., and Parker, G. H., "The Physics of an Optimized Flapping Wing Micro Air Vehicule," *Proceedings of the 47th AIAA Aerospace Science Meeting Including The New Horizons Forum and Aerospace Exposition*, AIAA Paper No. 2009-801, 2009.

[110] Ennos, A. R., "The Kinematics and Aerodynamics of the Free Flight of some Diptera," *Journal of Experimental Biology*, Vol. 142, 1989, pp. 49–85.

[111] Fry, S. N., Sayaman, R., and M.H.Dickinson, "The Aerodynamics of Hovering Flight in Drosophila," *Journal of Experimental Biology*, Vol. 208, 2005, pp. 2303–2318.

[112] He, J., Verstak, A., Watson, L. T., and Sosonkina, M., "Performance Modeling and Analysis of a Massively Parallel DIRECT—Part 1," *International Journal of High Performance Computing Applications*, Vol. 23, 2009, pp. 14–28.

[113] He, J., Verstak, A., Watson, L. T., and Sosonkina, M., "Performance Modeling and Analysis of a Massively Parallel DIRECT—Part 2," *International Journal of High Performance Computing Applications*, Vol. 23, 2009, pp. 29–41.

[114] He, J., Watson, L. T., and Sosonkina, M., "Algorithm 897: VTDIRECT95: Serial and Parallel Codes for the Global Optimization Algorithm DIRECT," *ACM Transactions on Mathematical Software*, Vol. 36, 2009, pp. 1–24.

[115] Svanberg, K., "The Method of Moving Asymptotes– a New Method for Structural Optimization," *International Journal for Numerical Methods in Engineering*, Vol. 24, 1987, pp. 359–373.

[116] Svanberg, K., "A Class of Globally Convergent Optimization Methods Based on Conservative Convex Separable Approximations," *SIAM Journal on Optimization*, Vol. 12, 2002, pp. 555–573.

[117] McClung, A., Maple, R., Kunz, D., and Beran, P. S., "Examining the Influence of Structural Flexibility on Flapping Wing Propulsion," *Proceedings of the 49th AIAA/ASME/ASCE/AHS/ASC Structures, Structural Dynamics, and Materials Conference*, AIAA Paper No. 2008-1816, 2008.

[118] Preidikman, S., *Numerical Simulations of Interactions Among Aerodynamics, Structural Dynamics, and Control Systems*, Ph.D. thesis, Virginia Tech, Blacksburg, VA, 1998.

[119] Preidikman, S. and Mook, D., "Time-Domain Simulations of Linear and Nonlinear Aeroelastic Behavior," *Journal of Vibration and Control*, Vol. 6, 2000, pp. 1135–1175.

[120] Shyy, W., Berg, M., and Ljungsqvist, D., "Flapping and Flexible Wings for Biological and Micro Air Vehicles," *Progress in Aerospace Science*, Vol. 35, 1999, pp. 455–505.

[121] Supekar, A. H., *Design, Analysis and Develpoment of a Morphable Wing Structure for Unmanned Aerial Vehicle Performance Augmentation*, Master's thesis, The University of Texas at Arlington, Arlington, TX.

[122] Khan, Z. A. and Agrawal, S. K., "Design of Flapping Mechanisms Based on Transverse Bending Phenomena in Insects," *Processdings of 2006 IEEE International Conference on Robotics and Automation*, 2006.

[123] Khan, Z. A. and Agrawal, S. K., "Optimal Hovering Kinematics of Flapping Wings for Micro Air Vehicles," *Journal of Aircraft*, Vol. 49, 2011, pp. 257–268.

[124] Fejtek, I. and Nehera, J., "Experimental Study of Flapping Wing Lift and Propulsion," *Aeronautical Journal*, Vol. 84, 1980, pp. 28–33.

[125] Cao, Z., Easterling, D., Watson, L., D. Li, K. C., and Feng, W.-C., "Power Saving Experiments for Large-Scale Global Optimisation," *International Journal of Parallel Emergent Distributed Systems*, Vol. 25, 2010, pp. 381–400.

[126] Easterling, D. R., Watson, L. T., and Madigan, M., "The DIRECT Algorithm Applied to a Problem in Biomechanics with Conformal Mapping," *Proceedings of the International Conference on Scientific Computing*, CSREA Press1, 2010.

[127] Hemker, T. and Werner, C., "DIRECT using Local Search on Surrogates," Tech. rep., 2011, Technishe Universitat Darmstadt.

[128] Panning, T. D., Watson, L. T., Allen, N. A., Chen, K. C., Shaffer, C. A., and Tyson, J. J., "Deterministic Parallel Global Parameter Estimation for a Model of the Budding Yeast Cell Cycle," Tech. rep., 2006, Computer Science Department, Virginia Tech.

[129] Kogiso, N., Watson, L. T., Gurdal, Z., Haftka, R. T., and Nagendra, S., "Design of composite laminates by a genetic algorithm with memory," *Mechanics of Composite Materials Structures*, Vol. 1, 1994, pp. 95–117.

[130] Nagendra, S., Jestin, D., Gurdal, Z., Haftka, R. T., and Watson, L. T., "Improved genetic algorithms for the design of stiffened composite panels," *Computers and Structures*, Vol. 58, 1996, pp. 543–555.

[131] Lentink, D., U. K. Muller, E. J. S., de Kat, R., van Gestel, W., Veldhuis, L. L. M., Henningsson, P., Hedenstrom, A., Vielder, J. J., and van Leeuwen, J. L., "How Swifts Control their Glide Performance with Morphing Wings," *Nature*, Vol. 446, 2007, pp. 1082–1085.

[132] Meseguer, J., Franchini, S., Perez-Grande, I., and Sanz, J. L., "On the Aerodynamic of Leading-edge High-lift Devices of Avian Wings," *Journal of Aerospace Engineering*, Vol. 219, 2005, pp. 63–68.

[133] Denny, M., "Dynamic Soaring: Aerodynamics for Albatrosses," *European Journal of Physics*, Vol. 30, 2009, pp. 75–84.

[134] Pennycuick, C. J., "Wingbeat Frequency of Birds in Steady Cruising Flight: New Data and Improved Predictions," *Journal of Experimental Biology*, Vol. 199, 1996, pp. 1613–1618.

[135] Videler, J. J., *Avian Flight*, Oxford Ornithology Series, New York, 2005.

[136] Tucker, V. A. and Parrott, C. C., "Aerodynamics of Gliding Flight in a Falcon and other Birds," *Journal of Experimental Biology*, Vol. 52, 1970, pp. 345–367.

[137] Pennycuick, C. J., *Bird Flight Performance: A Practical Calculation Manual*, Oxford Science Publications, New York, 1989.

[138] Withers, P. C., "An Aerodynamic Analysis of Bird Wings as Fixed Airfoils," *Journal of Experimental Biology*, Vol. 199, 1981, pp. 143–161.

[139] Dial, K. P., "Avian Forelimb Muscles and Nonsteady Flight: Can Birds Fly without Using the Muscles in Their Wings?" *The Auk*, Vol. 109, 1992, pp. 874–885.

[140] Bonser, R. H. C. and Purslow, P. P., "The Young's Modulus of Feather Keratin," *Journal of Experimental Biology*, Vol. 198, 1995, pp. 1029–1033.

[141] Tobalske, B. W. and Dial, K. P., "Flight Kinematics of Black-Billed Magpies and Pigeons over a Wide Range of Speeds," *Journal of Experimental Biology*, Vol. 199, 1996, pp. 263–280.

[142] Tobalske, B. W., Warrick, D. R., Clark, C. J., Powers, D. R., Hedrick, T. L., Hyder, G. A., and Biewener, A. A., "Three-Dimensional Kinematics of Hummingbird Flight," *Journal of Experimental Biology*, Vol. 210, 2007, pp. 2368–2382.

[143] Tian, X., Iriarte-Diaz, J., Middleton, K., Galvao, R., Israeli, E., Roemer, A., Sullivan, A., Song, A., Swartz, S., and Breuer, K., "Direct Measurements of the Kinematics and Dynamics of Bat Flight," *Bioinspiration and Biomimetics*, 2006, pp. 10–18.